# PROCESS INDUCED DEFORMATION OF COMPOSITE MATERIALS: AN EXPERIMENTAL METHODOLOGY, SYSTEMATIC REVIEW AND META-ANALYSIS

by

YUPING TAO

B.A.Sc, University of British Columbia, 2018

A THESIS SUBMITTED IN PARTIAL FULFILMENT OF

THE REQUIREMENTS FOR THE DEGREE OF

MASTER OF APPLIED SCIENCE

in

THE FACULTY OF GRADUATE AND POSTDOCTORAL STUDIES

(Materials Engineering)

THE UNIVERSITY OF BRITISH COLUMBIA

(Vancouver)

April 2021

The following individuals certify that they have read, and recommend to the Faculty of Graduate and Postdoctoral Studies for acceptance, the master's thesis entitled:

Process Induced Deformation of Composite Materials: An Experimental Methodology, Systematic Review and Meta-analysis

submitted by    Yuping Tao      in partial fulfillment of the requirements for

the degree of    Master of Applied Science

in                Materials Engineering

**Examining Committee:**

Anoush Poursartip, Professor, Materials Engineering, UBC
Supervisor

Göran Fernlund, Associate Professor, Materials Engineering, UBC
Supervisory Committee Member

Yasmine Abdin, Assistant Professor, Materials Engineering, UBC
Supervisory Committee Member

# Abstract

The ability to consistently produce composite structures with controlled tolerance remains a challenge for commercial aerospace applications. Dimensional discrepancies between the true geometry and designed geometry leads to custom shimming processes or forced assembly, which can be costly and/or reduce structural performance. Thus, further understanding and better management of process-induced deformation (PID) is needed.

In the present work, process induced deformation, manifesting itself as spring-in and warpage of L-shapes, is studied experimentally. A rigorous methodology is developed to address the gaps in the literature and identify the variabilities in the composite manufacturing processes. The methodology includes an accurate and automated analysis method whereby point cloud data of the L-shapes obtained by laser CMM is processed to distinguish the nuances of spring-in and warpage. Processing parameters such as laminate dimensions and cure cycles, which have been under-studied or the cause of disagreement, are shown to have meaningful impact on PID.

The second half of the work presents a systematic review conducted for 94 experimental studies and over 2000 process induced deformation specimens from the open literature. This dataset is believed to be representative and as thorough as possible. A meta-analysis was performed on a subset of specimens made with three materials systems: HEXCEL AS4/8552, TORAY T800/3900-2 and CYCOM IM7/5320-1. This systematic review reveals disagreements within the PID literature and highlights the high variability in the composite manufacturing process which hinders direct comparison across studies and full understanding of PID. The meta-analysis investigates the data consistency, and probes the influences of laminate thickness, layup type, gelation temperature and other processing parameters, providing insight into the spring-in phenomena as seen by the combined literature.

iii

# Lay Summary

Carbon fiber (aka. Carbon fiber reinforced polymer, CFRP) is nowadays increasingly used in aircraft structures. Comparing to their metal counterparts, CFRP structures can be made larger and more complicated which saves tremendous amounts of time and money during assembly and the production of aircraft.

However, controlling the precise dimensions of the composite structures is an on-going challenge. The manufactured composite components often have different dimensions from the nominal design. CFRP L-shapes are commonly used to join and stiffen various structures. They also capture the physics of the problem and are used as representative geometries to study this dimensional difference.

In this thesis, a methodology is developed for using L-shapes to experimentally investigate the dimensional changes. L-shapes are made to study how thickness, length and changes in the manufacturing process can affect the dimensional difference. Lastly, physical data in the open literature regarding this problem are combined to show useful insights.

# Preface

This thesis entitled "Process Induced Deformation of Composite Material – An Experimental Methodology, Systematic Review and Meta-analysis" presents the research conducted by Yuping Tao while under the supervision of Professor Anoush Poursartip at the University of British Columbia. All chapters in this thesis have been written by Yuping Tao under the supervision of Professor Anoush Poursartip.

All experiments discussed in Chapter 3 was designed and conducted by Yuping Tao under the assistance of Dr. Navid Zobeiry and the supervision of Professor Anoush Poursartip.

The original analysis procedure in Chapter 4 was developed by Yuping Tao with assistance from Alastair McKee at Convergent Manufacturing Technologies, Inc (CMT). Sam Reid at CMT programmed the analysis procedure into a robust and user-friendly Python code. The development process was entirely under the supervision of Professor Anoush Poursartip.

The systematic review and meta-analysis in Chapter 5 was designed and conducted by Yuping Tao under the supervision of Professor Anoush Poursartip.

# Table of Contents

# List of Tables

# List of Figures

# List of Symbols

| Sign | Description | SI Unit |
|------|-------------|---------|
| $\alpha$ | Degree of Cure | |
| H | Heat of reaction normalized by mass | $Jkg^{-1}$ |
| $H_t$ | Total heat of reaction | $Jkg^{-1}$ |
| l | Flange length | mm |
| R | Radius | mm |
| t | Thickness | mm |
| T | Temperature | °C |

# List of Abbreviations

| | |
|---|---|
| **CFRP** | Carbon Fiber Reinforced Polymer |
| **CMM** | Coordinate Measurement Machines |
| **CMT** | Convergent Manufacturing Technologies |
| **CRN** | Composites Research Network |
| **CTE** | Thermal Expansion Coefficients |
| **DMA** | Dynamic Mechanical Analysis |
| **DOC** | Degree of Cure |
| **gsm** | Gram per square meter |
| **MLS** | Moving Least Square |
| **NCAMP** | National Center for Advanced Materials Performance |
| **PCL** | Point Cloud Library |
| **PID** | Process Induced Deformation |
| **Prepreg** | Pre-impregnated Composites |
| **R&D** | Research and Development |
| **TC** | Thermocouple |
| **$T_g$** | Glass Transition Temperature |
| **TPI** | Tool Part Interaction |
| **UD** | Unidirectional |

# Acknowledgements

# Chapter 1: Introduction

Owning to their remarkable strength and stiffness to weight ratios, carbon fiber reinforced polymer (CFRP) have been widely adopted in strength critical structures, in particular nowadays in the aerospace industry. The base cost for composite materials is higher comparing to traditional materials, such as metal, but the lower cost in machining and assembling have largely offset it.

A major challenge for further reducing the manufacturing cost is consistently producing parts with controlled tolerances. Changes made to the manufacturing process, such as autoclave cure cycle modifications, can directly influence dimensions of the produced parts. Understanding the causality between process changes and part final geometry exactness is crucial to reduce iteration and costly shimming during assembly. Consequently, numerical and experimental studies have 666666666been conducted with the aim to predict the distortion behaviors. Physics-based models are generated to link processing parameters to the final dimensional change.

Process simulation and models need physical data as validation. Whenever discrepancy exists between the simulations and experiments, is it crucial to understand which one was problematic. Better again, instead of validating against a stand-alone dataset, having the resource and capability to cross-compare datasets can provide in-depth insights on the influence of processing parameters with much higher confidence.

L-shaped composite structures, widely used as brackets, are common subjects for studying dimensional fidelity. Once manufactured, residual stresses can drive a change in the enclosed angle of the L-shape and the flatness of the L-shape flanges, commonly known as spring-in and warpage.

In academia, considerable efforts have been made to understand the influence of various processing parameters and deformation mechanisms of the deformation. Typically, studies investigate the effect of one or a set of processing parameters on PID. However, non-standardized manufacturing strategies, deformation definitions and measurement methods have obstructed the full understanding of the system level problem. Few core experimental datasets have been generated throughout 1970s to-date, yet sizable discrepancies exist among them.

In industrial production environments, significantly more specimens are produced than academia. One common solution to process induced deformation is tool compensation. However, currently the exact compensated amount is typically achieved by iterative prototypes or decided based on experience which can be expensive and process specific.

In this work, a rigorous methodology has been developed to address the non-standardized manufacturing strategies, deformation definitions and measurement methods. The methodology was used to investigate an experimental dataset which probed the effects of laminate dimensions and cure cycles on PID of L-shapes. The second half of the work conducted a systematic review which combined existing datasets in the open literature and results from this work. A meta-analysis was also performed to shed light on the effects of the various processing parameters on PID.

# Chapter 2: Background and Literature Review

## 2.1 Prepreg Material Overview

The material of interest for this study is unidirectional (UD) prepreg carbon fiber with thermoset resin. Prepreg is commonly referred as a reinforcing fabric which has been pre-impregnated with a resin system, generally high performance epoxy [1]. Resin was already mixed with the hardener so prepregs are ready to be laid into the mold without the addition of any more resin upon using. Since the resin and hardener are already combined, prepregs need to be stored in freezers to retard the chemical reaction process. Once thawed, pre-preg are laid into the mold layer by layer, along with other consumables, which is then cured in an autoclave following specially designed cure cycles to form the final part.

## 2.2 Autoclave Processing Overview

The scope of this research is limited to components made with prepreg carbon fiber reinforced polymer combined with autoclave curing.

An autoclave is a machine which provides an environment of elevated temperature and pressure comparing to ambient temperature and pressure. An autoclave typically has a blower and thermal management hardware to circulate gas and achieve heating and cooling. It is a critical piece of equipment for the composite manufacturing because the high pressure it offers can result in parts having better compaction, higher fiber volume fraction and less porosity [2].

Once the composite parts are laid up, autoclave applies a vacuum, temperature and pressure cycle (AKA. Cure cycle) prescribed by the operator to cure the resin and solidify the composite material. The accuracy of the temperature and pressure applied by the autoclave has direct and significant impact on the quality, longevity and dimensional stability of the finished products. From the composite material engineering standpoint, it is essential to be able to control and monitor the parameters through the autoclave. Lastly, temperature and pressure history throughout the manufacturing cycle should be easily obtainable and analyzed to link process parameters to manufacturing outcomes.

## 2.3    Thermoset Resin

Matrix materials for advanced composite materials are either thermoset or thermoplastic polymers. This thesis focuses on thermoset polymeric resins. During the curing of a thermoset resin, low molecular weight, low viscosity monomers undergo irreversible cross-linking which converts the resin into a three-dimensional network. The cross-linking process is an exothermic chemical reaction and most often facilitated by the supply of external heat [1]. As cross-linking takes place, molecules become less mobile. When cross-linking reaches a point where the resin forms a rubbery solid and is no longer able to flow, the resin is considered as gelled. Once resin gels, the modulus starts to develop, and the resin is able to bear stress. Further reaction leads to additional cross-linking until the resin fully cures, forming one large molecular network.

### 2.3.1    Degree of Cure (DoC)

The degree of cure (DOC), α, of a thermoset resin system is a state variable that describes the resin cure progression. In other words, degree of cure defines the fraction of material reacted. Because

the cross-linking process is an exothermic reaction, the degree of cure is typically measured by the heat of reaction using a differential scanning calorimeter (DSC). Degree of cure ranges from 0 to 1 and is defined as:

$$\alpha = \left(1 - \frac{H}{H_t}\right) \cdot 100\%$$

Where H is heat of reaction normalized by mass. $H_t$ is the total heat of reaction [3]. DoC is an important parameter for process simulation because most resin properties are functions of the extent of resin cure at a given time.

### 2.3.2   Gelation

Gelation marks the resin transition from a viscous fluid to a rubbery solid [4][5]. Once resin gels, not only is it no longer able to flow, the resin modulus starts to develop and the resin is able to bear stress. For a given thermoset resin, gelation happens at a constant range of degree of cure independent of cure path. For AS4/8552, the degree of cure at gelation is around 0.55 [6].

### 2.3.3   Glass Transition Temperature ($T_g$) and Vitrification

$T_g$ for a thermoset resin marks the temperature range where resin transitions from a glassy solid to a soft, rubbery material. The transition can occur during either a heat up or a cool down. $T_g$ evolves with the material throghout the cure. Typically, $T_g$ is higher than the cure temperature for a fully cured thermoset resin. Once a thermoset resin is heated to its $T_g$, the cross-links in molecular arrangement still holds but is no longer frozen in place. Physically, the resin modulus decreases, and the resin becomes soft. Other material properties such as thermal expansion coefficients will also vary when material is heat to $T_g$. $T_g$ can also be reduced significantly by moisture absorption. [7]–[9]

5

Vitrification of a thermoset resin marks the transition from a rubbery state to a glassy state. This typically happens when $T_g$ exceeds the curing temperature during a cure cycle ($T_g > T + 28$ °C according to CMH-17, 2012). For example, if an uncured resin is subjected an isothermal hold, polymer cross-linking increases; the resin $T_g$ increases pass the isothermal hold temperature, resin vitrifies. When a rubbery resin is subjected to a cool-down and resin temperature drops below $T_g$, resin also vitrifies. Once vitrified, resin cure rate slows down drastically; and the curing reaction becomes diffusion dominant. However, unlike gelation, vitrification is reversable [5], [9], [10].

### 2.3.4 Thermal Expansion and Contraction

As thermoset composites are being processed with high temperature cure cycles, CTEs of the fiber and resin need to be carefully evaluated to understand internal stress development. Fiber and resin have different CTEs. Carbon fiber has a constant and very low (to slightly negative) CTE in the longitudinal direction [11], [12]. Whereas thermoset resin typically has higher CTE values and they evolve as cure progresses. Duffner characterized the resin CTE evolution into three distinct ranges: $CTE_{liquid}$, $CTE_{rubbery}$ and $CTE_{glassy}$. As the cure progresses and forms more cross-links, resin is less capable to expand or contract. Thus, $CTE_{liquid} > CTE_{rubbery} > CTE_{glassy}$ [9].

In the context of orthotropic fiber reinforced composites, because resin before the onset of gelation is a viscous liquid, minimal internal stresses are formed at this stage. However, once gelled, the resin-fiber interface is established; thermal strains in resin caused by cure cycle heat ups and cool downs can result in stresses within the laminates. Generally, CTEs in the fiber directions are lower than the CTEs in directions where there are no fiber constraints and are resin dominant. Hence, when temperature changes, different thermal strains are produced. This strain mismatch is one of the most prominent drivers for distortion of curved composites.

### 2.3.5    Cure Shrinkage

As cross-linking progresses, volume in the molecular arrangement and molecular chain mobility decrease. Physically, resin shrink in volume and become more viscous. Volumetric cure shrinkage for AS4/8552 has been reported around 4.95% in the literature [13].

Like thermal strain, the cure shrinkage strain in pre-preg also depends heavily on fiber orientation. Ersoy and Mehmet proved that cure shrinkage strain in the through-thickness direction is higher than the in-plane directions for a cross-ply laminate. This mismatch of cure shrinkage strain is another predominant driver for PID. Furthermore, the same study discovered the through-thickness cure shrinkage strains for cross-ply laminates were doubled that of unidirectional laminates due to fiber constraining the in-plane shrinkage [11], [14].

## 2.4    Deformation of L-shapes

Composite L-shapes deform in a complex manner during curing. The deformation involves the interaction between the corner area and the flanges. As shown in Figure 2.1, typically on a convex (male) tool, the enclosed angle of the L-shape decreases after cure while the flanges of the L-shape can also exhibit warpage. The driving mechanisms are different for the corner and flange deformation. Aggravating the situation, shearing between the plies links the corner deformation and flange deformation.

Although L-shape is a simple geometry, the deformation of an L-shape which can be affected by various sources and mechanisms hitherto not fully understood. The sources and mechanism causing an L-shape to deform during processing can be categorized into three levels: micro, macro and component (Table 2.1). The outcomes of these mechanisms are either some types of stress or bending moment that drives the change of shape of the composite part. The sources and mechanism are largely determined by the design of the component, selected material systems and processing conditions. The full list of processing parameters that could affect PID is listed in Table 2.2. These are the knobs to manipulate the sources and mechanism, which result in different amount of total stresses and deformation.

Adding to the complexity, the way spring-in is measured is inconsistent within the literature, which makes it challenging to collate the results from different researchers and understand this system level problem. The following sections will address these gaps and inconsistencies and review works in literature that studied the effects of different processing parameters on the corner and flange deformation.
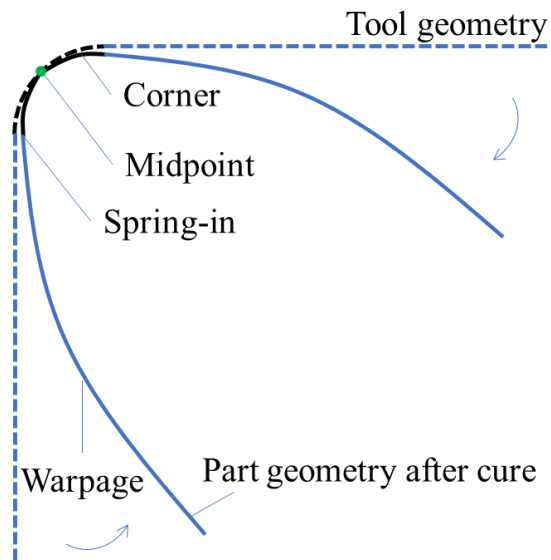
Figure 2.1 Schematic of L-shape deformation. Tool and part are plotted such that the midpoints are coincident

Table 2.1 Source and mechanism for process induced deformation on micro, macro and component level

|  | Source | Mechanism |
|---|---|---|
| Micro level | • Thermal strain (CTE)<br>• Cure shrinkage<br>• Vf gradient<br>• Elastic and viscoelastic properties | • Mismatch in through thickness and in-plane directions<br>• Mismatch between fiber and matrix |
| Macro level | • Temperature gradient<br>• DoC gradient<br>• Uneven resin flow | • Through thickness property gradient<br>• Shear lag |
| Component level | • Tooling:<br>  ▪ Thermal gradient<br>  ▪ Thermal strain<br>  ▪ Friction | • Heat transfer<br>• Tool part interaction |

Table 2.2 Processing parameters that can affect the sources and mechanism of process induced

deformation organized in ETPM framework

| Equipment | Tool | Part | Material & Processing |
|---|---|---|---|
| • Autoclave<br>• Oven<br>• Vacuum<br>• Airflow<br>• Part location<br>• Heat transfer coefficients | • Material (CTE)<br>  1. Steel<br>  2. Aluminum<br>  3. Invar<br>  4. Composite<br>• Substructure<br>• Tolerance | • Geometry<br>  1. Thickness<br>  2. C or L<br>  3. Length<br>  4. Angle<br>• Layup<br>• Ply drop off<br>• Core<br>• Insert | • Cure Cycle<br>  1. Pressure<br>  2. Temperature<br>• Bleeding<br>• Demolding<br>• Post process<br>  1. Machining<br>  2. Post curing<br>• Material<br>  1. Fiber<br>  2. Matrix<br>• Surface<br>  1. FEP<br>  2. Release agent<br>• Moisture |

### 2.4.1 Deformation of L-shapes: Spring-in Definition, Reporting format and Tooling Measurements

Considerable amount of experimental work has been done within the public literature regarding the origin and drivers for process induced deformation [14-48]. However, little attention has been paid to the standardization of the experimental approaches. The lack of standardization leads to variabilities across experimental data in the literature which obstruct the full understanding of PID. The lack of standardization can be reflected in the following issues:

1) Flange length dependent spring-in definition
2) Non-standardized reporting format
3) Lack of tooling inspection and compensation

The most widely adopted spring-in definition in literature treats L-shapes with different flange length the same. However, flange length can have significant impact on spring-in results if flange warpage exists.

Commonly for spring-in measurements in literature, dimensional data was first obtained either in 2D (image analysis, scanning) or in 3D (coordinate measurement machines, 3D full field scanners). Then a line (2D) or a plane (3D) was fitted to each flange of the specimen (e.g. [26], [36], [41], [50]). Subsequently the enclosed angle was calculated from the normal of the lines or the planes (Figure 2.2).

Pursuant to the abovementioned process, spring-in is typically reported as a single value (aka total spring-in), denoting the enclosed angle difference between the as built part and the tool. However,

if flange warpage exists, the spring-in angle is dependent on the length of the lines and planes as well as how they were fitted to the flanges (Figure 2.3).
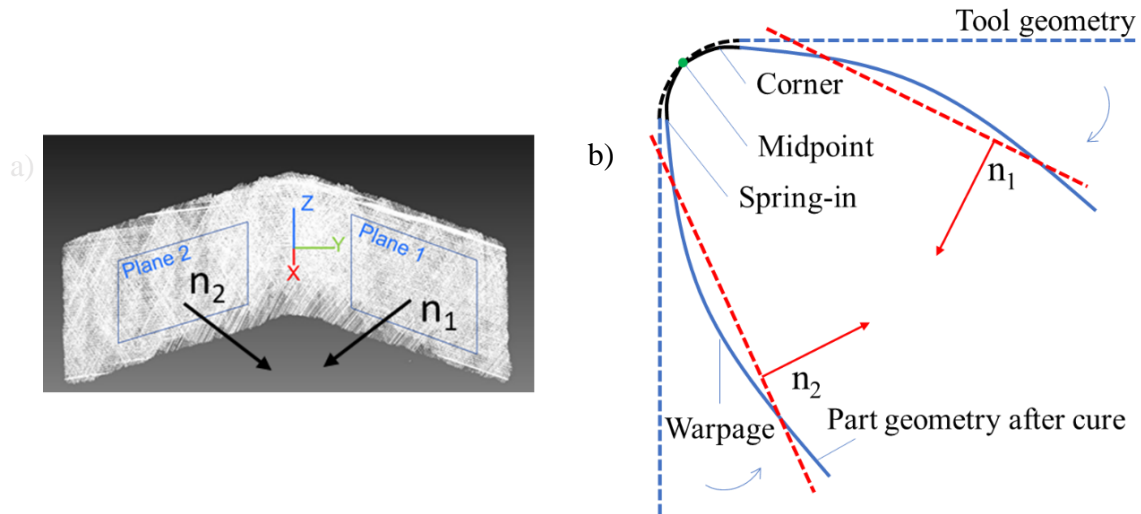


Figure 2.2 Traditional L-shape spring-in angle definition in a) 3D b) 2D; insufficient to characterize deformation with single spring-in value if flange warpage exists
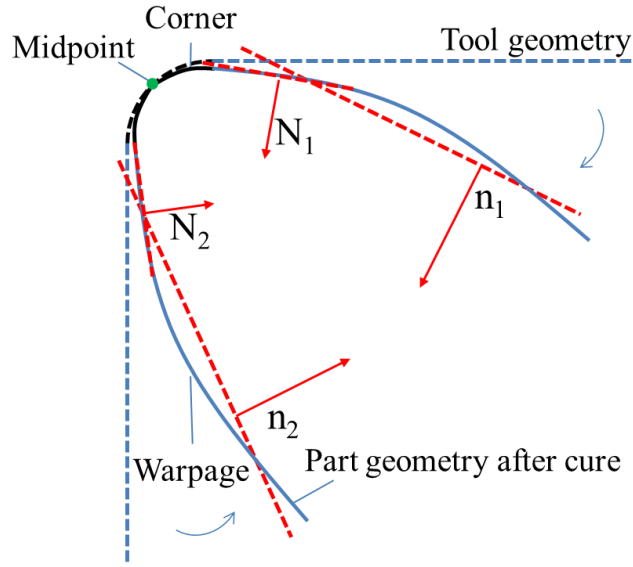
Figure 2.3 When flange warpage exists, angle formed by line fits at different sections of the flange can be different. $\angle$ (n1, n2) $\neq$ $\angle$ (N1, N2)

Few researchers have acknowledged that a single total spring-in angle value is insufficient to characterize L-shape distortion [18], [26], [36], [51], [52]. Rather, corner spring-in (which does not include the effects of flange warpage) should also be reported separately. However, there are no standards as to what results researchers should report. Albert et al. and Fortin reported spring-in and flange warpage in terms of the warped height and span of the specimens [53], [54]. Arafath et al. and Gordnian et al. supported reporting more than a single spring-in value; they reported corner spring-in and total spring-in values separately [31], [43]. Kappel et al. also supported that flange length should be considered as an essential parameter for warpage, however, specimens in their study did not show any significant flange warpage. Hence Kappel et al. reported total spring-in values [26].

The lack of standards not only makes cross-comparison difficult; it can also cause researchers to overlook processing parameters that could affect PID. For example, just 7 out of 92 studies with physical L-shape data in literature reported tooling measurement [36], [40], [41], [54]–[57]; and only 2 compensated spring-in angles with actual tool angles that could potentially deviate from the nominal specifications [36], [56]. Most studies reported spring-in values using the nominal tool angle; without mentioning the measurement of the tool. In those cases, the single reported spring-in value is merely a qualitative representation of the fabricated part. In the same front, the aerospace industry is much more rigorous with standardized measurement processes and well-defined tolerances for tooling and produced parts [58].

A standardized experimental approach specifying the preferred reporting items and a common spring-in definition that is independent on L-shape flange length can reduce the variabilities in the reported deformation across different studies. Measuring the tool and compensating the specimens fabricated from it can also increase the accuracy of the reported deformation. When data across studies are compared, the standardization can provide a common language in evaluating the results.

### 2.4.2  Deformation of L-shapes: Mechanisms

### 2.4.2.1  Material Anisotropy

The main driver for composite process induced deformation is material anisotropy. After being processed at an elevated temperature, composites undergo shape distortion. The through-thickness strain caused by resin cure shrinkage and thermal contraction is higher than the strain in the in-plane direction due to existence of the fiber [24], [49], [57], [59], [60]. The mismatch in strains drives interlaminar shear, bending of the corner section (corner spring-in) and bending of the flanges (warpage). The tradeoff between shear and bending for a given laminate thickness to length ratio largely determines the deformation of an L-shape [61]. Other mechanisms, such as tool part interaction and through thickness fiber volume fraction gradients can also impact the deformation. These mechanisms and associated processing parameters are discussed below.

Composites are intrinsically anisotropic. On a laminate level, CTE is higher in the through-thickness direction (matrix dominated) than that in the in-plane directions (fiber dominated). As temperature changes, this results in strain mismatch and curvature change in curved sections [62]. During the cool-down stage of a cure cycle, the temperature of an L-shape decreases from curing temperature (180 °C for AS4/8552 used in this study) to room temperature, causing more thermal contraction in the through-thickness direction than the in-plane directions. This strain mismatch in an angled laminate manifests in either interlaminar shear stress, or, bending stresses in the curved section and flanges.

Cure shrinkage causes further volume change on top of the thermal effects. Like thermal contraction, because fibers are aligned in the in-plane direction, the resin cure shrinkage is less

than that in the through-thickness direction where there is no fiber [49]. This strain mismatch also drives interlaminar shear and bending. However, it is important to point out that cure shrinkage and thermal effects are not necessarily occurring at the same time during a cure cycle.

Between gelation and vitrification, the resin interlaminar shear modulus is low comparing to in-plane modulus, some through thickness strain is released via inter-ply shearing (Figure 2.4b), alleviating some residual stresses and decreases overall deformation[24], [61]. Beside the ratio of in-plane modulus to resin interlaminar shear modulus, the amount of shear is also a function of specimen arc and flange length to thickness ratio (t/l). Thin laminates with long flanges are more difficult to shear comparing to short, thick laminates [39].

The remaining portion of the through-thickness strain that is not sheared out results in bending of the corner and the flanges. Upon de-molding, the deformation is released (Figure 2.4c). As mentioned previously, given all other processing conditions to be the same, the tradeoff between bending and shear is based on the L-shape geometry. Historically, Wisnom illustrated the tradeoff between shear and bending without incorporating the flanges [24]. In the extreme case where there is negligible shear stiffness, plies can shear freely against each other and there is no spring-in deformation. The latest analytical solution by Takagaki et al [61]. extended shear lag analysis to account for the effect of L-shape flanges. The study revealed the portion of residual stress that was not sheared out can cause bending in both the corner and flanges. The latest analytical solution is implemented in commercial software such as RAVEN from Convergent Manufacturing Technologies for rapid calculation of spring-in of L-shapes [63].

The strain mismatch and deformation caused by resin shrinkage is irreversible and commonly referred as non-thermoelastic deformation. Whereas the portion caused by thermal contraction is

referred as thermoelastic deformation. If the L-shape is heated back up, thermoelastic deformation

can be reversed.
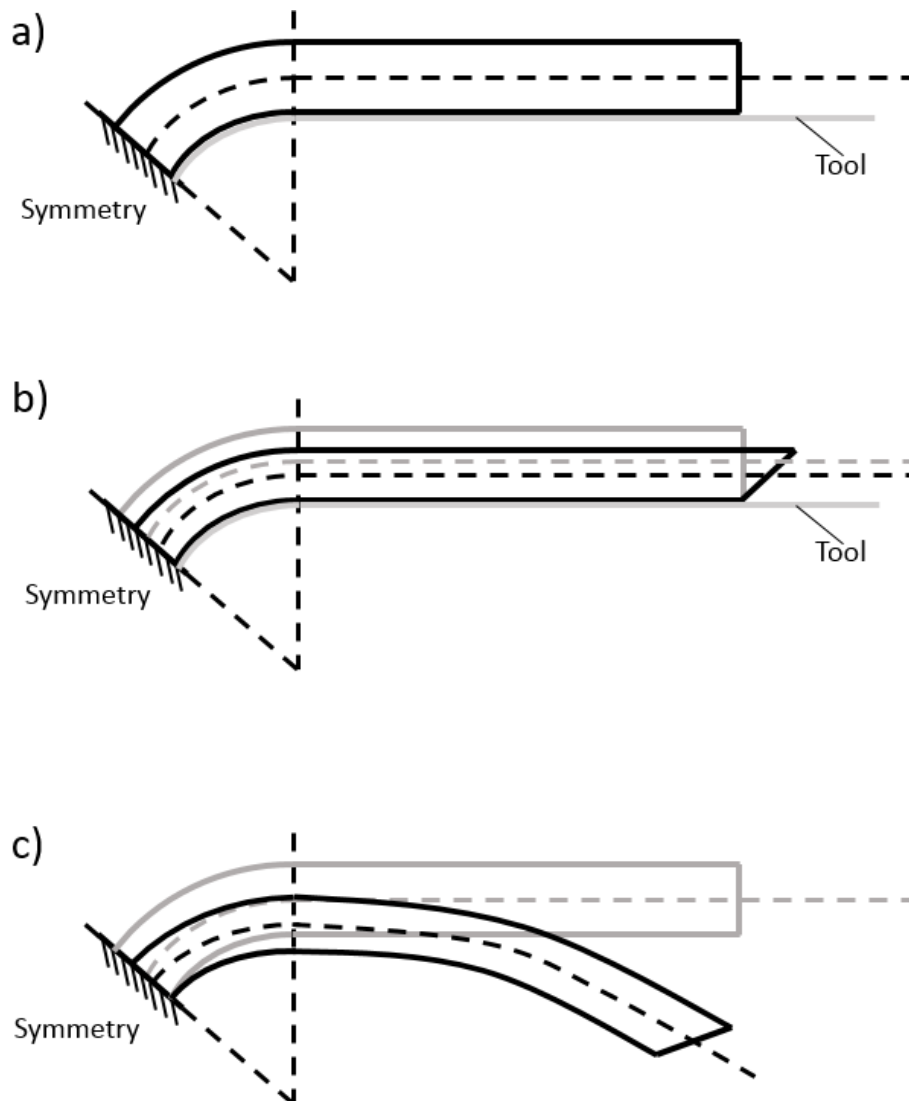


Figure 2.4 Half L-shape schematic due to symmetry a) initial shape on tool b) interlaminar shear

deformation on tool c) de-molded shape where interlaminar shear had taken place with bent

corner section and flange

### 2.4.2.2  Tool Part Interaction

In addition to the bending stresses caused by material anisotropy, tool part interaction is another driver for process induced deformation. Tool part interaction describes the coupling of the tool and the part during cure which induces residual stress and warpage. During the heat up of an autoclave cure cycle, the tool expands more than the laminate that is on the tool, imposing a tensile stress on the bottom of the laminate via friction/bonding (Figure 2.5 a). Since the resin degree of cure is still low, i.e. low shear stiffness, inter-ply slippage can release part of the tensile stress through the thickness of the laminate (Figure 2.5 b). This through thickness stress gradient is baked in as the cure progresses. Upon demolding, force equilibrium releases some of the tensile stress and results in a warped part (Figure 2.5 c). Tool part interaction is a function of part geometry, tool CTE, tool thickness, tool surface roughness, tool preparation specimen aspect ratio and cure cycle (material property evolution) [22], [64]–[66]. Although the boundary conditions are different comparing to flat plates, tool part interaction can be prominent in the flat flange portion in an L-shape.
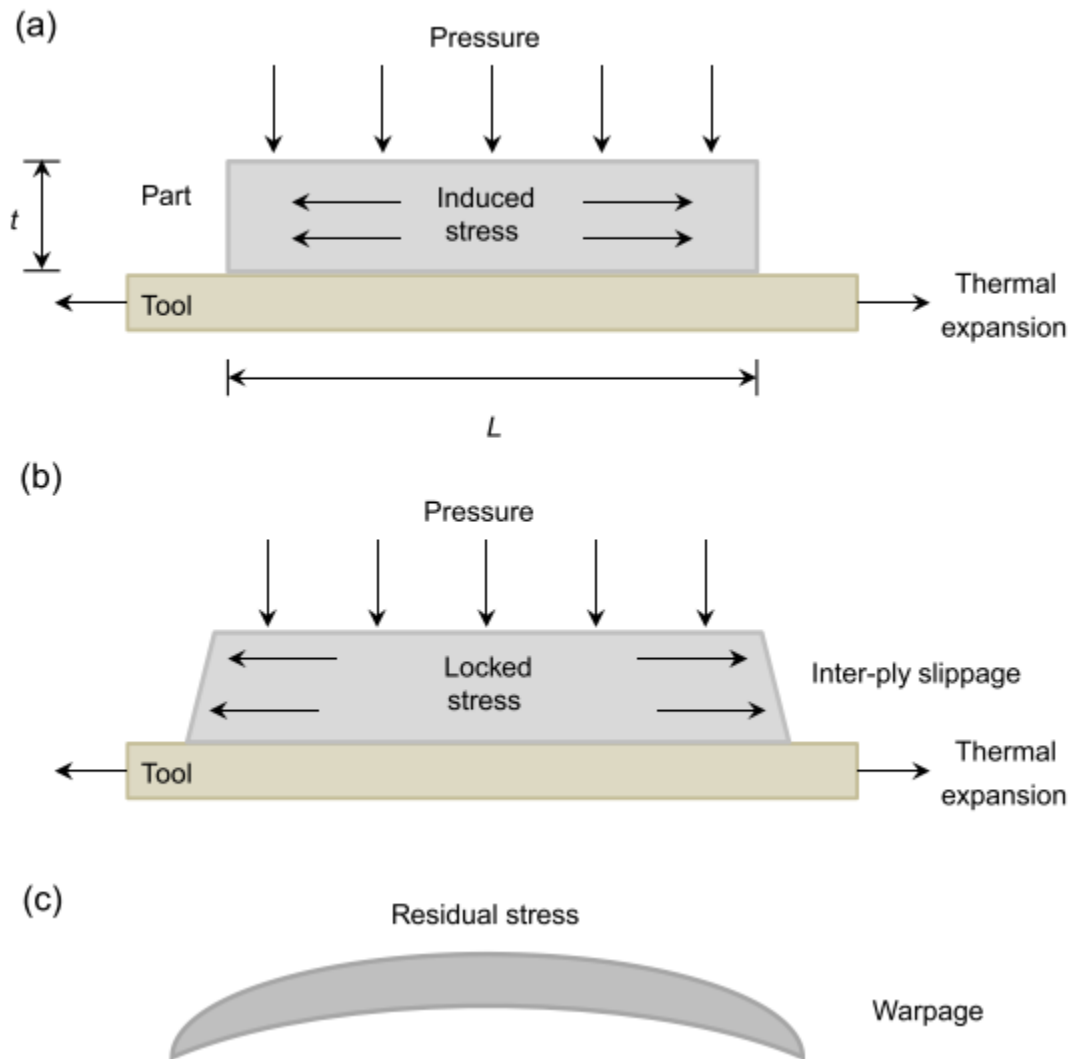
Figure 2.5 Development of tool part interaction and associated residual stress. a) tool expands more than the laminate in in-plane direction upon heating, inducing tensile stress in the laminate close to interface. b) Inter-ply slippage releases some tensile stress and through thickness stress gradient is locked in. c) Residual stress and warpage is formed upon demolding [5]

### 2.4.2.3    Other Mechanisms

Other process induced deformation sources and mechanisms such as fiber volume fraction gradient and through thickness time dependent vitrification (secondary effects) can also cause warpage [67], [68] and potential deformation in L-shapes.

Fiber volume fraction gradient is mainly related to specimens produced on single-sided tools. During processing, different setups can cause a variation in fiber volume fraction on the tool side and the bag side of the specimen, thus causing a through-thickness Vf gradient:

- If peel ply is used directly on top of the carbon fiber, the tool side of the specimen can develop a resin-rich layer while the bag side of the specimen can be relatively resin-poor
- If an FEP layer is used in-between the carbon fiber and breather cloth (Figure 3.21), the texture of the bag and the breather cloth can still imprint onto the bag side of the specimen, creating a microscopically uneven resin-rich layer. Being different from the resin-rich layer on the tool side, a Vf gradient can still exist.

Through-thickness fiber volume fraction gradient leads to varying stiffness and thermoelastic behavior from the top to the bottom of the laminate, potentially causing deformation.

The time dependent vitrification, aka, the pancake effect is a combination of through thickness property variance and tool part interaction. It describes the behavior where the top layers of the laminate were vitrified by the heated autoclave air earlier than the layers close to the tool. Compounding with tool part interaction, tensile strain was built into the bottom layers of the laminate. Tensile stain turns into compressive stain upon demolding, resulting in warpage [67].

### 2.4.3    Deformation of L-shapes: Effect of Cure Cycles

Process conditions can be modified to reduce residual stresses and process induced deformation. White and Hahn studied cure cycle optimization on residual stresses of flat graphite/BMI composite laminates [69]. They showed that slow cool down rate was able to enhance the stress relaxation which reduced the warpage by 12%. In addition, increased pressure during cool down was shown to have no impact on residual stress. Hugo et al. also suggested cool down slowly to reduce the "springback" (flat plate warpage) of Fiberite T300/976 graphite/epoxy composite [27]. Genidy, Russel and Madhukar used single fiber to experiment with cure cycles which minimized residual stresses during cure. Cure cycles were chosen such that thermal expansion of the matrix during heat up, matrix chemical cure shrinkage and matrix thermal contraction during cool down were balanced to produce the lowest amount of residual stress [70]–[72].

With additional mechanisms, few researchers have extended cure cycle modification to L-shapes, intending to reduce spring-in. Albert and Fernlund showed that two-hold cure cycles induced higher deformation than one-hold cure cycles for T800H/3900-2 [22], [57]. For IM7/5320-1, Arafath et al. showed cure cycle with lower initial hold temperature generated lower corner spring-in.

However, one important parameter within the process cycle modification is the resin gelation temperature. As the resin translates from a viscous fluid to a rubbery solid, resin modulus starts to develop, and resin can bear stresses. Stresses induced by thermal expansion during a heat-up stage between resin gelation and vitrification can have opposing effects to stresses induced by resin cure shrinkage, reducing specimen deformation [73]. Hence, having the resin gel at a lower temperature and timing the subsequent heat-up to the final cure temperature before the resin vitrifies can

effectively reduce spring-in. In fact, Gordian et al. [43] observed that spring-in is linearly correlated with gelation temperature for IM7/5320-1. However, only around 60 experimental L-shape specimen's data were found which focused on the effect of cure cycles, among which, discrepancies still exist (Chapter 5).

### 2.4.4   Deformation of L-shapes: Effect of Layup and Laminate Thickness

Thickness and layup are two of the most thoroughly studied processing parameters that can affect process induced deformation. Most studies in the literature reported the deformation (spring-in and warpage) decrease with increasing thickness [22], [26], [27], [29], [31], [46], [48], [49], [57], [59], [74]–[76]. This is expected because for a given flange length and layup the laminate bending stiffness increase as thickness increase. Further, thicker laminates better facilitate interlaminar shear, alleviating some residual stress and reducing deformation [61]. However, there were also a few studies reported laminate thickness has no influence on process induced deformation [15], [40], [41], [45], [77]. For warpage on the other hand, studies from the literature agree well among themselves, all indicating that thinner laminates warp more than thicker ones [22], [27], [57], [78].

Both sides of the argument also exist for whether layup influences spring-in. Several experimental studies stated that stacking sequence do not have a significant impact on spring-in [15], [22], [44], [45], [59], [99]. While others found layup affect spring-in in different ways [18], [26], [38], [40], [41], [57], [76], [79]. Multiple researchers suggested that the relative difference in in-plane and thru-thickness strain for different layup types could cause spring-in difference [18], [57], [79]. Others have related layup types to bending stiffness; laminates which are stiffer in the 0-direction (more 0 degree plies) would have less spring-in [26], [40], [41], [76]. Kappel suggested using

bending stiffness coefficient ($D_{22}$), which captures the effect of both layup sequence and laminated thickness, as a proxy for calculating spring-in [80].

### 2.4.5    Deformation of L-shapes: Effect of Flange Length

Flange length plays an important role in process induced deformation. Longer flange length can lead to increasing total spring-in in few different ways: hindering inter-ply shearing [61], increasing flange warpage due to tool part interaction [64] and the warped flanges are counted towards total spring-in during measuring. As a result, theoretically, total spring-in increase with increasing flange length. This has been experimentally observed by a few researchers [17], [26], [57]. However, data specifically focusing on the effect of flange length are limited.

### 2.5    Background and Literature Review Synthesis

Considerable amount of work has been done to understand the underlying mechanisms for process induced deformation. However, topics such as the effect of flange length and gelation temperature still have limited available data. Further, disagreements among the studies indicate that understanding the effects one (or a set of) processing parameter(s) with a small amount of data is a highly non-trivial task. Reasons listed in section 2.4.1 hinders the data coalition and comparison.

As more data are being generated and collected to progress the understanding of PID, a robust experimental approach which addresses the above-mentioned issues is necessary.  Further, a large amount of data is needed in order to better understand PID as a system level problem. One way to obtain a large amount of data is via pooling data within the literature.

## 2.6    Research Objectives and Approach

One goal of this research is to develop a rigorous methodology for experimentally studying PID of L-shapes and demonstrate the methodology by studying few processing parameters which either had little work found or the literature had disagreements upon. This methodology is designed to address the issues listed in section 2.4.1. One overarching theme is the generation, reduction and reporting of data. Hence, the methodology should standardize experimental approaches, measure methods and the reporting format in order to better understand PID and facilitate the collation of physical data from various studies.

Another objective is of this work is to obtain deeper insights by pooling data from specimens in the PID literature. Similar to systematic reviews and meta-analysis in medicine where clinical data are cumulated and summarized to keep clinicians abreast with current evidence-based medicine, this half of the study intends to consolidate previous process induced deformation datasets and provide insights of the current literature and trends regarding some processing parameters.

To achieve the above goals, the following objectives are defined:

- Incorporating tooling evaluation into the methodology for experimentally studying PID. Perform thermal characterization on the tool to make sure it is suitable for the intention of this study (section 3.3). Perform surface characterization of the tool to identify and quantify any defects or deviation from the nominal dimensions (section 3.4)
- Contribute a high-quality physical dataset designed to inquire the effect of laminate thickness, flange length and cure cycles on deformation of L-shapes. Document the

fabrication process intending to understand and quantify the causality between manufacturing steps and final deformation (section 3.5)

- Create a robust and automated analysis tool to define and quantify L-shape deformation. The analysis tool should take L-shape specimen point cloud as input; and generate outputs which precisely describe the L-shape deformation and compatible with the traditional spring-in results from literature (section 4.2). The analysis tool should also be capable of processing tooling surface data

- Report the adjusted L-shape deformation results according to tool characterization discoveries (section 4.5)

- Pooling physical L-shape data within open literature. Create database which document the processing parameters and results of the collected L-shapes. Perform meta-analysis and draw trends for the effect of various processing parameters on L-shape deformation. Evaluate how the results from this study stand within the literature data pool (Chapter 5)

# Chapter 3: Experiments

## 3.1    Introduction

This chapter presents the experimental design and procedures to study the effect of laminate thickness, flange length and cure cycle on deformation of L-shapes.

The material used in this study was HexPly AS4/8552 manufactured by HEXCEL Corporation, areal weight 190 gram per square meter (gsm) and 35% resin content (by weight). The material label is shown in Figure 3.1.



Figure 3.1 Label of Uni-directional HexPly AS4/8552 prepreg roll used in this study. Produced on 1st June, 2013 with 12K fiber tows.

8-ply and 16-ply specimens were made with the baseline cure cycle to investigate the effect of laminate thickness. L-shapes with 25.4 mm, 50.8 mm, 101.6mm and 152.4 mm flange length were selected to study the effect of flange length. Three different cure cycles, varying from one baseline

cure cycle, were designed with the assistance of RAVEN simulation software to inquire the effect of gelation temperatures and ramp rates.

The thermal behavior and surface profile of the invar tool were characterized in this study. The tool thermal characterization ensured the specimens at different locations on the tool had similar thermal history and would reach the target temperature ramp rates (section 3.3). Whereas the surface profile characterization shed insights on surface imperfections which could impact specimen deformation (section 3.4).

Furthermore, the manufacturing procedures for the AS4/8552 L-shape specimens are described in detail (section 3.5). Experiments were divided into two phases. Phase 1 focused on the effect of laminate thickness and flange length on the L-shape deformation. The focus of phase 2 was the effect of cure cycle and flange length. Once the specimens were cured and demolded, they were scanned by the CMM (section 3.6). The resultant point cloud files feed into the data reduction process in Chapter 4.

## 3.2 Cure Cycle Development

Cure cycles used to manufacture the L-shapes can induce thermal and chemical stresses which deform the specimens. Cure cycle parameters, such as resin gelation temperature and ramp rates can alter the amount of residual stresses within a specimen. Three cure cycles along with a baseline cure cycle were designed to induce different levels of stresses in L-shaped specimens and consequential deformation was analyzed.

RAVEN simulation software [63] was utilized to design the cure cycles in this study. The AS4/8552 cure kinetics model and material properties used in RAVEN were developed by the National Center for Advanced Materials Performance (NCAMP) [6]. Resin gelled when degree of cure reached 0.545. Tooling material – invar 36 properties were obtained from ASM Metals Handbook according to the invar model in Raven [81]. Nominal cure cycle temperatures are illustrated in this section for the record (Table 3.1). For all the cure cycles, pressure was ramped to 586 kPa (85 psi) at the beginning and held at 586 kPa for the duration of the cure cycle. Nominal cure cycle parameters are listed below. Actual parameters are listed in section 4.4

Table 3.1 4 Nominal cure cycles for manufacturing the L-shape specimens

|  | Ramp 1 (°C /min) | Hold 1 T (°C) | Hold 1 t (min) | Ramp 2 (°C /min) | Hold 2 T (°C) | Hold 2 t (min) | Ramp 3 (°C /min) | Hold 3 T (°C) | Hold 3 t (min) |
|---|---|---|---|---|---|---|---|---|---|
| CC1 | 1 | 180 | 120 | | | | | | |
| CC2 | 1 | 140 | 140 | 0.3 | 180 | 90 | | | |
| CC3 | 1 | 140 | 140 | 5 | 195 | 5 | -3 | 180 | 120 |
| CC4 | 1 | 140 | 140 | | | | | | |

Cure cycle 1 was the baseline manufacturer recommended cure cycle (MRCC). Resin in cure cycle 1 gels around 173 °C according to the NCAMP material model exercised in RAVEN. To

investigate how spring-in deformation relates to gelation temperature, cure cycle 2 and cure cycle 3 were designed such that resin gels at a distinguishably lower temperature - 140 °C. 140 °C also keeps the total cure time reasonable and industrially relevant. Cure cycle 2 and cure cycle 3 (Figure 3.3, Figure 3.4) have identical first ramp and first hold. The DoC at the end of the first hold was around 0.71 according to the NCAMP 8552 material model. Cure cycle 2 and cure cycle 3 were designed to query the impact of different ramp rates after vitrification on deformation of the L-shapes.

Cure cycle 2 was designed to have a slow second ramp so that the resin temperature stays 20 °C below the glass transition temperature (stay vitrified) during the second ramp and second hold.

Cure cycle 3 was designed to have a rapid second ramp, pushing the resin to de-vitrification. De-vitrification forces vitrified, glassy resin back into the rubbery state. The hypothesis was that softened resin could release (shear out) some of the stresses that was locked in prior to de-vitrification, results in lower residual stresses. Caution was taken when designing cure cycle 3 considering the thermal lag of the autoclave and the large thermal mass of the invar tool. A temperature over-shoot of 197 °C was implemented to heat up the tool as fast as possible.

Cure cycle 4 replicated the first hold of cure cycle 2 and cure cycle 3 (Figure 3.5). Resin at the end of cure cycle 4 was gelled and vitrified. The DoC of the L-shapes at the end cure cycle 1, 2, 3 were about 90%, while samples were partially cured in cure cycle 4 to a DOC of 70%.
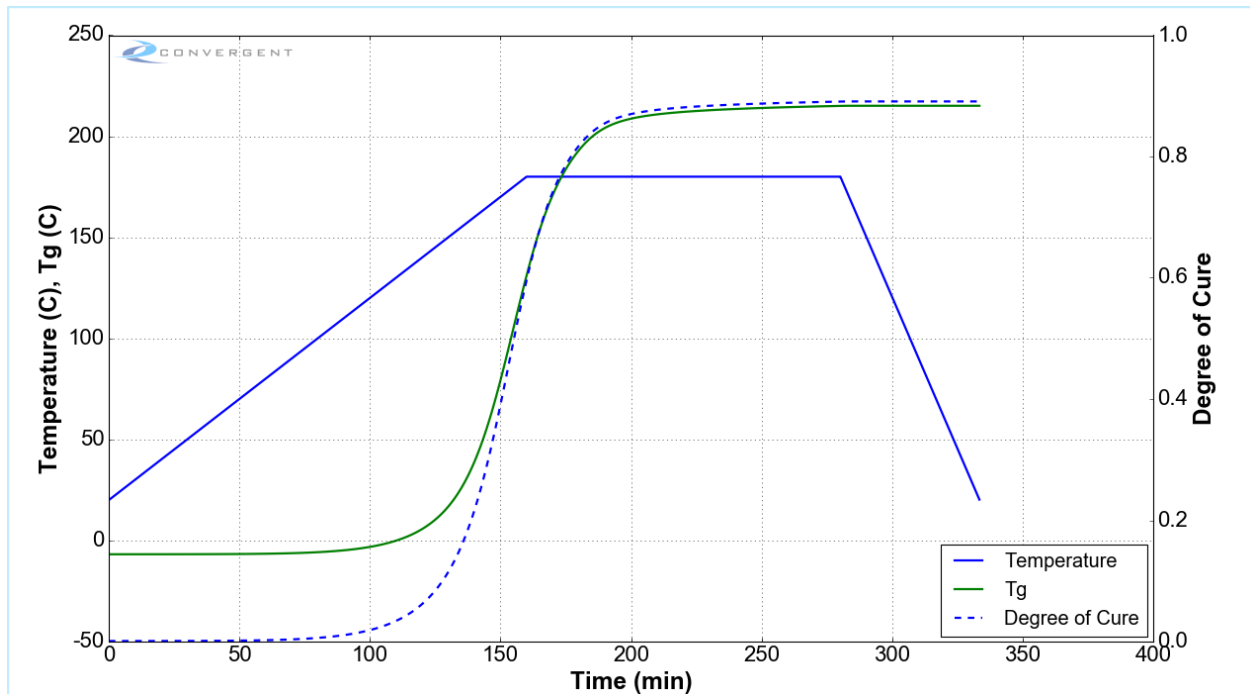
Figure 3.2 Cure cycle 1 nominal temperatures and degree of cure
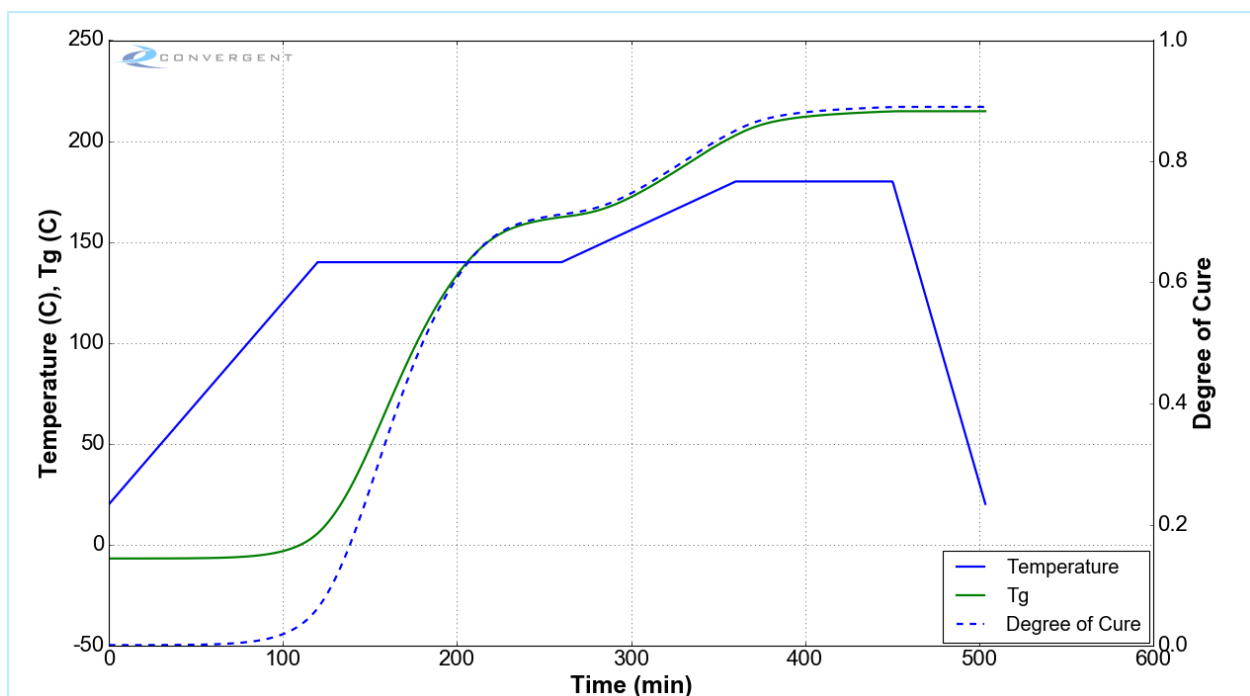


Figure 3.3 Cure cycle 2 nominal temperatures and degree of cure
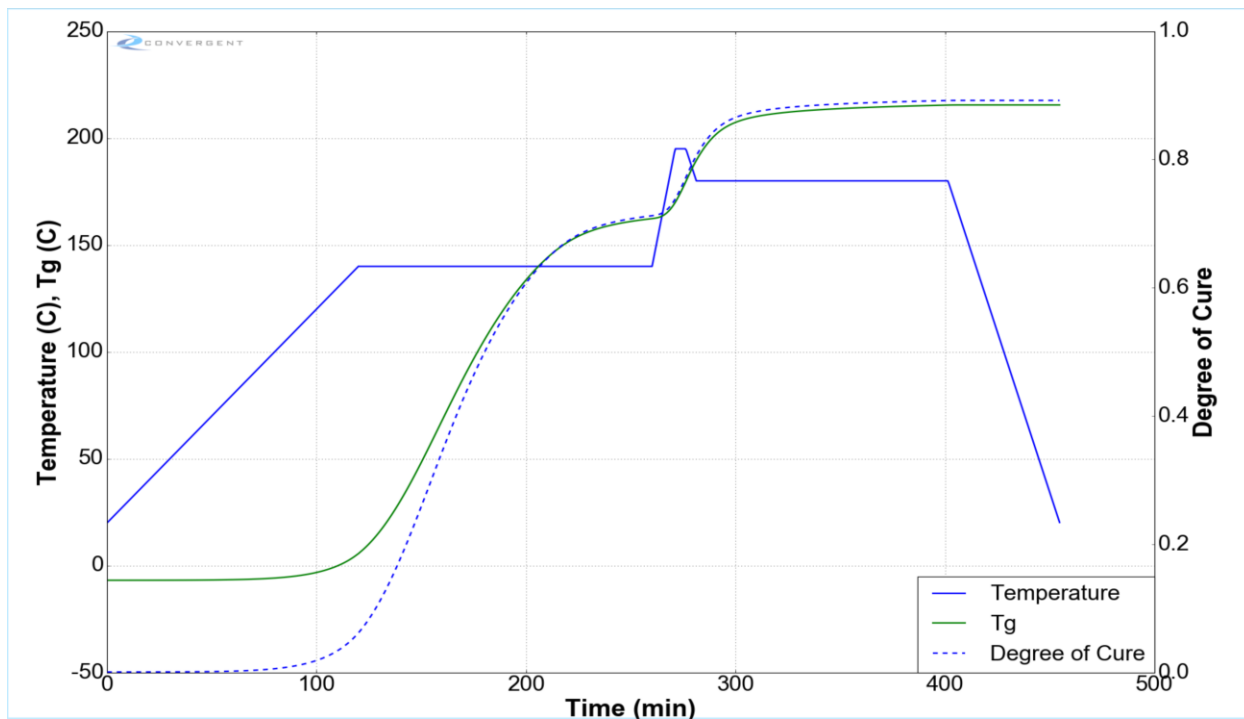
Figure 3.4 Cure cycle 3 nominal temperatures and degree of cure
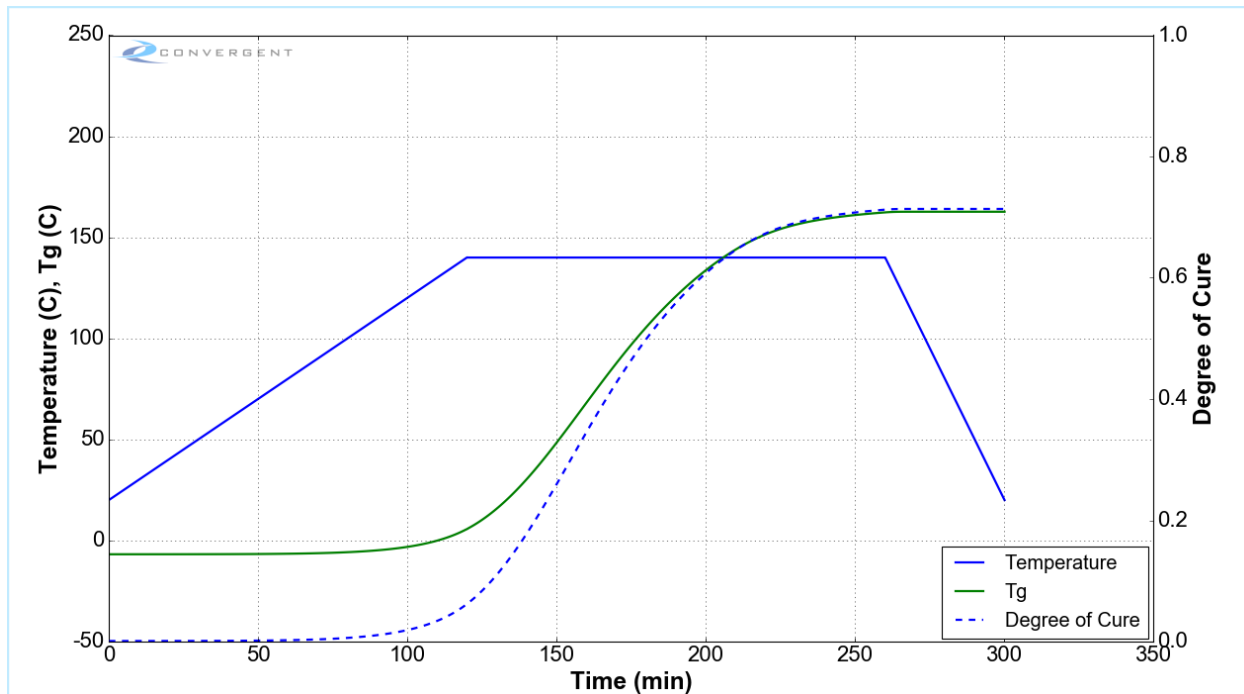


Figure 3.5 Cure cycle 4 nominal temperatures and degree of cure

### 3.3    Thermal Characterization of the Invar Tool

Specimens in this study were fabricated on the convex (male) portion of the same S-shaped invar tool as in Arafath et al. [31] and Gordnian et al. [43]. The nominal dimensions and locations where specimens were fabricated are shown in Figure 3.6. These locations were established by previous work to avoid non-uniform surface temperature during heat up caused by tooling substructures [31], [82].

To understand how the invar tool would respond to high ramp rates, it was tested against cure cycle 3, which was the most demanding cure cycle of the four. Cure cycle 3 contained a 5 °C/min ramp from 140 °C to 195 °C which was the maximum autoclave ramp rate and temperature. However, due to the large thermal mass of invar, the surface temperature ramp was less than 5 °C/min. The purpose of this thermal characterization was to ensure the specimen locations on the tool could consistently reach desired ramp rates.
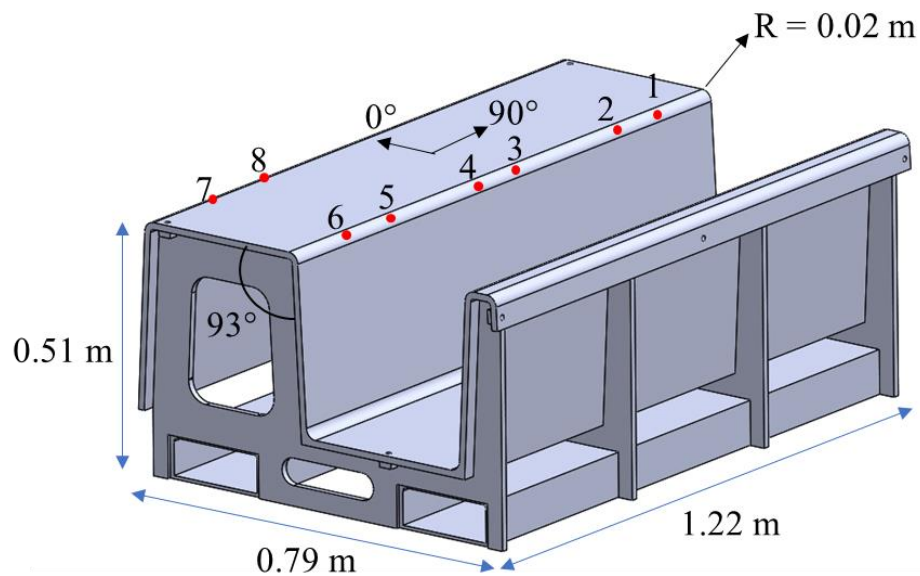


Figure 3.6 Schematic of invar tool that was used in this study

Thermocouples (TCs) were placed at position 1, 2, 5 and 7 where the phase 2 specimens were made (Figure 3.6). TCs were placed on the top, bottom of the tool as well as above the tool in the air at those positions. All TCs were place at the corner of the tool. TC placements, autoclave dry run and results were presented in the following subsections.

### 3.3.1  Thermocouple Placement

The procedure to place the thermocouples on the invar tool surface is described in this section and with graphic illustrations in Figure 3.7.

1. TC was first taped to the desired position.
2. The TC's tip was then covered with aluminum foil on the top and bottom. The purpose of the aluminum foil was to enable better contact and more even temperature measurement.
3. A thin sheet of silicone was then taped on top with double sided tape. The purpose of the silicone tape was to insulate the TC tip from the effect of surrounding environment.
4. Tacky tap was then used to cover the silicone sheet for further insulation.
5. Finally flash tape was used to hold everything down

All the TCs underneath the tool were setup with the same above-mentioned procedure. At position 1 and 7 there were weld spot underneath the tool. The TCs were placed directly on the weld, otherwise TCs were placed directly into the corners of the tool (Figure 3.8). The thermocouples were then numbered and mapped to the autoclave thermocouple ports of which the temperatures were recorded during the cure cycle (Figure 3.9).
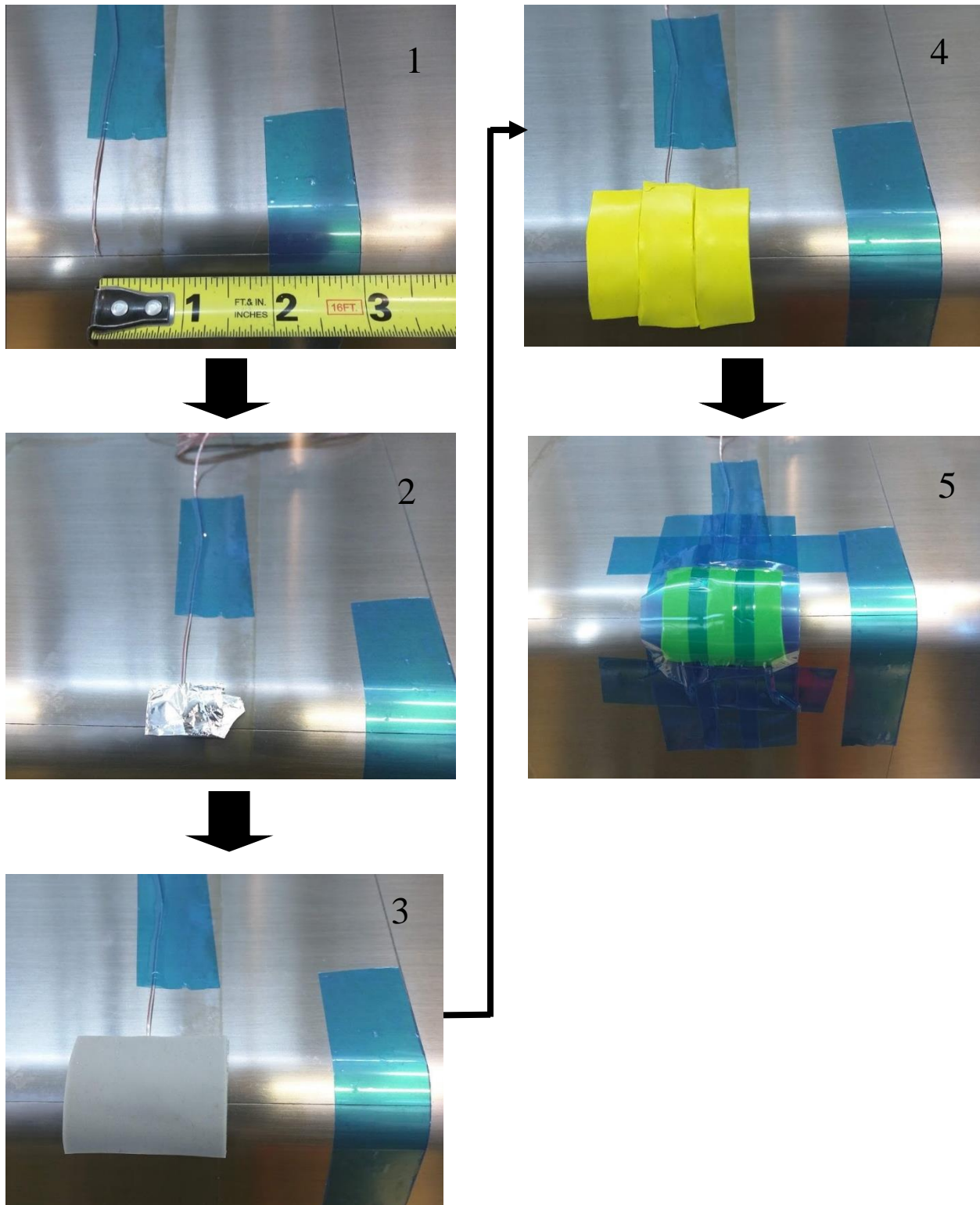
Figure 3.7 Procedure for placing thermocouples on tooling surface
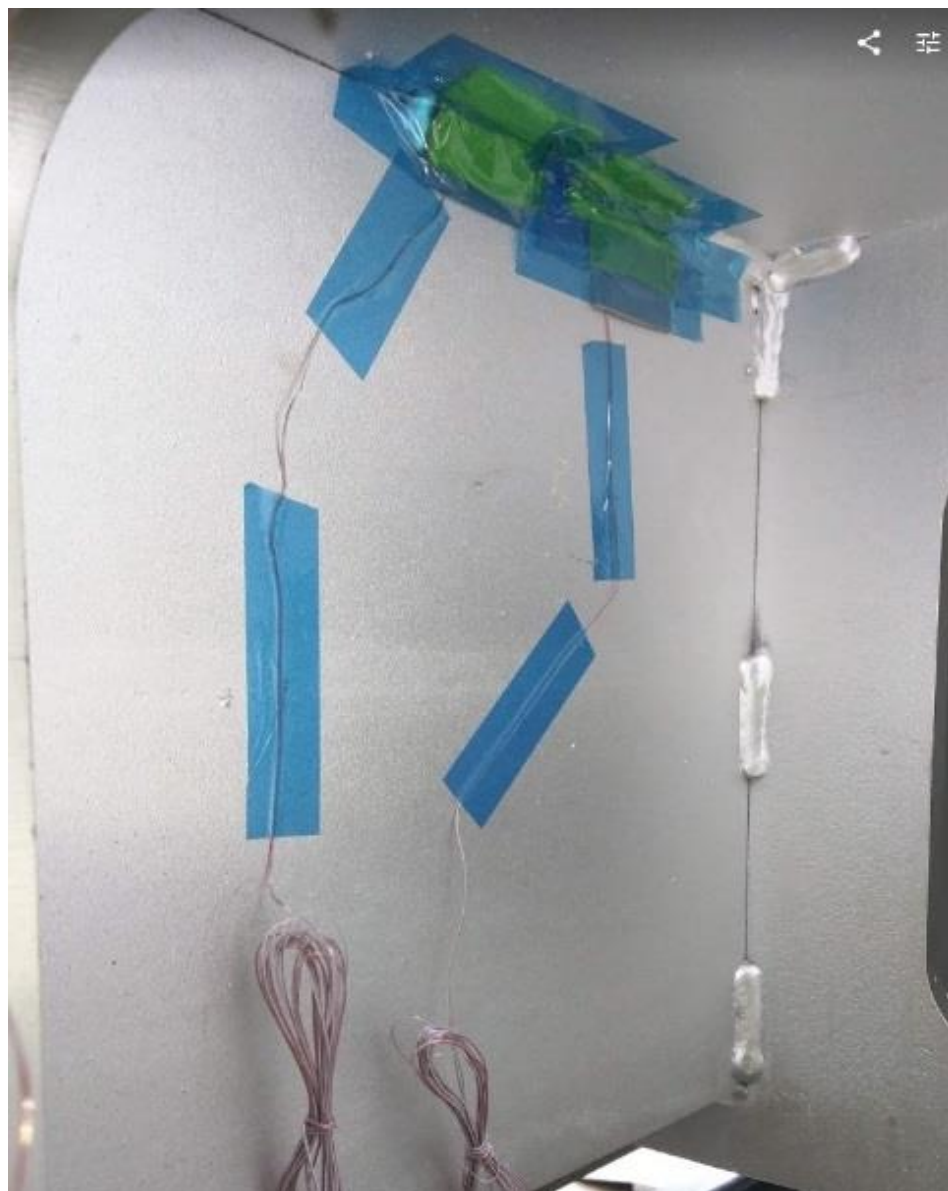
Figure 3.8 Placement of thermocouples underneath the tool face-sheets
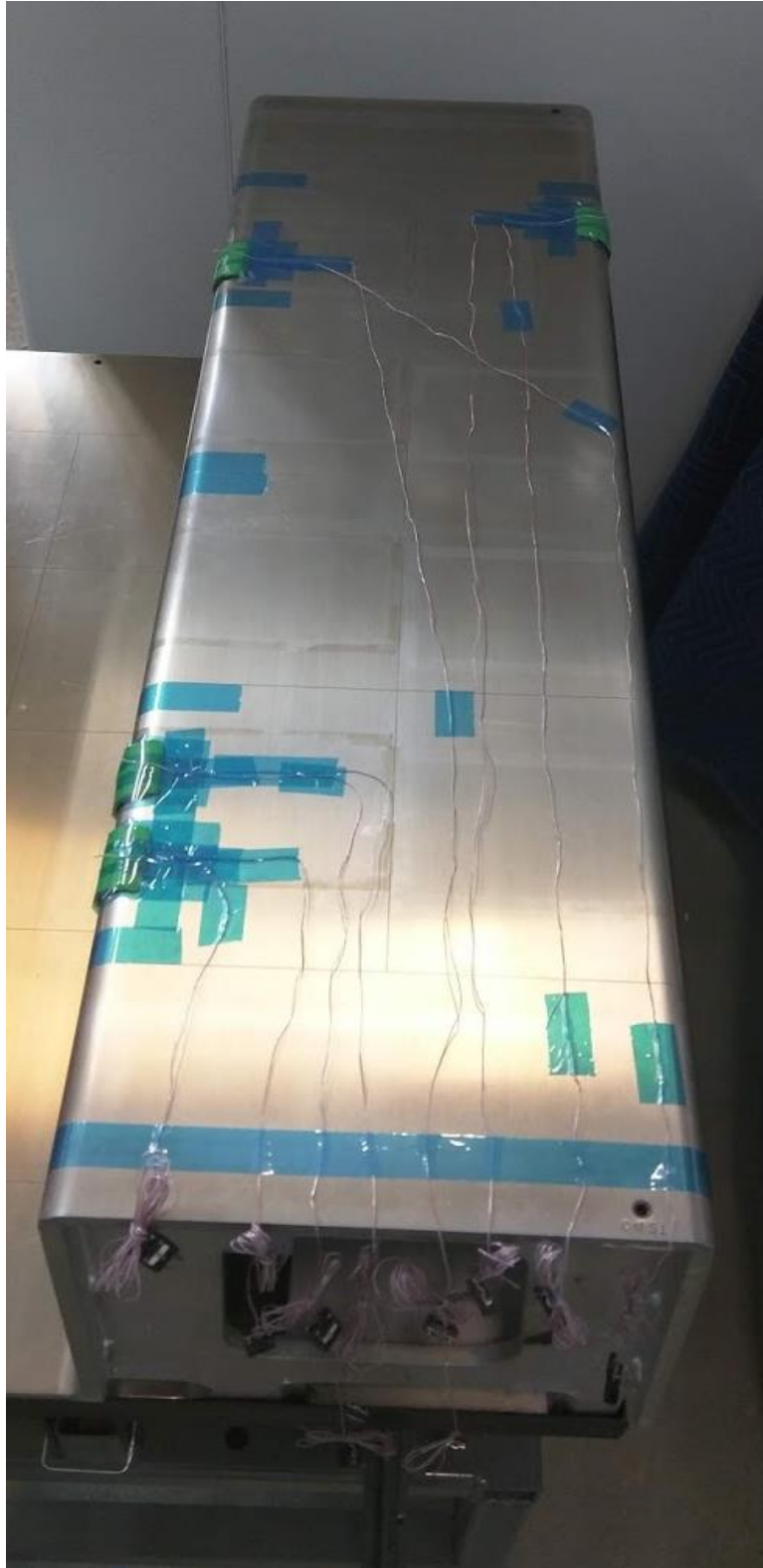
Figure 3.9 Invar tool with all thermocouples in place for thermal characterization

### 3.3.2    Autoclave Dry Run

To ensure the specimen locations on the tool have similar thermal behavior and would consistently reach desired ramp rates, the invar tool with TCs was tested with cure cycle 3. Since there was no specimen being cured and only the ramping response was of interest, the cure cycle holds were truncated to save time. The first hold was shortened from 150 mins to 30 mins. The second hold was shortened from 120 mins to 33 mins. The decision of truncating the holds were made during the cure cycle by commanding the autoclave to advance to the next stage when the tool TCs have all reached the targeted air temperature. Same pressure as the normal cure cycle 3 was applied.

Dry run temperature data are presented in Figure 3.10. The jigged series were TCs placed in the air. Fluctuations were results of the autoclave control system. The TCs that were placed against the tool surfaces had much smoother responses due to the large thermal mass of invar.

For the second ramp, the maximum programmable ramp rate in the autoclave is 7 °C/minute. However, the actual air temperature ramp rate within the autoclave was 5 °C/minute. Due to the large thermal mass of the invar tool, the ramp response of the tool surface was consequently 3.1 °C/minute for position 1, 2 and 5; 2.7 °C/minute for position 7 top surface and 2.5 °C/minute for position 7 bottom surface.
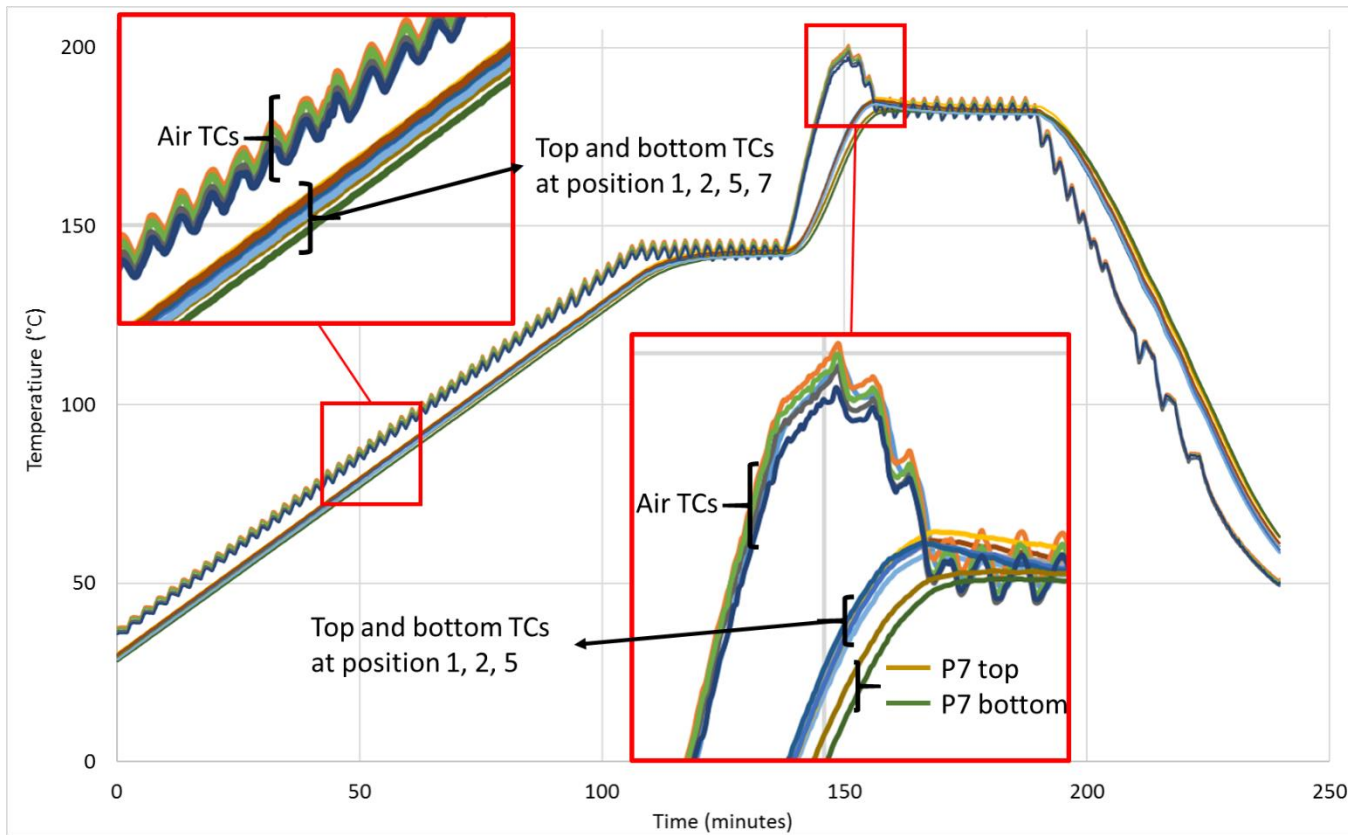
Figure 3.10 Invar tool thermal response under cure cycle 3

Air TCs had close values with the greatest difference being 3.78 °C between air TCs at position 2 and position 7 (happened at 150 mins). At the end of the second ramp, temperatures at the top of position 7 lagged the other positions by about 2.1 °C at maximum. This was because position 7 was located at the rear right of the autoclave where the air flow was worse, and HTCs were lower than the other positions [82]. However, surface TCs at position 1, 2 and 5 behaved similarly, showing no locational dependency.

Position 7 was consequently chosen to be the temperature monitoring position in all subsequent manufacturing runs. For every run a sacrificial specimen was placed at position 7 with a TC in the center mid-layer to monitor the worst-case curing condition (See section 3.5.3).

Overall, the dry run validated that position 1, 2 and 5 on the invar tool were able to reach 3.1 °C/minute in a synchronized manner. Position 7 lagged the other positions slightly due to poor autoclave airflow. Thus, it was sensible to place experimental specimens at location 1, 2 and 5 and place sacrificial temperature monitoring specimen at position 7.

## 3.4    Surface Profile Characterization of The Invar Tool

It is important to understand the tooling surface profile in order to fully understand the deformation of L-shaped specimens. A seemingly trivial but commonly made mistake in literature is comparing actual deformed part surface (or spring-in angle measurement) to ideal tool surface (ideal/nominal tool angle) or the model outputs (path 5, 6 in Figure 3.11). These comparisons can be inaccurate because the actual tooling imperfections are not considered. A good practice is to compare the actual deformed part surface (or angle) to the actual tool surface (angel) (path 1 in Figure 3.11).
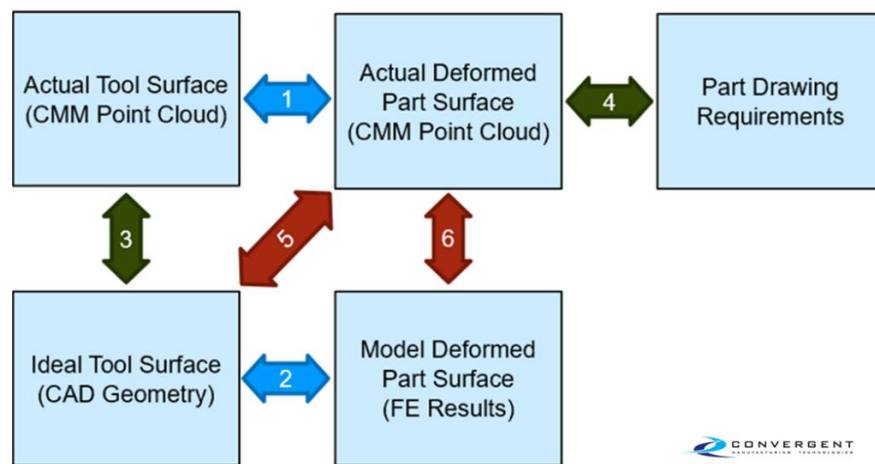


Figure 3.11 Different approaches when comparing surface dimensions in simulation space to physical space. Courtesy of Convergent Manufacturing Technologies

To obtain the L-shape specimen deformation in comparison to the tool, both the tool and the specimen surface profiles are required. Due to the large dimension and weight, the invar tool used was not able to be fit onto the laser CMM which was used to scan the specimens. Instead, a 2006 FARO arm Platinum, 6ft with a 3 mm touch probe were used to obtain the convex (male) portion surface profile of the tool (Figure 3.12). The accuracy of the FARO arm was around 20 µm (see details of the FARO arm in Appendix A).
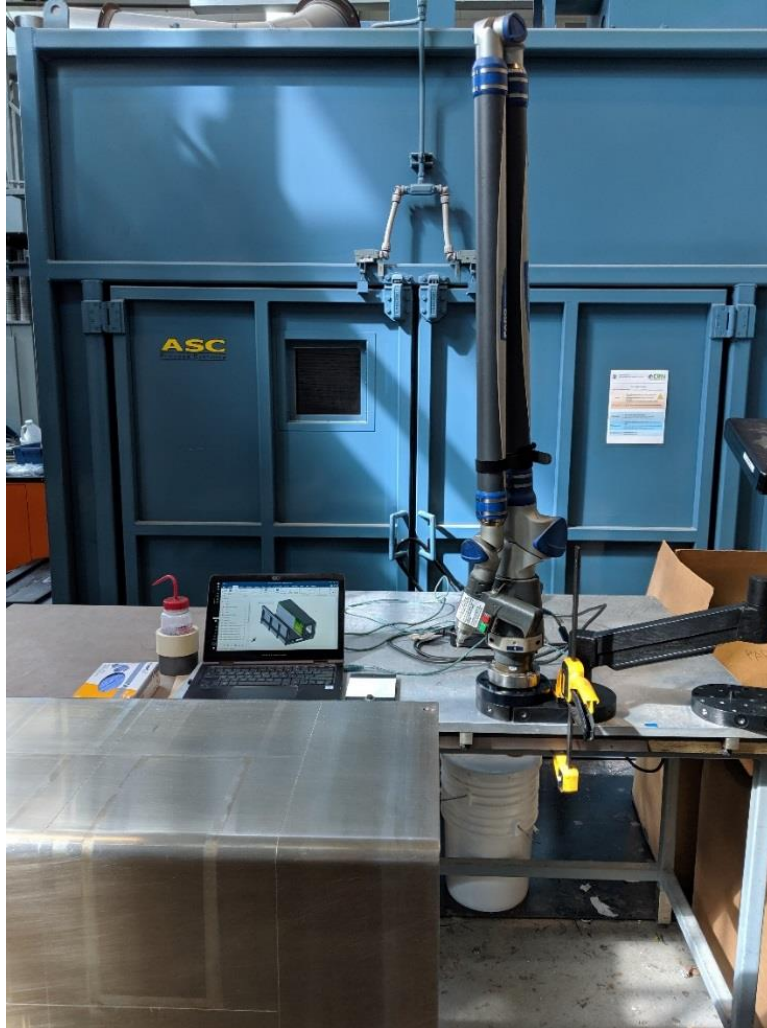
Figure 3.12 FARO arm setup for scanning surface profile of the invar tool

The FARO arm was bolted to a large aluminum plate which were fixed onto a workbench. The setup and the tool were placed on flat, stable ground surface in a minimum vibration environment. After following the calibration and alignment procedure provided, an 130,000-point point cloud was measured. The measurement method was set to "continuous" so that the probe took a measurement every 3 mm as it was lightly dragged across the surface of the tool. It was interesting to mention that when the probe was dragged across the tool surface, it was significantly easier to

make a scratch in the 0 direction than in the 90 direction (Figure 3.6). Kappel mentioned that the peripheral grinding process used to finish the tooling surfaces created anisotropy in roughness between the grinding direction and lateral direction [83]. The roughness in the grinding direction was measured to be four times smaller than the lateral direction. Kappel also showed the directional roughness difference decrease as the tool was being used due to release agent and residual resin filling up the surface. Since surface roughness was not a parameter of focus and all specimens were made with two layers of FEPs in this study; this topic was not pursued further. All the scanning measurements were performed in the 90 direction where the least scratches were created (Figure 3.13). The analysis of the tool point cloud and adjustment for specimen spring-in resutls is shown in section 4.2.4.
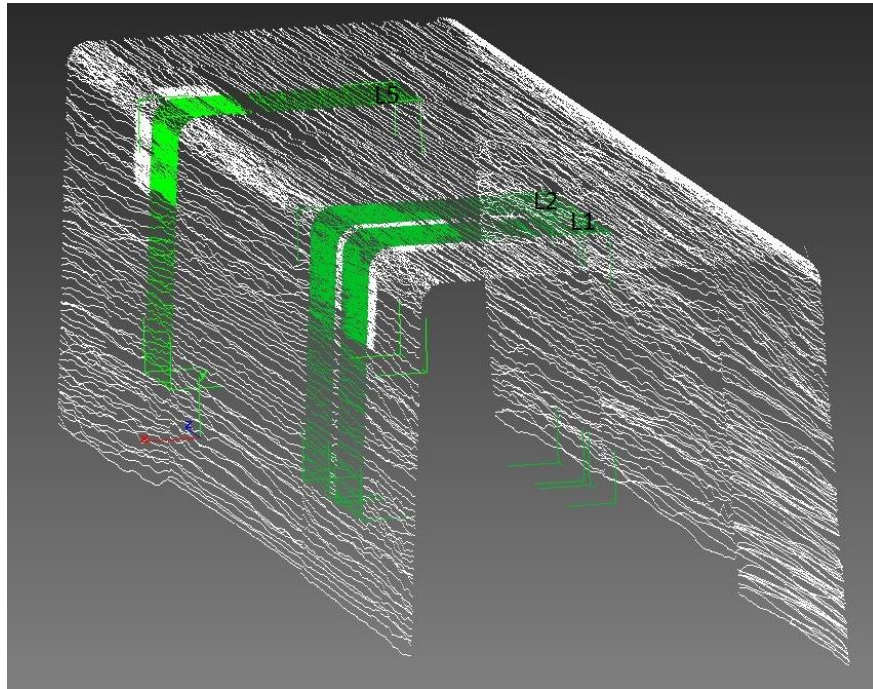


Figure 3.13 Point cloud file of the invar tool with specimen locations highlighted

## 3.5    Manufacturing of the L-shapes

This section describes the L-shape specimens manufacturing procedure. The characterized invar tool was prepared and pre-preg sheets were manually cut and laid up into desired geometries. The curing was done in the autoclave with the four cure cycles described in section 3.2.

69 L-shape specimens in total were manufactured. The L-shapes were 76.2 mm (3 inches) wide and have the flange length of 25.4, 50.8, 101.6 and 152.4 mm (1, 2, 4 and 6 inches). Three types of layups were employed: 8-ply cross-ply, 16-ply cross-ply and 16-ply unbalanced cross-ply. 8-ply and 16-ply resulted in cured laminated thicknesses of 3 mm and 6 mm. Each batch in phase 1 contained up to 8 specimens whereas each batch in phase 2 contained 4 specimens.

The location of the specimens on the invar tool followed Figure 3.14. The blue rectangles signify the high temperature flash tape used for position marking during fabrication. Arafath et al. showed that tooling sub-structures could pose constraints on the face-sheets at elevated temperatures, leading to a pillowing effect on the face-sheets [31]. Although the tool was made of invar, specimen locations were chosen carefully to avoid sub-structures underneath tooling face-sheets. A sacrificial specimen which contains a thermocouple in the middle was placed at location 7 in every batch. The testing matrices are listed below.
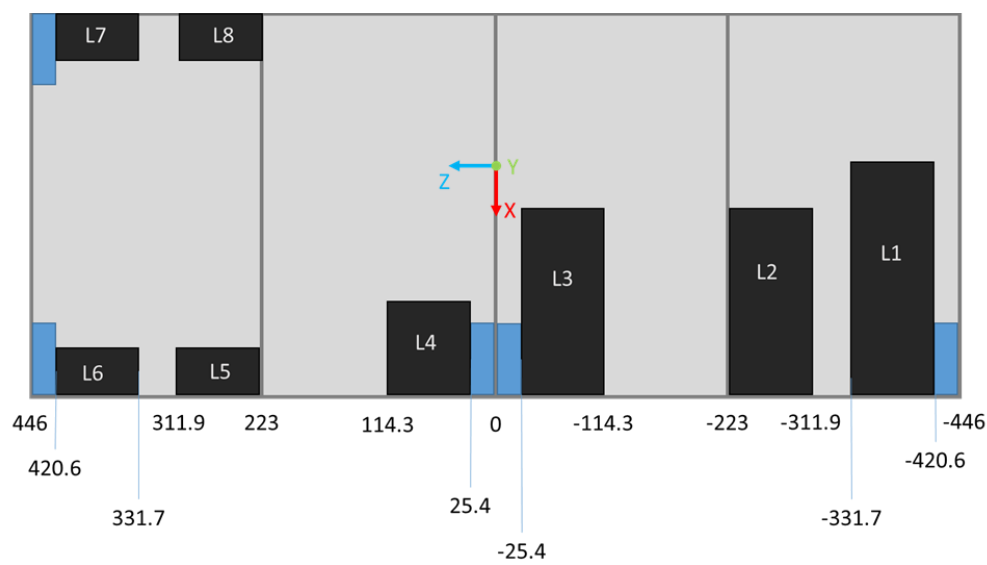


Figure 3.14 Specimen positions on invar tool. Top view. Unit in mm. LX: X is location number

Table 3.2 Phase 1 testing matrix

| Part name | Tooling | Part | | Material and Processing | |
|---|---|---|---|---|---|
| | Location | Layup | Flange length | Cure Cycle | TC |
| L1 | 8 | [90/0]4s | 152.4 | CC1 1-hold MRCC | NO |
| L2 | 7 | [90/0]4s | 50.8 | | YES |
| L3 | 6 | [90/0]2s | 50.8 | | NO |
| L4 | 4 | [90/03]2s | 50.8 | | NO |
| L5 | 5 | [90/0]4s | 50.8 | | NO |
| L6 | 1 | [90/0]2s | 152.4 | | NO |
| L7 | 3 | [90/0]2s | 101.6 | | NO |
| L8 | 2 | [90/0]4s | 101.6 | | NO |
| L9 | 4 | [90/03]2s | 50.8 | CC1 1-hold MRCC | NO |
| L10 | 5 | [90/0]4s | 50.8 | | NO |
| L11 | 6 | [90/0]2s | 50.8 | | NO |
| L12 | 7 | [90/0]4s | 50.8 | | YES |
| L13 | 1 | [90/0]2s | 152.4 | | NO |
| L14 | 2 | [90/0]4s | 101.6 | | NO |
| L15 | 8 | [90/0]4s | 152.4 | | NO |
| L16 | 3 | [90/0]2s | 101.6 | | NO |
| L17 | 7 | [90/0]4s | 50.8 | CC1 1-hold MRCC | YES |
| L18 | 6 | [90/0]2s | 50.8 | | NO |
| L19 | 4 | [90/03]2s | 50.8 | | NO |
| L20 | 5 | [90/0]4s | 50.8 | | NO |
| L21 | 8 | [90/0]4s | 152.4 | | NO |
| L22 | 1 | [90/0]2s | 152.4 | | NO |
| L23 | 2 | [90/0]4s | 101.6 | | NO |
| L24 | 3 | [90/0]2s | 101.6 | | NO |
| L25 | 4 | [90/0]4s | 50.8 | CC2 Slow 2nd ramp Test run | NO |
| L26 | 5 | [90/0]4s | 50.8 | | NO |
| L27 | 6 | [90/0]4s | 50.8 | | NO |
| L28 | 7 | [90/0]4s | 50.8 | | YES |

Table 3.3 Phase 2 testing matrix

| Part name | Tooling | Part | Material and Processing | |
| --- | --- | --- | --- | --- |
| | Location | Flange length | Cure Cycle | TC |
| L29 | 5 | 50.8 | CC1 1-hold MRCC | NO |
| L30 | 1 | 152.4 | | NO |
| L31 | 7 | 50.8 | | YES |
| L32 | 2 | 101.6 | | NO |
| L33 | 5 | 25.4 | CC2 Slow 2nd ramp | NO |
| L34 | 1 | 152.4 | | NO |
| L35 | 7 | 25.4 | | YES |
| L36 | 2 | 50.8 | | NO |
| L37 | 5 | 25.4 | | NO |
| L38 | 1 | 152.4 | | NO |
| L39 | 7 | 25.4 | | YES |
| L40 | 2 | 50.8 | | NO |
| L45 | 5 | 25.4 | CC3 Rapid 2nd ramp | NO |
| L46 | 1 | 152.4 | | NO |
| L47 | 7 | 25.4 | | YES |
| L48 | 2 | 50.8 | | NO |
| L49 | 5 | 25.4 | | NO |
| L50 | 1 | 152.4 | | NO |
| L51 | 7 | 25.4 | | YES |
| L52 | 2 | 50.8 | | NO |
| L57 | 5 | 25.4 | CC4 1-hold 140 °C | NO |
| L58 | 1 | 152.4 | | NO |
| L59 | 7 | 25.4 | | YES |
| L60 | 2 | 50.8 | | NO |
| L61 | 5 | 25.4 | | NO |
| L62 | 1 | 152.4 | | NO |
| L63 | 7 | 25.4 | | YES |
| L64 | 2 | 50.8 | | NO |
| L69 | 5 | 25.4 | | NO |

### 3.5.1 Tool Preparation

This section describes the tooling preparation process which was performed consistently for every batch of L-shape specimens.

The invar tool was first thoroughly cleaned with acetone. Then the tool was coated three times with LOCTITE Freekote 700-NC release agent to prevent the part from sticking to the tool. Every layer of Freekote was left 15 minutes to dry before the next coat was applied. Then 2 layers of FEPs were placed onto the tool at where specimens were to be manufactured. The FEPs were cut from the roll and transferred directly onto the tool to avoid any dust or foreign particulates being picked up through static (Figure 3.15). The FEPs were then smoothed onto the tool surface and fixed with high temperature tape at the corners and edges (Figure 3.16). The second layer of FEP, about 2.5 cm larger in length and width than the first layer, was applied the same way on top. A strip of high temperature tape was then used to mark the position where the pre-preg sheets were to be placed (Figure 3.17). The tool was then prepared for layup.



Figure 3.15 First layer of FEP sheet placed on the invar tool at specimen location

Figure 3.16 First layer of FEP sheet smoothed and taped with high temperature tape



Figure 3.17 Second layer of FEP placed on the specimen location. Smoothed and taped down with marking of specimen location

### 3.5.2 Pre-preg Sheets Cutting

Hexel AS4/8552, source 88 in CRN's inventory was taken out of the walk-in freezer the day before cutting. The sealed roll was left in a moisture-controlled layup room to thaw for 24 hours. Once the roll is thawed, it was placed onto a rack and a utility knife was used to cut the pre-preg into correct orientations and dimensions (Figure 3.18). The width of all specimens was 88.9 mm (3.5 inches). The radius of the invar tool was 20 mm and the angle of the profile was 93°. Consequently, the length of the L-shape plies were 93.72, 144.53, 246.13 and 347.73 mm (3.69, 5.69, 9.69, 13.69 inches). The utility knife blade was changed every dozen of plies to make sure all the edges of the pre-preg were cut clean. Any ply with defects from manufacturing was detected at this point and rejected. Once the pre-preg plies were cut, they were organized according to L-shape parts and sealed in a vacuum bag with a bag of desiccant. Once the cutting was done, the out time for the organized bags and pre-preg roll was documented and put back into the freezer waiting for the layup process.



Figure 3.18 Pre-preg sheets in the correct size and dimensions

### 3.5.3 Layup and Bagging

This section provides the detailed layup process for the L-shapes used in this thesis. Every batch of L-shapes took approximately 1 day to complete the layup. The layup was debulked with active vacuum overnight and autoclave cured the next day. The direction convention for the invar tool was such that the direction along the length of the tool was 90°; while the direction along the width of the tool being the 0 °direction. (Figure 3.19)
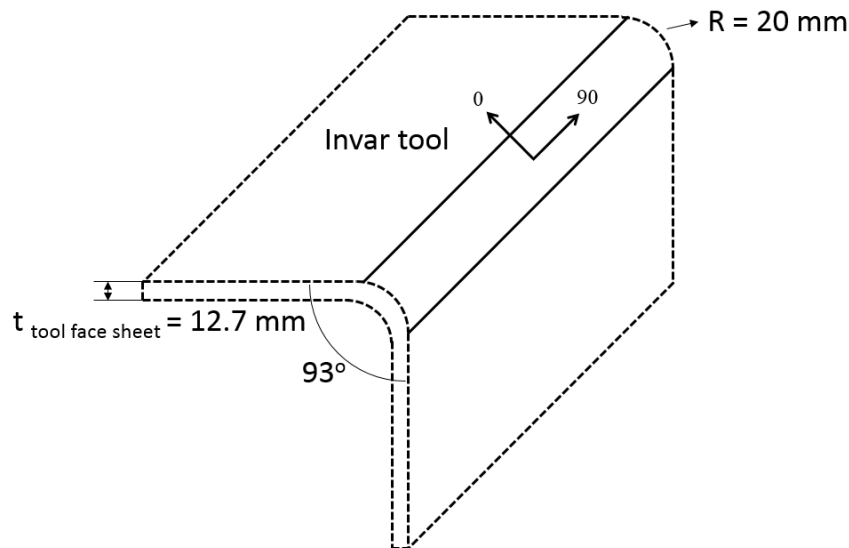


Figure 3.19 Schematic of invar tool dimensions and convention for layup orientation

Pre-preg sheets of correct size were laid up in a dust-controlled environment. A 90 ° layer was chosen to be the first layer so that the green charge could stick better to the FEP (Figure 3.20). A 0 ° layer in comparison needed to bend around the radius; which was more prone to lifting off from the non-sticking FEP sheets. A 90 ° first layer was used for all specimens in this study.

A de-bulk of 15 minutes was performed every 4 layers. During each de-bulk session, peel ply strips of 75 mm by 100 mm (about 3 inches by 4 inches) were placed adjacent to the pre-preg charge. The purpose of the peel ply strips was to create a breathing path, allowing entrapped air within the pre-preg charge to be ducted out to the vacuum port (Figure 3.20). Caution was taken to make sure the peel ply strips were in contact with the prepreg. Peel ply stripes were secured with two pieces

of high temperature flash tape. Then a piece of FEP sized slightly larger than the specimen, but did not cover all the peel ply was placed on top of the pre-preg charge to prevent the pre-preg from sticking to the breather cloth (Figure 3.21 left). Once the same procedure was repeated for all the parts in the batch, a large sheet of breather cloth was placed on top before everything was vacuum bagged.

Entrapped air within the pre-preg stack went through the peel ply strips, then through the breather cloth, reaching the vacuum port. The vacuum port was placed at the same location for every run (Figure 3.22). The same vacuum bag was used throughout the layup de-bulking process. A fresh vacuum bag was used after the final layer for autoclave curing. A vacuum leak test was performed at this stage. Midway through the layup, a thermocouple was inserted the middle of the specimen made at location 7 for ever batch of L-shapes to monitor the cure temperature (Figure 3.23, Figure 3.24, Figure 3.25)
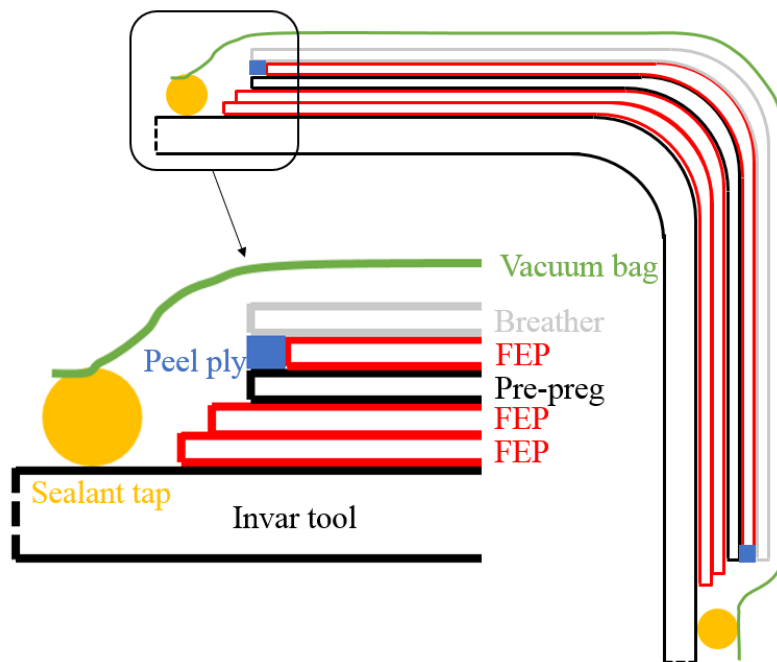


Figure 3.20 Layup schematic

Figure 3.21 Every four layers, peel plies were placed in contact with the pre-preg. A layer of FEP in placed on top as the specimen on the left. Stack is then ready for de-bulking



Figure 3.22 Specimens vacuum bagged and under de-bulk
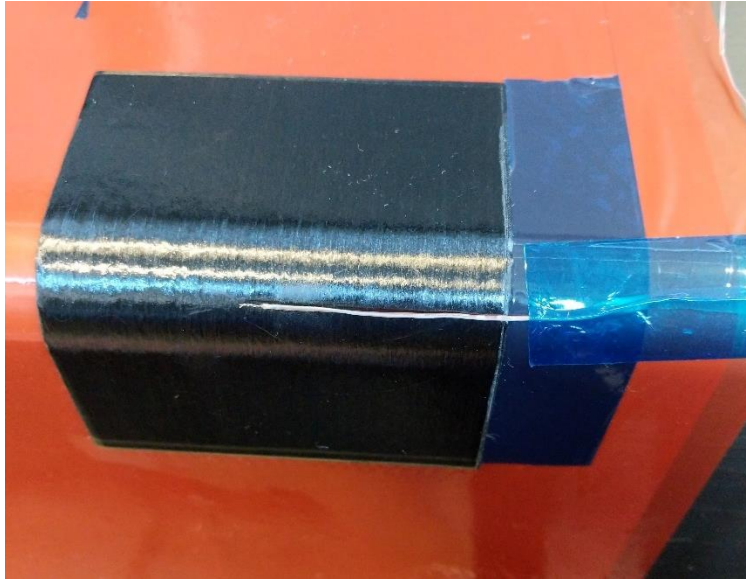
Figure 3.23 Thermal couple inserted in the middle of specimen at location 7 halfway through the layup
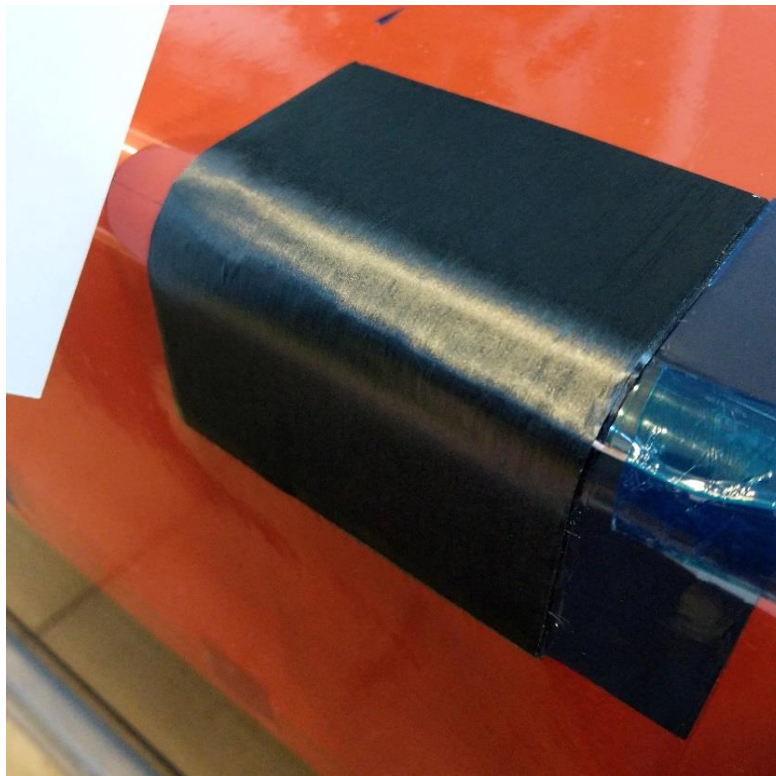


Figure 3.24 First layer of pre-preg after thermocouple is inserted, before de-bulking
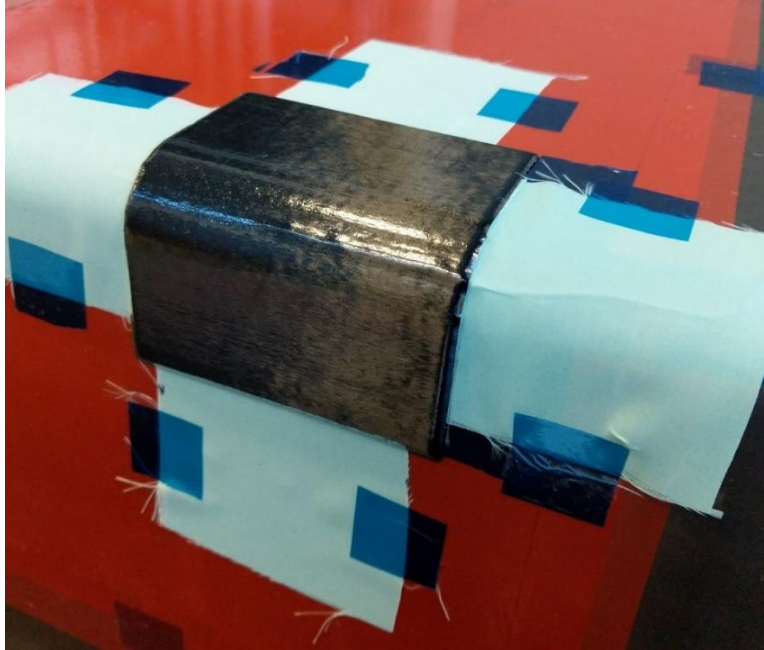
Figure 3.25 First debulking after the thermocouple is inserted

### 3.5.4   Autoclave Curing, Demolding and Trimming

Once the specimens were laid up and de-bulked overnight, they were cured in an autoclave strictly following the autoclave programming and operating procedure (Figure 3.26). Refer to section 2.2 and section 3.2 for autoclave information and cure cycles. Autoclave temperature and pressure were monitored and recorded throughout the curing process. Temperature and pressure data were collected after the cure.

Figure 3.26 Invar tool inside the autoclave after specimen layup

After the specimens were cured and cooled down to room temperature, they were demolded from the invar tool. Resin bleeding imprinted through the breather cloth were a sign of good vacuum seal (Figure 3.27). However, because breather cloth was highly porous, a large amount of bleeding indicates higher fiber volume fraction of the specimen, which may affect the specimen deformation (Figure 3.28). The amount of bleeding could be effectively controlled by sizing the peel ply strips and the FEP sheet on top of the specimen. From trial and error, it was found that when the third FEP covered the specimen plus approximately 2 inches of the peel ply, there was a minimal amount of bleeding into the breather cloth. A typical small amount of bleeding was shown in Figure 3.27. Resin in this case bled though the of peel ply for 2 inches in length and did not bleed excessively into the breather cloth. This setup can provide enough air path for the entrapped air to escape and maintain the correct fiber volume fraction of the specimen. Specimens with large amounts of

bleeding were documented and were further assessed during thickness measurement. Because the thickest specimens were 16 plies (around 3 mm), edge dams were not used. This resulted in blunt tapers at the edges of the specimens. (Figure 3.29)
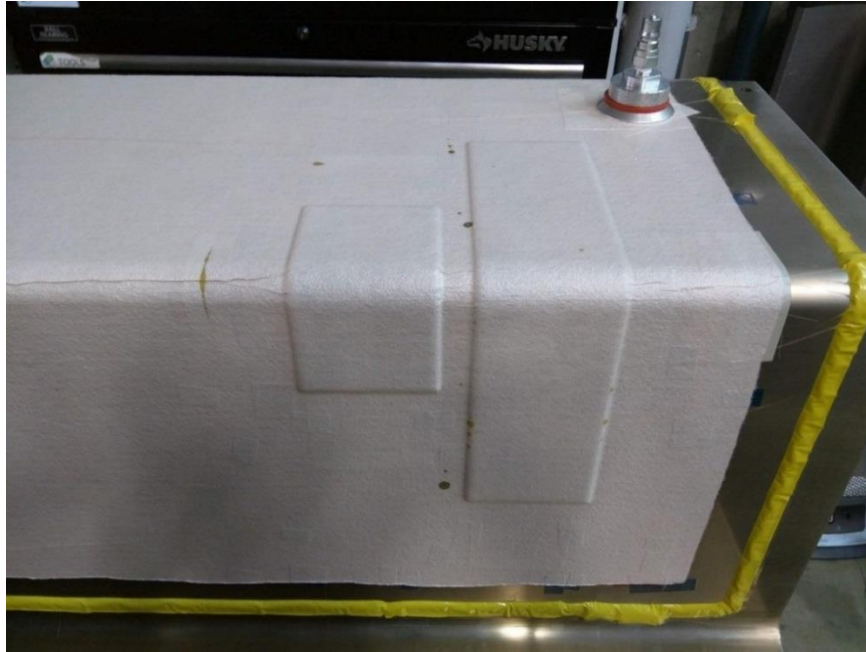


Figure 3.27 Minor bleeding, ideal
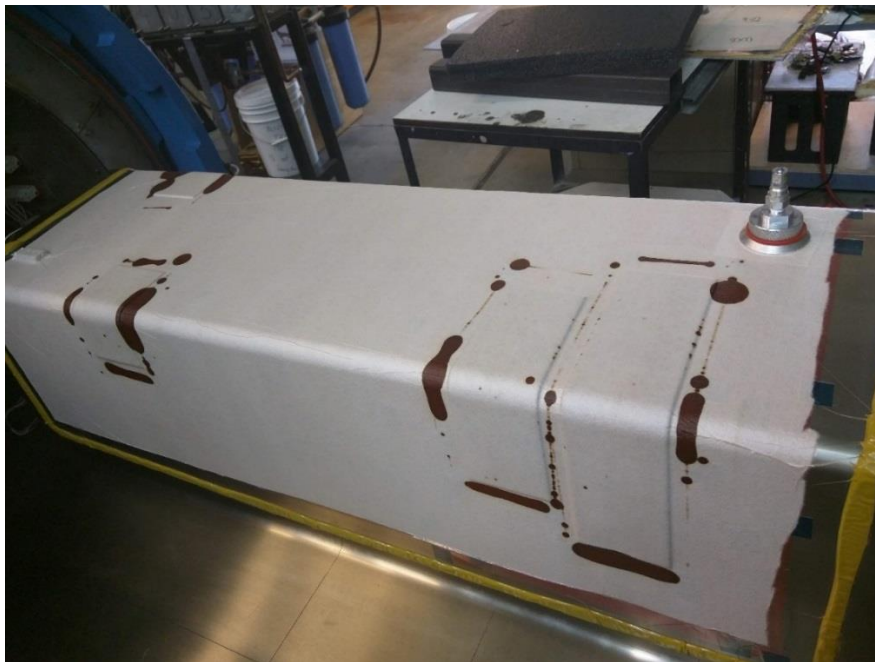


Figure 3.28 Specimens with large amounts of resin bleeding
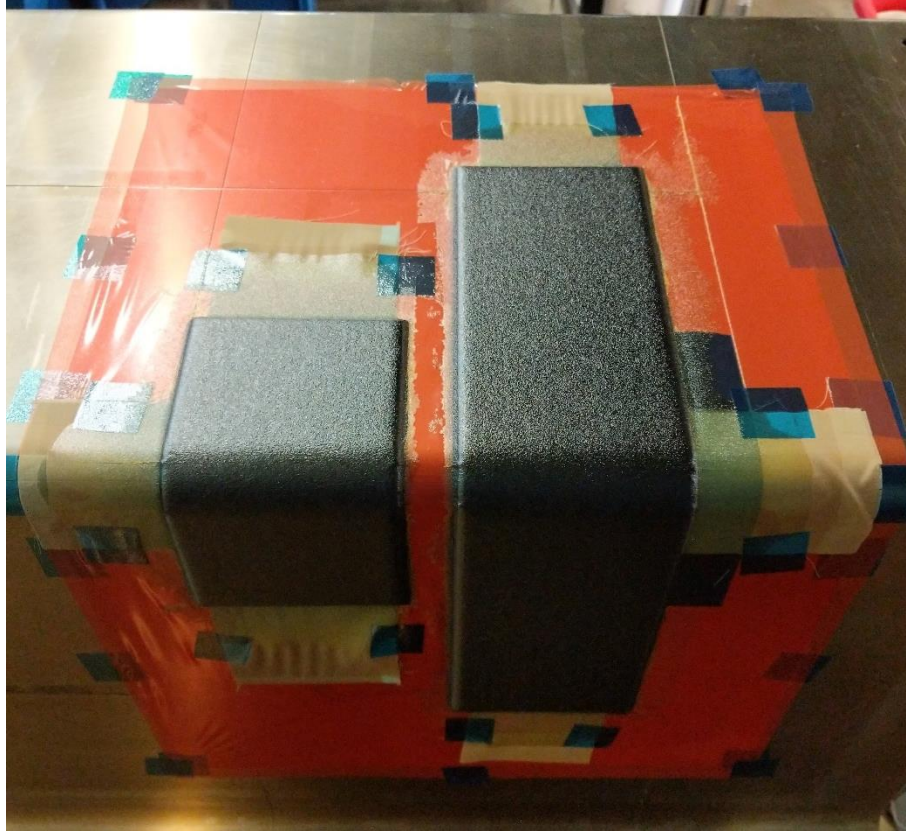
Figure 3.29 Typical specimens at tooling location 1 and 2 during demolding. Specimen edges were tapered from the vacuum bag. Resin bled to where FEP sheet (removed in this figure) stops

After the specimens were demolded, a high-speed diamond saw was used to trim the specimen edges. It is important to mention that the specimens were scanned by the laser CMM before and after trimming. The time between demolding and CMM scanning is typically within a few days to minimize the effect of moisture absorbance. The detailed scanning process will be explained in section 3.6. The edges were covered with masking tape to prevent delamination when trimming (Figure 3.30, Figure 3.31, Figure 3.32). 5 mm was trimmed around the specimen to cut off all the uneven thickness due to the small amount of bleeding and vacuum bag effect.
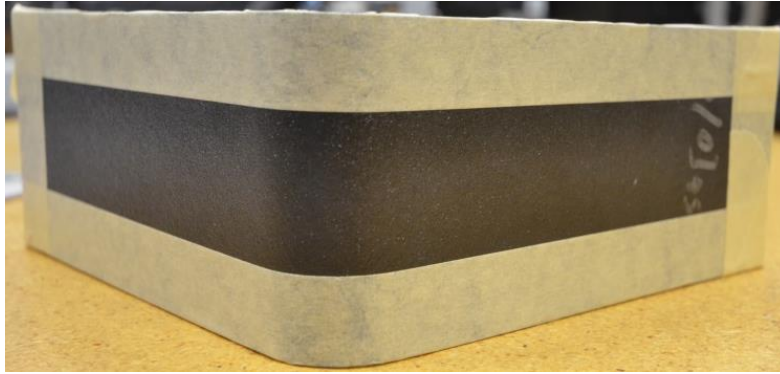
Figure 3.30 Masking tape covering the edges of the L-shape specimen before trimming
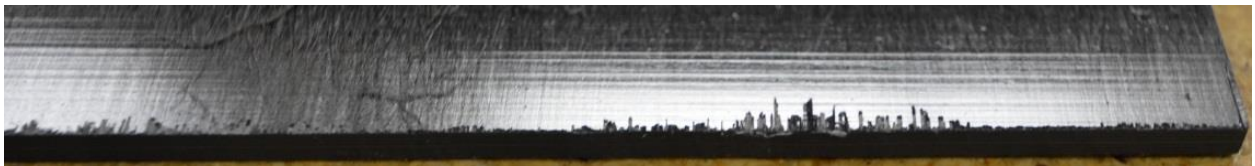


Figure 3.31 Edge delamination if not using masking tape



Figure 3.32 Comparison of before and after trimming of L-shape specimens

## 3.6 CMM Laser Scanning

Nikon C3 Hera 10.7.7 Coordinate Measurement Machine with XC65D laser head

Accuracy: 8 microns

The Nikon CMM machine was used to acquire accurate point cloud data of the specimens in this study. A laser head was used instead of the touch probe to ensure no external forces were deforming the specimen during the measuring process. The laser scanning head also generated dense point cloud (up to 1.6 million points in raw form) for each specimen which provided a rich data source for subsequent data reduction process. Specimens to be scanned were first cleaned and coated with a thin layer of developer spray (Figure 3.33). The developer spray decreases the reflectivity of the surface. However, a thick layer of developer can also affect the scanning accuracy. The lighting around the CMM machine was kept dark during all the scanning to ensure the laser was not affected by other light sources. Once the specimens were ready for scanning, the path of scanning was manually defined by a series of weight points. Each weight point had a 3D coordinate within the CMM operating envelope. To define a weight point, the laser beams were manually focused at a desired point on the specimen surface; and the coordinate was recorded. A 152-mm L-shape typically had two to three hundred weight points. During the scanning, the CMM laser head moved to each recorded weight point and take a measurement (Figure 3.34). The measurement is a group of points in the neighborhood of the weight point. The CMM software then merge all the measurements together to form a point cloud of the specimen.
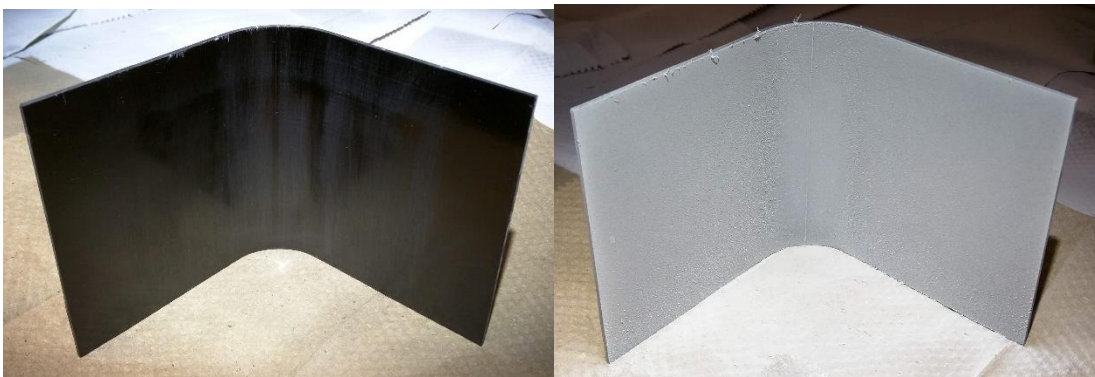


Figure 3.33 A specimen that was being cleaned and spray with a thin layer of developer

Once a point cloud was obtained, the 90° direction of the specimen point cloud was aligned with the z-axis (Figure 3.35). Center of the PC (defined as the mid-point of the intersection of Plane 1 and Plane 2) was aligned to the global origin. The point cloud was then rotated so that the opening of the L-shape faces the positive x-direction for the convenience of subsequent data reduction process.
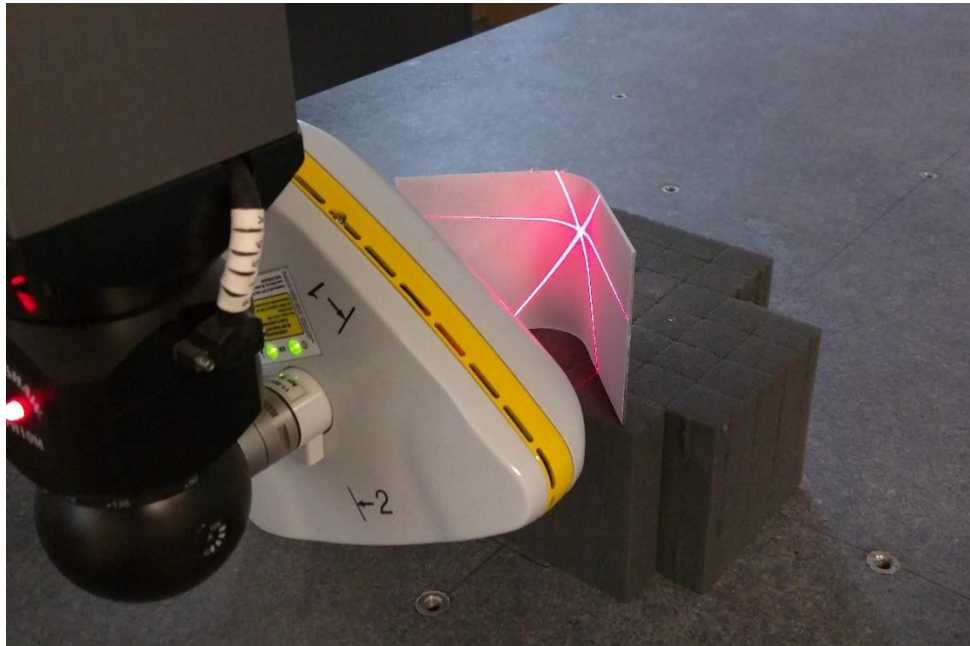


Figure 3.34 Specimen being scanned by the laser CMM
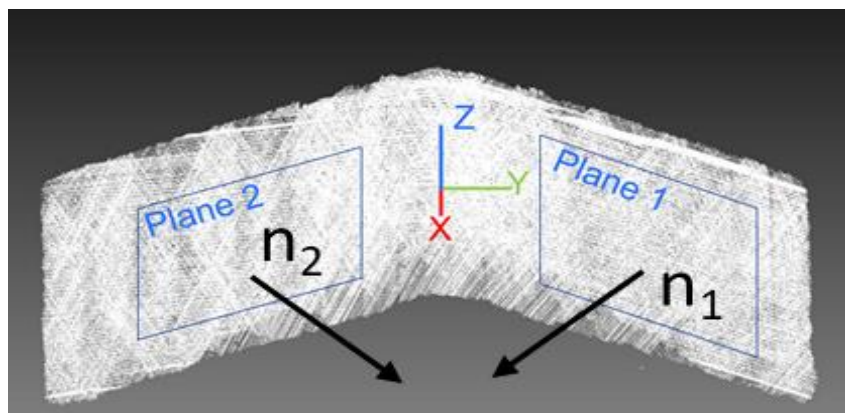


Figure 3.35 Raw point cloud with orientation. One fitted plane on each flange and normal vectors for the planes

## 3.7    Summary

The experimental design and procedure were described in this chapter. Four cure cycles were selected to explore the stress and deformation of composites L-shapes. Thermal characterization of the invar tool validated that location 1, 2 and 5 behaved similarly under demanding cure cycle conditions and location 7 lagged the other locations. Consequently, sacrificial specimen for temperature monitoring was chosen to be placed at location 7 for the worst-case curing scenario. Tooling surface profile scan provided the raw point cloud for upcoming tool analysis and compensation. Then L-shape specimens were manufactured at optimal locations on the tool. Once the specimens were cured and demolded, they were scanned by a laser CMM both before and after trimming.

In the next chapter, point cloud files from CMM scanning were fed into a Python data reduction process to extract spring-in and warpage results.  The same Python implementation was used to analyze the tool surface and compensate the specimens' deformation results.

# Chapter 4: Data Reduction and Results

## 4.1    Introduction

The literature starts to diverge in terms of measurement methods and analysis processes. As discussed in section 2.4.1, different deformation definitions and reporting formats across studies lead to results that are difficult to compare. Thus, it calls for a robust analysis process for a given measurement method so that results can be collated.

This chapter is separated into two major sections. The first section covers the development of a data reduction method and specimen thickness measurements. A robust Python code (attached in Appendix B) was developed which takes in the raw specimen point clouds and outputs spring-in plots that include the corner spring-in, total spring-in and warpage results. The code output was designed to ensure the results could be compared with spring-in results in the literature. The definitions of spring-in and warpage deformation were programmed in the python code. A case study demonstrates the difference between two different deformation definitions in section 4.2.3 and substantiates the importance of the definitions. The same Python code was then used to analyze the up-sampled tool surface point cloud to eliminate tooling effects from the nominal specimen deformation.

The second major section, section 4.5, is dedicated to the experimental results of this study. The effect of cure cycles, laminate thickness and flange length are outlined. The results are presented with spring-in profiles as well as in table and column chart formats. Lastly, sources of uncertainties for this study are discussed in section 4.7.

## 4.2 Data Reduction

A python script (attached in Appendix B) designed to create a robust data reduction process is explained in this section. The goal of the script was to extract local and quantitative spring-in and warpage deformation from the L-shape specimen point clouds. The same script was also used on the densified tool surface point cloud so the tooling effect can be subtracted from specimen deformation.

As mentioned in chapter 2, the most widely adopted spring-in definition in literature was flange length dependent. Following this definition, a typical result reports a single spring-in value and does not report flange warpage. Further, L-shapes with different flange lengths, which could have different amounts of flange warpage, were treated with the same method.

In comparison, the python script developed in this study computed spring-in values multiple times along the flange of the L-shapes, making the results not only flange length independent, but also comparable with the traditional methods. The interpretation of the python script results is presented in section 4.2.1.

A typical spring-in plot can reveal minor deformations from the effect of tooling surface and cure cycles. Capable of separating corner and flange deformation, this interpretation allows researchers to observe how different processing parameters and mechanisms affect the L-shape deformation locally.

Another advantage of using a script is that different spring-in and warpage definitions can be easily implemented so that different definitions could be compared. Two commonly used definitions of spring-in of L-shapes are compared in section 4.2.3. It was shown that minor differences in definitions could lead to up to 0.4° difference in spring-in values.

### 4.2.1 Python Implementation

The specimen CMM point clouds from section 3.6 were imported into a Jupyter Notebook. To exclude any measurements from on the edge of the specimens, 5 mm were digitally trimmed off the top and bottom edges of the point cloud (colored black in Figure 4.1). The point cloud was then equally divided into three sections widthwise. Each section of the point cloud was analyzed in 2D according to the steps in Table 4.1 to obtain the final spring-in plot. Steps g, h and i were also represented in terms of deviation plots to visualize the effect of flange warpage on the angle measurement. Note that the horizontal lines at deviation = 0 mm in steps g to i were the lines fitted during the corner/flange identification process. The angle between the two is not necessarily the nominal tool angle (93 °).
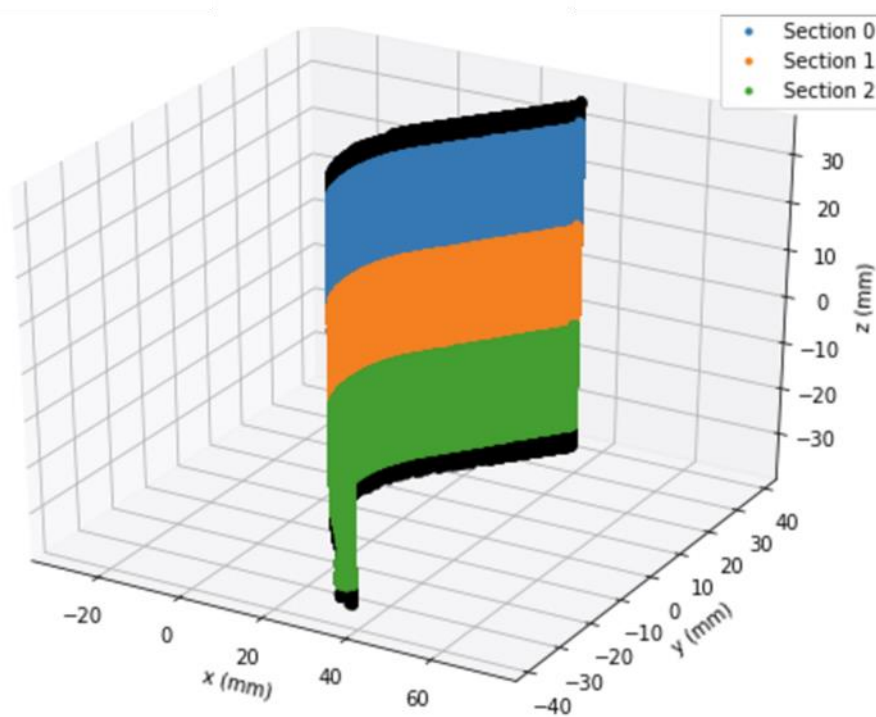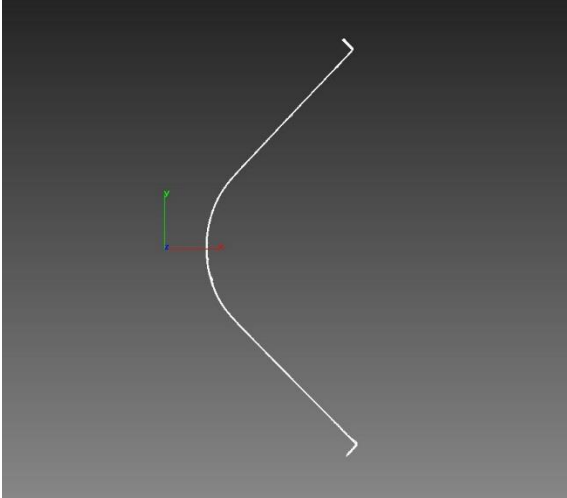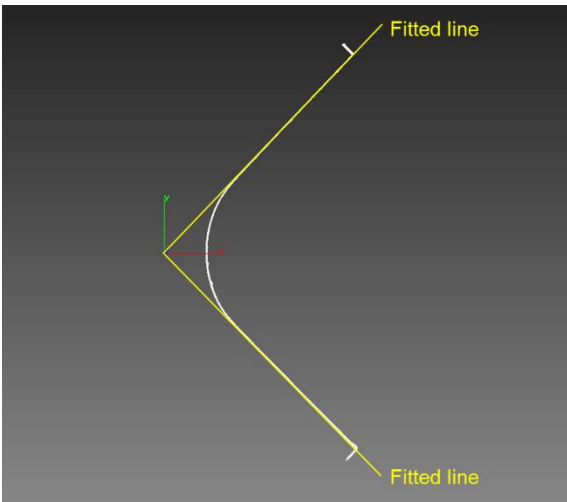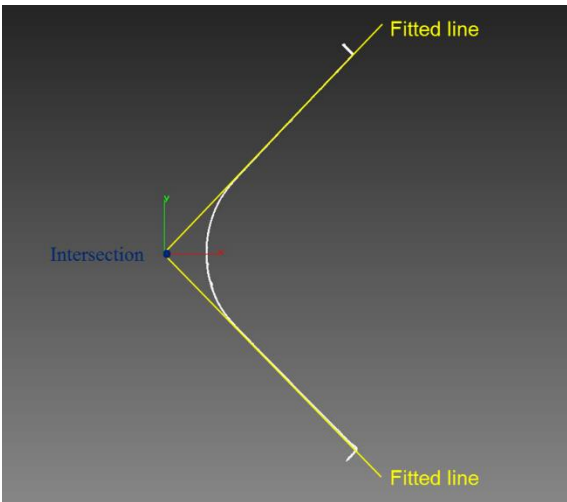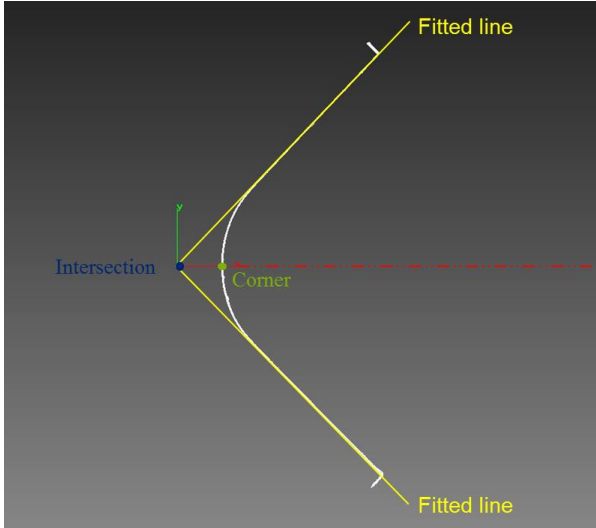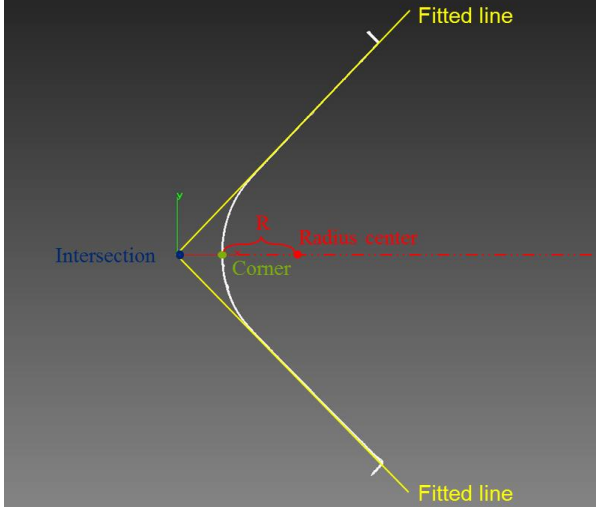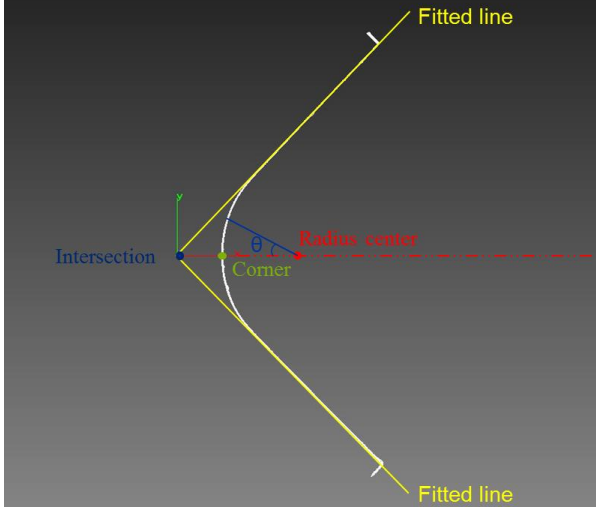


Figure 4.1 Point cloud file in Jupyter Notebook, edge trimmed, sectioned into three slices

Table 4.1 Data reduction procedure by Python

| | |
|---|---|
|  | Step a) In python, each sectioned point cloud was analyzed in 2D |
|  | Step b) Straight lines were fitted to the flanges |
|  | Step c) The intersection of the fitted lines was recorded |

| | |
|---|---|
|  | Step d) The closest point to the intersection on the 2D L-profile was defined as the corner |
|  | Step e) The point with distance R away from the corner along the vector from the intersection to the corner was defined as the center of the radius |
|  | Step f) The angle formed by the radius center to each point on the corner arch was calculated ($\theta$) |

Step g) Angles within half the theoretical enclosed angle (93°/2=46.5°) were defined as the corner (highlighted in black). The rest are defined as the flange
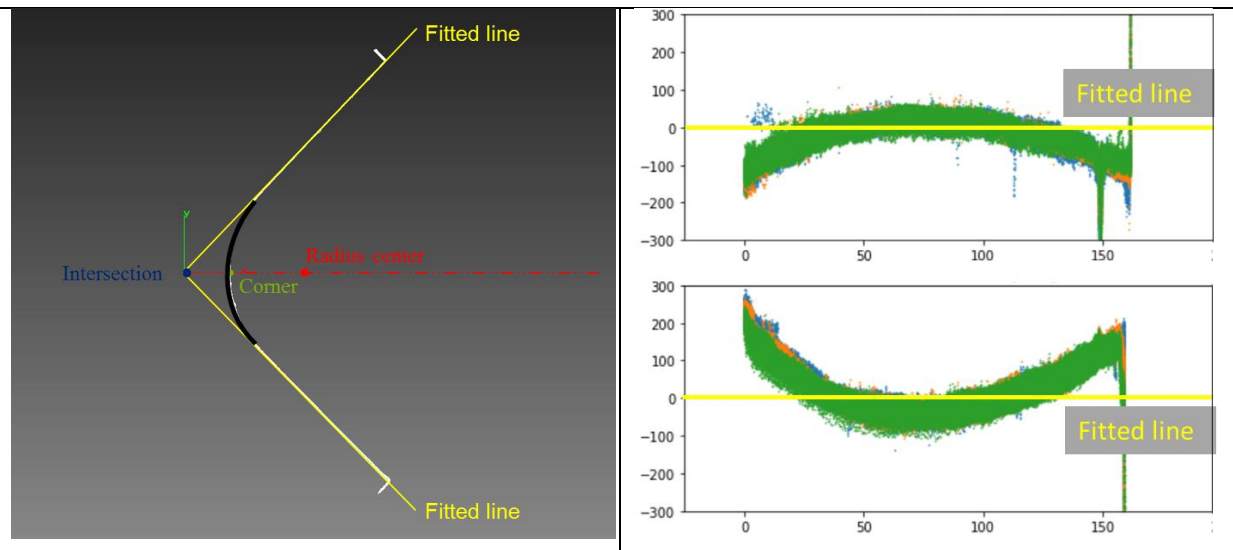


Step h) A buffer zone was defined as: the end of the corner arc to where the first angle measurement starts; aimed to make sure the angle measurements do not include any corner arc. The default buffer length = 5 mm
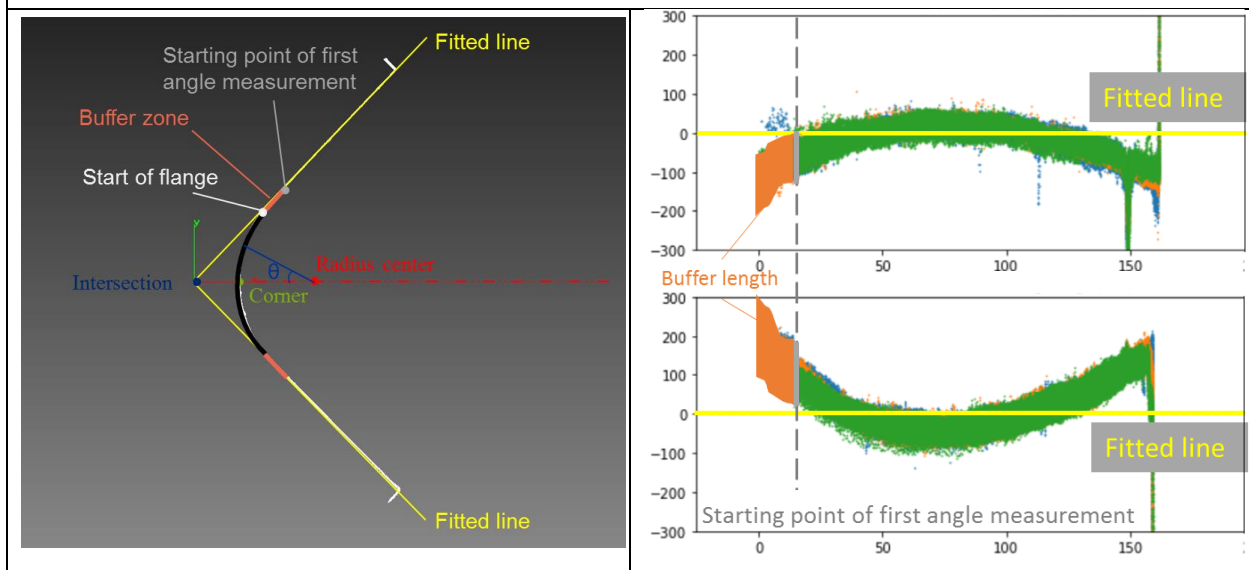
Step i) Vectors with increasing length were fitted to each flange section with the same starting point. Then the enclosed angles of vector pairs were computed. Default increment = 5 mm
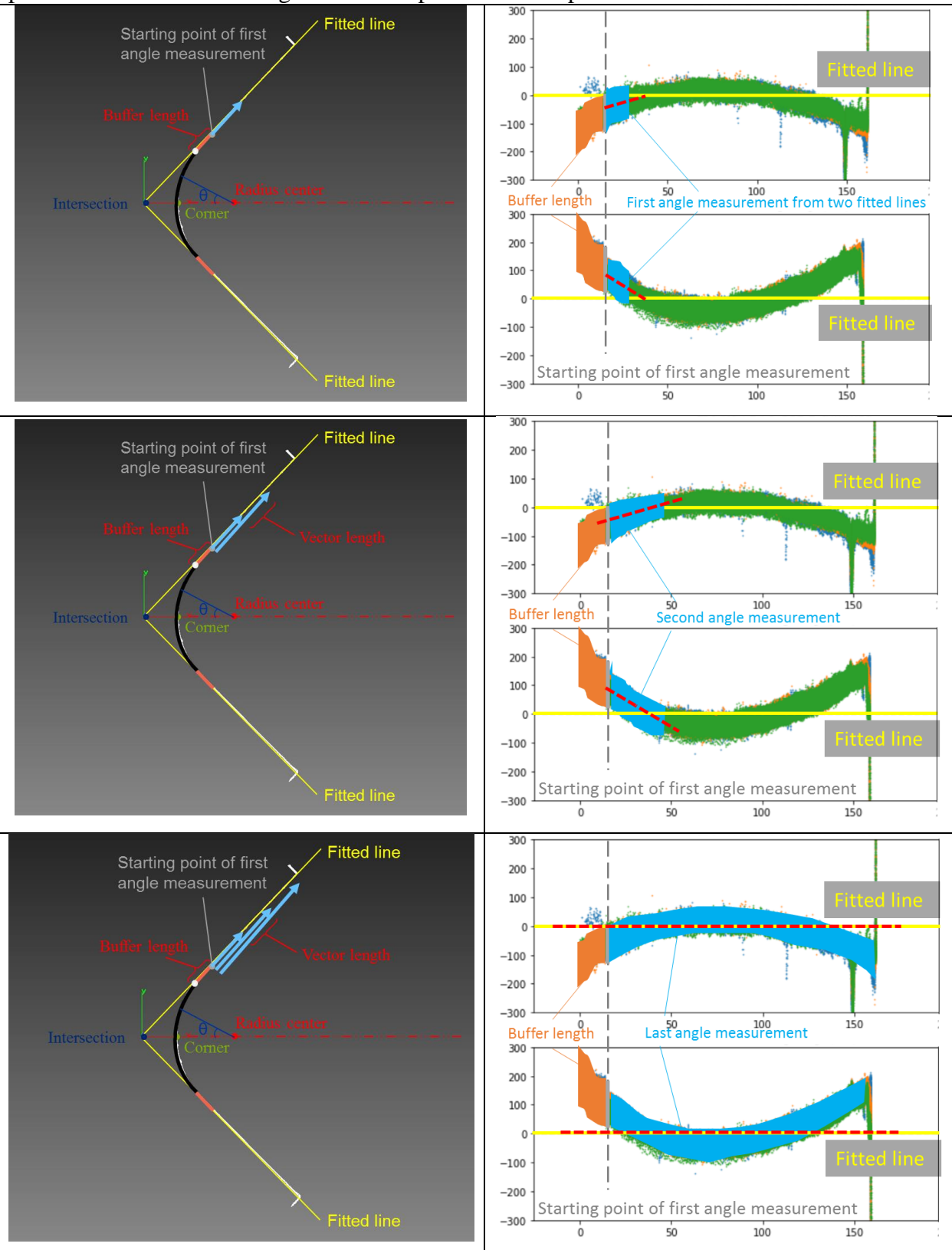
### 4.2.2    Results Interpretation

The abovementioned analysis process was repeated for each slice of the L-shape point cloud and averaged to generate one spring-in plot per L-shape. A typical result of the abovementioned script was a spring-in plot shown in Figure 4.2. The vertical axis was the angle formed by pairs of vectors subtracted the nominal tooling angle (93 °), i.e. nominal spring-in angle. The horizontal axis was the distance along the flanges of which the vectors were extended along. Each data point represented an angle measurement at a certain distance. The error bars represent the standard deviation of the three averaged slices. The first point represented the angle formed closest to the corner i.e. the first vector started at 10 mm (5 mm buffer length + 5 mm vector length) away from the corner. The last point represented the nominal total spring-in, spring-in at the corner plus flange warpage effect. The nominal total spring-in is equivalent to the traditional measurement method - - fitting to the entire flanges and measure the angle from the normal vectors.

The resultant spring-in plot not only included the corner and total spring-in values, but also showed insights on flange warpage and tooling surface effects. Specimens showed higher total spring-in values than corner spring-in values indicated warpage existed in all specimens. The more flanges warp, the larger angle formed by vectors at increasing length (Figure 4.3), thus, the spring-in plot would have a higher slope. In this incremental approach, as the vector length increased, more points were being averaged, so error decreased. Conversely, the measurements were more sensitive to scatter in the point cloud closer to the corner section. Details on uncertainties are expanded in section 4.7.2.

The effect of tool surface undulation can be observed in Figure 4.2. L30, made at location 1 exhibited different profile while having identical processing conditions comparing to L1, L15 and L21 made at location 8. The divot at around 40 mm in L30 is also consistently observed in other L-shape specimens. In section 4.2.4, "spring-in plots" are generated for up-sampled tool surface point cloud and subtracted from the corresponding specimen spring-in plots to eliminate the tool effects.
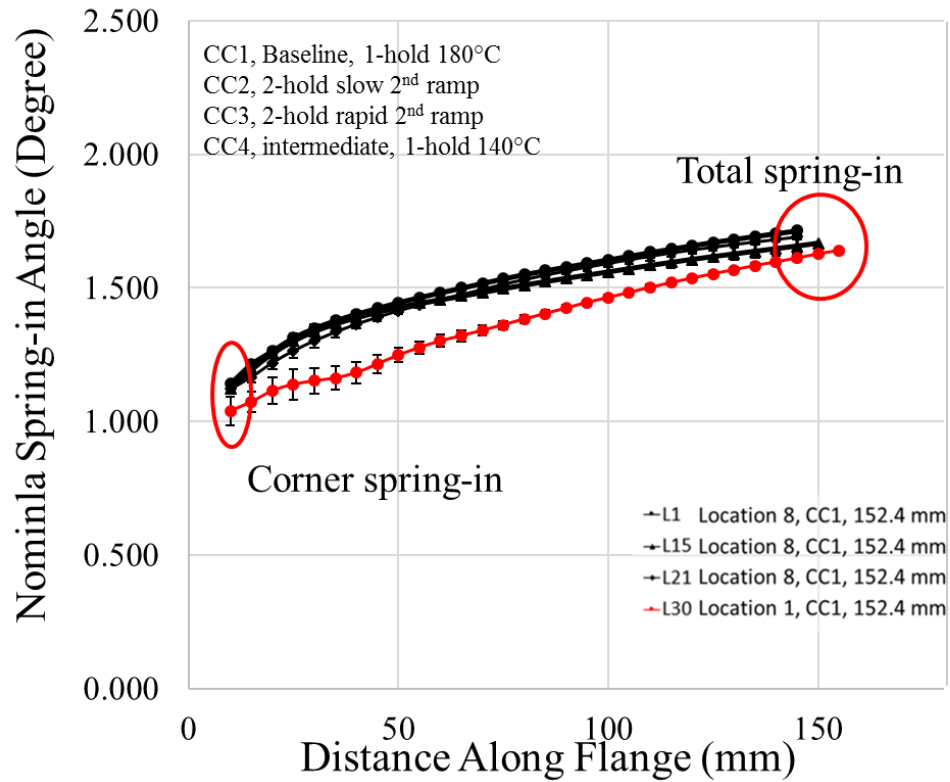
Figure 4.2 A typical python script output, spring-in plot
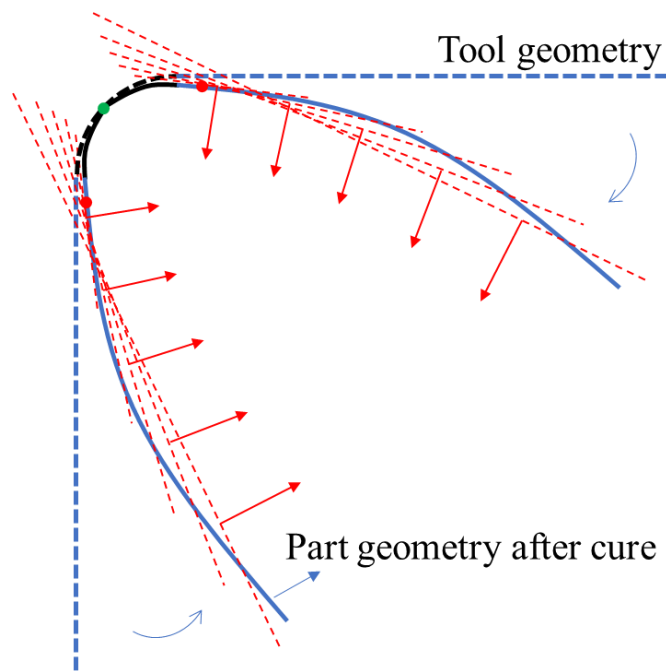


Figure 4.3 L-shape spring-in and warpage deformation schematic. Secant approach is demonstrated in red

### 4.2.3    Case study: Comparison of Two Different Spring-in Definitions

This section compares the incremental secant spring-in definition (which was described in the data reduction procedure in section 4.2.1) to a discontinuous secant approach to demonstrate small difference in definitions can lead to largely different results.

The discontinuous secant approach was also implemented in python; step a through g were the same as the secant approach. However, in step h, instead of using a *fixed starting point* on the flange and measured the angle formed by *incremental secant vectors*, the discontinuous secant approach used *floating starting points* and measured the angle formed by *secant vectors of fixed length*. Figure 4.4 showed the comparison of the two approaches and half of the L-profile was used to demonstrate the difference.

The secant vectors were also overlapped to average and smooth out the curve. 12.7 mm (½ inch) vectors with 6.35 mm (¼ inch) overlap (Figure 4.4 right) was tested from trial and error to produce reasonably smooth results while preserving the surface undulation details.
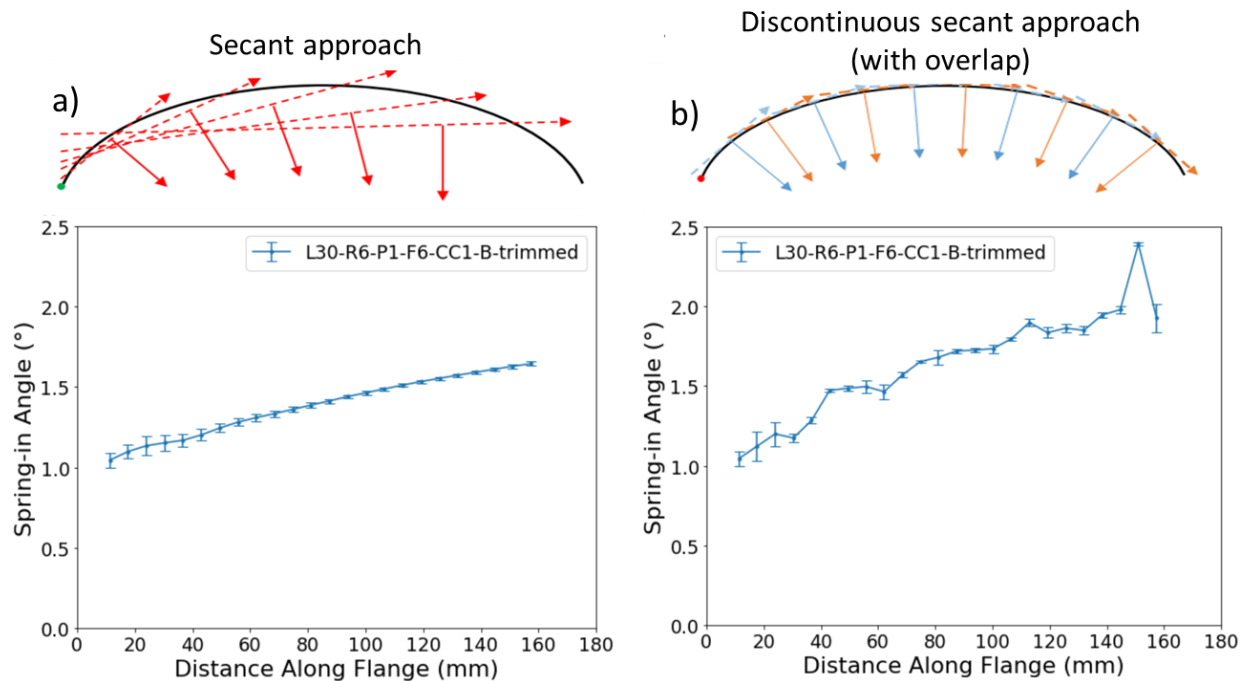


Figure 4.4 Incremental secant approach (a) vs discontinuous secant approach (b), half L-profile is shown, symmetry applies.

70

The minor difference in the two approaches was able to generate drastically different results. Because the vectors in the incremental secant approach was increasing in length (using higher number of points to fit vectors), it averaged out the undulations in the flanges and the flange warpage. The longer the vectors, the smaller the uncertainties. On the other hand, the discontinuous secant approach segregated the flanges by only using the points in the neighborhood of each measuring location so was more sensitive to surface undulation. The surface fluctuations exhibited in Figure 4.4 b were not visible by eye. Also, because the discontinuous secant approach segmented the flange, the flange warpage effect became accumulative, resulting in total spring-in values approximately 0.4° higher than the secant approach.

All analysis unless indicated in this thesis were done using the incremental secant approach because it was less sensitive to surface undulations and is more commonly used.

### 4.2.4 Tool Surface Point Cloud Analysis, Up-sampling and Corresponding Specimens Adjustments

In this section, the invar tool surface point cloud obtained in section 3.4 was isolated according to specimen location and analyzed in detail. The touch probe point cloud has much lower density than the specimen's laser point cloud. 130,000 points were obtained by the touch probe for the entire tool whereas a single specimen laser point could contain up to 1.6 million points. Thus, the tool point clouds were up-sampled (densified) so the Python implementation that was used for the specimens could be applied.

Angle deviation from the nominal 93° at different length were computed and angle vs distance plot ("spring-in plot") for different tool surface locations were generated. The tooling results were then subtracted from the specimen results to reveal the true specimen deformation.

#### 4.2.4.1 Raw Tool Surface Point Cloud Analysis

Starting with the invar tool surface point cloud obtained in section 3.4, the areas where the specimens were manufactured were isolated in the Nikon Focus Scan software following Figure 3.14. Subsequently, deviation plots are generated for the isolated tool point clouds (Figure 4.5 to Figure 4.12).

Since the longest flange length for L-shape specimens was 152.4 mm, undulation magnitudes are estimated over a 150 mm flange length on every surface. It was observed that location 1 and 2, 3 and 4, 5 and 6, and 7 and 8, where they are adjacent, have very similar undulation profiles and magnitude. Among all the locations, location 4, 5 and 6 have the largest surface undulations.
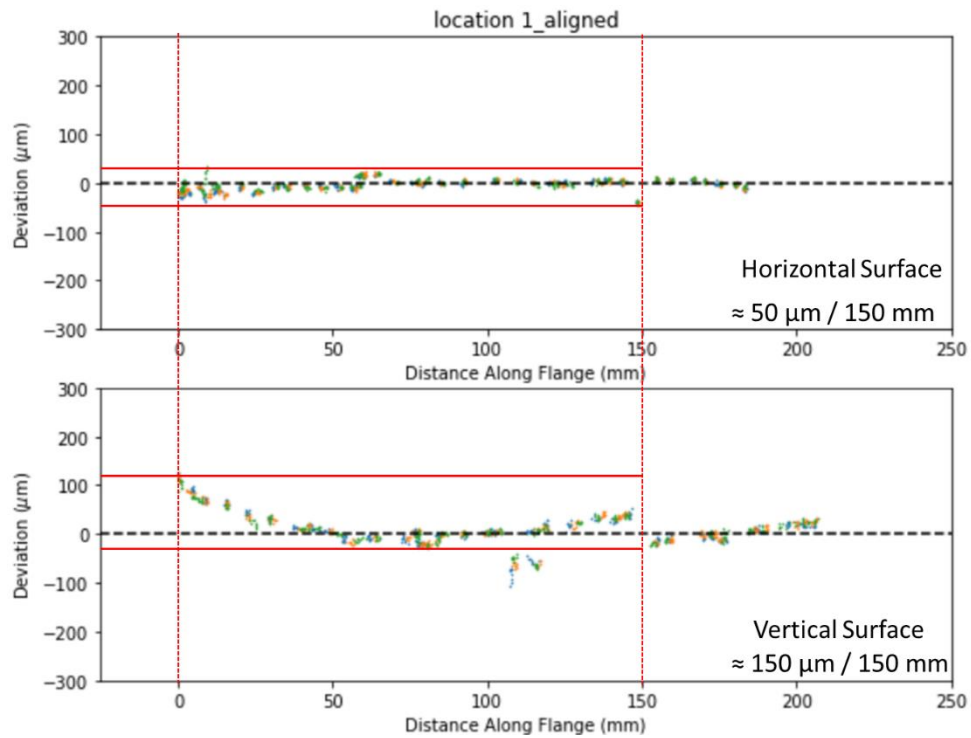
Figure 4.5 Tool surface point cloud at location 1 in 2D
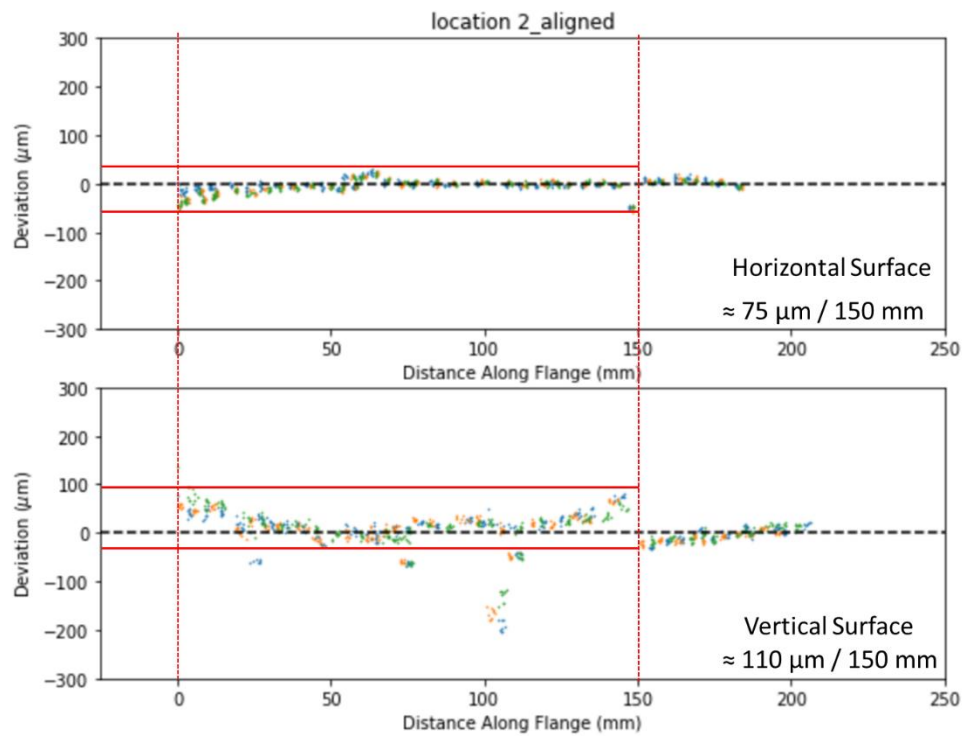


Figure 4.6 Tool surface point cloud at location 2 in 2D
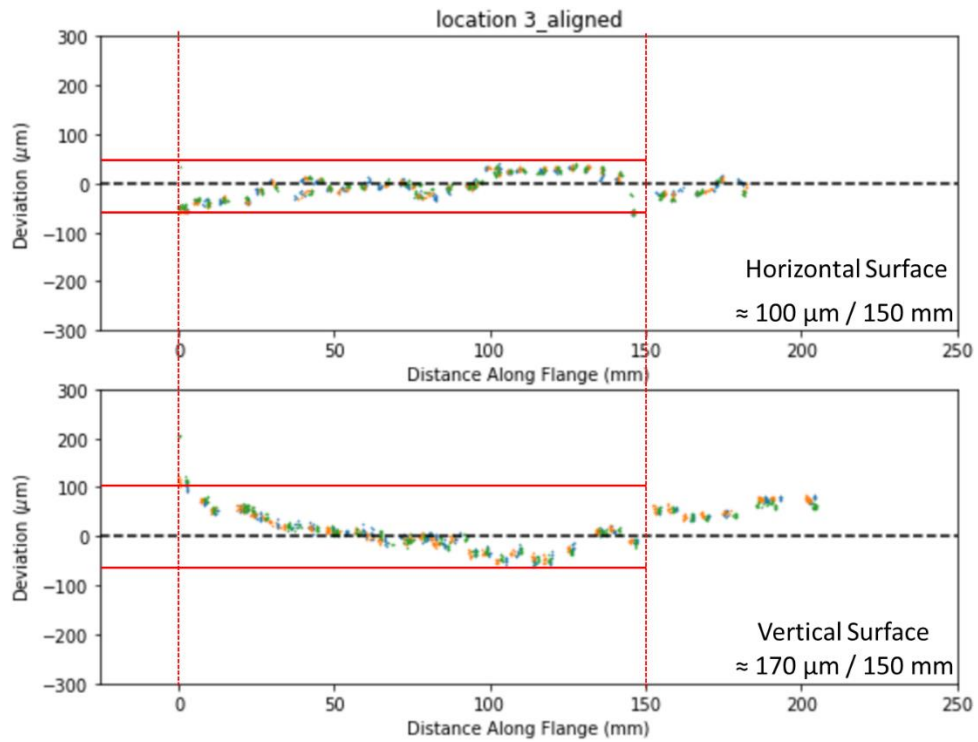
Figure 4.7 Tool surface point cloud at location 3 in 2D
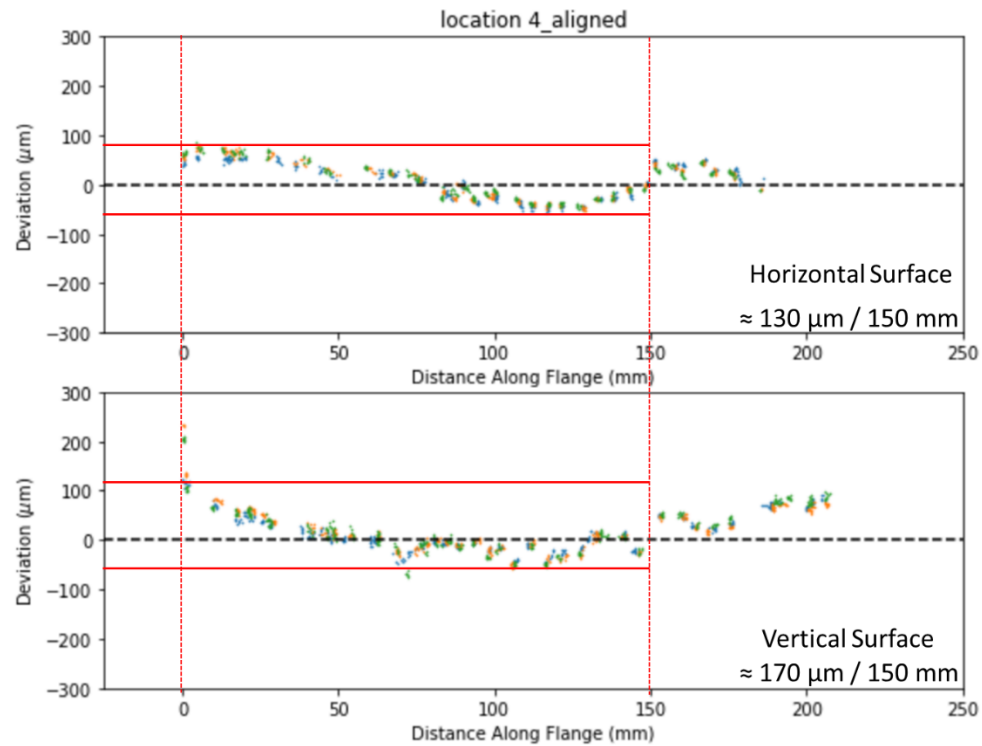


Figure 4.8 Tool surface point cloud at location 4 in 2D
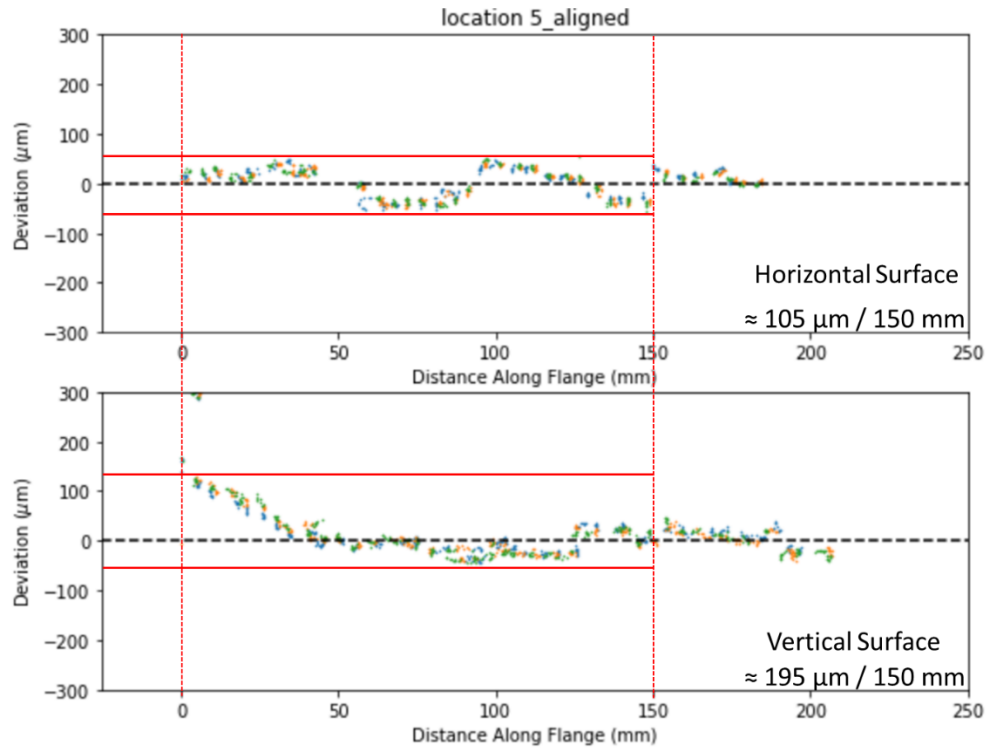
Figure 4.9 Tool surface point cloud at location 5 in 2D
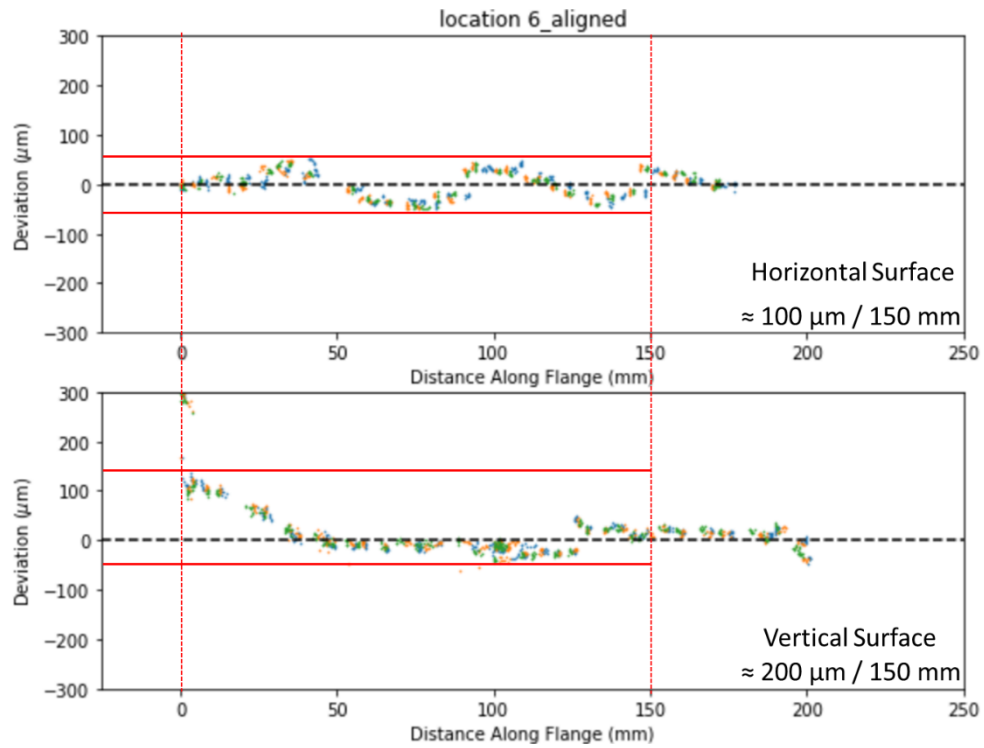


Figure 4.10 Tool surface point cloud at location 6 in 2D
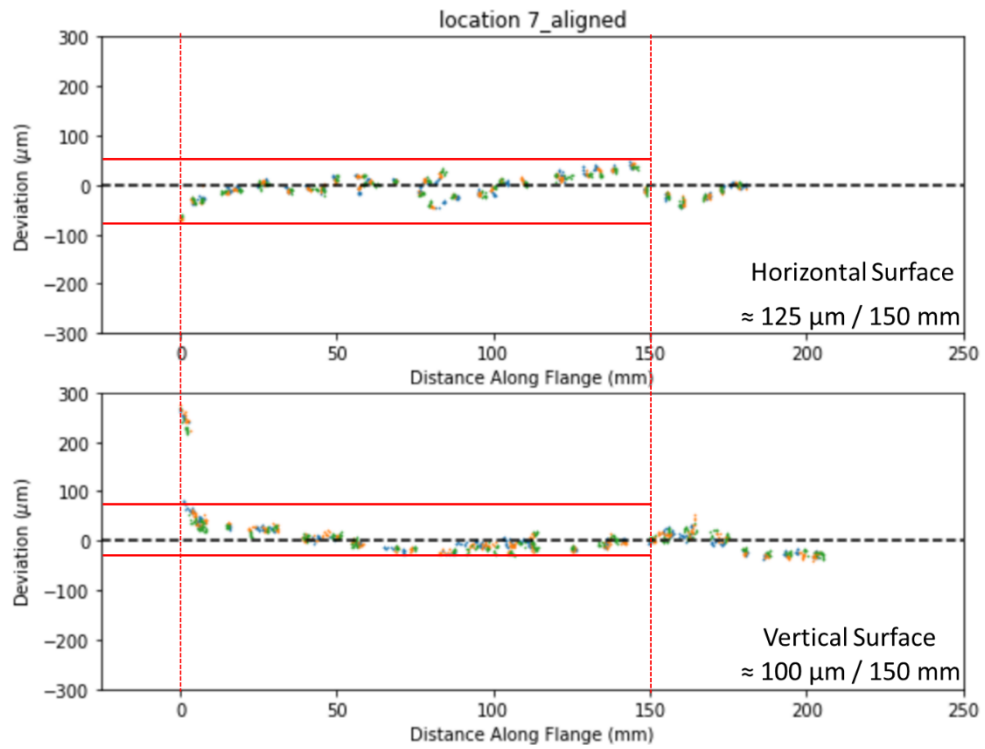
Figure 4.11 Tool surface point cloud at location 7 in 2D
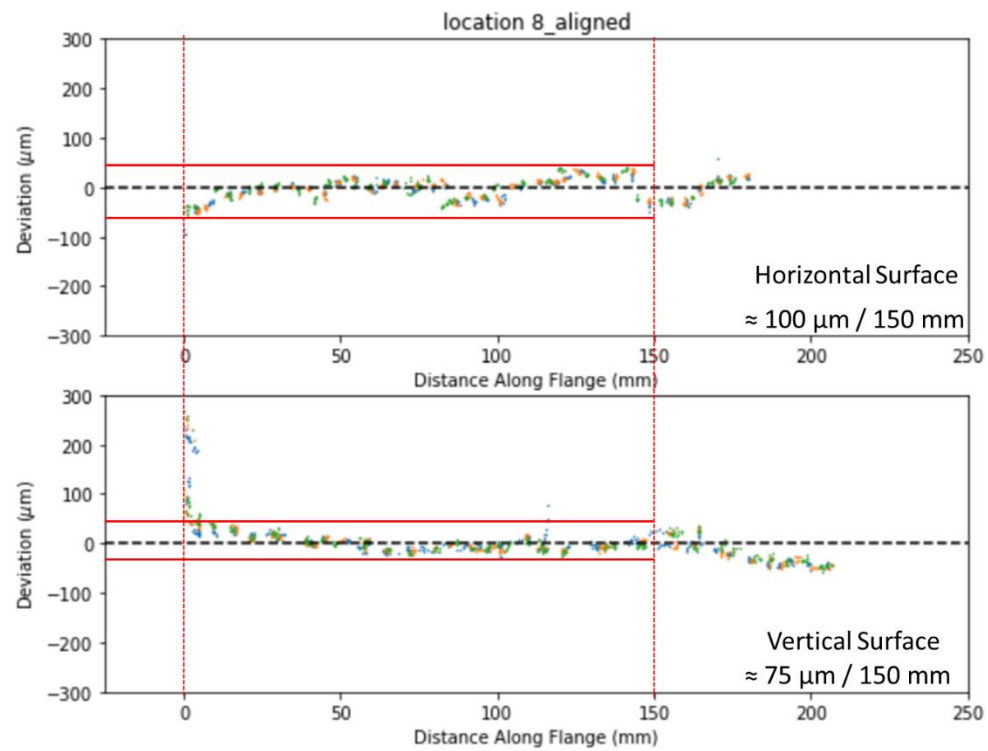


Figure 4.12 Tool surface point cloud at location 8 in 2D

Location 1 to 6 on the tool have a slope on the vertical surface from 0 to around 60 mm. At location 7 and 8, there is some vertical features at 0 mm in the vertical surface. It is part of the corner area being counted in. The average deviation over 60 mm for location 1 to 6 is 80 µm on the horizontal surface and 135 µm on the vertical surface. Following simple angle calculation:

$$\tan^{-1}\left(\frac{135 \times 10^{-6}}{60 \times 10^{-3}}\right) + \tan^{-1}\left(\frac{80 \times 10^{-6}}{60 \times 10^{-3}}\right) = 0.205\,°$$

Meaning for 60 mm flange length or shorter, the tool angle at location 1 to 6 is varying around the average of 93.205 °.

Sudden shifts (on the magnitude of 50 µm) were observed on the vertical surfaces at 150 mm at multiple locations. The reason for the sudden shift was unclear. At 150 mm from the corner on both the horizontal and vertical surfaces, there was a tool scribe line running along the 90 direction (Figure 4.13). The sudden shift could be due to the machining of the scribe line or a shift in the FARO arm setup. Since the longest L-shape flange length was 152 mm in flange length, the shift was not further investigated.



Figure 4.13 Scribe line at 150 mm away from the corner on the vertical flange. 3 mm FARO touch probe for reference

Due to the low density, the Python implementation was not able to accurately compute the angle vs distance at short flange length. The line fitting in step i of the python implementation would generate extremely inaccurate results because there were little points to be selected to fit (Figure 4.14).
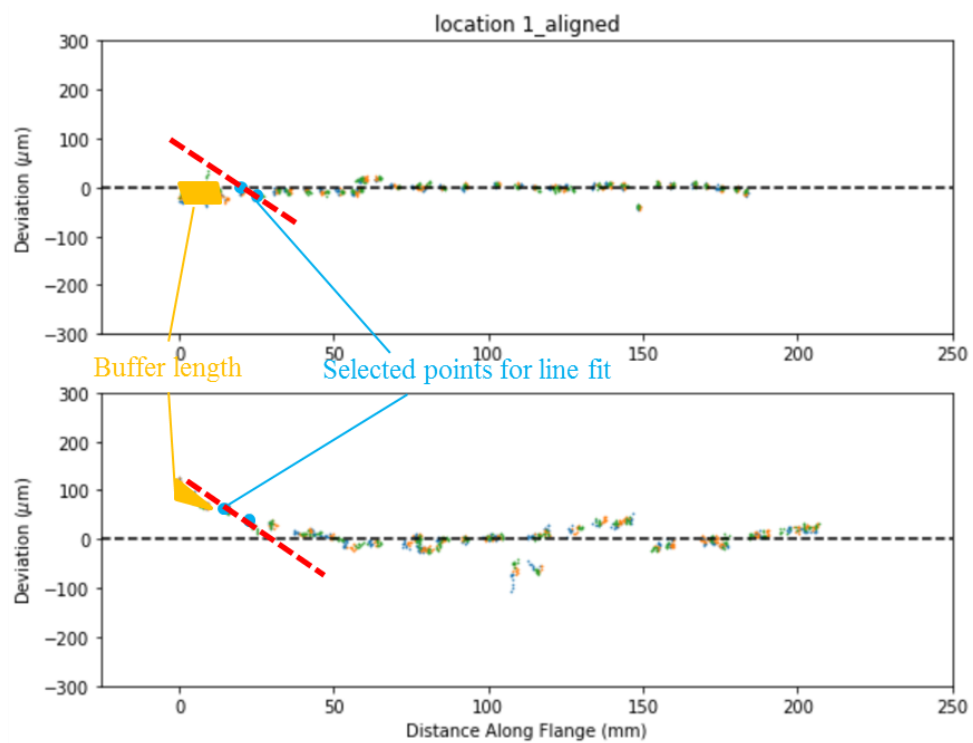


Figure 4.14 Inaccurate angle results were generated at short length when (red dotted) lines were fitted to the low density point cloud

Despite the surface undulations, the invar tool does meet the industrial geometrical dimensioning and tolerancing (GD&T) specifications for flatness. A typical surface flatness tolerance for aerospace composite part tooling is 0.25 mm (10 thou) [58]. In the next section, the sparse point clouds undergo an up-sampling process so they can be processed using the Python implementation.

### 4.2.4.2    Up-sampling using CloudCompare

The densification process was achieved by using CloudCompare software [84]. In the software, the function is located under Plugins > PCL wrapper > smooth using MLS, optionally up-sample [85]. The up-sampling process adds points uniformly to the point cloud until a metric which indicates the spacing between points are below a user specified value [86]. The up-sampled output point clouds were analyzed by the Python implementation iteratively to determine the best settings for up-sampling.
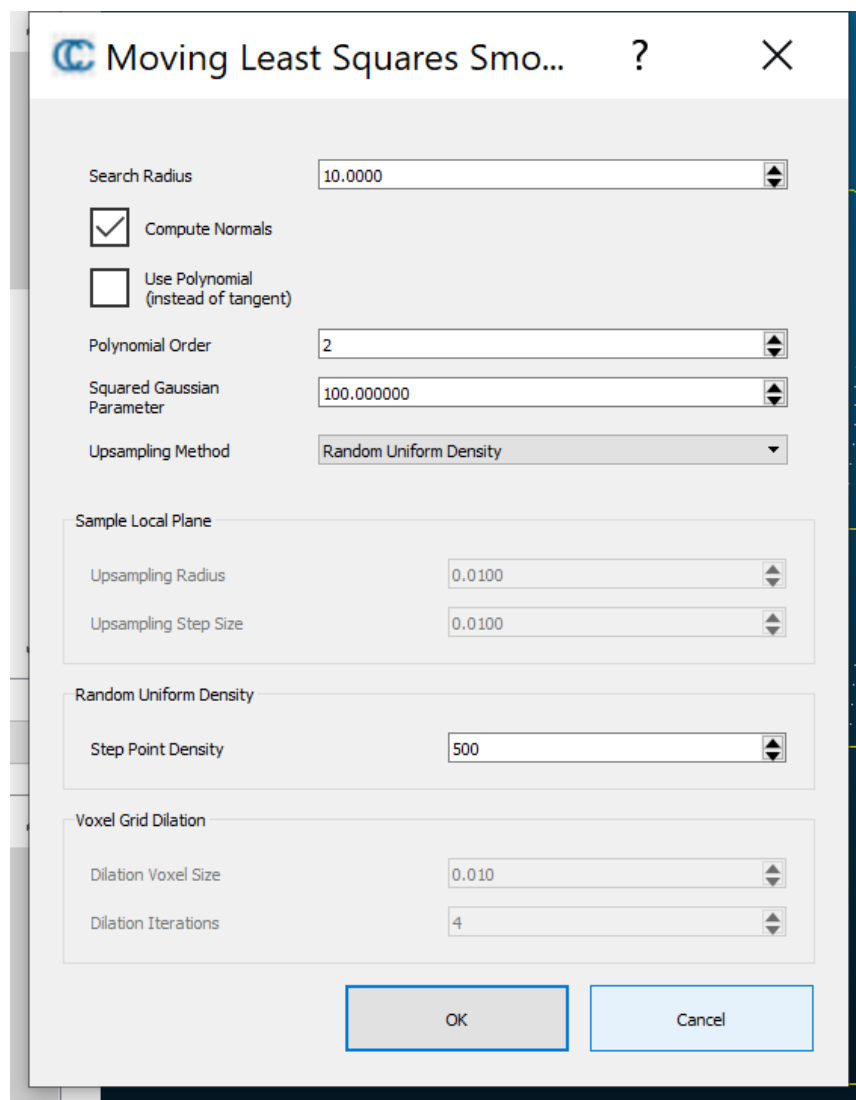


Figure 4.15 Settings for up-sampling using CloudCompareSettings for up-sampling is shown in Figure 4.15. The setup explains as following:

- "Search radius" was set to 10 mm based on iterative testing
- "Use Polynomial (instead of tangent)" in searching can sometimes cause the up-sampled results to diverge, hence, it was selected on if it generated convergent results. When "Use Polynomial (instead of tangent)" is checked, "Polynomial order" was set to 2
- "Squared Gaussian Parameter" is overwritten by "(search radius) ^ 2"
- "Step Point Density" was set to 500 based on iterative testing. This parameter determines the output point cloud density. Beyond 500, the eventual tool angle results do not change

The up-sampled point clouds were analyzed with the Python implementation using the same (buffer length, vector increments etc.) settings as the specimens. The Python outputs are shown in Figure 4.16. The first measurement started at 25 mm to ensure there are enough points for accurate line fitting and angle measurement.

It is shown that before 60 mm, tool angles can vary from 93.06 ° to 93.33 °. The average variation, around 0.2 °, agrees well with the observations in the deviation plots. As measuring distance increase, the tool angles average towards 93 °. Tool angle deviation from nominal was subtracted from the specimens' spring-in plots. As an example, the results in Figure 4.2 were adjusted and plotted in Figure 4.17 to show the tooling surface effects being eliminated. From here on, all spring-in results, including results in section 4.5 are referring to results adjusted according to the tool.

In summary, the error from the tooling surface was quantified to provide insights and confidence moving forward. Ignoring the effect of tool expansion at high temperature and two FEP sheets, the worst-case spring-in deviation arising from the tool was around 0.3°. To understand the effect of tooling surface to the greatest extend, further FE simulation considering the tool shape at high temperature and the effect of two layers of FEPs (25 µm thick per layer) is recommended.
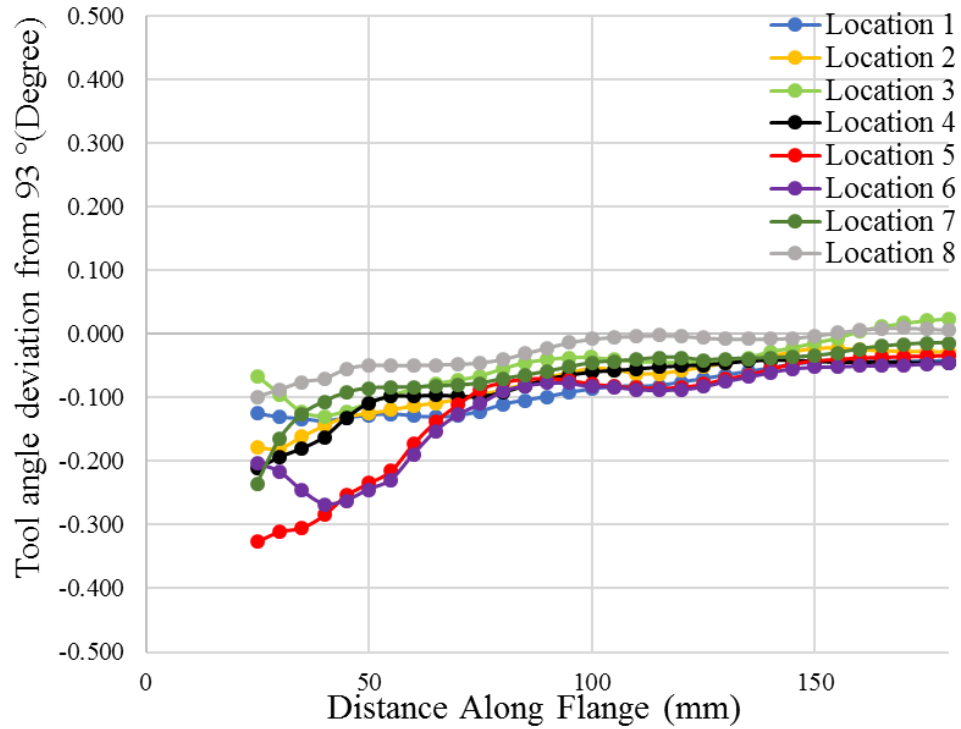
Figure 4.16 Tool angle deviation from nominal vs distance along the flange at specimen locations
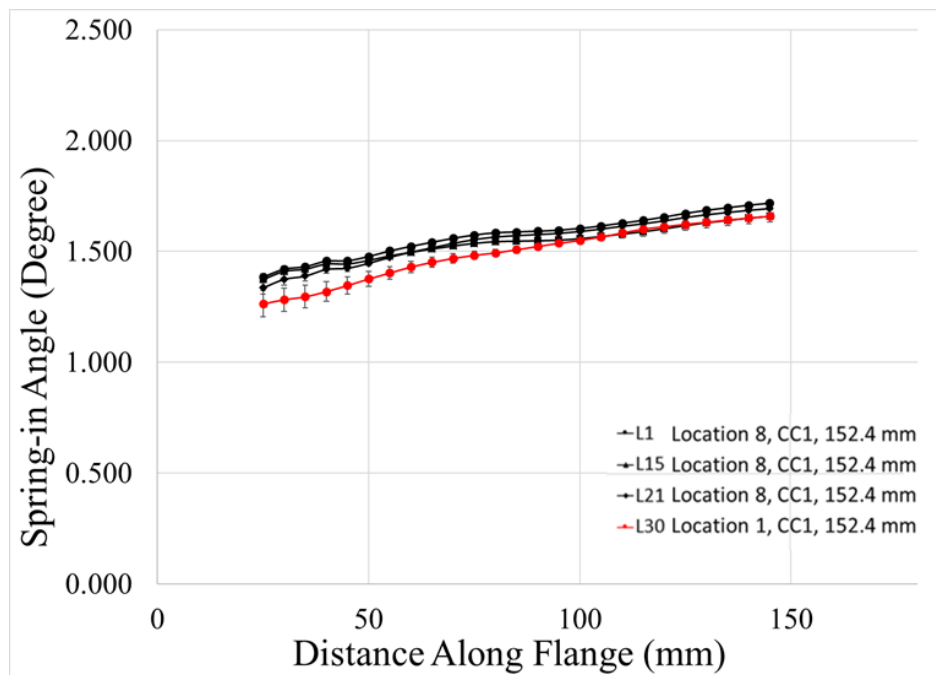


Figure 4.17 Specimen spring-in results adjusted according to tool angle deviation from nominal.

(Compare to Figure 4.2)

## 4.3    Specimen Thickness Measurement

Flange thickness were measured at numerous locations for all specimens. Thickness variability plays an important role in flange bending stiffness which can affect the deformation of the specimens. Thickness is also an indication of fiber volume fraction and consolidation during the manufacturing stage. For a flat laminate section under uniform pressure, such as the flange of an L-shape, resin bleeding can lead to higher fiber volume fraction which manifests as lower thickness. Due to the measurement setup, specimen corner thickness was not obtainable. However, no corner thinning was visually observed.

For each specimen that was produced, flange thickness was measured at the intersections of a 25.4 mm by 25.4 mm (1-inch by 1-inch) grid by a Mitutoyo digital micrometer (Figure 4.19). The grid was drawn on the tool side of the specimen. The complete thickness measurements are attached in Appendix C.

Four thickness measurements along the width of the specimen were averaged, resulting in average thickness measurements along the L-shape flanges (Table 4.2). The average specimen thickness was consistent for a given number of plies; being either 8 or 16. The average thickness of 16-ply specimens was 2.951 mm and average thickness of 8-ply specimens was 1.481 mm.

Due to resin bleeding, measurements closer to the corner of the L-shape specimens were consistently higher than the ends of the specimens. This observation correlates well with the peel ply placements in the experiments (section 3.5.3). The difference was approximately 0.09 mm for 152.4 mm specimens and decrease with decreasing flange length. This thickness gradient from the corner to the end of flanges can induce a fiber volume gradient along the flanges, potentially being one of the causes for the flange warpage observed in the specimens.

Average cured ply thickness (CPT) is plotted in Figure 4.20. Average CPT is not a function of cure cycle, flange length or laminate thickness. Average CPT for all specimens manufactured in this study was calculated to be 0.185 mm.

The breather cloth used on top of the specimens during cure imprinted a rough texture on the bag side suface of the specimens, introducing uncertainties to the thickness measurements. Howerer, the effect was smaller than measurement standard deviations.
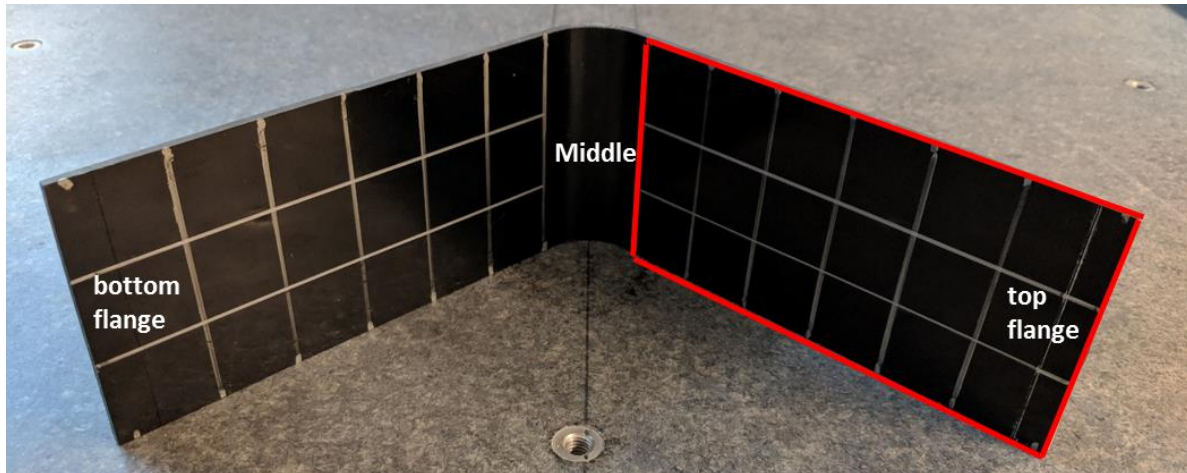


Figure 4.18 6-inch L-shape with 1-inch by 1-inch grid marked on the tool side, ready for thickness measurement

Figure 4.19 Thickness measurement of L-shape specimen with digital micrometer
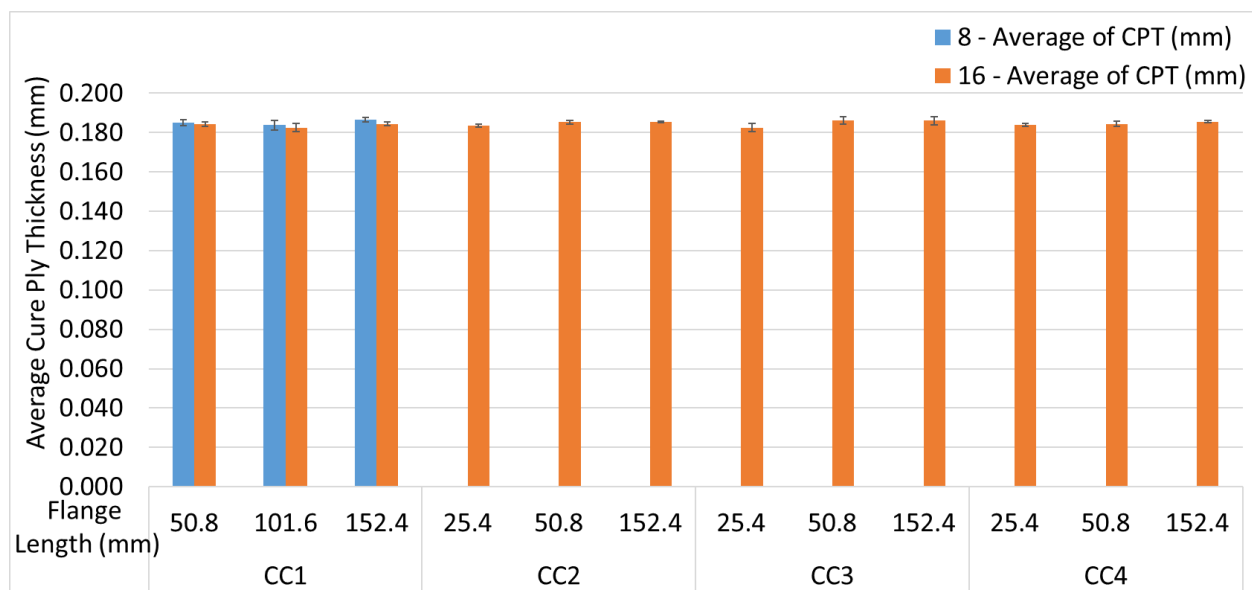


Figure 4.20 Average cure ply thickness organized by flange length, cure cycles and laminate thickness.

Table 4.2 Average specimen thickness along the flanges (all measurements are in mm)

| | Bottom flange | | | | | | | Corner | Top flange | | | | | | |
|---|---|---|---|---|---|---|---|---|---|---|---|---|---|---|---|
| L34 | 2.91 | 2.96 | 2.98 | 2.98 | 2.96 | 2.99 | 2.99 | / | 3.00 | 2.99 | 2.99 | 2.98 | 2.95 | 2.97 | 2.92 |
| L46 | 2.92 | 2.96 | 3.00 | 2.98 | 2.97 | 2.98 | 3.01 | / | 3.01 | 3.00 | 2.98 | 2.99 | 2.98 | 2.98 | 2.92 |
| L30 | 2.80 | 2.99 | 2.96 | 2.99 | 2.97 | 2.99 | 3.01 | / | 2.99 | 2.98 | 2.99 | 2.99 | 2.98 | 2.98 | 2.88 |
| L38 | 2.92 | 2.97 | 2.97 | 2.95 | 3.00 | 2.98 | 2.96 | / | 3.00 | 2.97 | 2.97 | 2.97 | 2.97 | 2.96 | 2.91 |
| L62 | 2.89 | 2.96 | 2.98 | 2.97 | 2.98 | 3.00 | 3.01 | / | 3.00 | 2.99 | 3.00 | 2.98 | 2.97 | 2.98 | 2.92 |
| L58 | 2.90 | 2.98 | 2.97 | 2.96 | 2.97 | 2.98 | 2.99 | / | 2.99 | 2.94 | 2.95 | 2.97 | 2.98 | 2.95 | 2.92 |
| L15 | N/A | N/A | N/A | N/A | N/A | N/A | N/A | / | 2.95 | 2.93 | 2.93 | 2.94 | 2.92 | 2.92 | 2.90 |
| L6 | 1.46 | 1.49 | 1.49 | 1.50 | 1.50 | 1.51 | 1.56 | / | 1.52 | 1.50 | 1.49 | 1.49 | 1.47 | 1.46 | 1.44 |
| L13 | 1.48 | 1.49 | 1.51 | 1.51 | 1.51 | 1.51 | 1.54 | / | 1.53 | 1.51 | 1.51 | 1.49 | 1.50 | 1.49 | 1.47 |
| L21 | 2.91 | 2.93 | 2.97 | 2.96 | 2.94 | 2.97 | 2.98 | / | 3.00 | 2.97 | 2.97 | 2.95 | 2.95 | 2.92 | 2.86 |
| L22 | 1.44 | 1.48 | 1.49 | 1.51 | 1.50 | 1.51 | 1.51 | / | 1.52 | 1.51 | 1.51 | 1.50 | 1.49 | 1.48 | 1.38 |
| L1 | 2.91 | 2.96 | 2.95 | 2.95 | 2.95 | 2.95 | 2.98 | / | 2.99 | 2.99 | 2.98 | 2.98 | 2.95 | 2.98 | 2.91 |
| L24 | / | / | 1.33 | 1.48 | 1.48 | 1.51 | 1.54 | / | 1.51 | 1.50 | 1.49 | 1.46 | 1.36 | / | / |
| L14 | / | / | 2.90 | 2.93 | 2.95 | 2.95 | 2.97 | / | 2.34 | 2.96 | 2.93 | 2.92 | 2.86 | / | / |
| L16 | / | / | 1.37 | 1.40 | 1.51 | 1.48 | 1.51 | / | 1.50 | 1.49 | 1.50 | 1.43 | 1.35 | / | / |
| L7 | / | / | 1.48 | 1.49 | 1.49 | 1.50 | 1.51 | / | 1.50 | 1.50 | 1.50 | 1.49 | 1.47 | / | / |
| L23 | / | / | 2.93 | 2.92 | 2.95 | 2.95 | 2.95 | / | 2.97 | 2.95 | 2.93 | 2.90 | 2.89 | / | / |
| L8 | / | / | 2.90 | 2.91 | 2.91 | 2.92 | 2.96 | / | 2.93 | 2.94 | 2.93 | 2.93 | 2.90 | / | / |
| L32 | / | / | 2.91 | 2.96 | 2.95 | 2.97 | 2.98 | / | 2.98 | 2.96 | 2.96 | 2.95 | 2.90 | / | / |
| L18 | / | / | / | / | 1.40 | 1.48 | 1.50 | / | 1.51 | 1.49 | 1.44 | / | / | / | / |
| L19 | / | / | / | / | 2.89 | 2.97 | 2.98 | / | 2.99 | 2.97 | 2.90 | / | / | / | / |
| L4 | / | / | / | / | 2.95 | 2.98 | 3.02 | / | 3.00 | 2.98 | 2.92 | / | / | / | / |
| L9 | / | / | / | / | 2.90 | 2.97 | 3.02 | / | 3.00 | 2.98 | 2.91 | / | / | / | / |
| L3 | / | / | / | / | 1.48 | 1.51 | 1.51 | / | 1.51 | 1.49 | 1.46 | / | / | / | / |
| L5 | / | / | / | / | 2.89 | 2.96 | 2.98 | / | 3.00 | 2.98 | 2.93 | / | / | / | / |
| L10 | / | / | / | / | 2.94 | 2.97 | 2.97 | / | 2.97 | 2.97 | 2.89 | / | / | / | / |
| L20 | / | / | / | / | 2.88 | 2.95 | 2.97 | / | 2.95 | 2.95 | 2.92 | / | / | / | / |
| L11 | / | / | / | / | 1.44 | 1.50 | 1.51 | / | 1.50 | 1.49 | 1.46 | / | / | / | / |
| L29 | / | / | / | / | 2.83 | 2.93 | 2.94 | / | 2.95 | 2.94 | 2.90 | / | / | / | / |
| L64 | / | / | / | / | 2.93 | 2.98 | 3.01 | / | 3.00 | 2.96 | 2.91 | / | / | / | / |
| L48 | / | / | / | / | 2.96 | 3.00 | 3.01 | / | 3.00 | 2.98 | 2.93 | / | / | / | / |
| L40 | / | / | / | / | 2.90 | 2.98 | 2.97 | / | 3.00 | 2.97 | 2.91 | / | / | / | / |
| L60 | / | / | / | / | 2.91 | 2.96 | 2.97 | / | 2.96 | 2.93 | 2.88 | / | / | / | / |
| L36 | / | / | / | / | 2.93 | 2.98 | 3.01 | / | 3.01 | 2.99 | 2.93 | / | / | / | / |
| L33 | / | / | / | / | / | 2.92 | 2.97 | / | 2.98 | 2.93 | / | / | / | / | / |
| L37 | / | / | / | / | / | 2.90 | 2.97 | / | 2.97 | 2.88 | / | / | / | / | / |
| L45 | / | / | / | / | / | 2.90 | 2.97 | / | 2.93 | 2.89 | / | / | / | / | / |
| L57 | / | / | / | / | / | 2.89 | 2.97 | / | 2.97 | 2.91 | / | / | / | / | / |
| L61 | / | / | / | / | / | 2.92 | 2.99 | / | 2.98 | 2.93 | / | / | / | / | / |

## 4.4 Specimen Temperature, Tg and Degree of Cure Evolution

The curing data for specimens manufactured in this study are presented in this section. Specimen temperature was measured by a TC placed in a sacrificial specimen at position 7 in every batch (Table 4.3). The TC was place in the center (width wise) and middle (through-thickness wise) of that specimen (see section 3.5.3 for fabrication details). Temperature of the sacrificial specimen was recorded during the cure cycle and subsequently imported into RAVEN to calculate the Tg and DoC evolution. RAVEN 0D basic simulation was used for this purpose. See section 3.2 for material model details. In the following reporting, air temperature of the autoclave during experiment was also added to the figures for reference. Note that the air temperature was measured by the autoclave at the exit vent; it was not the air temperature directly above position 7. It is also important to mention that data from position 7 was a conservative estimation of the actual specimen at location 1, 2 and 5 due to the slightly lagging temperature response (see section 3.3.2 for details).

Table 4.3 Actual temperature cycle measured at location 7 specimen in every run

|  | Ramp 1 (°C/min) | Hold 1 T (°C) | Hold 1 t (min) | Ramp 2 (°C/min) | Hold 2 T (°C) | Hold 2 t (min) | Ramp 3 (°C/min) | Hold 3 T (°C) | Hold 3 t (min) |
|---|---|---|---|---|---|---|---|---|---|
| CC1 | 1 | 180 | 120 |  |  |  |  |  |  |
| CC2 | 1 | 140 | 140 | 0.3 | 180 | 90 |  |  |  |
| CC3 | 1 | 140 | 140 | 2.5 | 180 | 120 | N/A | N/A | N/A |
| CC4 | 1 | 140 | 140 |  |  |  |  |  |  |

Temperature data with Tg and DoC of cure cycle 1 are shown in Figure 4.21. The temperature in the middle of specimen lagged the air temperature for around 13.0 °C during the ramp up. Resin in this case gelled at around 173 °C. At the end of the cure cycle, resin Tg reached 216.7 °C and DoC was 0.896.
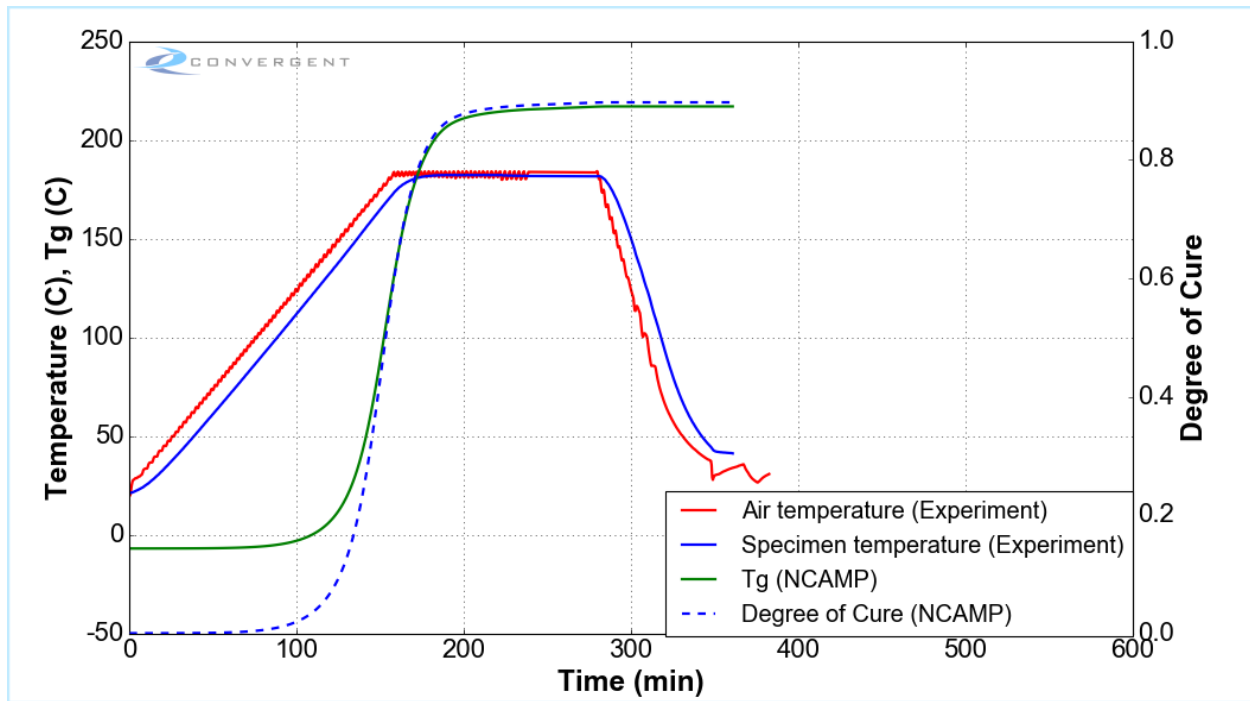


Figure 4.21 Cure cycle 1 specimen curing data

Figure 4.22 shows the curing data of cure cycle 2. The temperature in the middle of specimen lagged the air temperature for around 14.2 °C during the first ramp and 4.9 °C during the second ramp. Resin gelled (at 140 °C) and vitrified on the first hold as designed. Resin temperature was more than 20 °C below Tg after vitrification. At the end of the cure cycle, resin Tg reached 215.1 °C and DoC was 0.891.
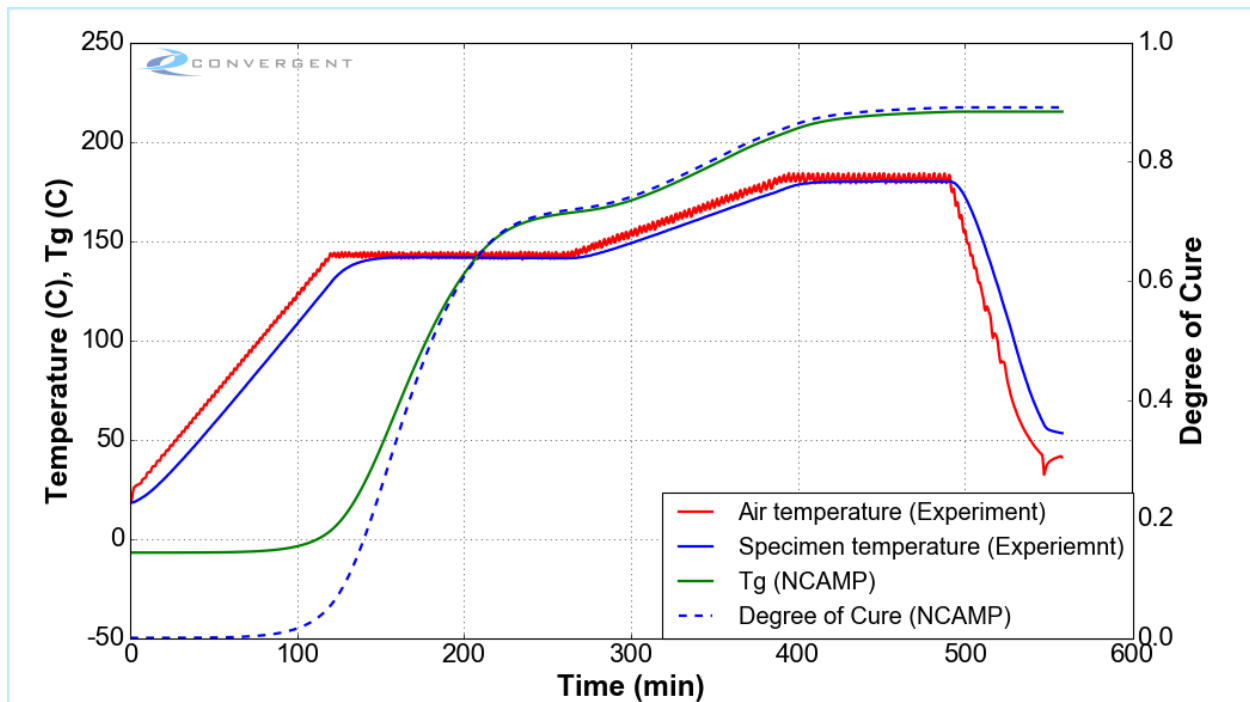

Figure 4.22 Cure cycle 2 specimen curing data

During the first ramp in cure cycle 3 (Figure 4.23), specimen temperature lagged autoclave air temperature by 13.57 °C. Like cure cycle 2, resin in cure cycle 3 gelled on the first hold at 140 °C and then vitrified. During the second rapid ramp, specimen temperature was brought close to Tg (4.9 °C difference), pushing resin into a rubbery state. As curing progressed, resin Tg kept increasing and became glassy again. See section 4.6 for a detailed discussion on this near devitrification behavior. At the end of the cure cycle, resin Tg reached 216.3 °C and DoC was 0.895.
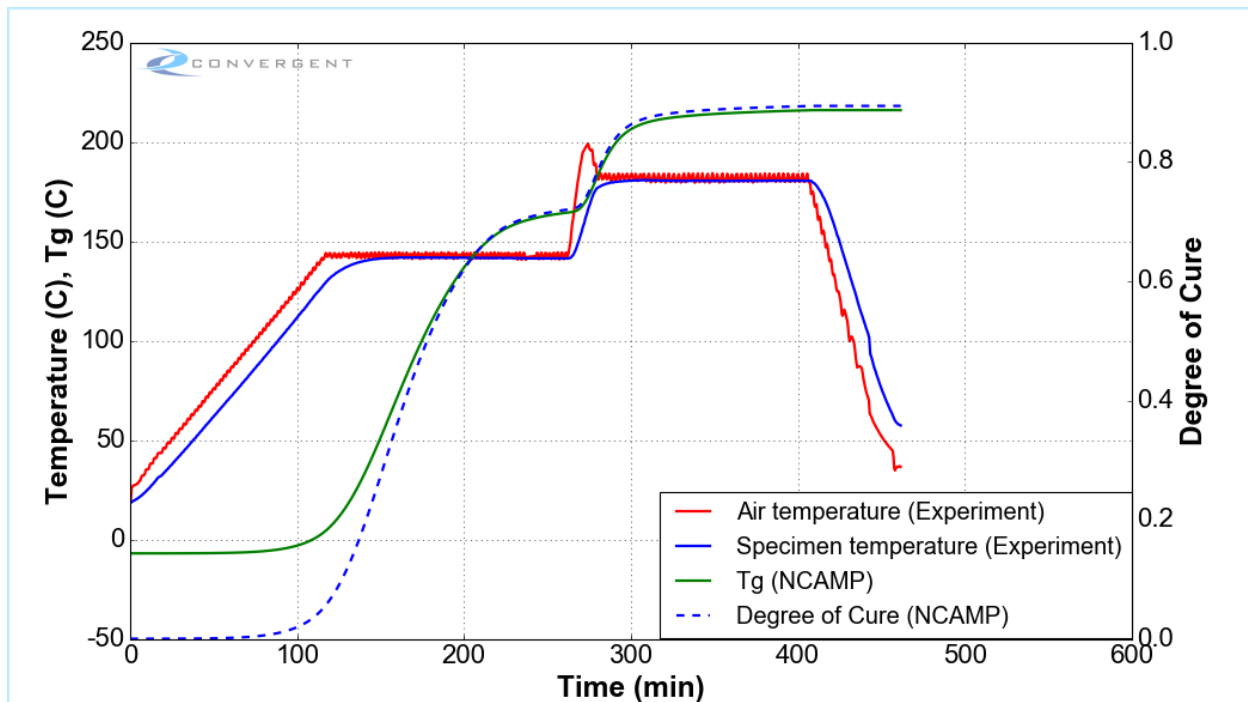


Figure 4.23 Cure cycle 3 specimen curing data

Cure cycle 4 was designed to reproduce the first portion of cure cycle 2 and cure cycle 3. Similar to previous cure cycles, the temperature lag in the sacrificial specimen comparing to the air temperature was 13.2 °C (Figure 4.24). Resin gelled around 140 °C and vitrified during the temperature hold. Tg at the end of cure cycle was 165.3 °C and DoC was 0.723.
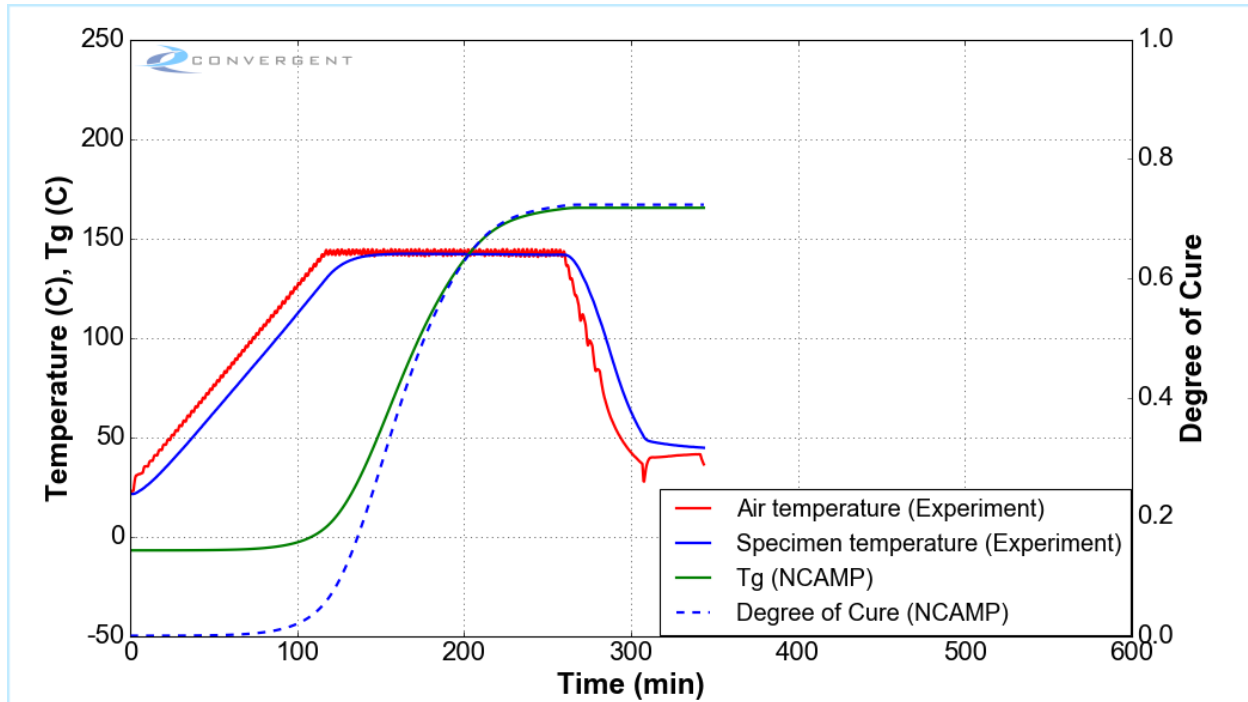


Figure 4.24 Cure cycle 4 specimen curing data

## 4.5    Specimen Deformation Results

Experimental results and observations of this study is presented in this section. The effect of laminate thickness, flange length and cure cycles are highlighted using tables, spring-in plots and cluster column charts for the most thorough representation. Error bars presented in this section represent the standard deviation of the averaged result if without further specification. As explained in section 4.2.2, the spring-in slopes were used as a representation of flange warpage.

### 4.5.1    The Effect of Laminate Thickness

Phase I of this study was dedicated to inquiring the effect of the laminate thickness and flange length. Specimens with $[90/0]_{2s}$ and $[90/0]_{4s}$ were made with Cure cycle 1 (baseline 1-hold 180 °C). Three different flange length: 50.8, 101.6, 152.4 mm (2, 4, 6 inches) were made for both layups. The experimental results are listed in the table below. For each flange length, spring-in plots and column charts are presented to visualize the comparison.

Table 4.4 Experimental results of 8-ply and 16-ply specimens, inquiry into the effect of laminate thickness

| | Corner spring-in | Corner spring-in Stdev | Total spring-in | Total spring-in Stdev | Warpage | Warpage Stdev |
|---|---|---|---|---|---|---|
| 50.8 mm L-shape | | | | | | |
| 8-ply | 1.474 | 0.053 | 1.591 | 0.096 | 0.0039 | 0.0017 |
| 16-ply | 1.452 | 0.021 | 1.466 | 0.027 | 0.0003 | 0.0006 |
| 101.6 mm L-shape | | | | | | |
| | Corner spring-in | Corner spring-in Stdev | Total spring-in | Total spring-in Stdev | Warpage | Warpage Stdev |
| 8-ply | 1.543 | 0.051 | 1.851 | 0.164 | 0.0037 | 0.0010 |
| 16-ply | 1.420 | 0.023 | 1.627 | 0.019 | 0.0030 | 0.0004 |
| 152.4 mm L-shape | | | | | | |
| | Corner spring-in | Corner spring-in Stdev | Total spring-in | Total spring-in Stdev | Warpage | Warpage Stdev |
| 8-ply | 1.493 | 0.039 | 1.994 | 0.126 | 0.0044 | 0.0008 |
| 16-ply | 1.360 | 0.058 | 1.685 | 0.026 | 0.0026 | 0.0005 |

**50.8 mm specimens**
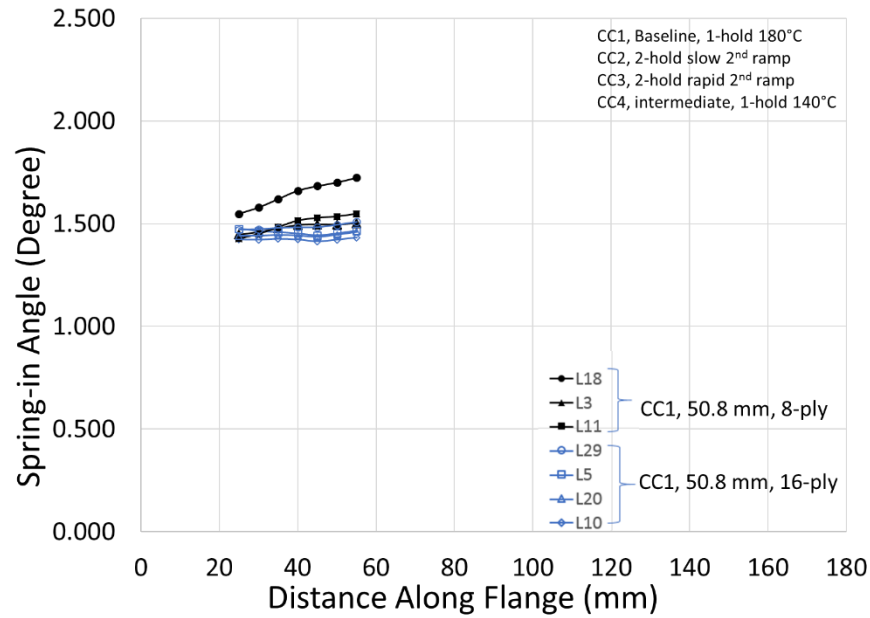


Figure 4.25 Spring-in profiles, 8-ply and 16-ply 50.8 mm specimens made with cure cycle 1
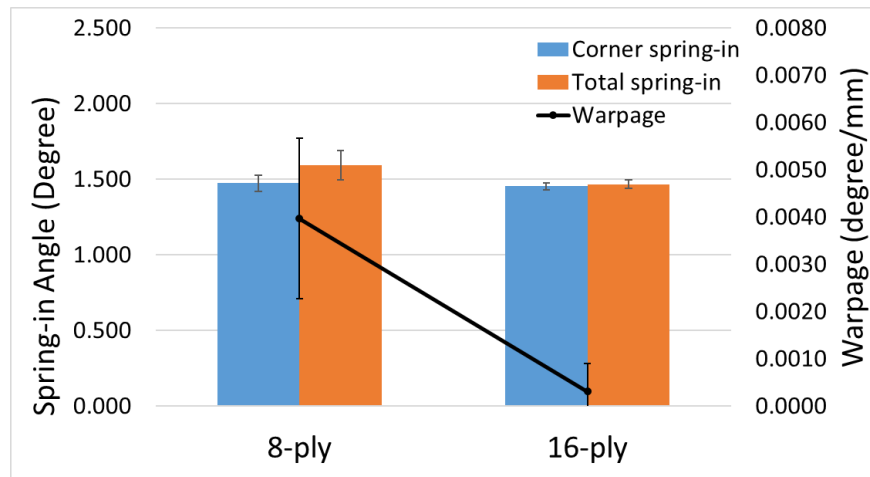


Figure 4.26 Experimental results, 8-ply and 16-ply 50.8 mm specimens made with cure cycle 1

For 50.8 mm flange L-shaped specimens, 8-ply showed similar corner spring-in comparing to 16-ply. However, 8-ply total spring-in was higher than 16-ply due to higher warpage (Figure 4.25 and Figure 4.26). Higher scatter was observed in the 8-ply results. Warpage of the 16-ply specimens were negligible (Figure 4.26).

**101.6 mm specimens**
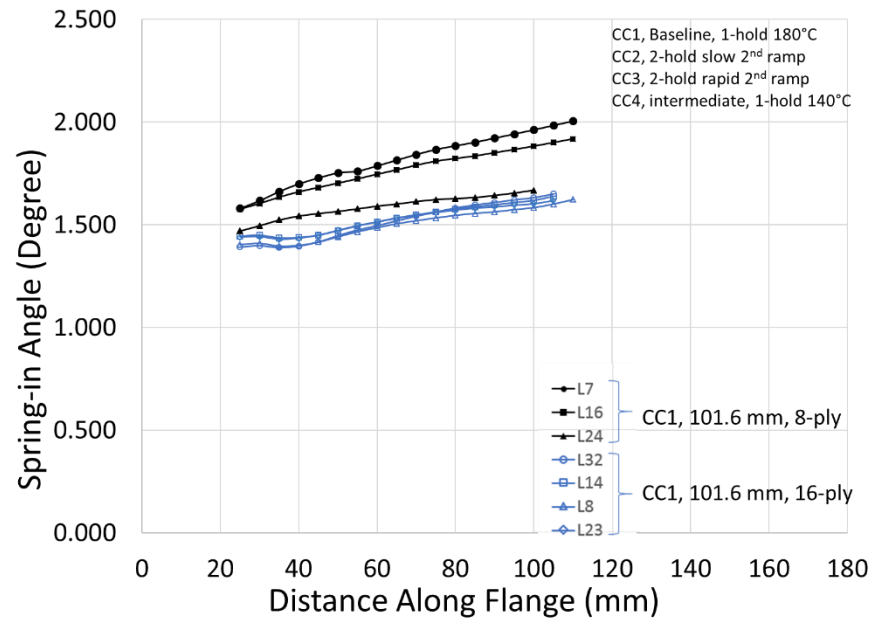


Figure 4.27 Spring-in profiles, 8-ply and 16-ply 101.6 mm specimens made with cure cycle 1
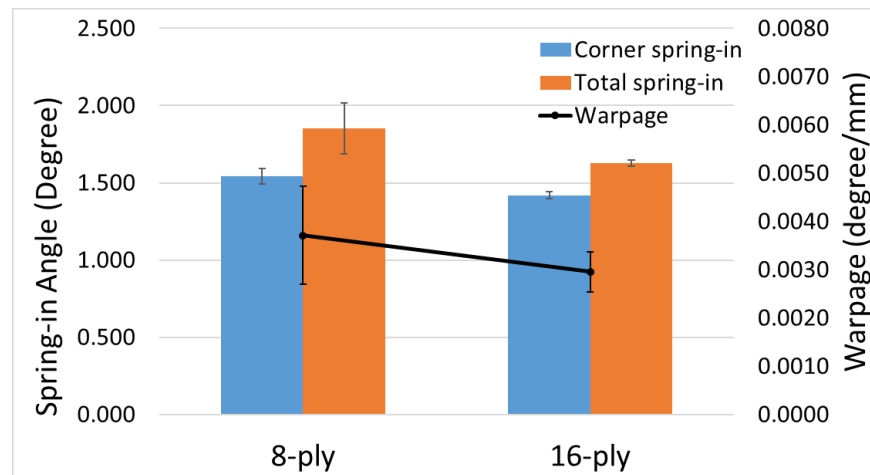


Figure 4.28 Experimental results, 8-ply and 16-ply 101.6 mm specimens made with cure cycle 1

101.6 mm L-shapes showed 8-ply laminates had higher corner and total spring-in than 16-ply ones with 8-ply specimens having higher scatter (Figure 4.27 and Figure 4.28). 8-ply specimens also showed higher warpage than 16-ply specimens (Figure 4.28).

**152.4 mm specimen**
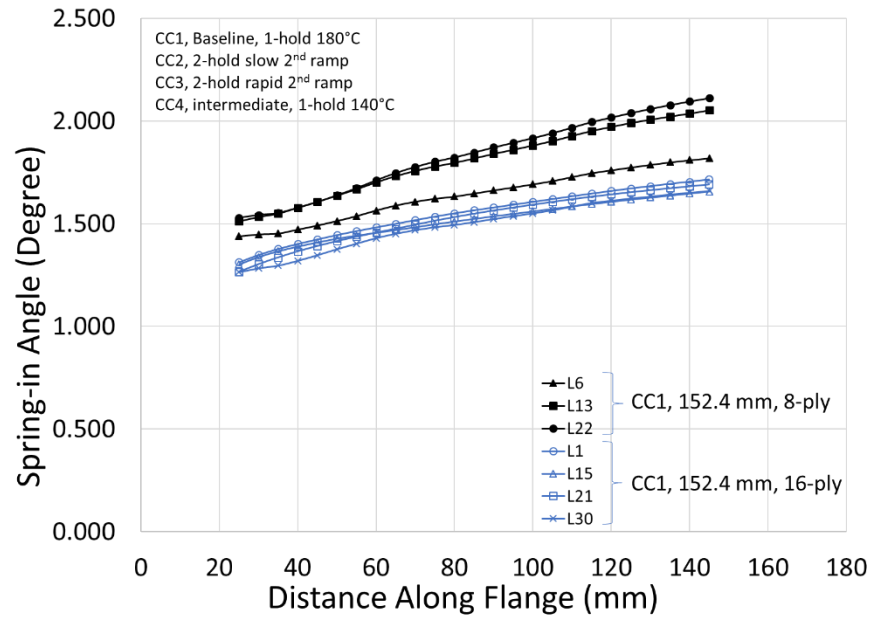


Figure 4.29 Spring-in profiles, 8-ply and 16-ply 152.4 mm specimens made with cure cycle 1
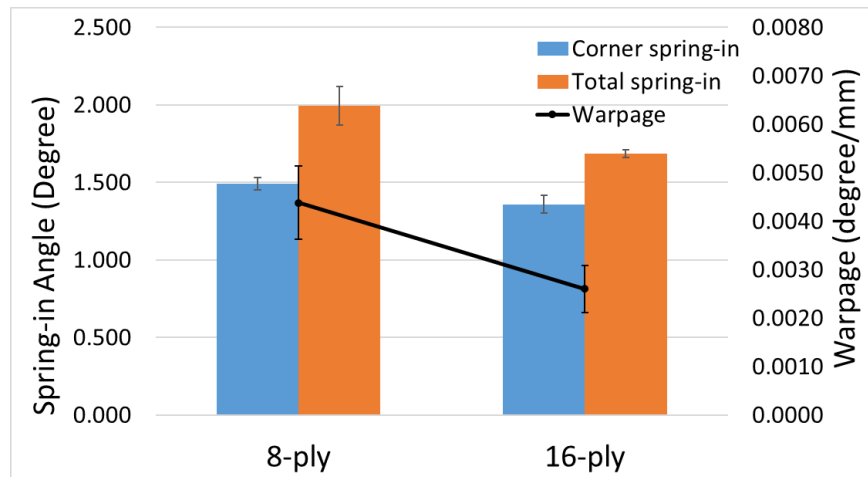


Figure 4.30 Experimental results, 8-ply and 16-ply 152.4 mm specimens made with cure cycle 1

Similar to the 101.6 mm specimens, 152.4 mm 8-ply specimens also showed higher corner spring-in, total spring-in and warpage than 16-ply specimens (Figure 4.29 and Figure 4.30).

In summary, results for the effect of thickness are:

- Corner spring-in decrease as laminate thickness increase
- Total spring-in decrease as laminate thickness increase
- For all three flange length, flange warpage decrease with increasing laminate thickness

Because literature showed L-shape thickness to length ratio (t/l) could influence interlaminar shearing, thus affect spring-in, the ratio was plotted against the spring-in and warpage results (Figure 4.31). Corner spring-in shows little dependence on t/l ratio, while warpage decrease as t/l ratio increase. As a result, the total spring-in decrease as t/l ratio increase. It is important to note that this plot and phenomenon do not isolate or show the extend of the effect of laminate thickness or flange length.
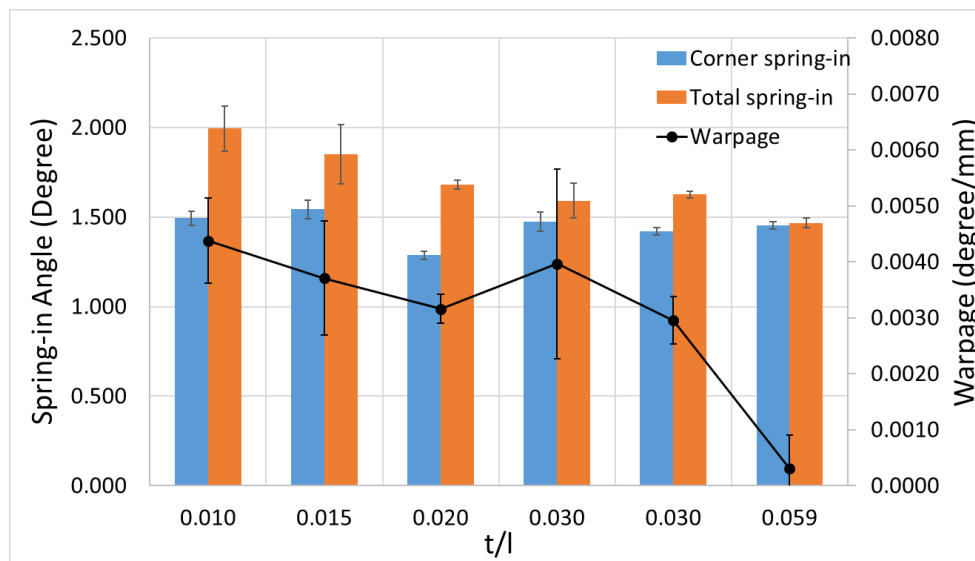


Figure 4.31 Thickness over flange length ratio (t/l) vs spring-in and warpage results

### 4.5.2 The Effect of Flange Length

Studies in literature consistently showed that spring-in increases with increasing flange length [17], [22], [53], [57], [87]. This stands true for *total* spring-in values as proven in this study by 25.4, 50.8, 101.6, 152.4 mm (1, 2, 4 and 6-inch) specimens made with different cure cycles. However, literature did not reveal that corner spring-in is almost invariant with flange length. The higher total spring-in was a consequence of longer flange length at a same curvature. Summary of the specimens are listed in table 4.4.

Table 4.5 Experimental results of 25.4, 50.8, 101.6, 152.4 mm flange specimens, inquiry into the effect of flange length

| | Corner spring-in | Corner spring-in Stdev | Total spring-in | Total spring-in Stdev | Warpage | Warpage Stdev |
|---|---|---|---|---|---|---|
| CC1 8 layers | | | | | | |
| 50.8 mm | 1.474 | 0.053 | 1.591 | 0.096 | 0.0041 | 0.0024 |
| 101.6 mm | 1.543 | 0.051 | 1.851 | 0.164 | 0.0037 | 0.0010 |
| 152.4 mm | 1.493 | 0.039 | 1.994 | 0.126 | 0.0044 | 0.0008 |
| CC1 16 layers | | | | | | |
| 25.4 mm | 1.421 | 0.032 | 1.433 | 0.027 | N/A | N/A |
| 50.8 mm | 1.452 | 0.021 | 1.466 | 0.027 | 0.0003 | 0.0006 |
| 101.6 mm | 1.420 | 0.023 | 1.627 | 0.019 | 0.0030 | 0.0004 |
| 152.4 mm | 1.360 | 0.058 | 1.685 | 0.026 | 0.0026 | 0.0005 |
| CC2 16 layers | | | | | | |
| 25.4 mm | 1.042 | 0.068 | 1.038 | 0.068 | N/A | N/A |
| 101.6 mm | 0.918 | 0.024 | 0.945 | 0.041 | 0.0008 | 0.0002 |
| 152.4 mm | 0.957 | 0.008 | 1.270 | 0.007 | 0.0027 | 0.0001 |
| CC3 16 layers | | | | | | |
| 25.4 mm | 1.127 | 0.000 | 1.117 | 0.002 | N/A | N/A |
| 101.6 mm | 1.075 | 0.008 | 1.086 | 0.017 | 0.0002 | 0.000 |
| 152.4 mm | 0.989 | 0.026 | 1.244 | 0.048 | 0.0023 | 0.000 |
| CC4 16 layers | | | | | | |
| 25.4 mm | 1.132 | 0.011 | 1.126 | 0.010 | N/A | N/A |
| 101.6 mm | 1.045 | 0.019 | 1.089 | 0.030 | 0.0014 | 0.0004 |
| 152.4 mm | 1.036 | 0.016 | 1.397 | 0.037 | 0.0032 | 0.0001 |

**CC1, 8 Layers**
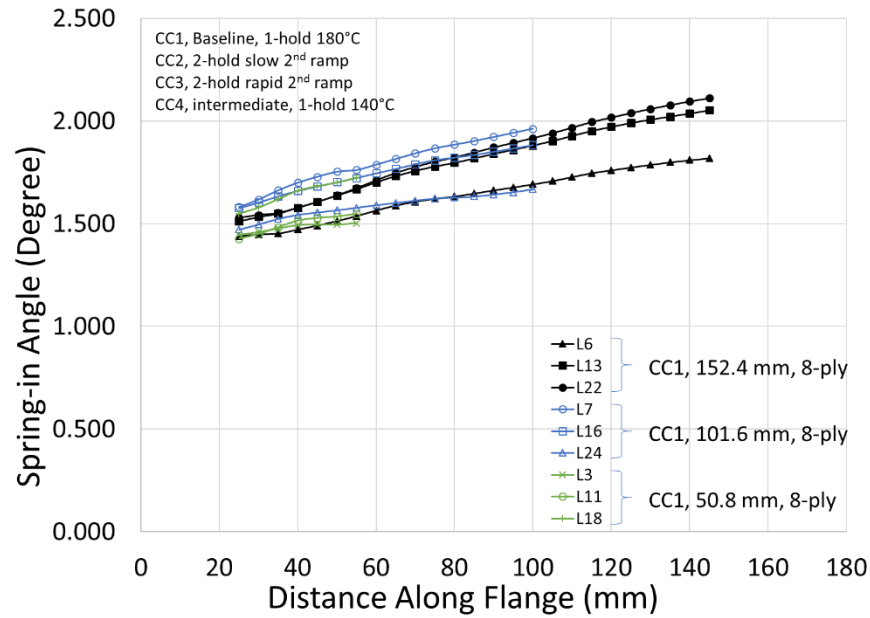


Figure 4.32 Spring-in profiles, 8-ply, 50.8, 101.6, 152.4 mm specimens made with cure cycle 1
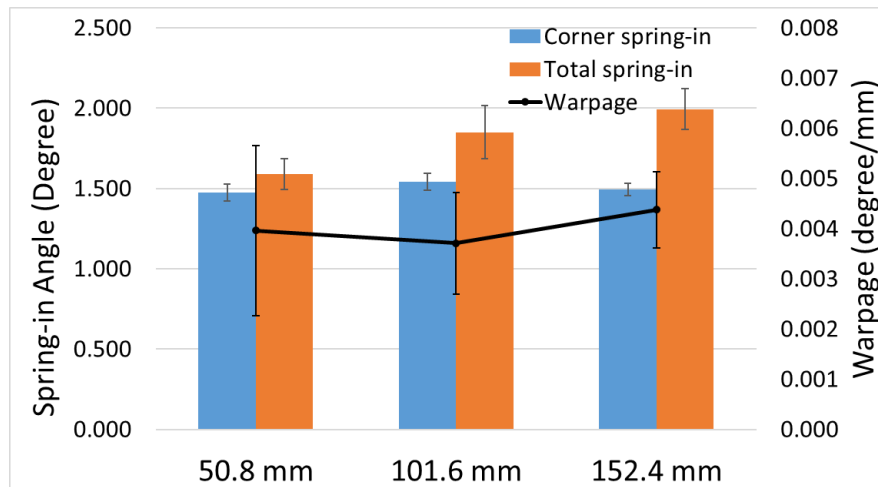


Figure 4.33 Experimental results, 8-ply, 50.8, 101.6, 152.4 mm specimens made with cure cycle 1

For 8-ply, 50.8, 101.6, 152.4 mm specimens made with cure cycle 1, the average corner spring-in and warpage were not a function of flange length. However, with similar corner spring-in and warped flanges with the same curvature, average total spring-in values increased with increasing flange length.

97

**CC1, 16 Layers**
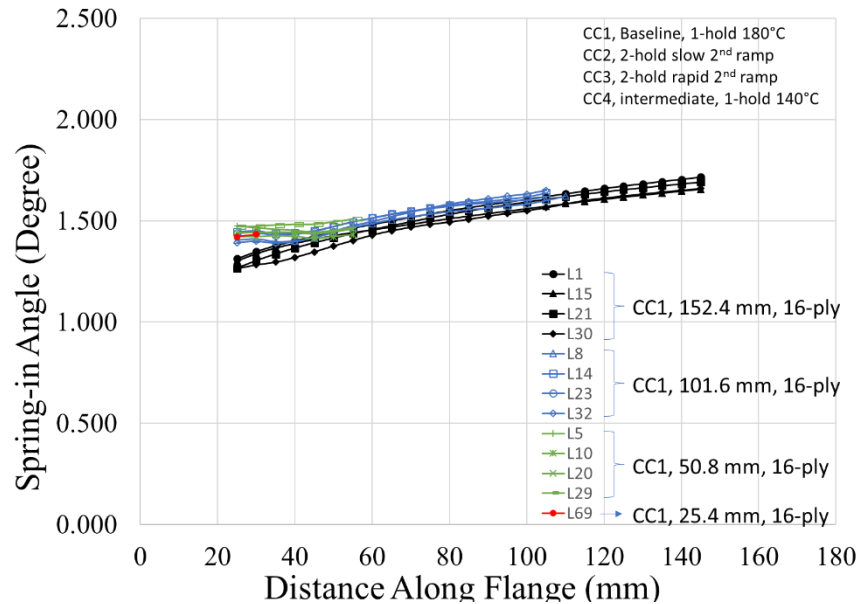


Figure 4.34 Spring-in profiles, 16-ply, 25.4, 50.8, 101.6, 152.4 mm specimens made with cure cycle 1
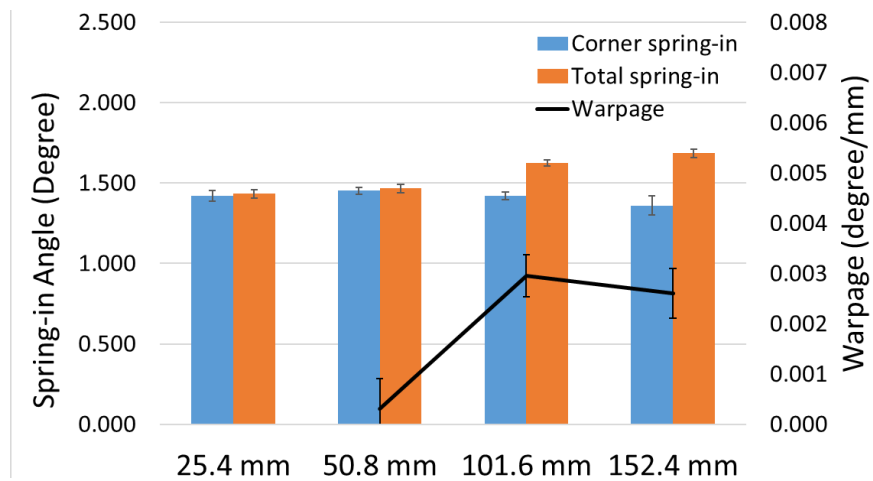


Figure 4.35 Experimental results, 16-ply, 25.4, 50.8, 101.6, 152.4 mm specimens made with cure cycle 1. 25.4 mm specimen warpage was excluded due to short span, little physical significance

For CC1, 16-ply specimens, average corner spring-in values varied little with increasing flange length. Warpage for 50.8 mm was nearly 0 but increased significantly going from 50.8 mm to 101.6 mm. As a result, total spring-in values increased with flange length due to constant corner spring-in and increasing length of warped flanges. Error bars for the single 25.4 mm specimen were the direct results from the data reduction process.

**CC2, 16 Layers**
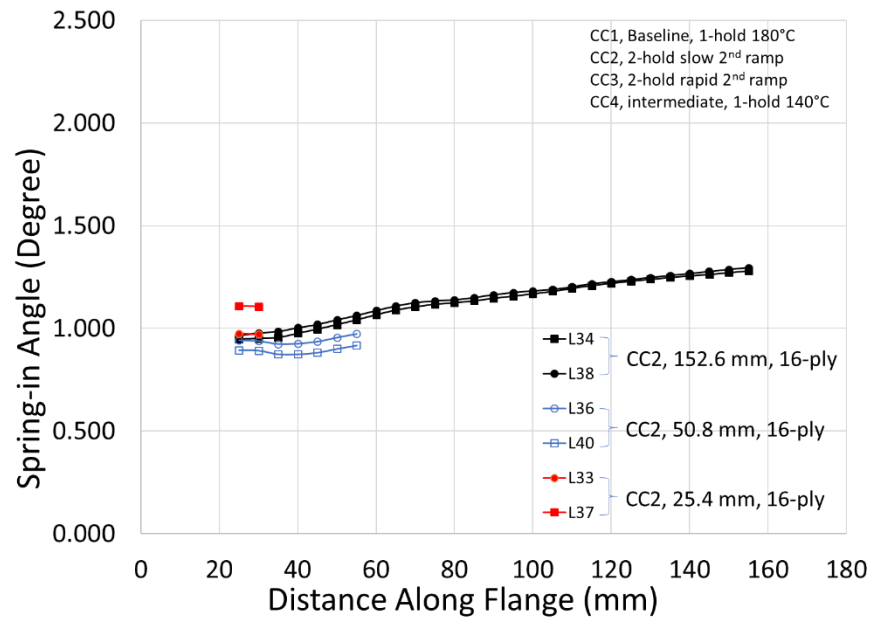


Figure 4.36 Spring-in profiles, 16-ply, 25.4, 50.8, 152.4 mm specimens made with cure cycle 2
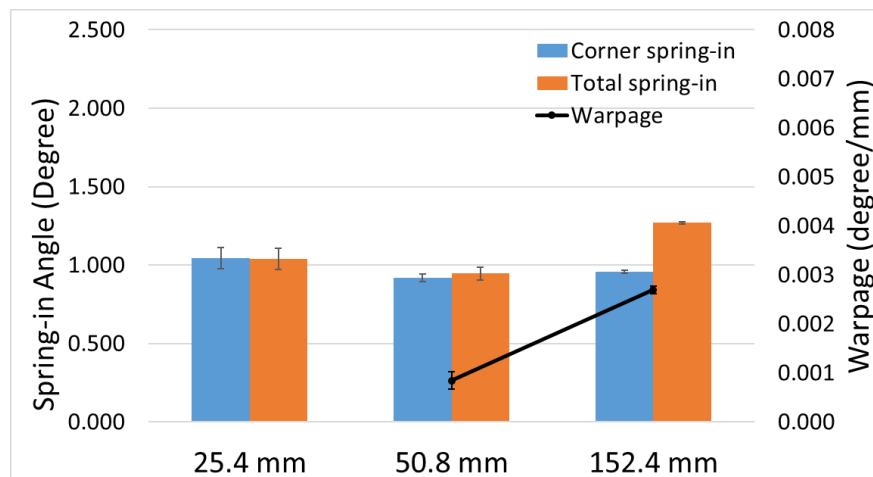


Figure 4.37 Experimental results, 16-ply, 25.4, 50.8, 152.4 mm specimens made with cure cycle 2

For 16-ply specimens made with CC2, two specimens were made for each flange length. Repeats of 25.4 mm specimen displayed high scatter in the spring-in results and the reason is unclear. Going from 50.8 mm to 101.6 mm, warpage increased significantly; total spring-in increased due to constant corner spring-in and increasing length of warped flanges.

**CC3, 16 Layers**
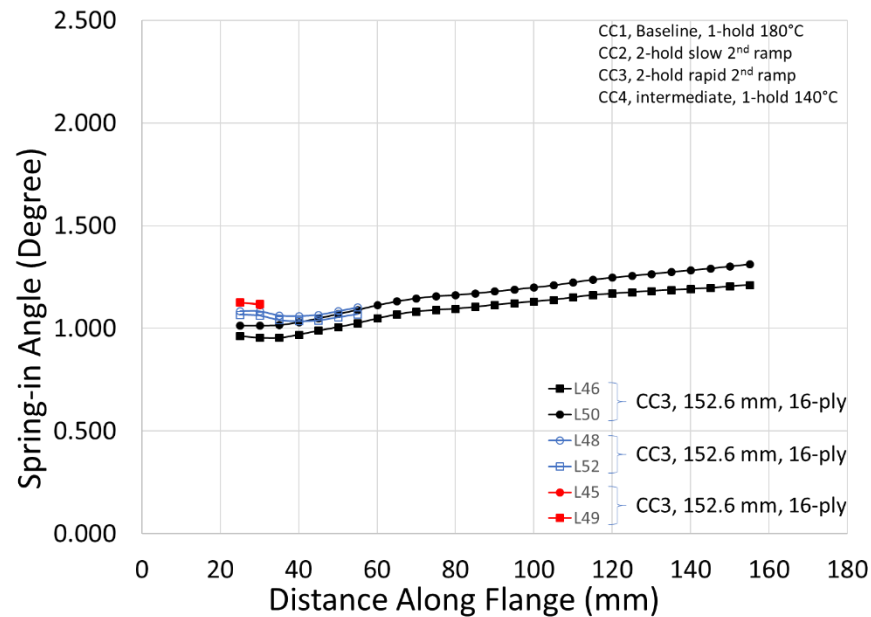


Figure 4.38 Spring-in profiles, 16-ply, 25.4, 50.8, 152.4 mm specimens made with cure cycle 3
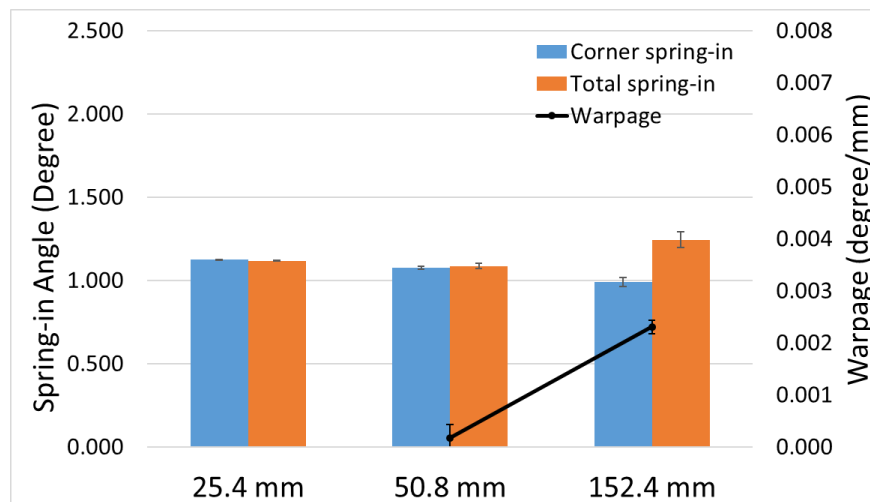


Figure 4.39 Experimental results, 16-ply, 25.4, 50.8, 152.4 mm specimens made with cure cycle 3

Specimens made with cure cycle 3 revealed very similar pattern as the specimens from cure cycle 2. The variation in corner spring-in values is around 0.16 ° between the three different flange length.

**CC4, 16 Layers**
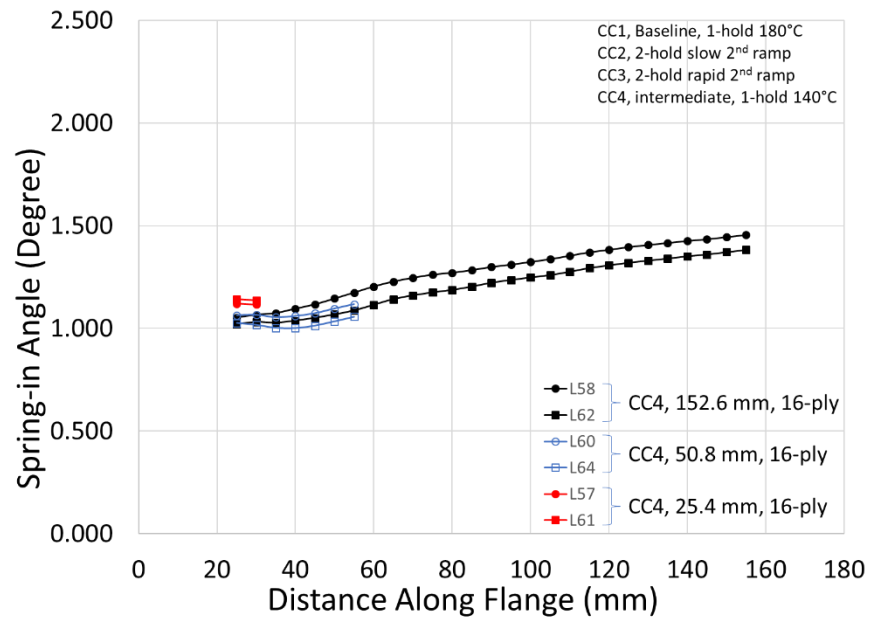


Figure 4.40 Spring-in profiles of 16-ply, 25.4, 50.8, 152.4 mm specimens made with cure cycle 4
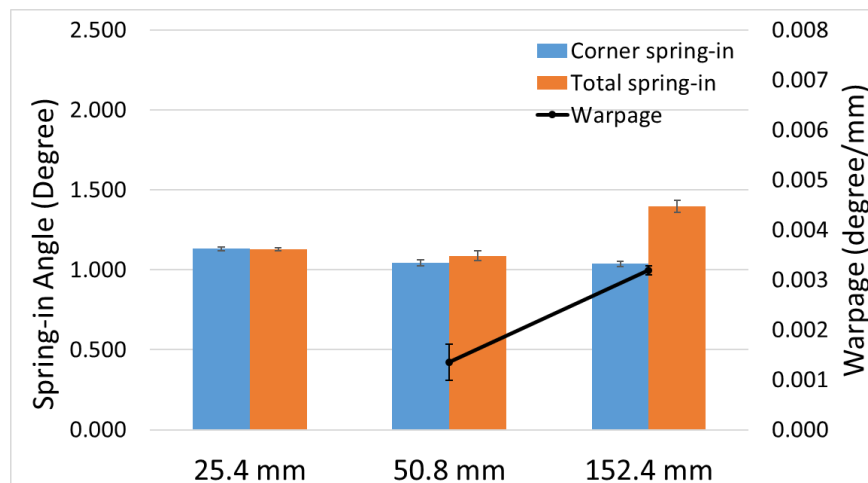


Figure 4.41 Experimental results, 16-ply, 25.4, 50.8, 152.4 mm specimens made with cure cycle 4

16-ply specimens made with cure cycle 4 again show consistent trend as in previous cases where corner spring-in varied little and total spring-in increased as a result of increasing length of warped flanges.

The key results for the effect of flange length are the following:

- Corner spring-in is not a function of flange length
- Warpage increases significantly from 50.8 mm to 152.4 mm for 16-ply specimens. However, this transition was not observed for 8-ply specimens. Instead, although scatter was high, 8-ply specimens showed close warpage values for 50.8 mm, 101.6 mm and 152.4 mm flange length. This phenomenon can be explained by the inter-ply shearing mentioned in Section 2.4.2.1. For 50.8 mm flange length, 16-ply specimens were able to shear more than the 8-ply ones, resulting in less bending stress and warpage
- Total spring-in values increase with flange length as a result of similar corner spring-in and increasing length of warped flanges

### 4.5.3    The Effect of Cure Cycle

Process conditions can be modified to reduce residual stresses and process induced deformation. In this section, specimens are compared to probe the effect of various cure cycle parameters on L-shape deformation. Gelation temperatures of 140 °C and 173 °C were compared as well as two different ramp rates after vitrification. Details about the cure cycle design can be found in section 3.20. Ramp rates of 0.3 °C/min and 5 °C/min were used for the second ramp to explore whether pushing resin close to devitrification would impact the L-shape deformation. Cure cycle 4 induced partially cured specimens where the specimens gelled and vitrified at 140 °C. Results of these specimens are listed in the table below.

Table 4.6 Experimental results of cure cycle 1 to 4, inquiry into the effect of cure cycle

| | Corner spring-in | Corner spring-in Stdev | Total spring-in | Total spring-in Stdev | Warpage | Warpage Stdev |
|---|---|---|---|---|---|---|
| 25.4 mm L-shape | | | | | | |
| CC 1 | 1.421 | 0.032 | 1.433 | 0.027 | N/A | N/A |
| CC 2 | 1.042 | 0.068 | 1.038 | 0.068 | N/A | N/A |
| CC 3 | 1.127 | 0.000 | 1.117 | 0.002 | N/A | N/A |
| CC 4 | 1.132 | 0.011 | 1.126 | 0.010 | N/A | N/A |
| 50.8 mm L-shape | | | | | | |
| | Corner spring-in | Corner spring-in Stdev | Total spring-in | Total spring-in Stdev | Warpage | Warpage Stdev |
| CC 1 | 1.452 | 0.021 | 1.466 | 0.027 | 0.0003 | 0.0006 |
| CC 2 | 0.918 | 0.024 | 0.945 | 0.041 | 0.0008 | 0.0002 |
| CC 3 | 1.075 | 0.008 | 1.086 | 0.017 | 0.0002 | 0.0003 |
| CC 4 | 1.045 | 0.019 | 1.087 | 0.030 | 0.0013 | 0.0004 |
| 152.4 mm L-shape | | | | | | |
| | Corner spring-in | Corner spring-in Stdev | Total spring-in | Total spring-in Stdev | Warpage | Warpage Stdev |
| CC 1 | 1.360 | 0.058 | 1.685 | 0.026 | 0.0026 | 0.0005 |
| CC 2 | 0.957 | 0.008 | 1.270 | 0.007 | 0.0027 | 0.0001 |
| CC 3 | 0.989 | 0.026 | 1.244 | 0.048 | 0.0023 | 0.0001 |
| CC 4 | 1.036 | 0.016 | 1.397 | 0.037 | 0.0032 | 0.0001 |

**25.4 mm Specimen**
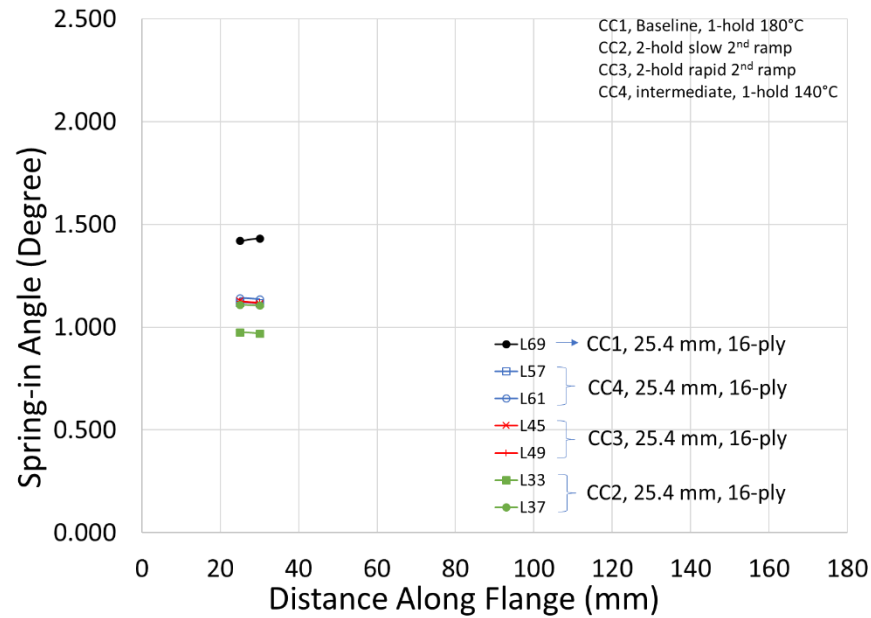


Figure 4.42 Spring-in profiles of 16-ply, 25.4 mm specimens made with cure cycle 1 to 4
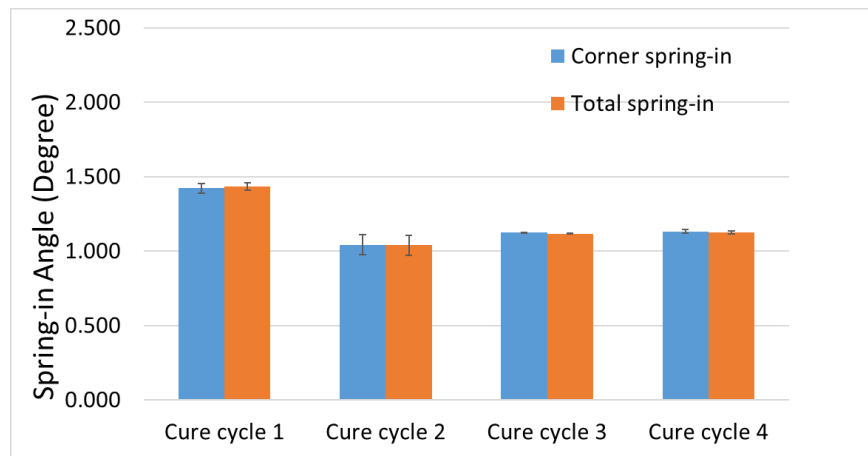


Figure 4.43 Experimental results 16-ply, 25.4 mm specimens made with cure cycle 1 to 4

L69, the specimen made with 1-hold MRCC gelled at 170 °C, exhibited high values of corner and total spring-in. The scatter for specimens made with cure cycle 2 was high. However, the average corner spring-in and total spring-in showed close values comparing to cure cycle 3, and 4. Warpage were not computed due to the short flange length.

**50.8 mm Specimens**
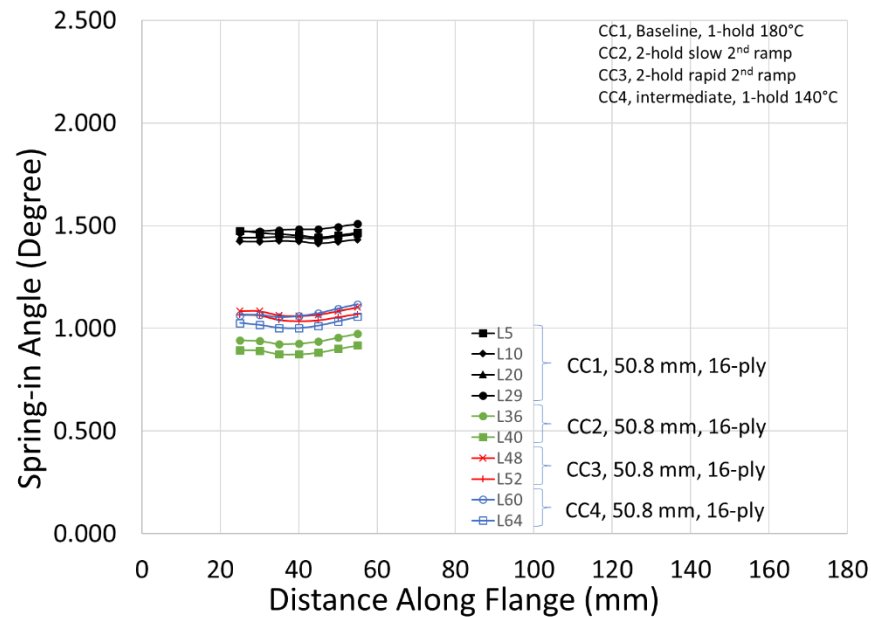


Figure 4.44 Spring-in profiles, 16-ply, 50.8 mm specimens made with cure cycle 1 to 4
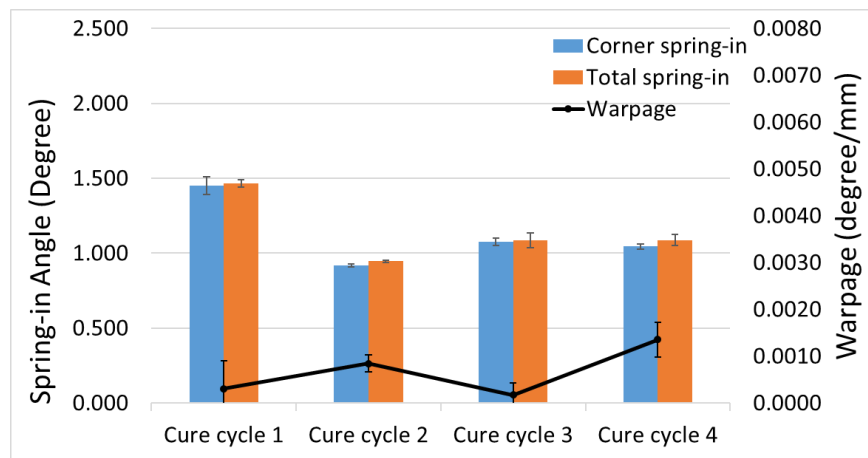


Figure 4.45 Experimental results, 16-ply, 50.8 specimens made with cure cycle 1 to 4

The 50.8 mm cure cycle 1 specimens exhibited the highest spring-in values. Cure cycle 3 and cure cycle 4 showed very close corner and total spring-in values. Average corner and total spring-in values from cycle 3 and 4 were 0.15 ° higher than those of cycle 2. Overall, 50.8 mm specimens showed low warpage.

**152.4 mm Specimens**
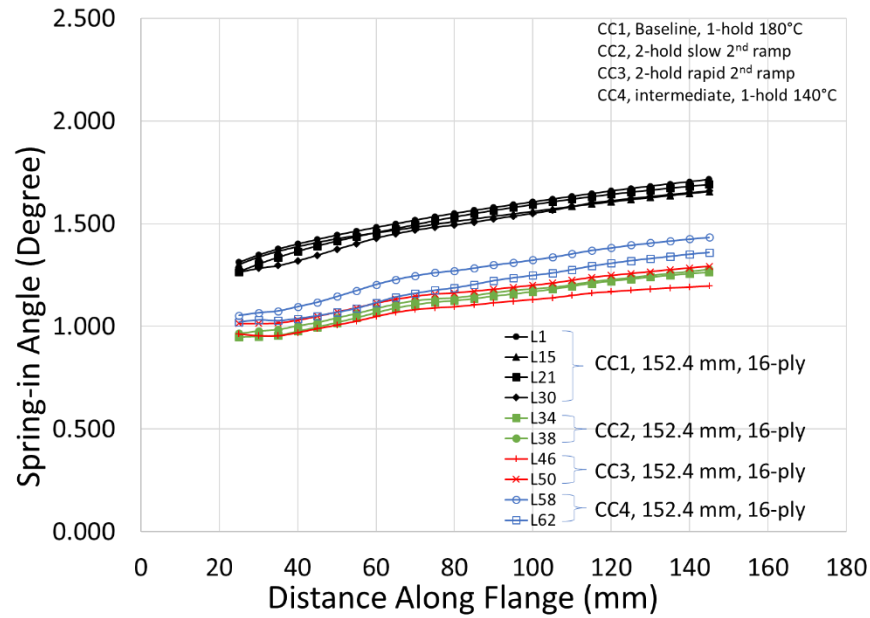


Figure 4.46 Spring-in profiles, 16-ply, 152.4 mm specimens made with cure cycle 1 to 4
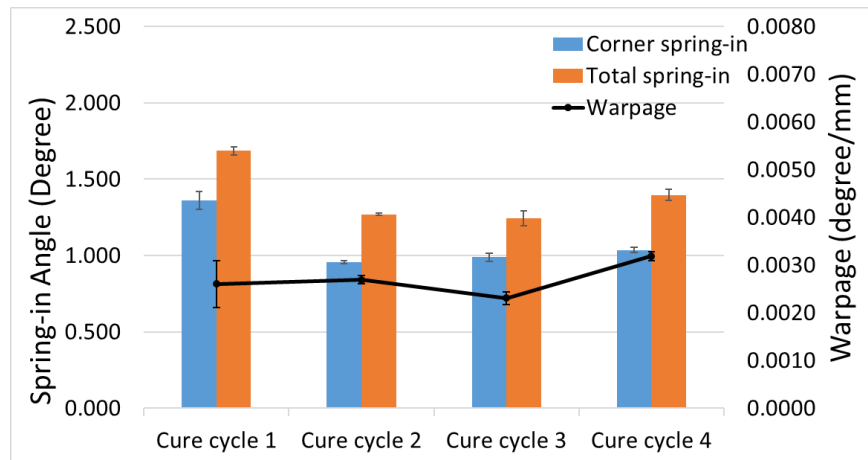


Figure 4.47 Experimental results, 16-ply, 152.4 mm specimens made with cure cycle 1 to 4

Cure cycle 1, the baseline MRCC, again produced the highest spring-in values for L30. Cure cycle 2, 3 and 4 generated similar corner spring-in values. Total spring-in from cure cycles 2 and 3 were very close (within 0.03 °) which were both lower than that of the partially cured, cure cycle 4 specimens. Cure cycle 4 again generated high warpage results.

For all three different flange length, cure cycle 1 consistently showed the highest corner and total spring-in values comparing to cure cycle 2, 3 and 4. This can be attributed to the higher gelation temperature of 173 °C. This observation agrees with Gordnian et al. where they showed spring-in of L-shapes was directly correlated to resin gel temperature [43]. Highlight results for the effect of cure cycles are:

- Specimens gelled at 140 °C consistently showed lower corner and total spring-in values than ones gelled at 170 °C

- Cure cycle 2, 3 and 4 generated similar spring-in results regardless of specimen flange length. Comparing all spring-in values (corner or total) from cycle 2, 3 and 4, the maximum difference was less than 0.16 °

- For 50.8 mm and 152.4 mm flange length, partially cured specimens made with cure cycle 4 generated slightly higher mean warpage values than the fully cured specimens from cure cycle 2 and 3. However, the reason to this observation is unclear

## 4.6 Discussion: The Effect of Cure Cycles on L-shape Deformation

Cure cycle 2, 3 and 4 generated similar spring-in results regardless of flange length. Connections in literature and experimental data that echoed this observation is first discussed in this section. Then a detailed breakdown for various stages in cure cycle 2, 3 and 4 is demonstrated. Stresses arose, with their corresponding deformation mechanisms, are discussed on a zone by zone basis. Resin degree of cure and Tg evolution throughout the three cure cycles are also included. Efforts are then made to shed light on the similar results generated by cure cycle 2, 3 and 4.

Cure cycle 2, 3 and 4 generated similar deformation results. This important observation indicates that once resin pass vitrification, the cure path and further resin curing advancements have little impact on the total residual stress level and specimen deformation. Literature and experimental data which endorse this observation were discovered. Gordnian et al. produced CYCOM IM7/5320-1 L-shapes using the identical invar tool and similar experimental conditions as this thesis [43] (Table 4.7). 10 different cure cycles were experimented by the study; among which three cure cycles were analogues to cycle 2, 3 and 4 in this thesis. The corner spring-in values of partially cured, 2-hold slow second ramp and 2-hold fast ramp from Gordnian were within 0.045 ° difference (Figure 4.48).

Table 4.7 Experimental conditions of Gordian et al. and this thesis

|  | Gordian et al. [48] | This thesis |
|---|---|---|
| Pre-preg material | CYCOM IM7/5320-1 | HEXCEL AS4/8552 |
| Tooling material | Invar | Invar |
| Tooling surface | Release agent | FEP |
| Corner Radius (mm) | 20 | 20 |
| Geometry | L | L |
| Flange length (mm) | 150 | 152.4 |
| Number of plies | 16 | 16 |
| Laminate type | Cross-ply | Cross ply |
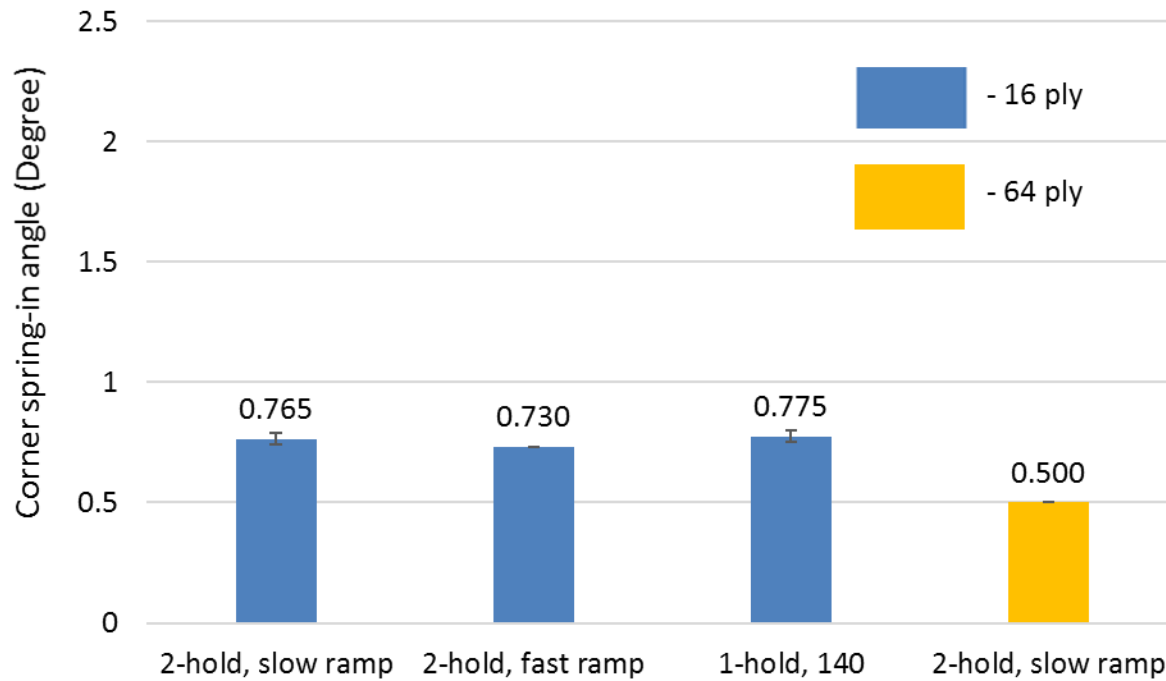
Figure 4.48 Gordnian [43], corner spring-in angles of CYCOM IM7/5320-1 L-shapes made with analogous cure cycles to those used in this thesis

A zone by zone breakdown for cure cycle 2, 3 and 4 is demonstrated in Figure 4.49. The goal is to describe each stress type with their corresponding deformation mechanisms in every zone, so to compare the three cure cycles and their results.

The simplest cure cycle 4 can be divided into two zones: $A_4$, where resin gelled and vitrified and $B_4$, the cool down from 140 °C to room temperature. Since the second hold did not exist, zone $C_4$, $D_4$, $E_4$ can be treated equal to zero. Resin was a liquid before reaching the onset of gelation, so resin cure shrinkage or thermal expansion will not result in any residual stresses. Resin reached gelation when specimen temperature was at 140 °C; DoC at 0.545 [6]. A three-dimensional network was then formed, and resin was able to bear stresses. Since fiber existed in 90° and 0° directions of a [90/0]ns laminate, through thickness contraction due to resin cure shrinkage was the predominant deformation at this stage. This through thickness cure shrinkage was weaved with two deformation mechanisms: shear and spring-in caused by through-thickness and in-plane cure shrinkage mismatch. Once gelled, resin was still rubbery and shear between plies took place. The resin interlaminar shear modulus was low comparing to in-plane modulus, some through thickness

cure shrinkage strain was released via inter-ply shearing, alleviating some residual stresses [24], [39]. Beside the ratio of in-plane modulus to resin interlaminar shear modulus, the amount of shear was also a function of specimen arc and flange length to thickness ratio. Since all specimens were 16 layers with the same 20 mm corner radius, the shorter the flanges, more prominent the inter-ply shear. This explains the observation in the effect of thickness for 50.8 mm flange length -- 16-ply specimens were able to shear more than the 8-ply ones, resulting in less bending stress and warpage. On the other hand, the cure shrinkage strain mismatch that was not able to shear out translates into bending stress in the L-shape corner and flanges.

As Tg exceeded specimen temperature in cure cycle 4, the amount of polymer cross-linking increased and resin approached vitrification (DoC around 0.71). Cure shrinkage started to compound with significant modulus development beyond vitrification. Since plies could not shear anymore, high residual stresses were developed.

Specimens in cure cycle 4 was cooled to room temperature once the resin reached vitrification. Thermoelastic contraction took place in zone $B_4$ from 140 °C to room temperature. Due to the existence of fibers in in-plane 90 and 0 directions, in-plane CTEs were lower than the through thickness direction which was resin dominant. As the specimen was cooled, the through thickness direction contracted more than the in-plane direction, leading to spring-in deformation.
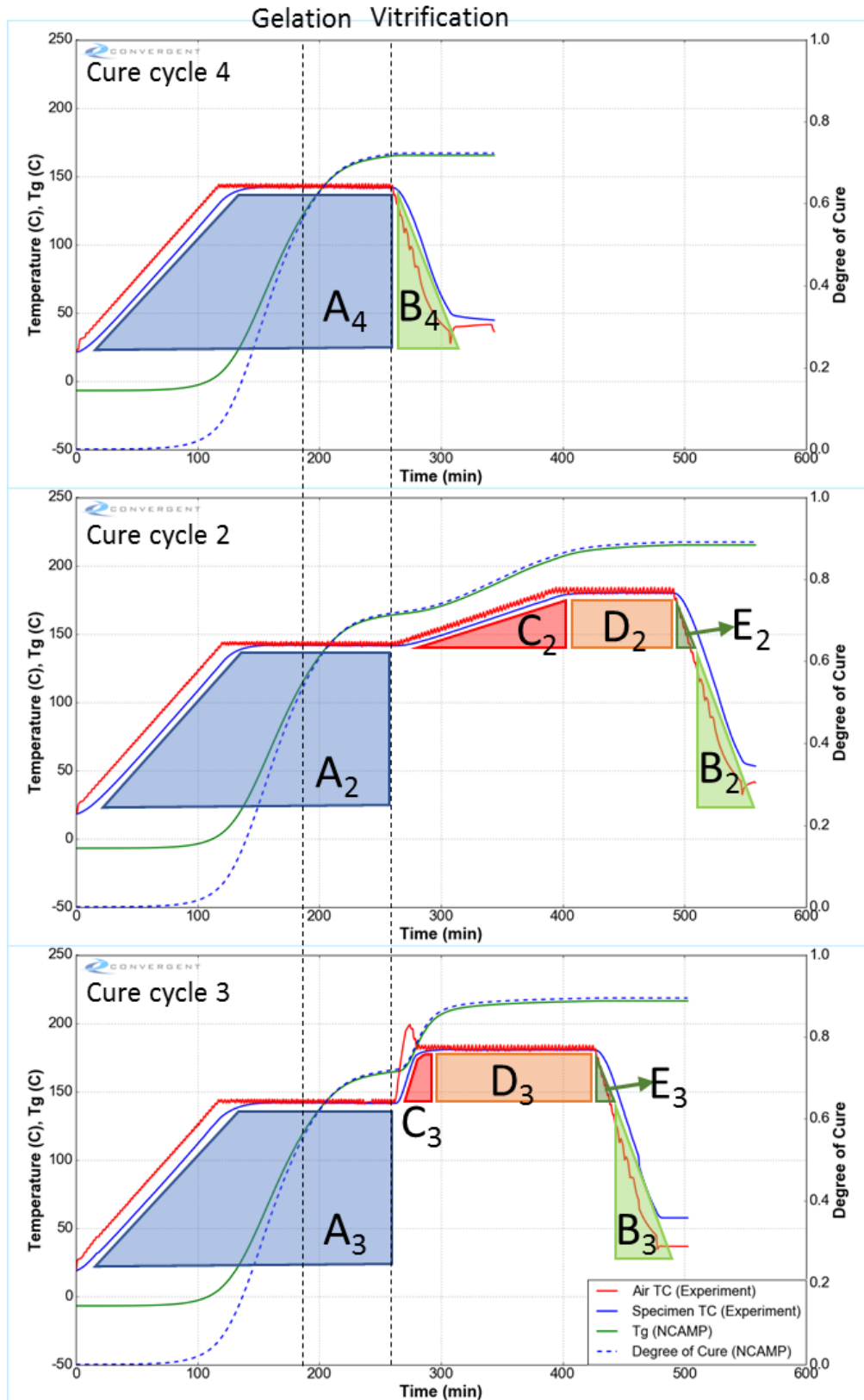
Figure 4.49 Cure cycle 2, 3 and 4 zone-based analysis

Zone $A_4$ and $B_4$ in cure cycle 4 can be extended to cure cycles 2 and 3. Since the first hold of cure cycles 2 and 3 were identical to cure cycle 4 before cool-down, the specimen deformation due to shear and in-plane and through thickness cure shrinkage mismatch up to resin vitrification were equivalent for the three cure cycles:

$A_4 = A_2 = A_3$

In addition, because the cool down rates were the same for the three cure cycles, specimen deformation due to thermoelastic contraction below 140 °C in cure cycles 2 and 3 were identical to the cool down portion in cure cycle 4:

$B_4 = B_2 = B_3$

The second isothermal holds in cure cycles 2 and 3 further cure the specimen comparing to cure cycle 4. Although cured at the same temperature (180 °C) and reach similar degree of cure, specimens from cure cycles 2 and 3 each possessed different evolution of stresses and mechanisms. The second holds were divided into three zone, ramp up from 140 °C 180 °C (zone $C_2$, $C_3$), isothermal hold at 180 °C (zone $D_2$, $D_3$) and ramp down from 180 °C to 140 °C (zone $E_2$, $E_3$). Discussion for each zone will unfold in order of increasing complexity.

Zone $E_2$ and $E_3$ were identical in terms of residual stress formation since the cure cycles ramped down from 180 °C to 140 °C with specimens at similar degree of cure. Vitrified specimens in $E_2$ and $E_3$ experienced spring-in due to thermoelastic contraction with glassy CTE; like in zone $B_2$ and $B_3$.

$E_2 = E_3$

Zone ($C_2+D_2$) and ($C_3+D_3$) contained different deformation mechanisms. $C_2$ hosted a slow ramp up at 0.3 °C/min from 140 °C to 180 °C. Since resin was already vitrified, stress due to resin thermal expansion with glassy CTE counteracts with stress from resin cure shrinkage. DoC in zone ($C_2+D_2$) advanced from 0.71 to 0.89. In zone $C_3$, specimen experienced a 5 °C/min ramp from 140 °C to 180 °C. The corresponding deformation due to cure shrinkage in zone $C_3$ was accompanied with two kinds of thermal expansion stresses – rubbery and glassy. At 277 min, resin temperature approached close to Tg (T-Tg = - 4.34 °C, NCAMP); resin was in a rubbery state with a rubbery CTE. Whereas outside the rubbery state, when the difference between T and Tg was large, resin

has a glassy CTE that is lower than the rubbery CTE. Furthermore, resin in $C_3$ went through a viscoelastic phase, interlaminar shear, similar to that in zone $A_4$, $A_2$ and $A_3$ could potentially happen again. The DoC during $(C_2+D_2)$ also advanced from 0.71 to 0.89. Although the DoC advancements were identical for $(C_2+D_2)$ and $(C_3+D_3)$, whether the amount of the cure shrinkage was identical was unclear.

Since cure cycle 2, 3 and 4 generated close spring-in results, it forces the following relationship in terms of residual stress development:

$(C_2+D_2+E_2) \approx (C_3+D_3+E_3) \approx (C_4+D_4+E_4) = 0$

This implies that the stresses developed after vitrification at 140 °C have little effect on deformation of L-shapes. The reason to this relationship is unclear. It is also unclear as to why the partially cured cure cycle 4 generated higher warpage values.

**4.7     Uncertainties in Experimental Procedure, Measuring and Data Reduction**

This section addresses the known unknowns and aleatory variabilities of the experimental procedure, laser CMM measuring and the python data reduction process. Some of these uncertainties were difficult to characterize and quantify, however, for the record, author was aware of these uncertainties.

**4.7.1     Uncertainties in Experimental Procedure**

Material consistency

- Pre-preg Age: the Hexcel AS4/8552 Uni-directional pre-preg material used in this study was manufactured on June 1$^{st}$, 2013 and was received on June 30$^{th}$, 2013. Specimens in Phase I of this study were manufactured in August 2016. Phase II specimens were made throughout late 2018 to 2019. However, the pre-preg material was properly stored in a walk-in freezer at -40 °C and there was no inconsistency observed for either cured or uncured material. The age of the pre-preg could be a source of variability if resin degree of cure had advanced or resin properties had changed as a result of the age.

- Intrinsic material consistency: the incoming material could have intrinsic material inconsistency such as in-plane fiber waviness or misalignment. Stewart demonstrated that in-plane fiber misalignment in thermally cured AS4/8552 had standard deviation of ±1.6° [88]. Such intrinsic inconsistency could result in fiber not being in the ideal direction during layup. Bellini et al. attributed his observation of spring-in in [90]n laminates to fiber misalignment [41]. See more detail in section 5.2.2.

Processing

- Tooling: although the tool surface profile met industrial standard, the minor surface undulation can still impact the deformation of the specimens. The surface undulation can affect the final spring-in results by up to 0.3 ° as showed in Section 4.2.4.1. Tooling dimension at curing temperature (180 °C) was unobtainable within the scope of this study. Although the tool was made of invar, when the tool was heated to high temperature, the

substructure could potential impose constrains and deform the face sheet. In addition, an internal study at Convergent Manufacturing technologies discovered the invar 36 tooling face sheet had temperature dependent CTEs. A small piece was cut off from the corner of the invar tool and it was shown that CTE in all three directions increased linearly with temperature: from about 1ppm to 4ppm between 20C and 200C [89]. Thus, to determine the exact surface profile of the invar tool at high temperatures, further numerical or FEA analysis is needed.

- Manual cutting, layup: Although great care was taken in cutting and laying up the pre-preg material, it was not as accurate as a cutting machine in combination with automatic tape layup machine. Minor misalignment of the pre-preg during layup could also have an impact on the final deformation of the specimens. Fibers in pre-preg were inextensible. For a single 0° ply with finite thickness, when the ply was bent around the corner, excess length could be created in the bottom of the ply causing waviness whereas the top of the ply contained straight fibers [88].

- Autoclave curing: autoclave air temperature fluctuated intrinsically (around ± 2.8 °C) as the specimens were being cured in the autoclave. However, the large thermal mass of the invar tool limited some of the air temperature fluctuation being transferred to the specimens. Specimen temperature lag on the invar tool during the ramp ups was 13 °C on average. Although the specimens were made at different locations on the tool within the autoclave, maximum care was taken to ensure the specimens experience the same thermal history.

- Physical aging: Physical aging increase the stiffness of the resin after resin vitrifies. Exposure to prolong period of temperature below Tg can decreases the free volume within the resin amorphous cross-linking, causing physical change in resin molecular structure [90]. Studies have suggested physical aging can cause modest increase in resin elastic modulus [91]–[94] which in the case of L-shapes, meaning increase in flange bending stiffness. For cure cycle 2 and 3, resin spent around 230 minutes and 130 minutes respectively below Tg after vitrification and before cooldown. Thus, specimens from cure cycle 2 potentially have stiffer flanges and were more resistant to bending stress comparing to cure cycle 3.

- Trimming by high speed diamond saw: Specimens were trimmed manually which could also lead to edge inconsistency and affect the internal stress of the specimens. However, by comparing the before and after trimming results the spring-in angle changed by less than 0.05 °.

### 4.7.2 Uncertainties in Data Acquisition and Analysis

- CMM scanning: CMM scanning error were experimentally characterized from three aspects: the scanning process itself, effect of weight points and the effect of developer spray. (Note: since the goal was to investigate CMM scanning error, spring-in plots presented in this section were not compensated by tooling.)

  One specimen – L38 was used for this inquiry. L38 was prepared following procedures in section 3.6, then it was scanned three times with the same weight points and developer spray. The specimen was untouched in between the scans. The results are shown in Figure 4.50. The maximum difference was around 0.05 ° between different scans at 85 mm along the flange.
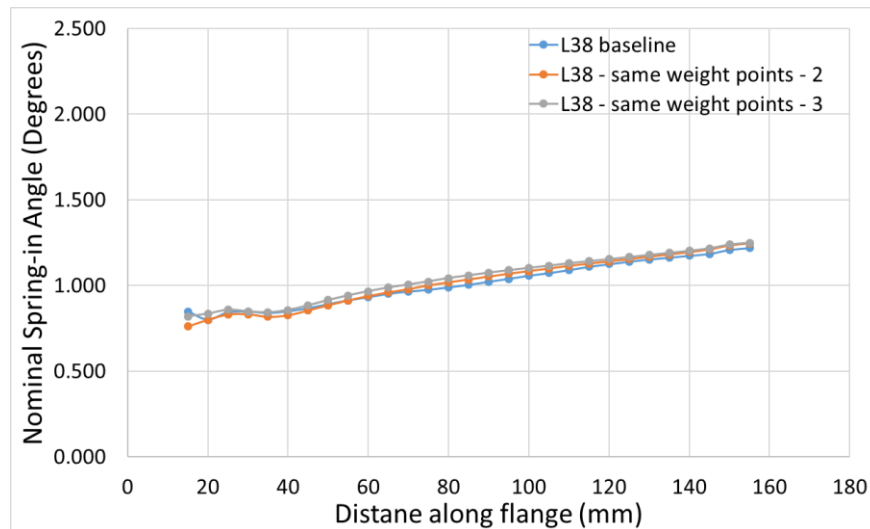


Figure 4.50 Scanning error characterization – multiple scans of L38 with the same weight points and developer spray.

Another set of weight points was employed to inquire the effect of weight points on the variability of the scanning process. The results are shown in Figure 4.51. The maximum difference was around 0.03 ° between the two scans at 85 mm along the flange.
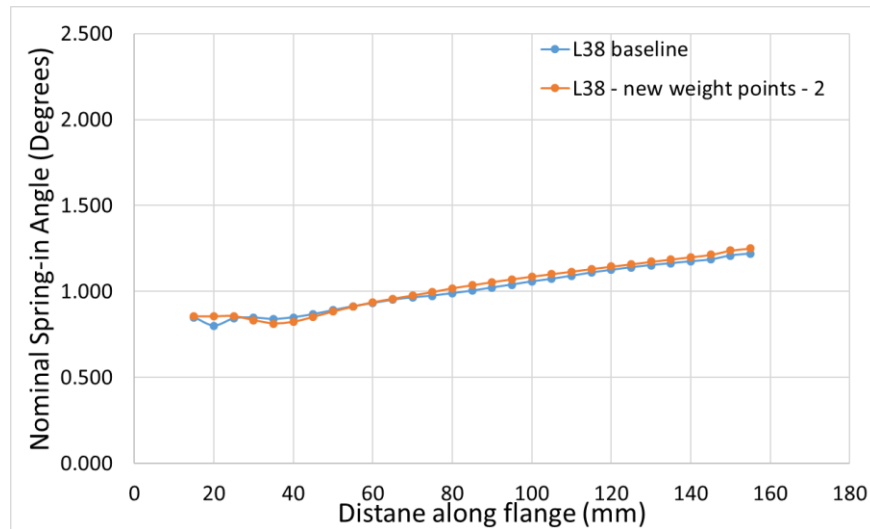
Figure 4.51 Scanning error characterization – two scans of L38 with the same developer spray but different weight points

Lastly, the developer spray was cleaned off from L38 and a new coat was applied. This process required the specimen to be removed from the CMM scanning position so for each trial a new set of weight points were employed. This experiment was repeated two times (Figure 4.52). The maximum difference was around 0.03 ° between different scans.
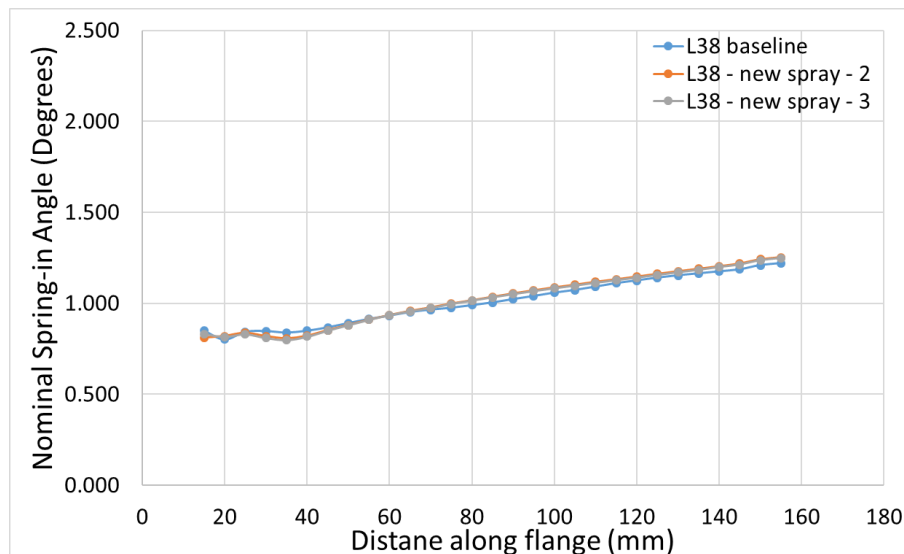


Figure 4.52 Scanning error characterization – multiple scans of L38 with new coats of developer spray and different weight points

It is shown the CMM scanning process was consistent with high repeatability. The variability from scan to scan with different weight points and developer sprays do not impact the results to a considerable scale.

- Data Reduction – the following errors were characterized:
  - Standard deviation on vectors that were fitted to each slice of the 2D point cloud. The distribution of the fitting vector slopes was assumed to be normal. Each pair of the fitted vectors were sampled 1000 times within the normal distribution to generate the error for angle measurements. As distance along the flange increase, the secant vector length increase and more points were taken into calculation, thus, the error decreases
  - When averaging the spring-in profiles of the three slices for each specimen, the error was the standard deviation of the three mean values
  - When averaging specimen repeats, the error was again the standard deviation of the mean values of each specimen. These errors were reported in tables and cluster column charts in section 4.5
  - Warpage value, aka the spring-in slope, for each specimen was obtained by exercising the OLSfit function in Python (code attached in Appendix B). OLSfit takes the list of distance along the flange and the corresponding spring-in angles and errors as input; returns the slope and slope error of the least square fit line as output.
- Thickness measurement: the bag-side rough surface is a resin rich layer with the texture of breather cloth (Figure 4.53). The thickest area is around 0.1 mm. However, this is within the standards deviation of the average thickness measurements.
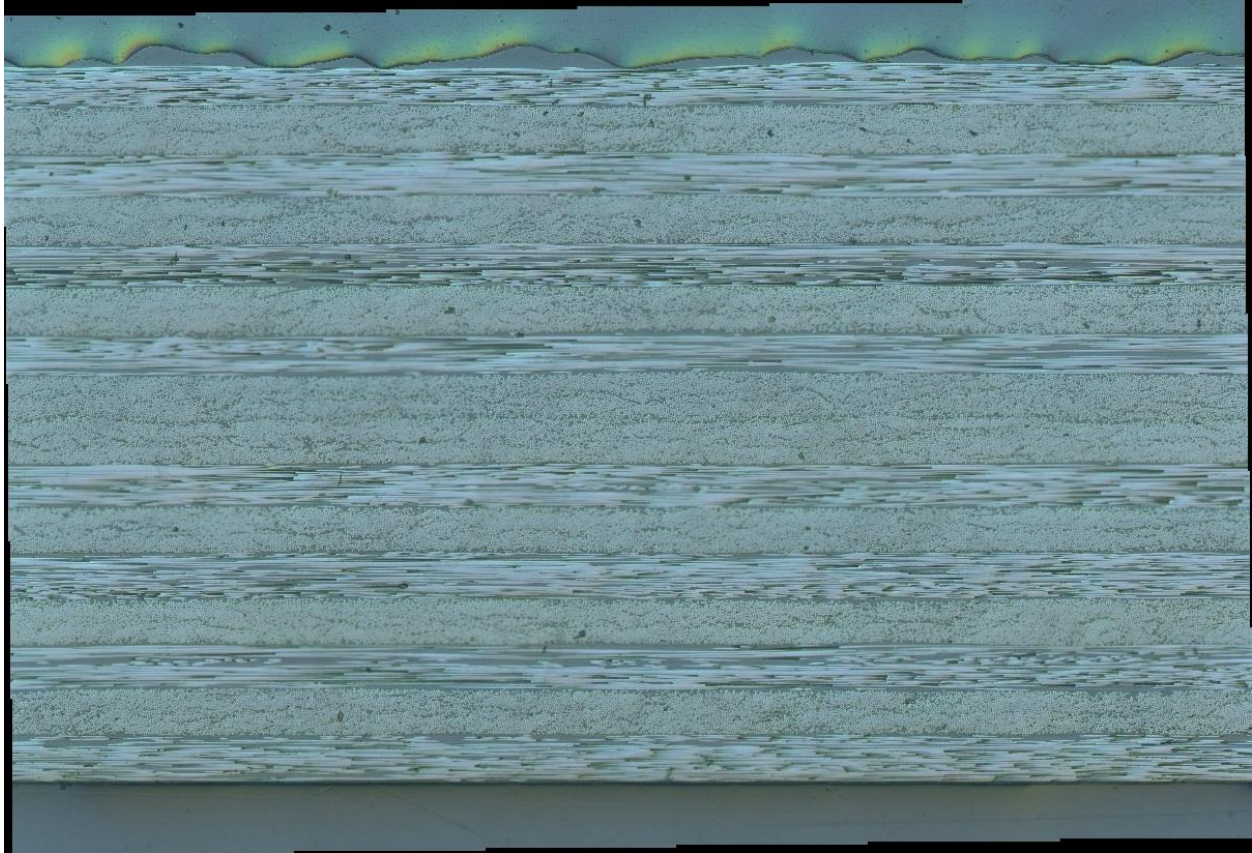
Figure 4.53 Microscopy of a [90/0]4s specimen. The bag-side resin rich layer is at the top

## 4.8   Summary

In this chapter, a robust data reduction method exercised using Python was discussed along with the importance of deformation definition of the L-shaped specimens. By programming two spring-in definitions into the data reduction process, it was reported that using the continuous vs discontinuous secant method can cause up to 0.4° discrepancies in total spring-in angles.

Specimen thickness were measured with a digital micrometer. The average specimen thickness was consistent for a given number of plies; being either 8 or 16.

Specimen actual thermal history were reported in section 4.4. Corresponding Tg and DoC evolution was calculated by RAVEN exercising the NCAMP AS4/8552 model.

Section 4.5 was dedicate to the experimental results of this study. Major conclusions for the effect of thickness are:

- Both corner and total spring-in decrease as laminate thickness increase

Major conclusions for the effect of flange length are:

- Corner spring-in is not a function of flange length
- Warpage decreases with increasing thickness to flange length (t/l) ratio
- Total spring-in values increase with flange length as a result of similar corner spring-in and increasing length of warped flanges

Major conclusions for the effect of cure cycles are:

- Specimens gelled at 140 °C consistently showed lower spring-in and warpage than ones gelled at 170 °C
- Cure cycle 2, 3 and 4 generated similar corner and total spring-in results regardless of specimen flange length.
- Cure cycle 4 generated partially cured specimens showed the higher warpage values than fully cured specimens which were also gelled at 140 °C

Sources of uncertainties for this study were also discussed. Known unknowns and aleatory variabilities of the experimental procedure, laser CMM measuring and the Python data reduction process were addressed quantitatively if possible.

# Chapter 5: Literature Data Pooling

## 5.1   Introduction

Decades of experimental and simulation work have been spent to understand how residual stresses lead to spring-in and warpage. However, studies often focus on the influence of one or a set of processing parameters on L-shape or C-shape deformation. In addition, experimental and data reduction approaches varies from study to study, and there is no set best practice for reporting the data. A few researchers have attempted to make detailed comparison across different studies in aiming to isolate major influencing parameters of PID [26], [42], [83]. However, none of the studies compared across more than 10 datasets; a common conclusion was that reliable comparisons were difficult to make due to the large number of combinations of processing parameters and little available data.

Similar to systematic reviews and meta-analysis in medicine where clinical data are combined and summarized to keep clinicians abreast with current evidence-based medicine, this chapter consolidates previous process induced deformation datasets and provide insights of the current literature and trends regarding some processing parameters. This study first provides an overview of 92 collected experimental studies within the public domain since the 1980s, including over 2070 experimental specimens. Then, a detailed meta-analysis is performed on three representative material systems: HEXCEL AS4/8552, TORAY T800/3900-2 and CYCOM IM7/5320-1. The meta-analysis includes 14 studies and around 800 specimens. Despite the limited number of specimens and heterogeneous experimental approach, trends were drawn with relatively high level of confidence.

## 5.2   Systematic Review Design

The database created in this study includes all available published experimental work regarding process induced deformation in composite materials. Studies were collected from major databases including Google Scholar, Engineering Village, ScienceDirect, SAGE Journals and Web of Science. The search keywords and some major conferences and journals from which the

studies were collected are listed in Table 5.1. To increase the size of the database, the included experimental studies had no restrictions for sample size or published time. The publication language of the collected studies, however, is limited to English.

Over 300 studies from 1975 to 2020 were screened by titles and abstracts. 92 studies [15], [16], [18]–[20], [22]–[27], [29]–[32], [35]–[45], [47]–[49], [51], [55], [57], [59]–[61], [64], [68], [69], [74], [76], [79], [83], [87], [95]–[142] with process induced deformation experimental data were selected to be included in this database (Figure 5.1). These studies were perused and the specimen information were documented. For each specimen mentioned in the collected studies, processing parameters listed in Table 5.2, if available, were collected using an Excel spreadsheet. These parameters were later used as filters and legends for data manipulation and display their effects on the deformation results.

Table 5.2 is an outcome of the experimental methodology developed by this thesis. The reporting of these parameters is hereby recommended because it provides comprehensive experimental details which ultimately aids data collation and better understanding of PID.
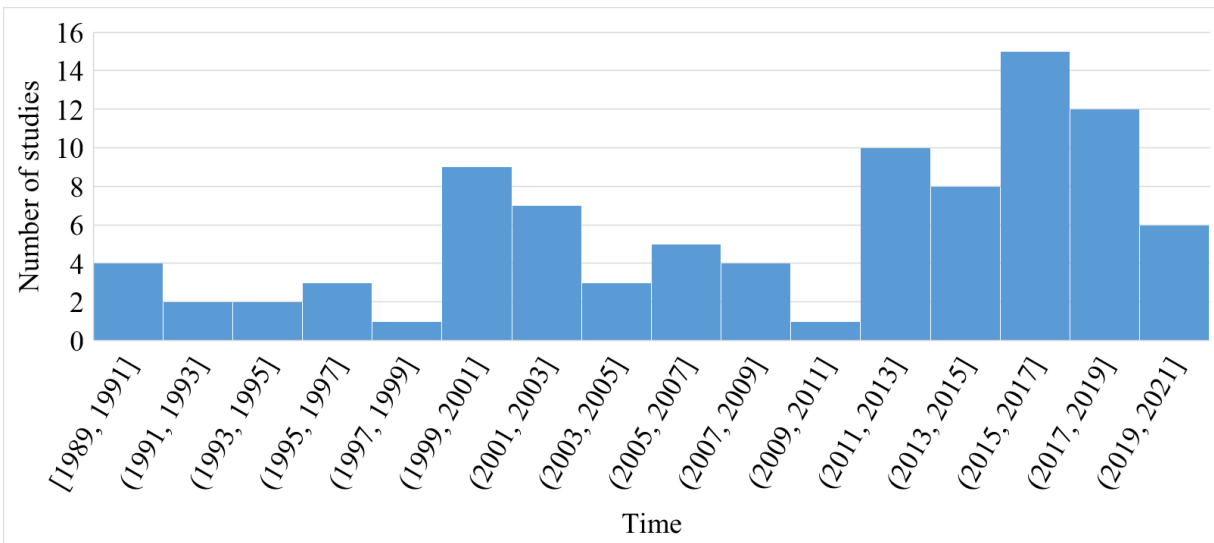


Figure 5.1 Number of studies with respect to time

Table 5.1 Search strategy, number of studies found in brackets

| Conferences | International SAMPE Technical Conference (9) |
| | International Conference of Composite Materials (2) |
| | International Council of the Aeronautical Sciences (2) |
| | NASA Technical Memorandum (1) |
| | Canadian-International Composites Conference (1) |
| | International Conference on Mechanical and Aerospace Engineering (1) |
| | European Conference on Composite Materials (1) |
| Journals | Composites Part A: Applied Science and Manufacturing (25) |
| | Journal of Composite Materials (16) |
| | Composite Structures (15) |
| | Composites Science and Technology (9) |
| | Journal of Reinforced Plastics and Composites (4) |
| | Composites Engineering (2) |
| | Applied Composite Materials (2) |
| | Composites (1) |
| | Composites Manufacturing (1) |
| | Journal of Thermoplastic Composite Materials (1) |
| | Mechanics of Composite Materials (1) |
| | Journal of Applied Polymer Science (1) |
| | Advanced Composite Materials (1) |
| | Journal of Engineering and Applied Sciences (1) |
| | Thin-Walled Structures (1) |
| | International Journal of Material Forming (1) |
| | Curved and Layered Structures (1) |
| | Journal of Industrial Textiles (1) |
| | Plastics, Rubber and Composites (1) |
| Search keywords | Composites material, Composite manufacturing, Residual stress, Dimensional/shape control/tolerance/stability/fidelity/distortion, Process induced deformation/distortion, PID, L-shape, C-shape, U-shape, Spring-in, Spring-back, warpage, curvature |

Table 5.2 Preferred reporting items for experimentally studying process induced deformation of fiber reinforced composite specimens. Followed to document processing parameters that were collected for each L-shape specimen found in the literature

| | | Item No. | Checklist item |
|---|---|---|---|
| **Equipment** | Equipment | 1 | Specify the equipment used for processing (e.g. autoclave) |
| **Tooling** | Tool material | 2 | Specify the tooling material and its properties (e.g. CTE) |
| | Tool geometry | 3 | Describe whether the tool is convex (male), concave (female) or double sided |
| | Tool sub-structure | 4 | State whether the tool has sub-structures and describe their effects on produced specimens |
| | Tool profile | 5 | Report tool profile measurements, measurement method, tolerance, tooling surface roughness and deviations from nominal specification if exist |
| **Part** | Geometry | 6 | Report specimen geometry (e.g. C, L or flat etc.), width, flange length, laminate thickness, corner radius, corner angle, web length (applicable to C-shapes) |
| | Layup | 7 | Describe specimen layup sequence |
| | Ply drop off | 8 | Report ply drop off or other special layup techniques |
| | Core | 9 | Indicate the use of core and core materials |
| | Surface profile | 10 | Report specimen surface profile after cure, measurement method and tolerance. The measurement method and tolerance ideally should be the same as those used to measure the tool. |
| **Material/ processing** | Composite Material | 11 | Report fiber material and matrix materials and their age |
| | Processing surface | 12 | Indicate the surface on which the specimens were processed (e.g. release agent or release film and their types) |
| | Cure cycles | 13 | Describe the actual specimen temperature, vacuum and pressure cycles, including ramp rates and hold times |
| | Bleeding | 14 | Report whether there was bleeding or resin loss |
| | Post processing | 15 | Report any procedures that could potentially alter specimens internal stress state, such as demolding, trimming, moisture exposure or post curing |
| **Results** | Results | 16 | Report spring-in angles, flange warpage, number of repeats, standard deviation, and material degree of cure |

From the over 2070 specimens that were collected, there were 1367 L-shape and C-shape specimens with spring-in data available. Also from the over 2070 specimens that were collected, HEXCEL AS4/8552, TORAY T800/3900-2 (and its' variants) and CYCOM IM7/5320-1 were among the most used material systems (Table 5.3). Note that material systems which were from a single source are highlighted in red in Table 5.3. Different from AS4/8552 and IM7/5320-1, T800/3900-2 (and its' variants) are interlayer toughened by thermo-plastic particles. These three relatively well-studied and characterized material systems covered 14 datasets (Table 5.4) and over 800 specimens with spring-in data. Hence, they were good representations of the state-of-the-art datasets and were chosen to be analyzed in detail in this chapter.

Table 5.3 Top 15 most used fiber and matrix material tabulated by number of specimens found in descending order

| Matrix \ Fiber | AS4 | W3L282-42 | IM7 | T300 | T800H | T800S | T800 | IMA | TOHO/TENAX HTS | Not reported | IM6 | GU230-E01injectex | T620 | F593 | Tenax HTS 12K NCF |
|---|---|---|---|---|---|---|---|---|---|---|---|---|---|---|---|
| 8552 | 651 | | 104 | | | | | | | | | | | | |
| F584 | | 252 | | | | | | | | | | | | | |
| 3900-2 | | | | | 95 | | 59 | | | | | | | | |
| 934 | | | 30 | 48 | | | | | | | | | | | |
| M21 | | | | | | 77 | | | | | | | | | |
| Cetex PPS | | | | 60 | | | | | | | | | | | |
| M21E | | | | | | | | 54 | | | | | | | |
| 5320-1 | | | 53 | | | | | | | | | | | | |
| RTM6 | | | | | | | | | 25 | 5 | | 15 | | | 3 |
| 6376 | | | | | | | | | 18 | 28 | | | | | |
| Not reported | | | | 1 | | 15 | | | | 9 | | | 15 | 6 | |
| 3501-6 | 16 | | 30 | | | | | | | | | | | | |
| PEEK | 38 | | | | | | | | | | | | | | |
| 3100 | | | | | | | | | | | 36 | | | | |
| 977-2 | | | 30 | | | | | 2 | | | | | | | |

Single source: W3L282-42/F584 [45]; IM7/8552 (no spring-in values available) [140]; T300/Cetex PPS [115]; T800S/M21[68]; IMA/M21E [120]

Table 5.4 Studies for the three materials systems of interest: Hexel AS4/8552, Toray T800/3900-2 and Cycom IM7/5320-1

| AS4/8552 | T800/3900-2 | IM7/5320-1 |
|---|---|---|
| Johnston et al. [18] | Albert and Fernlund [57] | Arafath et al. [31] |
| Hubert and Poursartip [79] | Fernlund et al. [76] | Gordnian et al. [43] |
| Fernlund et al. [76] | Arafath et al. [31] | / |
| Garstka [143] | Minakuchi et al. [50] | / |
| Wisnom et al. [24] | / | / |
| Kappel et al.[26] | / | / |
| Kappel [36] | / | / |
| Bellini et al. [40] | / | / |
| Bellini and Sorrentino [41] | / | / |
| This thesis | / | / |

## 5.3 Literature Datasets Overview

This section provides a high-level overview of the collected specimens in terms of angle distribution and quantity distribution. Gaps within the literature are also identified.

*Within each of the three material systems of interest, there is not an exact repeat of an experiment between any two different datasets. By exact repeat, all processing parameters must be the same.*

Figure 5.2 presents the angle distribution of the collected specimens in terms of layup type and further compares the distribution by the three material systems of interest. Note that all spring-in values presented here are traditional (total) spring-in values (as defined in section 2.4.1), as reported from literature. From a macro perspective, the average spring-in value of 1367 specimen is 1.258 ° with a standard deviation of 0.620 °. The 1367 specimens cover a wide spectrum of processing conditions and variables. The AS4/8552 specimens have a higher average at 1.367 ° with a standard deviation of 0.626 °. The standard deviation of AS4/8552 specimens are very close to that of the whole collection. T800/3900-2 and IM7/5320-1 exhibit tighter distribution with standard deviations being 0.350° and 0.487° respectively. When categorized into layup types, despite the processing conditions being different, quasi-isotropic layup has the highest spring-in values for the entire collection and the three material systems (Table 5.5). It is worth mentioning, *that all UD[90]n specimens display spring-in*.

The data at the ends of Figure 5.2 contains specimens made on concave tools, with extreme asymmetric layups or cure cycles specifically designed to cause less compaction. Once the above-mentioned conditions are filtered out, a tighter distribution is shown in Figure 5.3. Quasi-isotropic layup still showed high average spring-in values for the whole collection and T800/3900-2. UD[0]n showed low average spring-in for AS4/8552 and T800/3900-2 (Table 5.6).
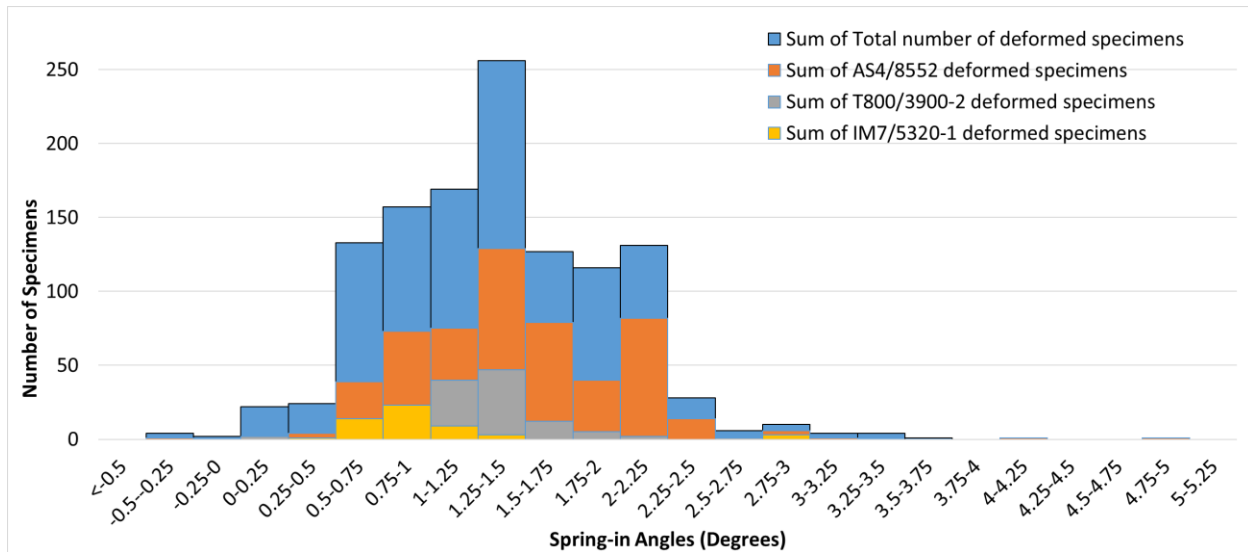
Figure 5.2 Spring-in angle distribution of all specimens and three material systems of interest

Table 5.5 Spring-in angle distribution statistic. Number of specimens are included in the brackets

| Layup | Whole Collection | AS4/8552 | T800/3900-2 | IM7/5320-1 |
|---|---|---|---|---|
| All layups | 1.258, 0.620 (1367) * | 1.367, 0.626 (532) | 1.218, 0.350 (135) | 0.996, 0.487 (53) |
| ±45 | 1.358, 0.731 (90) | 2.173, 0.290 (30) | N/A | N/A |
| Quasi | 1.360, 0.541 (323) | 1.619, 0.539 (69) | 1.261, 0.329 (57) | 1.220, 0.575 (27) |
| Crossply | 1.202, 0.640 (273) | 1.533, 0.692 (173) | 1.198, 0.118 (25) | 0.763, 0.186 (26) |
| UD [0]n | 1.126, 0.528 (365) | 1.084, 0.451 (181) | 1.180, 0.447 (49) | N/A |
| UD [90]n | 0.992, 0.436 (70) | 0.928, 0.305 (58) | N/A | N/A |

*x, y (z): average spring-in angle, standard deviation (number of specimens)
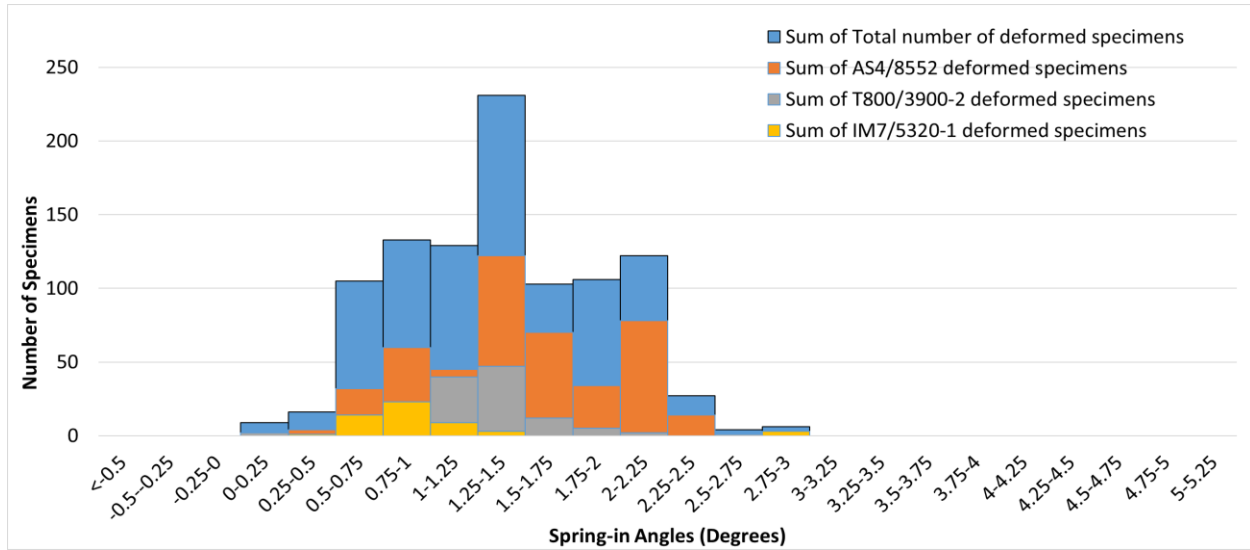
Figure 5.3 Spring-in angle distributions of specimens made on convex tools, with symmetrical layup and standard cure cycles

Table 5.6 Spring-in angle distributions statistics of specimens made on convex tools, with symmetrical layup and standard cure cycles. Number of specimens are included in the brackets

| Layup | Whole Collection | AS4/8552 | T800/3900-2 | IM7/5320-1 |
|---|---|---|---|---|
| All layups | 1.257, 0.491 (1089) * | 1.341, 0.466 (478) | 1.231, 0.344 (132) | 0.996, 0.487 (53) |
| ±45 | 1.465, 0.706 (76) | 2.173, 0.291 (30) | N/A | N/A |
| Quasi | 1.297, 0.395 (205) | 1.387, 0.172 (58) | 1.294, 0.306 (54) | 1.220, 0.575 (27) |
| Crossply | 1.228, 0.433 (240) | 1.439, 0.453 (163) | 1.198, 0.118 (29) | 0.763, 0.186 (26) |
| UD [0]n | 1.196, 0.517 (321) | 1.143, 0.350 (157) | 1.180, 0.447 (49) | N/A |
| UD [90]n | 0.814, 0.290 (54) | 0.721, 0.168 (50) | N/A | N/A |

*x, y (z): average spring-in angle, standard deviation (number of specimens)

Due to the broad inclusion criteria, the database collected specimens with a wide variety of processing conditions. The number of specimen distribution for a few high impact processing parameters are shown in Figure 5.4. Most of the specimens captured by the database were made with autoclaves (Figure 5.4a). Concave or convex tooling can induce different deformation mechanism and opposites results. Convex tools can cause corner thinning whereas concave tools can lead to corner thickening [21]. Fiber volume fraction gradient can also decrease the laminate curvature on a concave tool while increase the curvature for laminates made on a convex tool [55]. Double sided tools (or close molds) were typically used for RTM or hot-pressed specimens. Most of the specimens found were made on convex tools (Figure 5.4b).
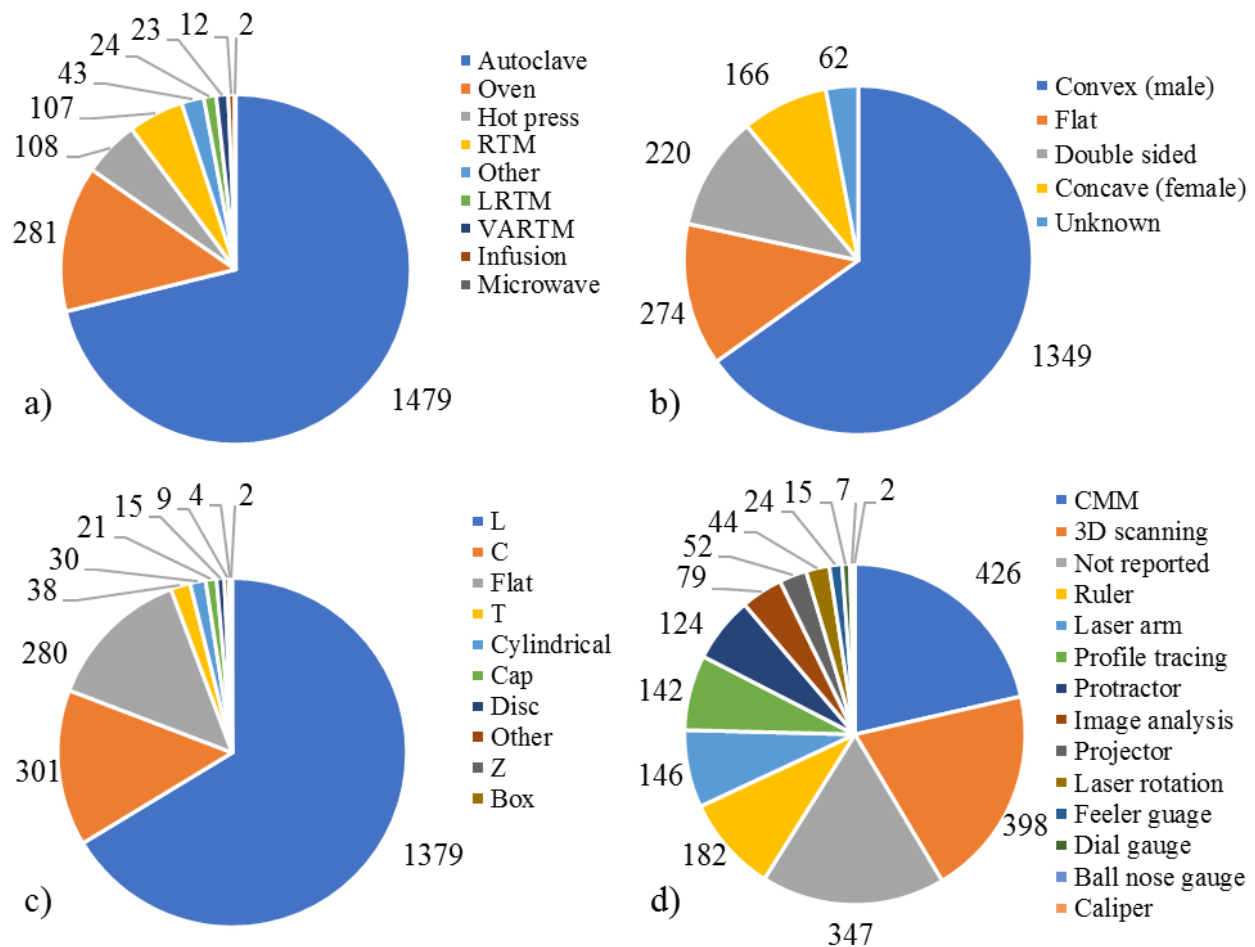


Figure 5.4 Distribution of specimens organized by a) processing method b) tooling geometry c) specimen geometry d) deformation measuring method

129

Methods with varying accuracy levels were used to measure specimen deformation. Most of the specimens were measured with coordinate measuring machines or some types of 3D scanning. 2D methods such as profile tracing and image analysis were also used in aiming to capture the side profile of the specimens. It is important to point out that around 20% of the specimens did not have the measurement method reported (Figure 5.4d). Also, very few studies mentioned the measurement of tooling [36], [40], [41], [54]–[57] and even less studies compensated spring-in angles with actual tool angles that could potentially deviated from the nominal specifications [36], [56]. As shown in section 4.2.4 that tooling surface undulations can introduce up to 0.3 ° error in spring-in measurement for short flange length. Ideally, tool surfaces should be evaluated using the same method and to the same tolerance as the manufactured specimens to eliminate the effects of tool surface deviation.

In combination with the factors summarized in section 2.4.1, the reasons as to why the literature has yet to fully understand process induced deformation can be summarized as following:

1. Variation in processing conditions
2. Inadequate spring-in definition
3. Non-standardized reporting format
4. Lack of tooling inspection & compensation
5. Variation in measurement methods
6. Lack of data

Variation in processing conditions implies there are many input variables to process induced deformation as a system level problem. Points 2 to 5 summarize the variabilities emerge during the manufacturing, data collecting and reduction process. Last but not the least, the lack of data aggregates the issue. The above reasons are true independent of whether physics-based simulation approach or data centric approach is adopted.

## 5.4    Inquiry into the PID Literature

This section reviews the literature regarding the effects of various processing parameters on process induced deformation. For each processing parameter, the theoretical influences based on analytical solutions or literature broad agreements are discussed. Then, results from studies that have specifically focused on these parameters are reviewed.

This section evaluates few processing parameters regarding the tool, the part and the material & processing. Corner radius and tooling material are first discussed.
Then, the effects of layup type, laminate thickness and flange length, which can impact the shearing and bending behaviors, are investigate. Gelation temperature is then explored because it can affect the amount of thermal induced strain and cure shrinkage strain. Consequently, this and the following sections are organized to answer the following list of questions:

- What is the effect of corner radius?
- What is the effect of the tooling material?
- What is the effect of layup type?
    - Do [90]n have spring-in?
    - Do [45/-45]n have extremely high spring-in?
- What is the effect of laminate thickness?
- What is the effect of flange length?
- What is the effect of gelation temperature?

The literature review for the effect of layup type, laminate thickness, flange length and cure cycles were covered in section 2.4.3 to section 2.4.5. Key concepts such as the fundamental drivers for spring-in were covered in section 2.4.20.

### 5.4.1    The Effect of Corner Radius

Existing analytical solutions attempt to capture the non-linear relationship between the material properties, geometrical parameters and total spring-in [52], [61]. The geometrical parameters include corner radius, nominal corner angle, flange length and laminate thickness. For a given set of material system, specimen angle, layup type and laminate thickness, the total spring-in is a function of flange length and corner radius.

Studies in literature disagree on the effect of corner radius on spring-in of L-shapes. Throughout history and with various material systems, many researchers have experimentally proven that corner radius has very little to no effect on spring-in [15], [26], [41], [59], [77], [113], [144]. However, the counterargument that corner radius could impact spring-in is equally strong and corroborated with experimental data. For example, Rennick and Radford isolated the thermo-elastic response from the non-thermal-elastic response as they heated up the cured L-shape specimens to curing temperature. They discovered as the specimen shape changed with increasing corner radius, the non-thermo-elastic contribution decreased. Whereas the thermo-elastic response was independent of the corner radius [38], [49]. The phenomenon was not depicted by the analytical solution developed by Radford at the time. However, Radford stated that the phenomenon could be related to local corner thinning which was less severe for larger radii or other unknown corner radius related mechanisms. Jain et al. created an extensive physical L-shape dataset found that spring-in was independent of corner radius when radius-to-thickness ratios were greater than 1 [45]. Kappel et al. developed the largest physical dataset of AS4/8552 L-shapes with more than 200 specimens [26]. They discovered that unidirectional and bi-axial layup L-shapes has increasing spring-in with increase corner radius, whereas this same trend did not exist in quasi-isotropic and cross-ply specimens. Last but not the least, Roozbehjavan et al.'s simulation results showed that spring-in increase with corner radius for $[0/45/90/-45]_4$ L-shapes [29].

This disagreement within the literature could potentially be due to the narrow bandwidth in terms of corner radius, flange length and laminate thickness experimented in the individual studies. This scenario makes a good candidate for using data pooling to understand the effect of corner radius on process induced deformation.

132

### 5.4.2    The Effect of Tooling Material

Tooling material plays an important role in process induced deformation, especially in tool part interaction. The difference in coefficients of thermal expansion (CTEs) causes tools made of different material to expand different amounts under the same cure cycle. Compounding with the CTE difference and the frictional coupling between the tool and the composite material, tool material have a significant effect on part warpage [64].

The literature, however, disagrees on whether tooling material affects process induced deformation. A few studies showed tooling material has no impact on spring-in of L-shapes [26], [27], [29], [145]. On the other hand, many found the opposite [36], [46], [57], [75], [77]. Albert pointed out that tooling material, along with laminate thickness and length, are processing parameters that can affect warpage [57]. Wiersma et al. used finite element analysis with a viscoelastic model to predict the amount of "springback" (spring-in) of L-shaped parts. He concluded that tooling expansion during the cure cycle can affect the spring-in of unidirectional angled laminated by as much as 12 % [77]. Fernlund et al. further refined the discovery, finding that tooling material as an extrinsic parameter had little effect on corner spring-in; but it is an important parameter for tool part interaction which drives flange warpage [22]. Arafath et al. supported Fernlund et al.'s finding with T800/3900-2 experiments which will be discussed in this section [31].

### 5.4.3    Spring-in of [90]n Laminates

As mentioned, the fundamental driver for spring-in is the in-plane and through thickness strain difference. Since the properties in the in-plane and through thickness directions of a [90]n laminate are resin dominated and similar, the common understanding is that spring-in would be minimum for [90]n L-shape and C-shape specimens.

However, non-negligible spring-in has been observed in [90]n specimens in literature. Johnston et al. attributed this finding to flange warpage caused by tool part interaction [18]. Kappel et al., did not observe any flange warpage, explained that this phenomenon could be due to through-thickness

Vf gradient or tool part interaction [26]. Bellini and Sorrentino on the other hand attributed this observation to potential fiber misalignment where some fibers were not exactly in the 90-direction as in the ideal scenario. The fiber crossing essentially can be considered as fiber in 0-direction for which effect was not negligible [41]. Neither Kappel or Bellini and Sorrentino pursued with further investigation and the exact cause for this observation is unclear.

## 5.5 Literature Data Pool

Following the list of questions in section 4, this section presents the pooled data for HEXCEL AS4/8552, TORAY T800/3900-2 (and its' variants) and CYCOM IM7/5320-1 from the literature. Although, limited specimens were available considering the 30-year time span, some clear trends can still be observed. These observed trends indicate parameters that have significant impacts on specimen spring-in. Unless specified, error bars presented in the charts of this section represent the standard deviation of the literature pooled data in each scenario.

Since no single exact repeat of experiment was found, section 5.5.6 compares some specimens with similar experimental conditions; inquiring the consistency across literature datasets.

### 5.5.1 The Effect of Corner Radius

This section demonstrates how to use data-pooling to gather experimental data from different studies and investigate the effect of corner radius. To tackle this problem, the following procedure is followed:

- Collect specimens from studies that have studied the effect of corner radius on spring-in, forming a stand-alone dataset. The purpose of this step is to establish a baseline (without assuming the correctness of the stand-alone dataset) while determining the material systems and the rough processing condition envelop the analysis will focus on.

  In this case, T300/934 (used by Patterson et al. and Jain et al. [15] [45]) and AS4/8552 (used by Kappel et al., Bellini et al. and Bellini and Sorrentino [26], [74], [78]) were two of the material systems used to study the effect of corner radius on spring-in with the greatest number of specimens. The two material systems have 48 and 67 specimens respectively. Since the use of AS4/8552 was much more recent and have more data available, it was chosen to proceed with the analysis.

- Add extra specimens with the same material systems and similar processing conditions from other studies to enrich the isolated dataset. As mentioned before, AS4/8552 was the most widely studied material system with lots of specimens available. Specimen with similar processing conditions from this thesis, Fernlund et al. [76], Kappel [36] and Cicek [32] were added to the isolated dataset. The added specimens had to meet the following requirements to align with the isolated dataset's processing conditions:
  - Gel temperature around 180 °C
  - Flange length around 50 mm to 80 mm
  - Relatively thin laminates, ranging from 4 to 16 plies
  - Made on a convex (male) tool

- The enriched dataset was then sorted by layup type and laminate thickness since they are two of the most influencing processing parameters. Tooling material was also introduced as an additional controlled parameter.

Similar analysis format is extended to the other processing parameters of interest.

Data-pooling showed no dependence of spring-in angle on the corner radius (Figure 5.5). Exception is the 4-ply $\pm$ 45 specimens made on the invar tool where a clear increasing trend of spring-in was observed with increasing corner radius. Note that all $\pm$ 45 specimens came from a single source [26], so further research and more experimental data should be added to confirm the observation. The reason as to why the corner radius only affect $\pm$ 45 laminates made on invar was unclear. However, it can be concluded that corner radius is shown to have no effect on spring-in with other types of laminate layups and thickness.
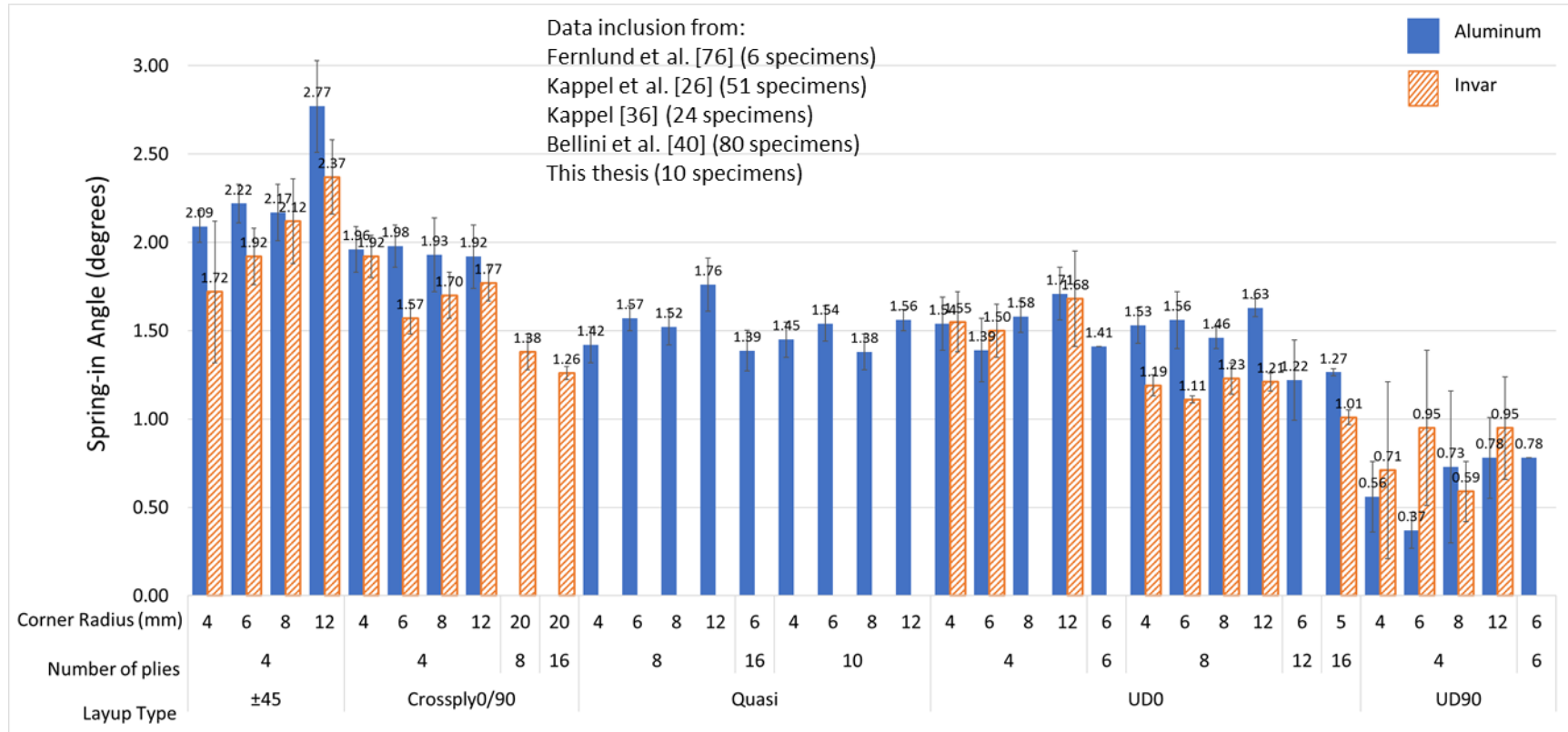
Figure 5.5 The effect of corner radius on spring-in

### 5.5.2   The Effect of Tooling Material

Most specimens found in literature that related to this topic were AS4/8552. Fewer were T800/3900-2 specimens. Comparisons were made for specimens with the same laminate type, number of plies and similar gelation temperatures. All IM7/5320-1 specimen were made on invar tools, so there was no available comparison.

### 5.5.2.1   AS4/8552

AS4/8552 specimens were available in cross-ply and UD[0] layups. Gelation temperature for all specimens in this section ranged from 172 °C to 180 °C. There were not enough specimens outside this gelation temperature range for investigating the effect of tooling material. The results were presented such that for each layup type, specimens with the same number of plies were compared for the effect of tooling material.

Average total spring-in values of 140 cross-ply AS4/8552 specimens are presented in Figure 5.6. All spring-in values were average total spring-in, which include the effect of flange warpage. Since no other filters were applied, the 140 specimens included different flange length, surface conditions as well as C and L geometries. Because a clear trend was revealed, the filters were not further refined. For the same number of plies, the trend is that the higher tool material CTE, the higher the spring-in (composite < invar < aluminum).

Similarly for 149 UD[0]n specimens (Figure 5.7), specimens made on invar tools consistently showed lower spring-in than specimens made on aluminum tools. The exception was 4-ply specimens where the average spring-in of specimens made on invar tools were 0.095 ° higher than that of the specimens made on aluminum tools. One potential reason could be that the two specimens on aluminum tool from Bellini and Sorrentino [41] were made with FEP films while the rest 4-ply specimens were made with release agent. The 4-ply thin laminate with low bending stiffness could also resulted in higher scatters, adulterating the results.
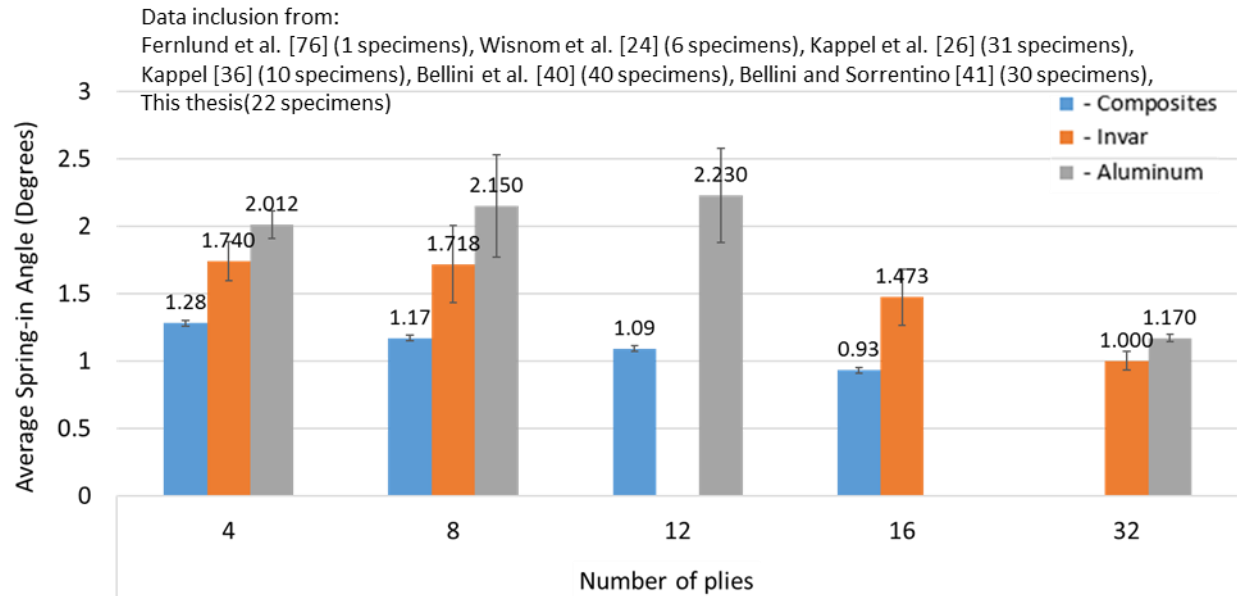
Figure 5.6 Average spring-in angle for different tooling materials for cross-ply AS4/8552 specimens gelled at 180 °C
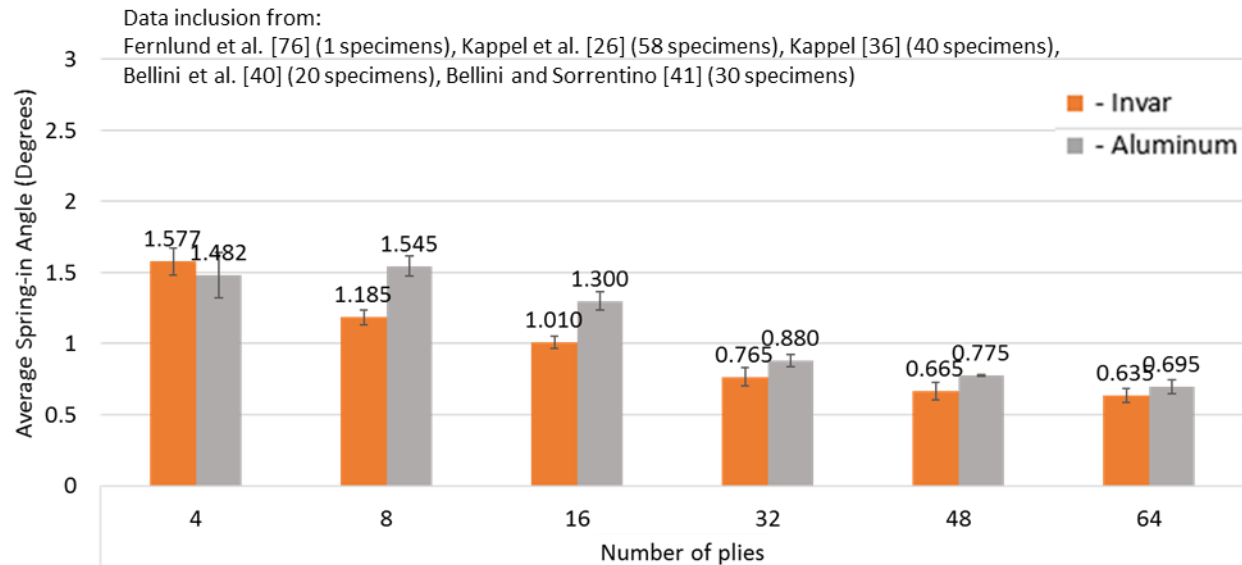


Figure 5.7 Average spring-in angle for different tooling materials for UD[0] AS4/8552 specimens gelled at 180 °C

### 5.5.2.2    T800/3900-2 and Variants

49 specimens from 4 datasets were available for T800/3900-2 and its variants in quasi-isotropic and UD[0]n layup. Because less comparisons than AS4/8552 were available, all the specimens were plotted in Figure 5.8. Tooling angle was filtered to be either 90 ° or 93 ° to be consistent with AS4/8552 specimens. Same as the AS4/8552 scenario, L-shapes and C-shapes with different surface conditions were included in this analysis. However, unlike AS4/8552, no obvious trend was observed. One of the reasons could be the variation in the material systems and different measurement methods used by the 4 datasets (Table 5.7).

Table 5.7  Material systems and measurement methods used by 4 T800/3900-2 datasets, effect of tooling materials

|  | Albert et al. [57] | Fernlund et al. [76] | Arafath et al. [31] | Minakuchi et al. [50] |
|---|---|---|---|---|
| Material system | T800/3900-2 | T800H/3900-2 | T800H/3900-2 | T800S/3900-2B |
| Measurement method | Photo copier + protractor | Jig + protractor | CMM | 3D scanner |

For quasi 8-ply, the average spring-in from invar tool was 0.41 ° less than that of the steel tool. 3 specimens for quasi 8-ply invar were from Arafath et al. [31] where one specimen for the steel tool was from Albert et al. [57]. Processing conditions for the two studies are listed in Table 5.8. The major differences between the two datasets were specimen size, layup sequence and measurement method. Arafath et al.'s specimens had flange length of 150 mm while Albert et al.'s was 89 mm. Arafath et al. had 0 ° direction plies on the very top and bottom of the laminate, increasing the bending stiffness of the specimens, while Albert et al. had 90 ° direction plies on the outside. Arafath et al. used CMM laser scanning (same as this thesis) whereas Albert et al. measured the spring-in angle by photo-copying the C-profile and measuring with a digital protractor. These three factors compounded with the 8-ply thin laminate and small number of specimens could likely be the causes of the difference.
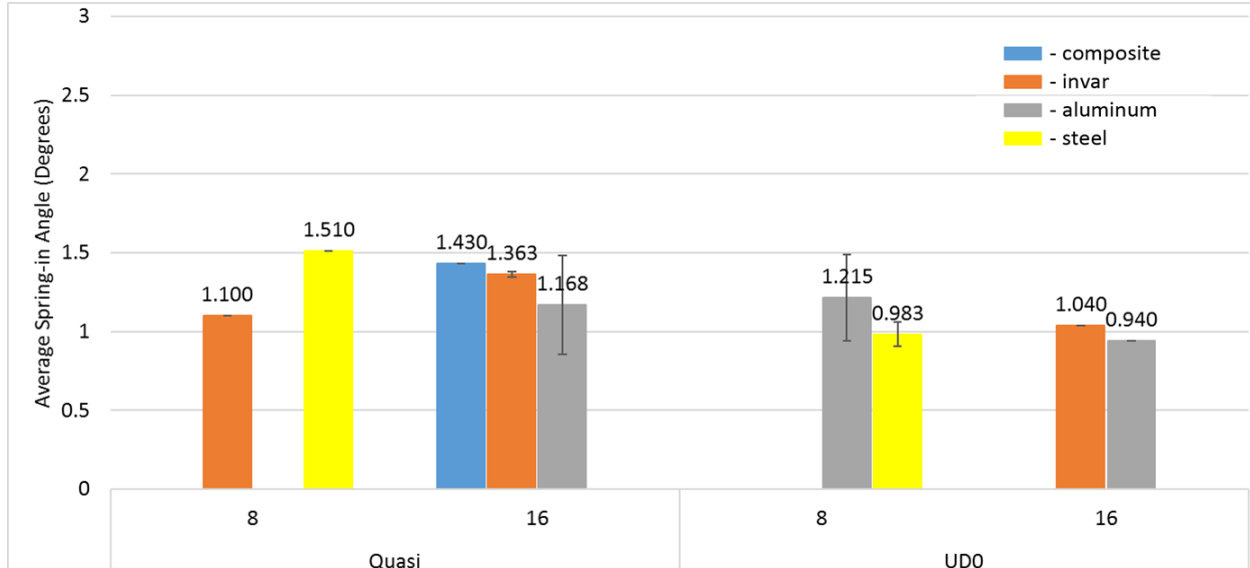
Figure 5.8 Average spring-in angle for different tooling materials for T800/3900-2 specimens gelled at 180 °C

Table 5.8 Processing conditions for quasi-isotropic 8-ply T800/3900-2 specimens from Arafath et al. [31] and Albert et al. [57], the effect of tooling material

|  | Arafath et al. [31] | Albert et al. [57] |
|---|---|---|
| Tooling material | Invar | Steel |
| Tooling surface | Release agent | Release agent |
| Corner Radius (mm) | 20 | 6 |
| Geometry | C | C |
| flange length (mm) | 150 | 89 |
| Number of plies | 8 | 8 |
| T-gel | 180 | 180 |
| Laminate type | Quasi ([0/45/-45/90]s) | Quasi ([90/-45/0/45]s) |

Another observation was that values for aluminum quasi-isotropic 16-ply were much lower than expected with a high scatter. This was because it included a dataset from Fernlund et al. [76] which had an average spring-in value around 0.5 ° less than the rest of the specimens in the same category. Fernlund et al. used a custom designed jig and digital protractor to measure spring-in which was the likely cause of the lower values. The result after excluding Fernlund's dataset is shown in Figure 5.9 where an increase in values for aluminum quasi-isotropic 16-ply can be observed. Specimens made on aluminum tool showed higher spring-in values than ones on steel tools for UD[0] 8-ply laminates which was expected. However, invar UD[0] 16-ply specimens showed

slightly higher value than aluminum UD[0]16. There was one only one specimen for each case and specimen on aluminum tool was made with FEP while specimen on invar tool was made with release agent which could attribute to the difference.
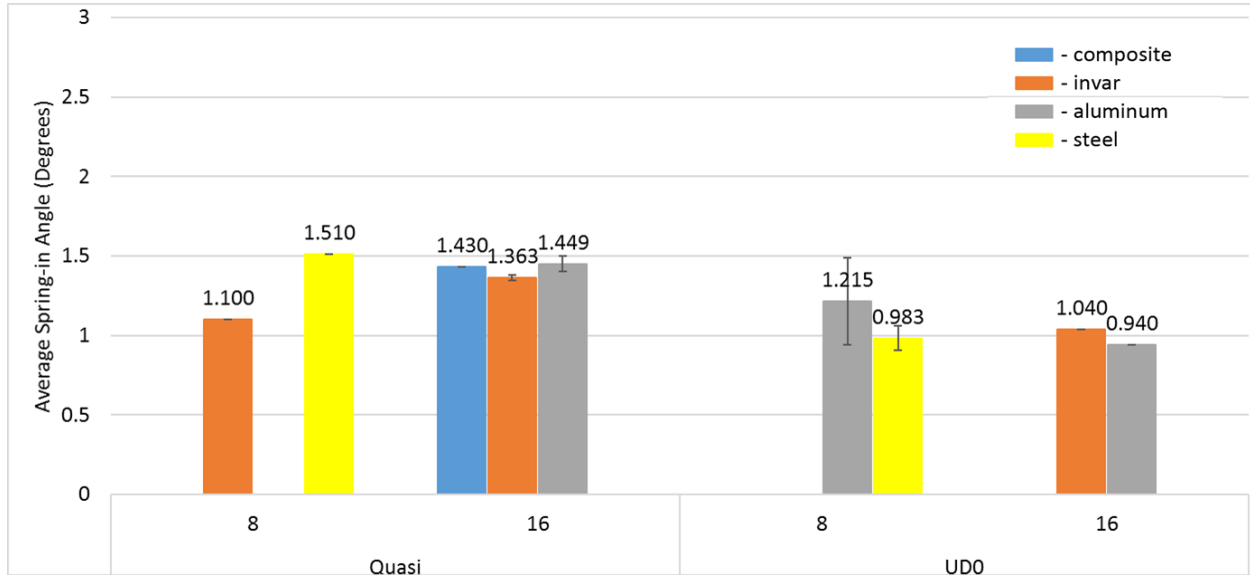


Figure 5.9 Average spring-in angle for different tooling materials for T800/3900-2 specimens gelled at 180 °C. Excluding Fernlund et al. [76]

### 5.5.3    The Effect of Thickness and Layup

The specimens of interest for this section were categorized by material systems. Then for AS4/8552, specimens were further divided into ones made on invar tools and ones made on aluminum tools. Due to limited number of specimens collected, T800/3900-2 (and its' variants) and IM7/5320-2 specimens were not further categorized.

### 5.5.3.1 AS4/8552

AS4/8552 L-shaped specimens in literature which were made on invar tools are shown in Figure 5.10. The vertical axis is the total spring-in angle collected from literature. Specimens were categorized by different layup types in the horizontal axis with number of plies as the legend. The filtering criteria for the data were only invar tool and L-shaped geometry. Thus, Figure 5.10 contains specimens from numerous researchers with multifaceted processing conditions. Observation are the following:

- [0/90] ([90/0]) cross-ply and UD0 show decreasing spring-in with increasing thickness
- For 4-ply laminates, ±45 > cross ply 0/90 > UD 0 > UD 90
- For 8-ply laminates, cross ply 0/90 > UD 0
- For 32-ply laminates, cross ply 0/90 ≈ Quasi > UD 0. Note all specimens from this category were from Kappel [36]

Similarly, all the L-shaped AS4/8552 specimens in the literature which were made on aluminum tools were shown in Figure 5.11. The observations are the following:

- Quasi and UD0 show decreasing spring-in with increasing thickness
- For 4-ply laminates, ± 45 > cross ply 0/90 > UD 0 > UD 90
- For 6-ply laminates, cross ply 0/90 > UD 0 ≈ UD 45 > UD 90
- For 8-ply laminates, Quasi ≈ UD 0. Note all specimens from this category were from Kappel et al. [26]
- For 12-ply laminates, cross ply 0/90 > UD 0
- For 16-ply laminates, Quasi ≈ UD 0
- For 32-ply laminates, cross ply 0/90 ≈ Quasi > UD 0. Note all specimens from this category were from Kappel [36]

The 6-ply and 12-ply cross-ply 0/90 specimens showed high spring-in results due to unbalanced layup ([0/90/0]s and [0/90/0]2s). Both layups were from Bellini et al. [40]. 10 experimental repeats were performed for each configuration.
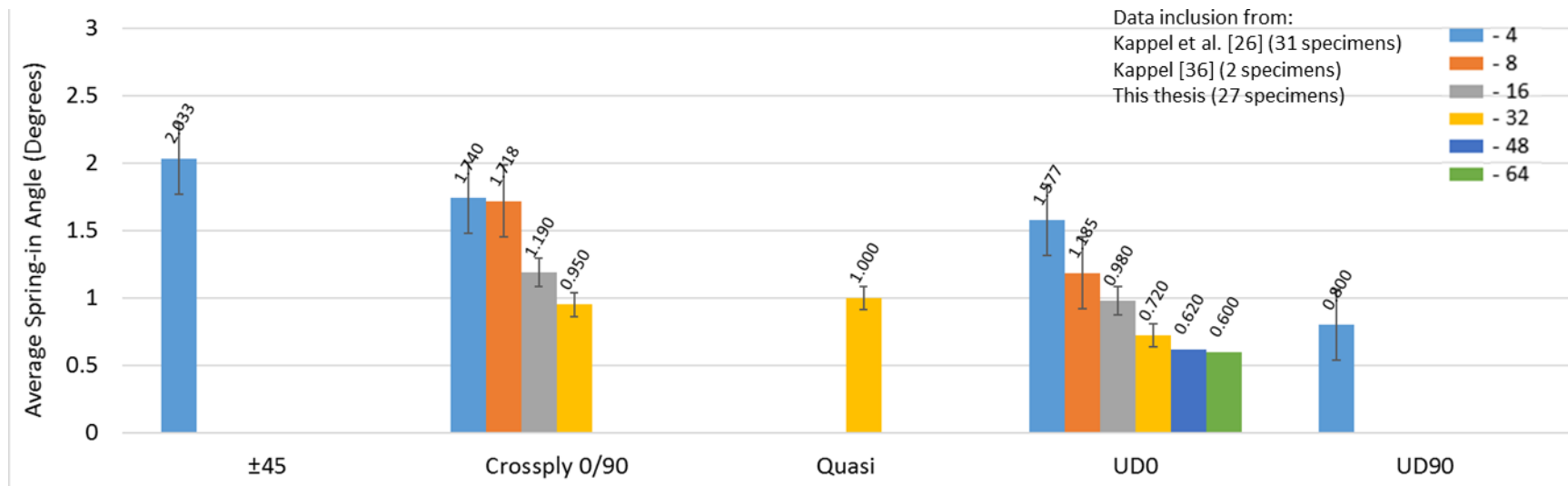
Figure 5.10 Spring-in value vs layup type with number of plies as legend. 60 AS4/8552 L-shape specimens made with invar tool
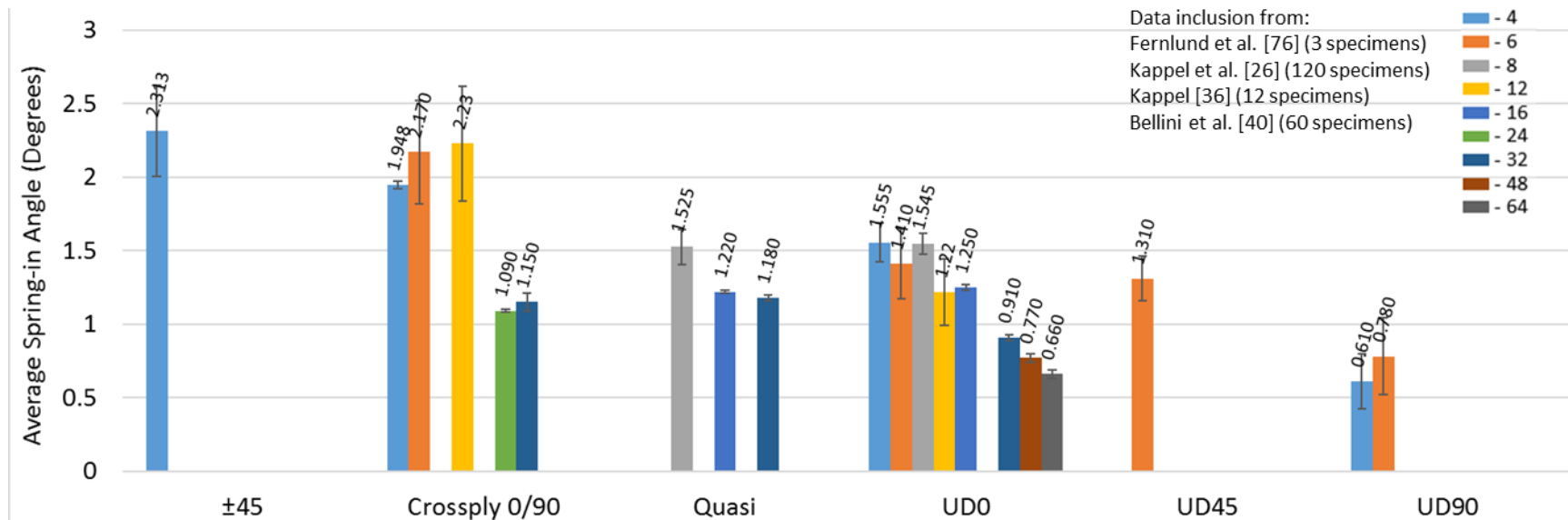


Figure 5.11 Spring-in value vs layup type with number of plies as legend. 195 AS4/8552 L-shape specimens made with aluminum tool

144

### 5.5.3.2 Spring-in of [90]n Laminates

The literature data-pooling from multiple studies showed that 58 AS4/8552 [90]n specimens, despite having different processing conditions, had considerable amount of spring-in, as shown in Figure 5.12.

Table 5.9 Processing conditions for 4 studies with [90]n specimens

|  | Johnston et al. [18] | Kappel et al. [26] | Bellini et al. [40] | Bellini and Sorrentino [41] |
|---|---|---|---|---|
| Tooling material | Aluminum | Aluminum | Aluminum | Aluminum |
| Tooling surface | Release agent | Release agent | FEP | FEP |
| Corner Radius (mm) | 4.6 | 4, 6, 8, 12 | 6 | 5 |
| Geometry | L | L | L | C |
| flange length (mm) | 51 | 40 | 80 | 100 |
| Number of plies | 12, 24, 48 | 4 | 6 | 4 |
| T-gel | 172.5, 177 | 180 | 180 | 180 |
| Laminate type | UD90 | UD90 | UD90 | UD90 |
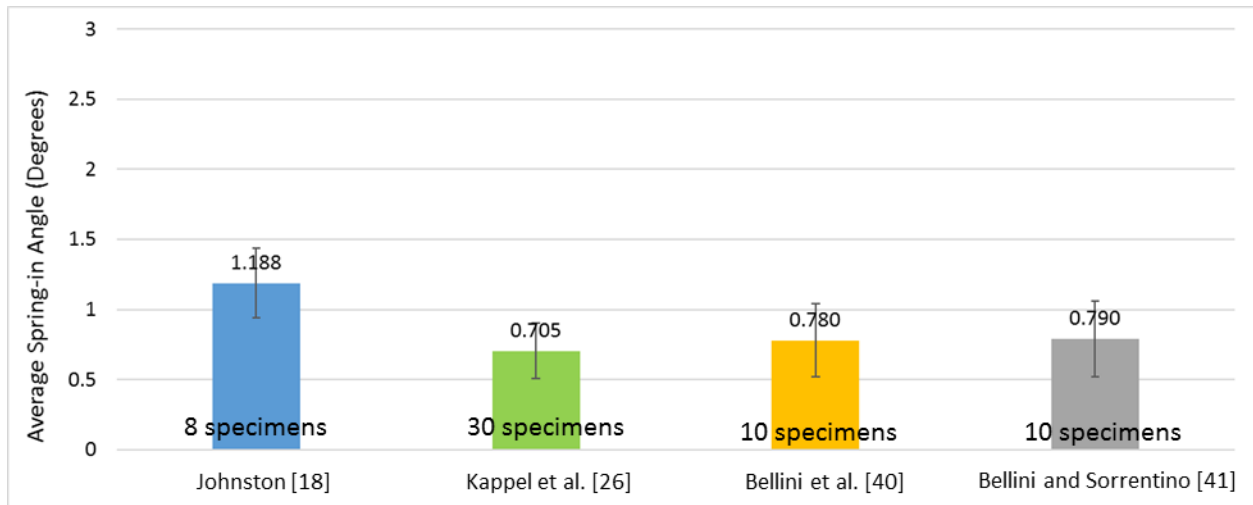


Figure 5.12 Average spring-in angle of [90]n specimen from 4 different studies

### 5.5.3.3    T800/3900-2

The effects of laminate thickness and layup on spring-in of L-shapes made from T800/3900-2 (and its' variants) in the literature are shown in Figure 5.13. Same as AS4/8552, the only filter applied here is the L-shape geometry. However, due to small number of specimens, the data were not further categorized by tooling material like that for AS4/8552. The observations are the following:

- 8-ply and 16-ply have high scatter
- Mean spring-in values exhibit decrease spring-in with increase laminate thickness for quasi-isotropic and cross-ply laminates

The pattern of Quasi > Cross-ply > UD0 could be observed with the mean values but with high scatter. Overall, more data is required for further investigation.
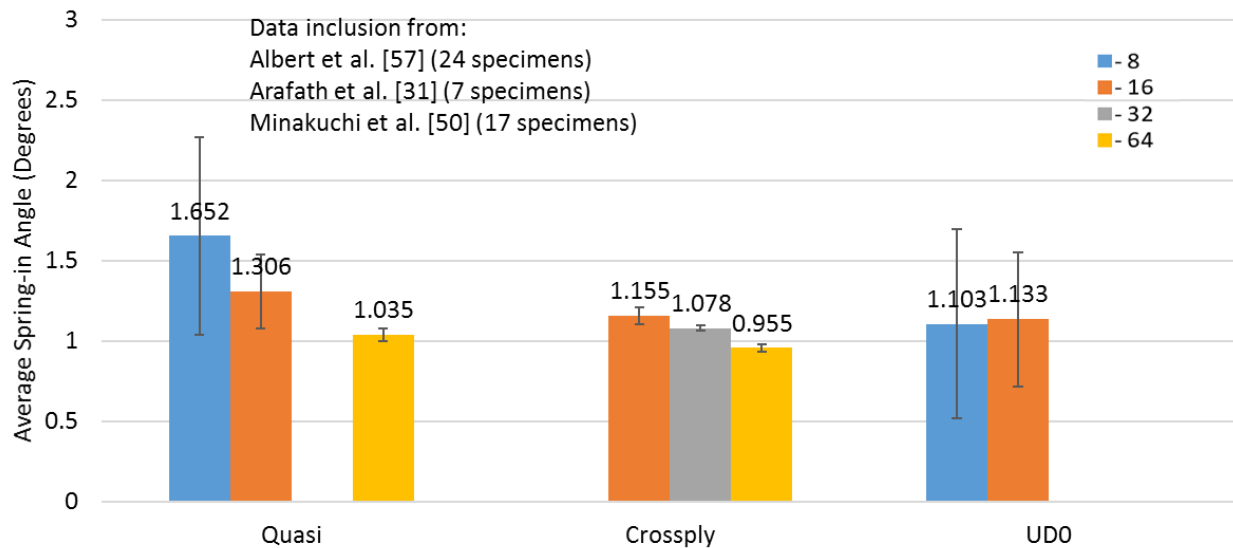


Figure 5.13 Spring-in value vs layup type with number of plies as legend. 48 T800/3900-2 L-shaped specimens

### 5.5.3.4    IM7/5320-1

Average spring-in results of IM7/5320-1 specimens from Arafath et al. [31] and Gordnian et al. [43] are shown in Figure 5.14. All specimens in this category were made on the same invar tool using the identical 121 °C gelled cure cycle. 9 quasi-isotropic C-shape specimens from Arafath et al. showed decreasing total spring-in with increasing thickness. For 16-ply specimens, 2 cross-ply L-shapes from Gordnian et al. showed lower total spring-in comparing to Arafath's specimens. The 16-ply spring-in value difference can be contributed by the layup and/or geometry.
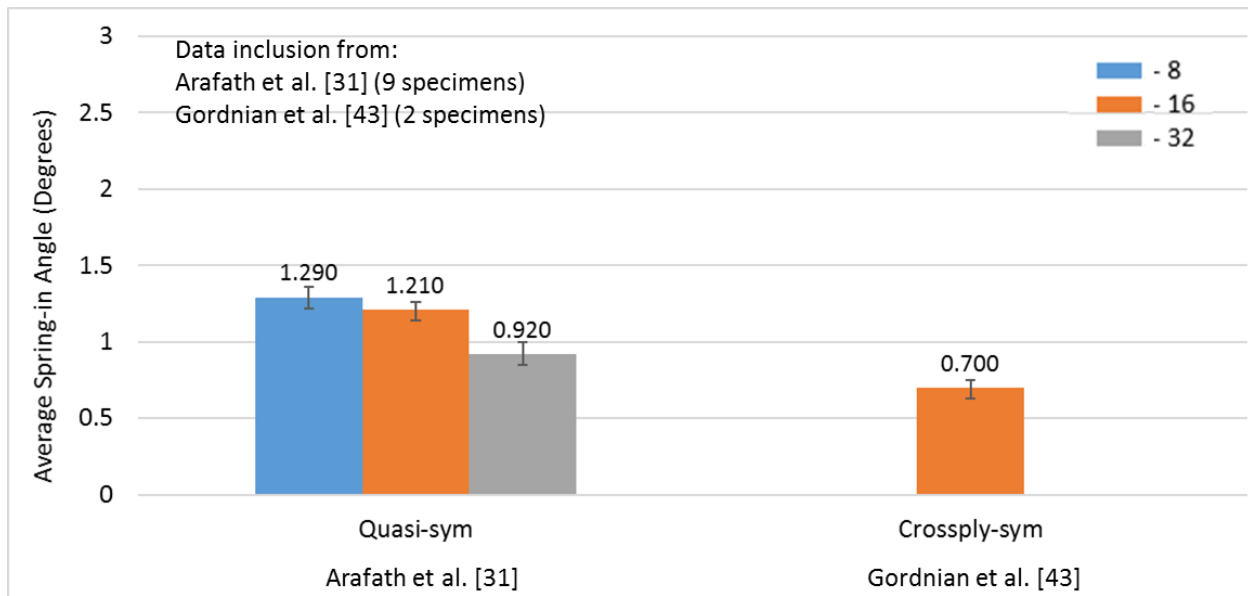


Figure 5.14 Spring-in value vs layup type with number of plies as legend. 11 IM7/5320-1 specimens

### 5.5.4    The Effect of Flange Length

Limited comparison cases were found for the effect of flange length. Increasing spring-in with increasing flange length can be observed for 151 4, 8 and 16-ply AS4/8552 cross-ply specimens (Figure 5.15). The specimen gelation temperature was filtered to 172 °C to 180 °C.  The average total spring-in of 10 8-ply, 100 mm flange length specimens from Bellini et al. were higher than the rest of the 8-ply specimens due to the C-shape geometry (the rest of 8-ply specimens were L-shapes). Little comparisons were found for other layup types, laminate thicknesses and material

systems due to lack of data. The reported total spring-in values without warpage information also obstruct further analysis.
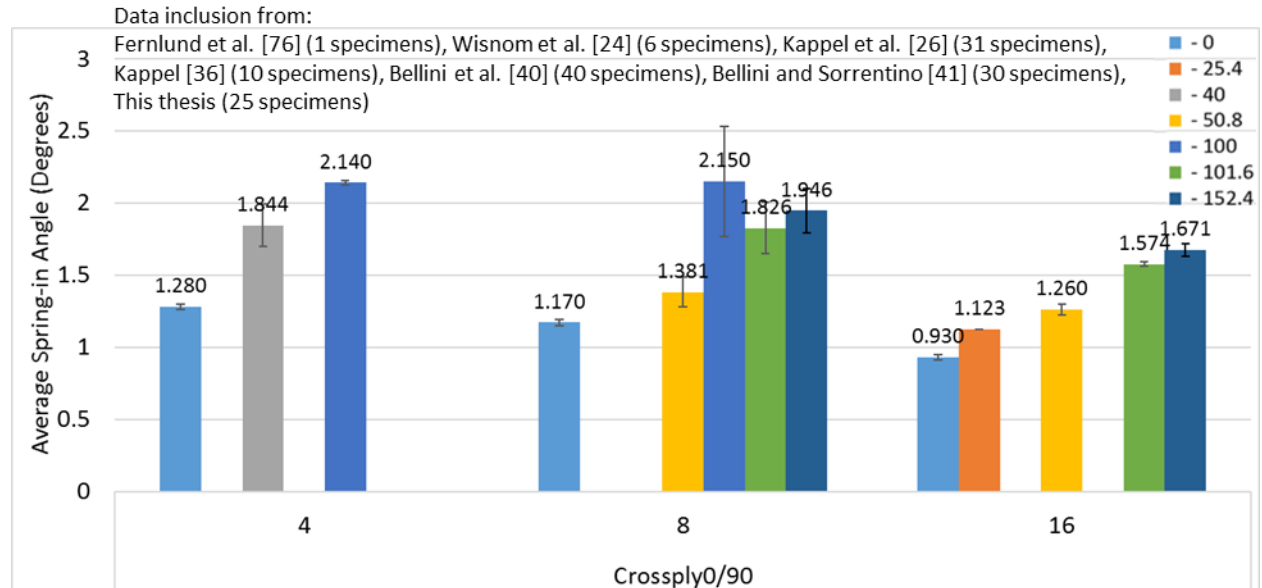


Figure 5.15 Average total spring-in values of 4, 8 and 16 ply AS4/8552 cross-ply specimens, legend is flange length.

### 5.5.5    The Effect of Gelation Temperature

The effect of gelation temperature on spring-in for AS4/8552 and IM7/5320-1 is presented in this section. There were not enough specimens in the literature pool to draw comparisons for T800/3900-2 (and its' variants).

The gelation temperature of the specimens can be calculated by integrating the appropriate material cure kinetics equation for the temperature history of interest. Cure kinetics equations for AS4/8552 [6], T800/3900-2 [146], and IM7/5320-1 [147] are available as standard material models in the RAVEN thermochemical calculator V3.13.1 [63]. The relevant temperature histories based on tooling and cure cycle information provided in the literature were used to calculate the specimen gelation temperatures, using the automated feature in the software.

### 5.5.5.1    AS4/8552

Specimens with similar processing conditions from Bellini and Sorrentino [41] and this thesis. were used to inquire the effect of gelation temperature on AS4/8552. The processing conditions are listed in Table 5.10. Section 4.5.3 of this work clearly showed spring-in increased when gelation temperature increased from 140 °C to 173 °C. For 8-ply cross-ply layup, Bellini's specimens which were gelled at 180 °C had higher average total spring-in comparing to specimens gelled at 173 °C from this thesis (Figure 5.16). It was established that the difference in corner radius have minimum impact on the spring-in results.  However, aluminum tooling and C-shaped geometry used by Bellini could contribute to the high 0.43 ° difference in average spring-in values.

Table 5.10 Processing conditions for AS4/8552 specimens from this thesis and Bellini and Sorrentino [41], the effect of gelation temperature

|  | This thesis | This thesis | Bellini and Sorrentino [41] |
|---|---|---|---|
| T-gel | 140 | 173 | 180 |
| Tooling material | Invar | Invar | Aluminum |
| Tooling surface | FEP | FEP | FEP |
| Corner Radius (mm) | 20 | 20 | 5 |
| Geometry | L | L | C |
| Flange length (mm) | 50, 100, 150 | 50, 100, 150 | 100 |
| Number of plies | 16 | 8, 16 | 8 |
| Laminate type | Cross-ply [0/90]n | Cross-ply [0/90]n | Cross-ply [0/90]n |
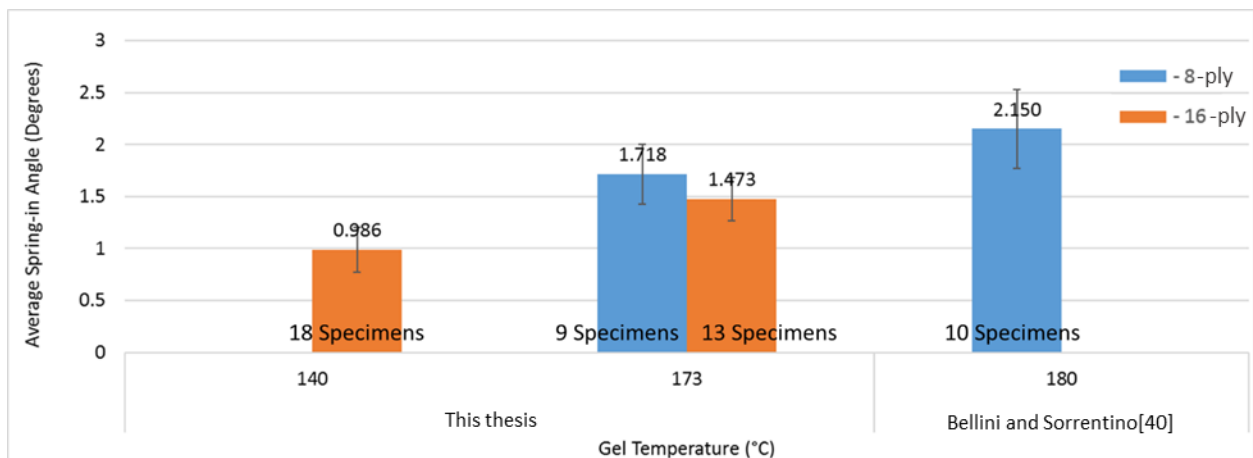


Figure 5.16 Average spring-in angle vs gel temperature for AS4/8552 specimens from this thesis and Bellini and Sorrentino [41]. Legend is number of plies of the laminates

### 5.5.5.2 IM7/5320-1

In the context of the effect of gelation temperature on spring-in of IM7/5320-1 L-shapes, the major specimen contributors in the literature were Arafath et al. [31] and Gordnian et al. [43]. Processing conditions for the two datasets are list in Table 5.11. The two studies used the same invar tool (so did this thesis). Specimens from both studies were 16-plies. The layup type and specimen geometry were different between the two datasets so the spring-in angles cannot be compared for similar gel temperatures. However, both studies showed that lower gelation temperature lead to less deformation. Gordnian especially, revealed a linear trend between the average spring-in value and gelation temperature Figure 5.17.

Table 5.11 Processing conditions for 16-ply IM7/5320-1 specimens from Arafath et al. [31] and Gordnian et al. [43], the effect of gelation temperature

| | Arafath et al. [31] | Gordnian et al. [43] |
|---|---|---|
| Tooling material | Invar | Invar |
| Tooling surface | Release agent | Release agent |
| Corner Radius (mm) | 20 | 20 |
| Geometry | C | L |
| Flange length (mm) | 150 | 150 |
| Web length (mm) | 300 | N/A |
| Number of plies | 16 | 16 |
| Laminate type | Quasi | Cross-ply |
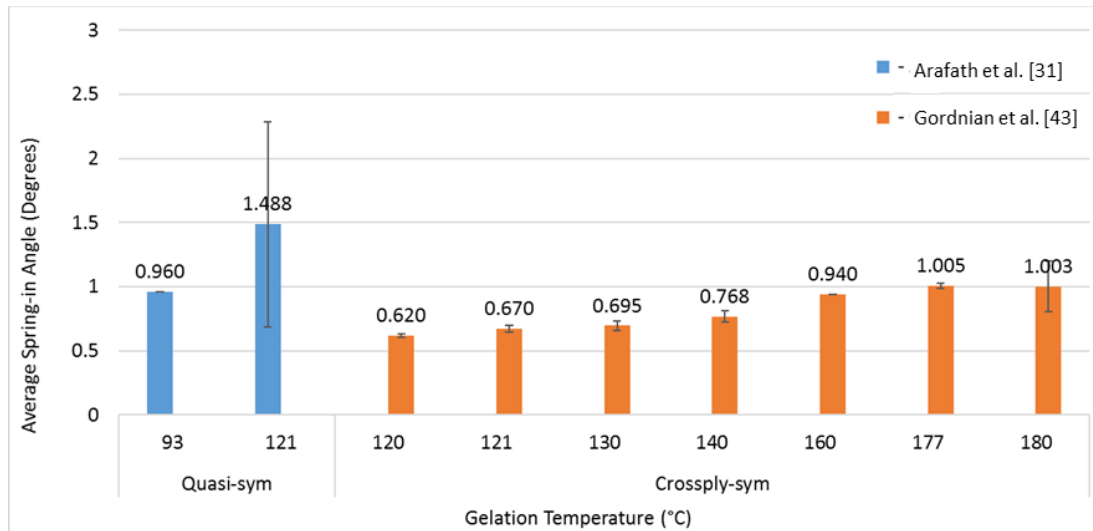


Figure 5.17 Average spring-in angle vs gel temperature for 37 16-ply IM7/5320-1 specimens, Arafath et al. [31] and Gordnian et al. [43]

150

### 5.5.6    Similar Experiments and Variance

Due to the processing parameter multitude of composite manufacturing, there was no single exact repeat of experiment were found for the three material systems of interest. The purpose of this section is to compare specimens with similar experimental conditions; showing the literature consistency across datasets. Despite some processing conditions being different, results from different studies should follow the known and proven trends. Similar experiments from different studies for AS4/8552 and T800/3900-2 are presented in Table 5.12. There were not data comparisons for IM7/5320-2.

### 5.5.6.1    AS4/8552

The first similar case is a comparison between AS4/8552 specimens from Kappel [36] and this thesis. Cross-ply L-shapes with flange length around 50 mm were made on invar tools. Specimen gelation temperatures were different by 7 °C. Kappel's 32-ply specimen was 0.3° lower than the 16-ply specimens from this thesis. which agrees well with the trend that thicker laminates have lower spring-in despite the difference in corner radius and surface conditions.

Second cross-dataset comparison is from Fernlund et al. [76], Kappel et al. [26] and Kappel [36]. In all cases, 180 °C gelled UD[0]n specimens were made on aluminum tools with release agent. Specimen flange length and corner radius were also similar.  Four 8-ply specimens from Kappel et al. [26] showed the highest spring-in which agrees with thinner laminates produces higher spring-in. However, the 16-ply Kappel [36] specimen was 0.2 ° higher than the Fernlund et al. [76]'s 12-ply specimen. Since there was only one specimen from Kappel and Fernlund et al. in this comparison, the latter observation has relatively low statistical confidence.

### 5.5.6.2    T800/3900-2

Three case comparisons of T800/3900-2 (and its variants) were found. First case includes one specimen from Albert et al. [57] and three specimens from Arafath et al. [31]. Despite the difference in flange length and corner radius, the specimens from two datasets show identical results. Although in theory, with all other processing conditions being equal, longer flange length might affect spring-in; T800/3900-2 has a thermoplastic particle toughened inter-layer which could potentially exhibit different shearing behavior. More data is needed for further analysis.

The second case is a comparison between Minakuchi et al. [50] and Arafath et al. [31]. All specimens in this case were 16-ply cross-ply laminates gelled at 180 °C. Despite the tooling material, surface condition, geometry and flange length being different, Arafath et al.'s 12 specimen showed 0.163 ° higher average spring-in value than Minakuchi et al.'s specimens. This observation agrees well with the establishment that laminate type and thickness have profound effects on spring-in.

Lastly, UD[0]n specimens from Albert et al. [57] and Arafath et al. [31] were compared. All specimens in this case were 16-ply C-shapes made with release agent. Some major differences were tooling material, flange length and gelation temperature. Although specimens from Albert et al. had shorter flanges and lower T-gel comparing to those from Arafath et al., the results were within 0.2 ° difference due to the same layup and laminate thickness.

.

Table 5.12 Experiments with similar processing conditions and their variance. Differences in processing conditions are highlighted in red

| Study | Material | # of specimens | Tooling Material | Tooling Surface | Corner Radius (mm) | Geometry | Flange length (mm) | Web length (mm) | # of plies | T-gel | Laminate type |
|---|---|---|---|---|---|---|---|---|---|---|---|
| Kappel [61] — 0.95 | AS4/8552 | 1 | Invar | Release agent | 5 | L | 50 | N/A | 32 | 180 | Crossply 0/90 |
| This thesis — 1.26 | AS4/8552 | 4 | Invar | FEP | 20 | L | 50.8 | N/A | 16 | 173 | Crossply 90/0 |
| | | | | | | | | | | | |
| Kappel [61] — 1.25 | AS4/8552 | 1 | Aluminum | Release agent | 5 | L | 50 | N/A | 16 | 180 | UD0 |
| Fernlund et al. [19] — 1.06 | AS4/8552 | 1 | Aluminum | Release agent | 6 | L | 50 | N/A | 12 | 180 | UD0 |
| Kappel et al. [1] — 1.56 | AS4/8552 | 4 | Aluminum | Release agent | 6 | L | 40 | N/A | 8 | 180 | UD0 |
| | | | | | | | | | | | |
| Albert et al. [18] — 1.41 | T800/3900-2 | 1 | Aluminum | Release agent | 6 | L | 57 | N/A | 16 | 180 | Quasi |
| Arafath et al. [52] — 1.41 | T800H/3900-2 | 3 | Aluminum | Release agent | 20 | L | 150 | N/A | 16 | 180 | Quasi |
| | | | | | | | | | | | |
| Minakuchi et al. [50] — 1.155 | T800S/3900-2B | 11 | Aluminum | Film | 6.4 | L | 60 | N/A | 16 | 180 | Crossply 0/90 |
| Arafath et al. [52] — 1.318 | T800H/3900-2 | 12 | Invar | Release agent | 20 | C | 150 | 300 | 16 | 180 | Crossply 0/90 |
| | | | | | | | | | | | |
| Albert et al. [18] - Aluminum — 1.155 | T800/3900-2 | 2 | Aluminum | Release agent | 6 | C | 57 | 102 | 16 | 135 | UD0 |
| Albert et al. [18] - Steel — 1.2 | T800/3900-2 | 2 | Steel | Release agent | 6 | C | 57 | 102 | 16 | 135 | UD0 |
| Arafath et al. [52] - Invar — 1.04 | T800H/3900-2 | 1 | Invar | Release agent | 20 | C | 150 | 300 | 16 | 180 | UD0 |

0    0.5    1    1.5    2
Average total spring-in (degrees)

## 5.6　Discussion

### 5.6.1　The Effect of Corner Radius

The data pooling results disagree with the analytical solution from Takagaki et al and Ding et al. [52], [61]. The pooled dataset included specimens with corner radius to thickness ratio (R/t) range of 0.422 to 33.784 and flange length to thickness ratio (L/t) range of 0 to 135.135. Analytical solutions from Ding et al. for AS4/8552 suggested that when $R/t > 1$ or $L/t > 1$, the total spring-in would increase substantially with increasing ratios of R/t or L/t for unidirectional and quasi-isotropic 90 ° L-shapes [52]. However, this was only observed for 8-ply quasi-isotropic L-shapes (all from a single source [26]) and not for UD [0] and other laminate thicknesses.

### 5.6.2　The Effect of Tooling Material

A clear trend of increasing spring-in deformation with increasing tooling material CTE was observed for AS4/8552,.However, when the same filters were applied to T800/3900-2 and its variants, the positive correlation of spring-in values with tooling material CTE was only observed for 8-ply quasi-isotropic and UD [0]n layup. The discrepancies in T800/3900-2 can potentially be attributed to the variation in material systems, processing parameters, measuring method and lack of data.

Researchers have shown tooling material affects spring-in by driving warpage in the flanges. Thus, a reporting method which isolates the flange warpage and corner spring-in component would be better suited to investigate the effect of tooling material. Additional investigation with large specimen quantities are required to confirm this conclusion and isolate the effect of tooling materials on spring-in of L-shapes.

### 5.6.3　The Effect of Thickness and Layup

By pooling physical specimens from the literature, the results substantiate that laminate thickness and layup have significant impact on process induced deformation.

In summary, it was observed that the L-shape average total spring-in decrease with increasing thickness for cross-ply, quasi-isotropic and UD[0]n laminates. Bellini et al. observed minimal amount of impact of laminate thickness on spring-in [40], [41] but his data stands well among all other studies within the literature, substantiating the trend. The ± 45 > cross ply 0/90 ≈ Quasi > UD 0 > UD 90 trend emerged for AS4/8552 specimens made on invar and aluminum tools which aligned with the theories mentioned in section 2.4.4. Since the clear trends for layup sequence and laminated thickness are observed before the application of any filters for other processing conditions, the effect of laminate thickness on spring-in of L-shape are deemed as significant. Although, more data is needed to validate the full trend for other material systems.

### 5.6.4    Spring-in of [90]n Laminates

The findings that [90]n specimens consistently exhibit around 0.8° of average spring-in is contrary to common understandings. More data analyzed with a method which can separate corner spring-in from total spring-in would help confirm the potential reasons discussed in section 5.4.3.

### 5.6.5    Spring-in of [45/-45]n Laminates

± 45 AS4/8552 layup has extremely high average total spring-in values of over 2°. This is likely because there was no fiber in the 0-direction, so the bending stiffness of the flanges are low. This theory extends to cross-ply and quasi-isotropic layups. For specimens of the same number of plies, a cross-ply layup would have twice as much 0-direction plies as a quasi-isotropic layup. So quasi-isotropic layups are not as stiff and more prone to bending comparing to cross-ply layups.

### 5.6.6    The Effect of Flange Length

Although 151 cross-ply AS4/8552 specimens were observed to follow the theoretical positively correlated trend regarding flange length and spring-in, little comparison cases were found for other layup and material systems. Further, the reported total spring-in values without flange warpage information leaves the effect of flange length on corner spring-in unknown.

### 5.6.7 The Effect of Gelation Temperature

Increasing spring-in with increasing gelation temperatures was observed with AS4/8552 and IM7/5320-1 specimens. More AS4/8552 specimens with a wider gelation range is needed to further validate this observation.

No comparison cases were found for T800/3900-2 and its variants. The thermo-plastic toughened interlayer for T800/3900-2 could potentially introduce different behaviors comparing to AS4/8552 and IM7/5320-1. Another limitation is that lower gelation temperatures might lead to longer cure cycle times in a production enviroment. Therefore, the trade-off between production time and dimensional control should be considered.

### 5.6.8 Similar Experiments and Variance

Many researchers have pointed out that it was very difficult to execute a detailed comparison with the results available in the literature. This was because the numerous processing parameters can vary compounding with uncertainties from the complex manufacturing process and pre-preg intrinsic variability [26], [42], [124]. Although few specimens with similar processing conditions were drawn from the database to compare, it revealed a significant deficiency of physical data. For the limited comparison cases presented in this section, the discrepancies in spring-in angles, up to 0.5 °, were somewhat justifiable via established trends. This discrepancy magnitude was large considering typical spring-in simulation prediction accuracies are 0.1° to 0.2° [41]–[43], [80], [131], [148]. Experimental results are often used for validation and taken as the ground truth. To effectively cross-compare and isolate the effects of various processing parameters, more data with lower variability is necessary

## 5.7    Summary of Literature Data Pooling

Experimental specimens in the open literature were pooled to create a database and inquire the effect of various processing parameters on process induced deformation. The current database collected over 2000 specimens since the 1970s. However, this study showed that this quantity is far from enough to fully understand the effects of over 30 processing variables on process induced deformation.

Reporting total spring-in values alone was also insufficient to reflect the current understanding of the complex deformation mechanisms. Many researchers have supported reporting corner spring-in and total spring-in (containing the effects of flange warpage) separately. The meta-analysis from this work also substantiates more systematic reporting schemes to reveal deeper insights. A "best-practice" methodology developed by the authors for studying process induced deformation experimentally is herein recommended.

From the database, a meta-analysis was performed to three representative materials systems: HEXCEL AS4/8552, TORAY T800/3900-2 (and its variants) and CYCOM IM7/5320-1. Processing parameters such as laminate thickness, layup, gelation temperature and tooling materials were observed to have significant impact on process induced deformation (Table 5.13). However, more data and a more organized reporting format are needed in order to understand causalities between the processing variables and PID from a fundamental science perspective.

Table 5.13 Summary of effect of various processing parameters on process induced deformation

| Parameter | AS4/8552 | T800/3900-2 | IM7/5320-1 | A/T [1] |
|---|---|---|---|---|
| Corner Radius | No clear trends | / | / | 7/12 [2] |
| Tooling material (CTE) | + | + (Weak) | / | 7/11 [3] |
| Layup | Observed trend * | Observed trend ** | Observed trend *** | 19/25 [4] |
| Laminate thickness | - | - | - | 24/31 [5] |
| Flange length | + | / | / | 5/5 |
| Gelation Temperature | + | / | + | 2/3 [6] |

/: no data or not enough data for investigation

[1] Agreed/Total: Number of studies which agreed with the trend found in meta-analysis/Total number of studies which have investigated the specific topic

[2] The rest 5 studies discussed corner radius affecting spring-in under specific conditions (Refer to Section 5.4.1)

[3] The rest 4 studies showed tooling material has no significant impact on spring-in [26], [27], [29], [145]

Observed trend *: ±45 > cross ply 0/90 ≈ Quasi > UD 0 > UD 90

Observed trend **: cross ply 0/90 > Quasi > UD 0 with high scatter

Observed trend ***: Quasi > cross ply 0/90

[4] Out of 25 studies which have investigated the effect of layup on process induced deformation, 19 studies agreed that layup have an impact. 6 suggested layup has no significant impact on spring-in [15], [22], [44], [45], [59], [99]

[5] 6 studies showed laminate thickness had no impact on spring-in [15], [16], [40], [41], [45], [77]. 1 study showed laminate thickness positively affects deformation for T-shape geometry [44]

# Chapter 6: Conclusion and Future Remarks

## 6.1    Conclusion

Deformation of L-shaped pre-preg CFRP specimens is a systems level problem where the multiple deformation sources and mechanisms can emerge from various steps of the production process. Precisely predicting the final geometry can have tremendous benefits in saving time and cost from iterative experiments. Decades of work have been spent to understand the effect of various processing parameters on the L-shape deformation. However, studies often take a cross-sectional view of the system level problem by focusing on one or a set of processing parameters. Limited experimental data is available in the open literature and there is no set best practice for reporting the data. Very little studies and data were focusing on the effect of cure cycles on deformation of L-shape made with pre-preg in autoclaves. Experimental and data reduction approaches varies from study to study, making cross-validation difficult. The resultant datasets in the open literature is sparse which hinders full understanding of process induced deformation.

In this work, a rigorous methodology was developed to address the above-mentioned issues in literature and control the variabilities in the composite manufacturing processes. The methodology was then used on 69 specimens which were systematically generated to investigate the effect of laminate thickness, flange length and cure cycle on L-shape deformation. During experimenting, the surface profile and thermal behavior of the invar tool was rigorously characterized. A FARO arm with touch probe was used to generate the point cloud for the invar tool surface. Although the tool meets tolerance requirements in an industrial setting, as much as 0.3 ° spring-in deviation can be caused by the tooling surface undulation. Dry autoclave run was performed to ensure desired temperature and ramp rates can be reached with the large thermal mass of invar. The takeaway from tooling characterization is that tools cannot be assumed perfect. On top of other deformation mechanisms and manufacturing uncertainties, tools introduce non-negligible variabilities to L-shape deformation.

A novel and robust data reduction and reporting process (implemented as a python code) was developed as a part of the methodology. A laser CMM non-intrusively measured the specimens

and generated dense 3D point clouds. The code collapse 3D point clouds into 2D profiles where angle measurements were taken. The result reports spring-in profiles which include corner spring-in values and flange warpage details. Spring-in values traditionally reported in literature are also reflected on the spring-in profiles, as total spring-in values. Unlike the data traditionally reported in the literature, this flange length independent result allows corner spring-in and warpage to be analyzed separately and linked to different deformation mechanisms. Different definitions of spring-in showed discrepancies up to 0.4° for the same specimen, which again, calls for a necessary data reduction and reporting standard. Tooling surface was analyzed using this same data reduction process and subtracted from the specimen to reveal true deformation.

Thermal history, thickness, and deformation of the 69 AS4/8552 specimens were presented in detail. The average specimen thickness was consistent for either 8-ply or 16-ply specimens. Thickness was independent of cure cycle or flange length. By analyzing the specimen spring-in profiles, it was observed that:

- For a fixed layup, flange length and cure cycle, corner spring-in, total spring-in and flange warpage decrease as laminate thickness increase.
- When layup, and cure cycle were fixed variables, corner spring-in is not a function of flange length. However, flange warpage increases as flange thickness to length ratio decrease. Hence, for a given thickness, total spring-in increases with flange length due to constant corer spring-in and the increasing length of warped flanges
- Specimens gelled at 140 °C consistently showed lower spring-in and warpage than ones gelled at 170 °C
- Once resin pass vitrification, the cure path and further resin curing advancements have little impact on the total residual stress level and specimen deformation
- For specimens gelled at 140 °C, partially cured specimens showed the high warpage values than fully cured specimens

A systematic literature review was conducted for 94 experimental studies and over 2000 process induced deformation specimens. The systematic review revealed disagreements within the PID literature and further summarized the obstacles for fully understanding process induced deformation as:

1. Variation in processing conditions
2. Inadequate spring-in definition
3. Non-standardized reporting format
4. Lack of tooling inspection & compensation
5. Variation in measurement methods
6. Lack of data

A meta-analysis was performed to a representative subset of specimens made with three materials systems: HEXCEL AS4/8552, TORAY T800/3900-2 and CYCOM IM7/5320-1. Although trends regarding laminate thickness, layup and gelation temperature were observed, the meta-analysis confirms the necessities of more data and a standardized experimental methodology in order to compare the data across different studies.

This study expanded the knowledge base for process induced deformation of composite manufacturing. These results and techniques demonstrated a systematic approach to generate, reduce and report L-shape data for PID such that data can be compared across studies. An expanding database for physical L-shapes was created to aid the fully understanding of process induced deformation as a system level problem.

## 6.2    Contributions

The contribution of this thesis is the following:

- Assessing the state-of-the-art open literature for L-shape process induced deformation. Discovered the inconsistency in measurement methods and flange length dependent spring-in definition

- Developed a rigorous methodology which demonstrates the good practice of L-shape experimentation. Including steps such as tooling thermal and surface characterization, proper documentation of manufacturing details as well as data reduction and reporting.

- An automated data reduction process (implemented as a python script) for reducing large point cloud data which outputs intuitive spring-in profiles. The spring-in profiles including information such as corner spring-in, flange warpage and total spring-in (what the literature reports traditionally). The script is robust so to include various spring-in definitions

- An experimental dataset which compensates tooling surface defect, showing the effect of laminate thickness, flange length and cure cycles on L-shape deformation

- A comprehensive systematic review which identified disagreements within the PID literature and summarized the obstacles for fully understanding process induced deformation. The systematic review collected over 2000 process induced deformation specimens from 1970s to-date to create a database and aid the full understanding of PID as a system level problem.

- A meta-analysis performed to a representative subset of specimens made with three materials systems: HEXCEL AS4/8552, TORAY T800/3900-2 and CYCOM IM7/5320-1. The analysis extracted trends of various processing parameters on L-shape deformation. The inconsistency and lack of experimental data was revealed, highlighting the need for a standard way to measure and report L-shape data.

## 6.3   Future Work

Although this thesis demonstrated a good practice to study process induced deformation of L-shapes, several future projects can be established to strengthen the process and explore more unknowns. The following tasks would deepen the understanding of this topic:

- Scan tooling with laser CMM. Having the tool and specimen inspected at the same caliber would eliminate the uncertainties from point cloud up-sampling. High accuracy tooling point cloud can aid understand the direct linkage between tooling surface undulation and deformed specimen profile. Tooling point cloud can also potentially be used as input for FE models.

- Experimentally obtain tooling surface profile at curing temperature. This has been achieved by simulation, however if there exist a scanning system which is integrated with autoclave, the exact tooling surface can be obtained. The actual thermal deformed tool can be compared to simulation for validation.

- Varying processing parameters and material systems to enrich the dataset. Make L-shapes with just release agent instead of using FEP. Flange warpage might increase due to increased tool part interaction. Use release agent instead of using FEP is more industrial relevant. Other material systems such as T800/3900-2 can potentially be used. C-shape geometry can be implemented with modification to the data reduction process. Once there are enough data, potential machine learning or principal component analysis can be done once large amounts of organized data is accumulated.

# Bibliography

[1]     F. C. Campbell, "Manufacturing Processes for Advanced Composites, Chapter 1," 2004.

[2]     F. C. Campbell, "Manufacturing Processes for Advanced Composites, Chapter 8," *Manuf. Process. Adv. Compos.*, pp. 241–301, 2004.

[3]     ASTM E2160-04, "Standard Test Method for Heat of Reaction of Thermally Reactive Materials by Differential Scanning Calorimetry," vol. 04, no. Reapproved 2018, pp. 1–5, 2018.

[4]     F. C. Campbell, "Manufacturing Processes for Advanced Composites, Chapter 3," 2004.

[5]     N. Zobeiry and A. Poursartip, *The origins of residual stress and its evaluation in composite materials*. 2015.

[6]     D. Van Ee and A. Poursartip, "NCAMP Hexply Material Properties Database for use with COMPRO CCA and Raven," *Natl. Cent. Adv. Mater. Perform.*, p. 141, 2009.

[7]     E. T. Inc, "Tg - Glass Transition Temperature for Epoxies," 2012. [Online]. Available: http://www.epotek.com/site/files/Techtips/pdfs/tip23.pdf. [Accessed: 13-Jul-2020].

[8]     F. C. Campbell, "Manufacturing Processes for Advanced Composites, Contents," *J. Petrol.*, vol. 369, no. 1, pp. 1689–1699, 2004.

[9]     C. Duffner, "Experimental Study of the Pre-gelation Behaviour of Composite Prepreg," *J. Chem. Inf. Model.*, vol. 53, no. 9, pp. 1689–1699, 2019.

[10]    J. Gotro, "Thermoset Characterization Part 7: Introduction to Vitrification - Polymer Innovation Blog," 2014. [Online]. Available: https://polymerinnovationblog.com/thermoset-characterization-part-7-introduction-vitrification/. [Accessed: 13-Jul-2020].

[11]    N. Ersoy and M. Tugutlu, "Cure Kinetics Modelling and Cure Shrinkage," *ICCM 17 Int. Conf. Compos. Mater.*, pp. 6–11, 2009.

[12]    N. Ersoy and M. Tugutlu, "Cure Kinetics Modeling and Cure Shrinkage Behavior of a Thermosetting Composite Nuri," *Polym. Eng. Sci.*, 2010.

[13]    T. Garstka, N. Ersoy, K. D. Potter, and M. R. Wisnom, "In situ measurements of through-the-thickness strains during processing of AS4/8552 composite," *Compos. Part A Appl. Sci. Manuf.*, vol. 38, no. 12, pp. 2517–2526, 2007.

[14]    N. Ersoy, T. Garstka, K. Potter, M. R. Wisnom, D. Porter, and G. Stringer, "Modelling of

the spring-in phenomenon in curved parts made of a thermosetting composite," *Compos. Part A Appl. Sci. Manuf.*, vol. 41, no. 3, pp. 410–418, 2010.

[15]  J. M. Patterson, G. S. Springer, and L. P. Kollar, "Experimental observations of the spring-in phenomenon," *Proc. 8th Int. Conf. Compos. Mater.*, p. 1991, 1991.

[16]  D. W. Radford and R. J. Diefendorf, "Shape Instabilities in Composites Resulting from Laminate Anisotropy," *J. Reinf. Plast. Compos.*, vol. 12, no. 1, pp. 58–75, 1993.

[17]  G. Fernlund, R. Courdji, A. Poursartip, L. Hendrickson, K. Nelson, and P. George, "Process induced deformations of the Boeing 777 Aft Strut Trailing Edge Fairing," *Int. SAMPE Tech. Conf.*, vol. 33, no. March, pp. 347–355, 2001.

[18]  A. Johnston, R. Vaziri, and A. Poursartip, "A plane strain model for process-induced deformation of laminated composite structures," *J. Compos. Mater.*, vol. 35, no. 16, pp. 1435–1469, 2001.

[19]  J. . Svanberg and J. . Holmberg, "An experimental investigation on mechanisms for manufacturing induced shape distortions in homogeneous and balanced laminates," *Compos. Part A Appl. Sci. Manuf.*, vol. 32, no. 6, pp. 827–838, Jun. 2001.

[20]  K. J. Yoon and J. S. Kim, "Effect of thermal deformation and chemical shrinkage on the process induced distortion of carbon/epoxy curved laminates," *J. Compos. Mater.*, vol. 35, no. 3, pp. 253–263, 2001.

[21]  P. Hubert, A. Johnston, A. Poursartip, and K. Nelson, "Cure kinetics and viscosity models for Hexcel 8552 epoxy resin," *Int. SAMPE Symp. Exhib.*, vol. 46 II, no. July 2014, pp. 2341–2354, 2001.

[22]  G. Fernlund, A. Poursartip, G. Twigg, and C. Albert, "Residual Stress, Spring-in and Warpage in Autoclaved Composite Parts," *14th Int. Conf. Compos. Mater.*, no. Figure 1, 2003.

[23]  J. . Svanberg and J. . Holmberg, "Prediction of shape distortions. Part II. Experimental validation and analysis of boundary conditions," *Compos. Part A Appl. Sci. Manuf.*, vol. 35, no. 6, pp. 723–734, Jun. 2004.

[24]  M. R. Wisnom, K. D. Potter, and N. Ersoy, "Shear-lag analysis of the effect of thickness on spring-in of curved composites," *J. Compos. Mater.*, vol. 41, no. 11, pp. 1311–1324, 2007.

[25]  K.-T. Hsiao and S. Gangireddy, "Investigation on the spring-in phenomenon of carbon nanofiber-glass fiber/polyester composites manufactured with vacuum assisted resin

transfer molding," *Compos. Part A Appl. Sci. Manuf.*, vol. 39, no. 5, pp. 834–842, May 2008.

[26]  E. Kappel, D. Stefaniak, and C. Hühne, "Process distortions in prepreg manufacturing – An experimental study on CFRP L-profiles," *Compos. Struct.*, vol. 106, pp. 615–625, Dec. 2013.

[27]  G. S. S. Hugo Sarrazin, Beomkeun Kim, Sung-Hoon Ahn, "Effects of Processing Temperature and Layup on Springback," *Journal of Reinforced Plastics and Composites*, vol. 14, no. 12. pp. 1252–1258, 1995.

[28]  J. S. Lightfoot, M. R. Wisnom, and K. Potter, "A new mechanism for the formation of ply wrinkles due to shear between plies," *Compos. Part A Appl. Sci. Manuf.*, vol. 49, pp. 139–147, 2013.

[29]  P. Roozbehjavan *et al.*, "Experimental and numerical study of distortion in flat, L-shaped, and U-shaped carbon fiber-epoxy composite parts," *Journal of Applied Polymer Science*, vol. 131, no. 13. 2014.

[30]  Y. Miao *et al.*, "Study on the effect of cure cycle on the process induced deformation of cap shaped stiffened composite panels," *Appl. Compos. Mater.*, vol. 20, no. 4, pp. 709–718, 2013.

[31]  A. Arafath *et al.*, "CCMRD 9.2 Dimensional Control for Large Complex Aerospace Structures Phase 2. Final Report," 2015.

[32]  K. F. Cieck, "Experimental and Numerical Study of Spring-in Angle in Corner Shaped Composite Parts," 2014.

[33]  E. Kappel, D. Stefaniak, and G. Fernlund, "Predicting process-induced distortions in composite manufacturing - A pheno-numerical simulation strategy," *Compos. Struct.*, vol. 120, pp. 98–106, 2015.

[34]  L. Sorrentino and C. Bellini, "Validation of a Methodology for Cure Process Optimization of Thick Composite Laminates," *Polym. - Plast. Technol. Eng.*, vol. 54, no. 17, pp. 1803–1811, 2015.

[35]  G. Y. Fortin, "Thesis - Gabriel Yves Fortin," no. April, 2016.

[36]  E. Kappel, "Forced-interaction and spring-in − Relevant initiators of process-induced distortions in composite manufacturing," *Compos. Struct.*, vol. 140, pp. 217–229, Apr. 2016.

[37]  M. N. Bin Mohd Nasir, M. A. Seman, L. Mezeix, Y. Aminanda, A. Rivai, and K. M. Ali, "Effect of the corner angle on spring-back deformation for unidirectional L-shaped laminate composites manufactured through autoclave processing," *ARPN J. Eng. Appl. Sci.*, vol. 11, no. 1, pp. 315–318, 2016.

[38]  T. S. Rennick and D. W. Radford, "Components of manufacturing distortion in carbon fiber/epoxy angle brackets," *International SAMPE Technical Conference*, vol. 28. pp. 189–197, 1996.

[39]  K. Takagaki, S. Minakuchi, and N. Takeda, "Process-induced strain and distortion in curved composites. Part II: Parametric study and application," *Compos. Part A Appl. Sci. Manuf.*, vol. 103, pp. 219–229, 2017.

[40]  C. Bellini, L. Sorrentino, W. Polini, and A. Corrado, "Spring-in analysis of CFRP thin laminates: numerical and experimental results," *Compos. Struct.*, vol. 173, pp. 17–24, Aug. 2017.

[41]  C. Bellini and L. Sorrentino, "Analysis of cure induced deformation of CFRP U-shaped laminates," *Compos. Struct.*, vol. 197, pp. 1–9, Aug. 2018.

[42]  A. Bernath, F. Groh, W. Exner, C. Hühne, and F. Henning, "Experimental and numerical study of the spring-in of angled brackets manufactured using different resins and fiber textiles," *J. Compos. Mater.*, 2019.

[43]  K. Gordnian, A. Forghani, R. Brockman, and A. Poursartip, "Experimental and numerical investigation of effects of cure cycle on process-induced-distortions of carbon fibre reinforced composites," *Int. SAMPE Tech. Conf.*, vol. 2019-May, 2019.

[44]  A. Stephan, E. Schwinge, J. Mueller, and H. Oery, "On the springback effect of CFRP stringers: An experimental, analytical and numerical analysis," *International SAMPE Technical Conference*, vol. 28. pp. 245–254, 1996.

[45]  L. K. Jain, B. G. Lutton, Y. W. Mai, and R. Paton, "Stresses and deformations induced during manufacturing. Part II: A study of the spring-in phenomenon," *Journal of Composite Materials*, vol. 31, no. 7. pp. 696–719, 1997.

[46]  A. a Johnston, "An integrated model of the development of process-induced deformation in autoclave processing of composite structures," *Univ. Br. Columbia*, no. April, pp. 1–367, 1997.

[47]  M. I. Naji and S. V. Hoa, "Curing of thick angle-bend thermoset composite part: curing

cycle effect on thickness variation and fiber volume fraction," *Journal of Reinforced Plastics and Composites*, vol. 18, no. 8. pp. 702–723, 1999.

[48]   J. M. Ganley and A. K. Maji, "Explaining spring-in in filament wound carbon fiber epoxy composites 2000 ganley," *J. Compos. Mater.*, vol. 34, no. 14, pp. 1216–1239, 2000.

[49]   D. W. Radford and T. S. Rennick, "Separating sources of manufacturing distortion in laminated composites," *Journal of Reinforced Plastics and Composites*, vol. 19, no. 8. pp. 621–641, 2000.

[50]   S. Minakuchi, K. Sawaguchi, K. Takagaki, S. Niwa, and N. Takeda, "Effect of inter-laminar toughened layers on process-induced strain and deformation of L-shaped composites," *Adv. Compos. Mater.*, vol. 28, no. 5, pp. 445–461, 2019.

[51]   F. Groh, E. Kappel, C. Hühne, and W. Brymerski, "Investigation of fast curing epoxy resins regarding process induced distortions of fibre reinforced composites," *Compos. Struct.*, vol. 207, no. July 2018, pp. 923–934, 2019.

[52]   A. Ding, J. Wang, and S. Li, "Understanding process-induced spring-in of L-shaped composite parts using analytical solution," *Composite Structures*, vol. 250. 2020.

[53]   C. Albert, "Spring-in of Angled Thermoset Composite Laminates," no. September, 1997.

[54]   G. Y. Fortin and G. Fernlund, "Effect of tool temperature on dimensional fidelity and strength of thermoformed polyetheretherketone composites," *Polym. Compos.*, vol. 40, no. 11, pp. 4376–4389, 2019.

[55]   D. W. Radford, "Volume fraction gradient induced warpage in curved composite plates," *Compos. Eng.*, vol. 5, no. 7, pp. 923–934, Jan. 1995.

[56]   K. F. Çiçek, M. Erdal, and A. Kayran, "Experimental and numerical study of process-induced total spring-in of corner-shaped composite parts," *J. Compos. Mater.*, vol. 51, no. 16, pp. 2347–2361, 2017.

[57]   C. Albert and G. Fernlund, "Spring-in and warpage of angled composite laminates," *Compos. Sci. Technol.*, vol. 62, no. 14, pp. 1895–1912, 2002.

[58]   Y. Tao, "Boeing - personal communication." 2020.

[59]   D. a Darrow and L. V Smith, "Isolating Components of Processing Induced Warpage in Laminated Composites," *J. Compos. Mater.*, vol. 36, no. 21, pp. 2407–2419, 2002.

[60]   N. Ersoy, K. Potter, M. R. Wisnom, and M. J. Clegg, "Development of spring-in angle during cure of a thermosetting composite," *Compos. Part A Appl. Sci. Manuf.*, vol. 36, no.

12, pp. 1700–1706, Dec. 2005.

[61]   K. Takagaki, S. Minakuchi, and N. Takeda, "Process-induced strain and distortion in curved composites. Part I: Development of fiber-optic strain monitoring technique and analytical methods," *Compos. Part A Appl. Sci. Manuf.*, vol. 103, pp. 236–251, 2017.

[62]   R. H. Nelson and D. S. Cairns, "Prediction of dimensional changes in composite laminates during cure," *International SAMPE Symposium and Exhibition (Proceedings)*, vol. 34, no. pt2. pp. 2397–2410, 1989.

[63]   C. M. Technology, "RAVEN simulation software." Vancouver, 2017.

[64]   G. Twigg, A. Poursartip, and G. Fernlund, "Tool-part interaction in composites processing. Part I: Experimental investigation and analytical model," *Compos. Part A Appl. Sci. Manuf.*, vol. 35, no. 1, pp. 121–133, 2004.

[65]   X. Zeng and J. Raghavan, "Role of tool-part interaction in process-induced warpage of autoclave-manufactured composite structures," *Compos. Part A Appl. Sci. Manuf.*, vol. 41, no. 9, pp. 1174–1183, Sep. 2010.

[66]   V. Kaushik and J. Raghavan, "Experimental study of tool–part interaction during autoclave processing of thermoset polymer composite structures," *Compos. Part A Appl. Sci. Manuf.*, vol. 41, no. 9, pp. 1210–1218, Sep. 2010.

[67]   T. W. K. Rohwer, E. Kappel, D. Stefaniak, "Spring-in and Warpage - Progress in Manufacturing Aspects," *Mech. Compos. Mater.*, vol. 49, no. 2, pp. 193–200, 2012.

[68]   D. Stefaniak, E. Kappel, T. Spröwitz, and C. Hühne, "Experimental identification of process parameters inducing warpage of autoclave-processed CFRP parts," *Compos. Part A Appl. Sci. Manuf.*, vol. 43, no. 7, pp. 1081–1091, Jul. 2012.

[69]   S. R. White and H. T. Hahn, "Cure Cycle Optimization for the Reduction of Processing-Induced Residual Stresses in Composite Materials," *J. Compos. Mater.*, vol. 27, no. 14, pp. 1352–1378, 1993.

[70]   M. S. M. ; M. S.GENIDY, "A new methode to reduce cure-induced stresses in thermoset polymer composites, Parte I: Test method," vol. 34, no. 22. pp. 1926–1947, 1990.

[71]   J. D. Russell, M. S. Madhukar, M. S. Genidy, and A. Y. Lee, "New method to reduce cure-induced stresses in thermoset polymer composites, Part III: Correlating stress history to viscosity, degree of cure, and cure shrinkage," *J. Compos. Mater.*, vol. 34, no. 22, pp. 1926–1947, 2000.

[72] M. S. Madhukar, "Monitoring fiber stress during curing of single fiber glass- and graphite-epoxy composites," *NASA Tech. Memo. 4568*, no. November, 1994.

[73] C. Li, N. Zobeiry, K. Keil, S. Chatterjee, and A. Poursartip, "Advances in the Characterization of Residual Stress in Composite Structures," *Proc. 44th SAMPE Tech. Conf. Seattle, Washingt. June 2-5*, no. January 2014, p. 15, 2014.

[74] K. S. Kim and H. T. Hahn, "Residual stress development during processing of graphite/epoxy composites," *Compos. Sci. Technol.*, vol. 36, no. 2, pp. 121–132, Jan. 1989.

[75] Q. Zhu, P. H. Geubelle, M. Li, and C. L. Tucker, "Dimensional accuracy of thermoset composites: Simulation of process-induced residual stresses," *J. Compos. Mater.*, vol. 35, no. 24, pp. 2171–2205, 2001.

[76] G. Fernlund *et al.*, "Experimental and numerical study of the effect of cure cycle, tool surface, geometry, and lay-up on the dimensional fidelity of autoclave-processed composite parts," *Compos. - Part A Appl. Sci. Manuf.*, vol. 33, no. 3, pp. 341–351, 2002.

[77] H. W. Wiersma, L. J. B. Peeters, and R. Akkerman, "Prediction of springforward in continuous-fibre/polymer L-shaped parts," *Composites Part A: Applied Science and Manufacturing*, vol. 29, no. 11. pp. 1333–1342, 1998.

[78] G. Fernlund *et al.*, "Finite element based prediction of process-induced deformation of autoclaved composite structures using 2D process analysis and 3D structural analysis," *Compos. Struct.*, vol. 62, no. 2, pp. 223–234, 2003.

[79] P. Hubert and A. Poursartip, "Aspects of the compaction of composite angle laminates: an experimental investigation," *J. Compos. Mater.*, vol. 35, no. 1, pp. 2–26, 2001.

[80] E. Kappel, "A zone-based approach to predict process-induced distortions of composite structures based on a 'spring-in reference curve'," *Compos. Struct.*, vol. 209, no. October 2018, pp. 143–149, 2018.

[81] J. R. Davis, *Metals Handbook Desk Edition, 2nd Ed. (2nd Edition)*. 1998.

[82] J. Park, N. Zobeiry, and A. Poursartip, "Tooling materials and their effect on surface thermal gradients," *Int. SAMPE Tech. Conf.*, no. March, pp. 2554–2568, 2017.

[83] Erik Kappel, "Process Distortion in Composite Manufacturing," Otto-von-Guericke University of Magdeburg, Germany, 2013.

[84] EDF R&D, "CloudCompare." Daniel Girardeau-Montaut, Accessed on October 19, 2020.[Online]. Available:https://www.danielgm.net/cc/, 2020.

[85] "Point Cloud Library (PCL): pcl::MovingLeastSquares< PointInT, PointOutT > Class Template Reference," *Creative Commons Attribution 3.0.* [Online]. Available: https://pointclouds.org/documentation/classpcl_1_1_moving_least_squares.html#ab0865f62d90c9fb0f45dd96e587fe84e. [Accessed: 17-Nov-2020].

[86] M. Alexa, J. Behr, D. Cohen-Or, S. Fleishman, D. Levin, and C. T. Silva, "Computing and rendering point set surfaces," *IEEE Trans. Vis. Comput. Graph.*, vol. 9, no. 1, pp. 3–15, 2003.

[87] E. Kappel, D. Stefaniak, D. Holzhüter, C. Hühne, and M. Sinapius, "Manufacturing distortions of a CFRP box-structure – A semi-numerical prediction approach," *Compos. Part A Appl. Sci. Manuf.*, vol. 51, pp. 89–98, Aug. 2013.

[88] A. L. Stewart and A. Poursartip, "Characterization of fibre alignment in as-received aerospace grade unidirectional prepreg," *Compos. Part A Appl. Sci. Manuf.*, vol. 112, no. February, pp. 239–249, 2018.

[89] Y. Tao, "Convergent Manufacturing Technologies - Personal Communication." Vancouver, 2020.

[90] G. M. Odegard and A. Bandyopadhyay, "Physical aging of epoxy polymers and their composites," *J. Polym. Sci. Part B Polym. Phys.*, vol. 49, no. 24, pp. 1695–1716, 2011.

[91] H. W. Hu, "Physical Aging in Long Term Creep of Polymeric Composite Laminates," *J. Mech.*, vol. 23, no. 3, pp. 245–252, Sep. 2007.

[92] X. Shi, B. M. D. Fernando, and S. G. Croll, "Concurrent physical aging and degradation of crosslinked coating systems in accelerated weathering," *J. Coatings Technol. Res.*, vol. 5, no. 3, pp. 299–309, 2008.

[93] C. G.'Sell and G. B. McKenna, "Influence of physical ageing on the yield response of model DGEBA/poly(propylene oxide) epoxy glasses," *Polymer (Guildf).*, vol. 33, no. 10, pp. 2103–2113, Jan. 1992.

[94] E. S.-W. Kong, G. L. Wilkes, J. E. McGrath, A. K. Banthia, Y. Mohajer, and M. R. Tant, "Physical aging of linear and network epoxy resins," *Polym. Eng. Sci.*, vol. 21, no. 14, pp. 943–950, Oct. 1981.

[95] N. Zahlan and J. M. O'Neill, "Design and fabrication of composite components; the spring-forward phenomenon," *Composites*, vol. 20, no. 1, pp. 77–81, 1989.

[96] J. A. Barnes, G. Byerly, M. C. LeBouton, and N. Zahlan, "Dimensional stability effects in

thermoplastic composites - towards a predictive capability," *Compos. Manuf.*, vol. 2, no. 3–4, pp. 171–178, 1991.

[97] G. Fernlund, K. Nelson, and A. Poursartip, "Modeling of process induced deformations of composite shell structures," *Int. SAMPE Symp. Exhib.*, vol. 45, no. January, 2000.

[98] X. L. Liu, R. Sweeting, and R. Paton, "An investigation into spring-in of curved composite angles," *Int. SAMPE Tech. Conf.*, vol. 33, pp. 338–346, 2001.

[99] D. A. Darrow and L. V. Smith, "Evaluating the spring-in phenomenon of polymer matrix composites," *Int. SAMPE Tech. Conf.*, vol. 33, pp. 326–337, 2001.

[100] J. M. Svanberg, "Shape distortion of non-isothermally cured composite angle bracket," *Plast. Rubber Compos.*, vol. 31, no. 9, pp. 398–404, 2002.

[101] M. Gigliotti, M. R. Wisnom, and K. D. Potter, "Development of curvature during the cure of AS4 / 8552 [ 0 / 90 ] unsymmetric composite plates," vol. 63, pp. 187–197, 2003.

[102] G. Twigg, A. Poursartip, and G. Fernlund, "An experimental method for quantifying tool-part shear interaction during composites processing," *Compos. Sci. Technol.*, vol. 63, no. 13, pp. 1985–2002, 2003.

[103] S. Clifford, N. Jansson, W. Yu, V. Michaud, and J.-A. Månson, "Thermoviscoelastic anisotropic analysis of process induced residual stresses and dimensional stability in real polymer matrix composite components," *Compos. Part A Appl. Sci. Manuf.*, vol. 37, no. 4, pp. 538–545, Apr. 2006.

[104] M. R. Wisnom, M. Gigliotti, N. Ersoy, M. Campbell, and K. D. Potter, "Mechanisms generating residual stresses and distortion during manufacture of polymer–matrix composite structures," *Compos. Part A Appl. Sci. Manuf.*, vol. 37, no. 4, pp. 522–529, Apr. 2006.

[105] G. Fernlund and A. Floyd, "Process Analysis and Tool Compensation for Curved Composite L-Angles," *Sixth Can. Compos. Conf.*, no. March, pp. 1–11, 2007.

[106] Y. Hirano, T. Mizutani, Y. Iwahori, and Y. Nagao, "AN investigation on spring-in behavior of Va-RTM composite wing structure," *ICCM Int. Conf. Compos. Mater.*, pp. 1–7, 2007.

[107] T. Sproewitz, J. Tessmer, and T. Wille, "Thermal aspects for composite structures - from manufacturing to in-service predictions," *ICAS Secr. - 26th Congr. Int. Counc. Aeronaut. Sci. 2008, ICAS 2008*, vol. 2, pp. 3032–3041, 2008.

[108] K. J. Teoh and K. T. Hsiao, "Spring-in prediction for cylindrical composite specimens

manufactured with vartm," *Int. SAMPE Tech. Conf.*, 2009.

[109] M. Gigliotti, J. Molimard, F. Jacquemin, and A. Vautrin, "Maximum curvatures of 0/90 plates under thermal stress: Modelling and experimental validation," *Compos. Sci. Technol.*, vol. 69, no. 1, pp. 93–96, Jan. 2009.

[110] K. J. Teoh and K.-T. Hsiao, "Improved dimensional infidelity of curve-shaped VARTM composite laminates using a multi-stage curing technique – Experiments and modeling," *Compos. Part A Appl. Sci. Manuf.*, vol. 42, no. 7, pp. 762–771, Jul. 2011.

[111] K. Zimmermann and B. Van Den Broucke, "Assessment of process-induced deformations and stresses in ultra thick laminates using isoparametric 3D elements," *Journal of Reinforced Plastics and Composites*, vol. 31, no. 3. pp. 163–178, 2012.

[112] T. W. K. Rohwer, E. Kappel, D. Stefaniak, "Spring-in and Warpage - Progress in Manufacturing Aspects," *Mech. Compos. Mater.*, vol. 49, no. 2, pp. 193–200, 2012.

[113] E. Kappel, D. Stefaniak, and C. Hühne, "Semi-analytical spring-in analysis to counteract CFRP manufacturing deformations by tool compensation," *28th Congr. Int. Counc. Aeronaut. Sci. 2012, ICAS 2012*, vol. 3, pp. 2124–2133, 2012.

[114] P. Causse, E. Ruiz, and F. Trochu, "Spring-in behavior of curved composites manufactured by Flexible Injection," *Compos. Part A Appl. Sci. Manuf.*, vol. 43, no. 11, pp. 1901–1913, 2012.

[115] P. Han *et al.*, "The prediction of process-induced deformation in a thermoplastic composite in support of manufacturing simulation," *Proceedings of the Institution of Mechanical Engineers, Part B: Journal of Engineering Manufacture*, vol. 227, no. 10. pp. 1417–1429, 2013.

[116] Y. Mahadik and K. Potter, "Experimental investigation into the thermoelastic spring-in of curved sandwich panels," *Compos. Part A Appl. Sci. Manuf.*, vol. 49, pp. 68–80, 2013.

[117] E. Kappel, "Spring-in of curved CFRP/foam-core sandwich structures," *Compos. Struct.*, vol. 128, pp. 155–164, 2015.

[118] L. Sorrentino and C. Bellini, "Compaction influence on spring-in of thin composite parts: Experimental and numerical results," *J. Compos. Mater.*, vol. 49, no. 17, pp. 2149–2158, 2015.

[119] K. Çinar and N. Ersoy, "Effect of fibre wrinkling to the spring-in behaviour of L-shaped composite materials," *Compos. Part A Appl. Sci. Manuf.*, vol. 69, pp. 105–114, 2015.

[120] L. Mezeix *et al.*, "Spring-back simulation of unidirectional carbon/epoxy flat laminate composite manufactured through autoclave process," *Compos. Struct.*, vol. 124, pp. 196–205, 2015.

[121] N. Li, Y. Li, X. Hao, and J. Gao, "A comparative experiment for the analysis of microwave and thermal process induced strains of carbon fiber/bismaleimide composite materials," *Compos. Sci. Technol.*, vol. 106, pp. 15–19, 2015.

[122] F. Groh, E. Kappel, C. Hühne, and F. Meyer, "Process-induced distortions of composite structures due to through-thickness fibre volume fraction gradients," *ECCM 2016 - Proceeding 17th Eur. Conf. Compos. Mater.*, vol. d, no. June, pp. 26–30, 2016.

[123] O. G. Kravchenko, S. G. Kravchenko, and R. B. Pipes, "Chemical and thermal shrinkage in thermosetting prepreg," *Compos. Part A Appl. Sci. Manuf.*, vol. 80, pp. 72–81, 2016.

[124] K. Çinar and N. Ersoy, "3D finite element model for predicting manufacturing distortions of composite parts," *J. Compos. Mater.*, vol. 50, no. 27, pp. 3791–3807, 2016.

[125] A. Ding, S. Li, J. Wang, A. Ni, L. Sun, and L. Chang, "Prediction of Process-Induced Distortions in L-Shaped Composite Profiles Using Path-Dependent Constitutive Law," *Appl. Compos. Mater.*, vol. 23, no. 5, pp. 1027–1045, 2016.

[126] Q. Wang, Z. Guan, R. Wang, H. Nie, and T. Jiang, "Numerical simulation on process-induced deformation of autoclaved V-shaped composite parts," *Proc. 2016 7th Int. Conf. Mech. Aerosp. Eng. ICMAE 2016*, pp. 23–28, 2016.

[127] O. G. Kravchenko, S. G. Kravchenko, and R. B. Pipes, "Cure history dependence of residual deformation in a thermosetting laminate," *Compos. Part A Appl. Sci. Manuf.*, vol. 99, pp. 186–197, 2017.

[128] H. Hu, S. Li, J. Wang, L. Zu, D. Cao, and Y. Zhong, "Monitoring the gelation and effective chemical shrinkage of composite curing process with a novel FBG approach," *Compos. Struct.*, vol. 176, pp. 187–194, 2017.

[129] L. Sun, J. Wang, A. Ni, S. Li, and A. Ding, "Modelling and experiment of process-induced distortions in unsymmetrical laminate plates," *Compos. Struct.*, vol. 182, no. September, pp. 524–532, 2017.

[130] B. Wucher, P. Martiny, F. Lani, T. Pardoen, C. Bailly, and D. Dumas, "Simulation-driven mold compensation strategy for composites: Experimental validation on a doubly-curved part," *Compos. Part A Appl. Sci. Manuf.*, vol. 102, pp. 96–107, 2017.

[131] M. Benavente, L. Marcin, A. Courtois, M. Lévesque, and E. Ruiz, "Numerical analysis of viscoelastic process-induced residual distortions during manufacturing and post-curing," *Compos. Part A Appl. Sci. Manuf.*, 2018.

[132] H. Wang, L. Chen, F. Ye, and J. Wang, "A multi-hierarchical successive optimization method for reduction of spring-back in autoclave forming," *Compos. Struct.*, vol. 188, no. November 2017, pp. 143–158, 2018.

[133] A. Corrado, W. Polini, L. Sorrentino, and C. Bellini, "Geometrical deviation analysis of CFRP thin laminate assemblies: Numerical and experimental results," *Compos. Sci. Technol.*, vol. 168, no. May, pp. 1–11, 2018.

[134] F. Bosi, A. Schlothauer, and S. Pellegrino, "Cure-induced deformation of ultra-thin composite laminates," *AIAA/ASCE/AHS/ASC Struct. Struct. Dyn. Mater. Conf. 2018*, no. 210049, pp. 1–10, 2018.

[135] A. Ding, J. Wang, A. Ni, and S. Li, "A new analytical solution for cure-induced spring-in of L-shaped composite parts," *Compos. Sci. Technol.*, vol. 171, no. December 2018, pp. 1–12, 2019.

[136] W. Chen and D. Zhang, "Improved prediction of residual stress induced warpage in thermoset composites using a multiscale thermo-viscoelastic processing model," *Compos. Part A Appl. Sci. Manuf.*, vol. 126, no. July, p. 105575, 2019.

[137] E. Hörberg, T. Nyman, M. Åkermo, and S. Hallström, "Thickness effect on spring-in of prepreg composite L-profiles – An experimental study," *Compos. Struct.*, vol. 209, no. August 2018, pp. 499–507, 2019.

[138] T. Gajjar, D. B. Shah, S. J. Joshi, and K. M. Patel, "Experimental and simulation investigation on spring-in deformation for L-shape component," *Curved Layer. Struct.*, vol. 6, no. 1, pp. 169–180, 2019.

[139] G. Struzziero, D. Nardi, J. Sinke, and J. J. E. Teuwen, "Cure-induced residual stresses for warpage reduction in thermoset laminates," 2020.

[140] G. C. Pereira, M. I. Yoshida, P. LeBoulluec, W. T. Lu, A. P. Alves, and A. F. Avila, "Application of artificial intelligence models for predicting time-dependent spring-back effect: The L-shape case study," *Compos. Sci. Technol.*, vol. 199, no. July, 2020.

[141] M. Al-Dhaheri, K. A. Khan, R. Umer, F. van Liempt, and W. J. Cantwell, "Process-induced deformation in U-shaped honeycomb aerospace composite structures," *Compos. Struct.*,

vol. 248, no. February, p. 112503, 2020.

[142] K. Shaker, Y. Nawab, and A. Saouab, "Experimental and numerical investigation of reduction in shape distortion for angled composite parts," *Int. J. Mater. Form.*, vol. 13, no. 6, pp. 897–906, Nov. 2020.

[143] T. Garstka, "Separation of Process Induced Distortions in Curved Composite Laminates," University of Bristol, Bristol, UK, 2005.

[144] C. K. Huang and S. Y. Yang, "Warping in advanced composite tools with varying angles and radii," *Compos. Part A Appl. Sci. Manuf.*, vol. 28, no. 9–10, pp. 891–893, Jan. 1997.

[145] L. K. Jain and Y. W. Mai, "Stresses and deformations induced during manufacturing. Part I: Theoretical analysis of composite cylinders and shells," *Journal of Composite Materials*, vol. 31, no. 7. pp. 672–695, 1997.

[146] D. Dykeman, "Minimizing uncertainty in cure modeling for composites manufacturing," *Electron. Theses Diss. 2008+*, no. March, p. 304, 2008.

[147] J. Kratz, K. Hsiao, G. Fernlund, and P. Hubert, "Thermal models for MTM45-1 and Cycom 5320 out-of-autoclave prepreg resins," *J. Compos. Mater.*, vol. 47, no. 3, pp. 341–352, 2013.

[148] A. Ding, S. Li, J. Wang, and A. Ni, "A new analytical solution for spring-in of curved composite parts," *Compos. Sci. Technol.*, vol. 142, pp. 30–40, 2017.

[149] "Plotting Data with ErrorBars and Fitting a Line." [Online]. Available: http://www.ap.smu.ca/~agolob/phys2300/blog/climate-change/. [Accessed: 15-Aug-2020].

# Appendices

## Appendix A  FARO arm for Invar Tool Scanning

The FARO arm unit was leased from a local company, CANAM Tool Inc. for the period of 1 week (July 9th – July 31st, 2019). CANAM was responsible for transportation to and from Composites Research Network. The serial number and unit tag is shown in Figure A.1

CANAM Contact:

████████████

██████████

███████████████



Figure A.1 FARO arm case tag

## Appendix B  Python Data Reduction Script

The script used for reducing L-shape specimen point clouds is described in this section. The functions and features were described in section 4.2.1. This analysis procedure was developed with assistance from Alastair McKee at Convergent Manufacturing Technologies, Inc (CMT). Sam Reid at CMT programmed the analysis procedure into a robust and user-friendly Python code.

```
In [1]:
%%javascript
IPython.OutputArea.prototype._should_scroll = function(lines) {
    return false;
}
```

```
In [2]:
import matplotlib.pyplot as plt
import numpy as np
import springInLFlange as slf

%matplotlib notebook
FIGSIZE = (9, 7)
```

```
In [3]:
# Step 1: Load all the data scans in the provided directory to a dictionary of
 dataframes

#path = C\Users\gavintao\notebooks\Convergent collaboration\demo

data = slf.loadData('demo')
```

```
In [4]:
# Step 4: Section each scan by z

trim = 5 # length in mm to trim from top and bottom of scan
numSlices = 3 # number of slices to measure spring in for each L
sections = {}

for name, df in data.items():
    sectionList = slf.getScanSections(df, numSlices, trim) # first section the
 scan
    sections[name] = sectionList
```

```
In [5]:
# Check out how the sections turned out
```

```python
for name, df in data.items():
    fig = plt.figure(figsize=FIGSIZE)
    ax = fig.add_subplot(111, projection='3d')
    sectionList = sections[name]

    ax.set_xlabel('x (mm)')
    ax.set_ylabel('y (mm)')
    ax.set_zlabel('z (mm)')
    ax.set_title(name)
    ax.axis('equal')

    ax.plot(df['x'], df['y'], df['z'], 'k.', label='Full Scan')
    for i, section in enumerate(sectionList):
        ax.plot(section['x'], section['y'], section['z'], '.', label='Section
{}'.format(i))

    ax.legend()
```

The cell below is the one that performs the actual spring in measurement. It is important that the user be aware of the following variables and behaviour, in order of appearance.

1. **TrueRadius** -- Defines the true radius of the tool in (mm)
2. **trueCornerAngle** -- Defines the true angle of the corner in degrees
3. **buffLength** -- Length beyond the identified corner which spring in measurement begins (mm)
4. **flangeFactor** -- Factor of total x length beyond and below mean x which defines the band of points used to fit a line to each flange.
5. **buffAngle** -- A buffer beyond the true angle of the corner to include as corner points (radians). Not needed if a buffLength is used.
6. **continuous** -- A flag that dictates measurement behaviour. If set to **True** the start of the vector used for the angle measurement is fixed at the buffer, and the end continuously increases in steps of **vectorLength** along the flange. If set to **False** the start and end of the vector used for the angle measurement move together, so that spring in measurements are made using vectors of constant length defined by **vectorLength**. The shifts are defined by **stepSize**
7. **vectorLength** -- Read the definition of **continuous** above.
8. **stepSize** -- Read the definition of **continuous** above. Set to 0 if **continuous** = True is used
9.

```
In [6]:
# Step 6: Measure spring-in for each section
trueRadius = 20
trueCornerAngle = 93
buffLength = 5
flangeFactor = 1/3
buffAngle = 0 * np.pi/180
continuous = True

vectorLength = 12.7
stepSize = 0

for name, df in data.items():
    sectionList = sections[name]
    sectionList = slf.getCornerOfSections(sectionList, flangeFactor)
    sectionList = slf.measureSpringIn(sectionList,
                                      continuous = True,
```

180

```
                                      buffLength = buffLength,
                                      buffAngle = buffAngle,
                                      trueRadius = trueRadius,
                                      trueAngle = trueCornerAngle,
                                      deltaLength = vectorLength,
                                      stepSize = 0)
```

In [7]:
```python
# Step 8: Average angles over all sections

meanAngles = {}
stdDevAngles = {}

for name, df in data.items():
    sectionList = sections[name]
    meanAngles[name] = slf.getAngleAverageOverSections(sectionList)
```

In [8]:
```python
# 3d plots showing corner and flange sections

cornerAngle = trueCornerAngle * np.pi / 180

for name, df in meanAngles.items():
    fig = plt.figure(figsize=FIGSIZE)
    ax = fig.add_subplot(111, projection='3d')
    sectionList = sections[name]
    for i, section in enumerate(sectionList):
        flangeSection = section.drop(section[section['angle'] <= cornerAngle /
 2 + buffAngle].index)
        cornerSection = section.drop(section[section['angle'] > cornerAngle /
2 + buffAngle].index)


        ax.plot(flangeSection['x'], flangeSection['y'], flangeSection['z'], '.
', markersize=2)
        ax.plot(cornerSection['x'], cornerSection['y'], cornerSection['z'], '.
', markersize=2, color='k')

    ax.set_title(name)
    ax.axis('equal')
    ax.set_xlabel('x (mm)')
    ax.set_ylabel('y (mm)')
```
In [9]:
```python
# 2d plots showing corner and flange sections
```

```python
cornerAngle = trueCornerAngle * np.pi / 180

for name, df in meanAngles.items():
    sectionList = sections[name]
    fig, ax = plt.subplots(figsize=FIGSIZE)
    for i, section in enumerate(sectionList):
        flangeSection = section.drop(section[section['angle'] <= cornerAngle /
 2 + buffAngle].index)
        cornerSection = section.drop(section[section['angle'] > cornerAngle /
2 + buffAngle].index)
        line = section.lines[i][0]

        ax.plot(flangeSection['x'], flangeSection['y'], '.', markersize=1)
        ax.plot(cornerSection['x'], cornerSection['y'], '.', markersize=3, col
or='k')


    ax.set_title(name)
    ax.axis('equal')
    ax.set_xlabel('x (mm)')
    ax.set_ylabel('y (mm)')

In [10]:
# deviation plots

thresh = 1
trueRadius = 20
for name, df in meanAngles.items():
    sectionList = sections[name]
    fig, ax = plt.subplots(2, 1, figsize=FIGSIZE)
    for i, section in enumerate(sectionList):
        s = section.loc[section['angle'] >= cornerAngle / 2 + buffAngle]

        flange1 = s.drop(s[s['y'] < section.radiusCentreY].index)
        flange1['distance'] = np.sqrt((flange1['x'] - flange1['x'].loc[flange1
['angle'].idxmin()])**2 +
                                      (flange1['y'] - flange1['y'].loc
[flange1['angle'].idxmin()])**2)

        flange2 = s.drop(s[s['y'] > section.radiusCentreY].index)
        flange2['distance'] = np.sqrt((flange2['x'] - flange2['x'].loc[flange2
['angle'].idxmin()])**2 +
```

```python
                                                   (flange2['y'] - flange2['y'].loc
[flange2['angle'].idxmin()])**2)

        ax[1].plot(flange1['distance'], flange1['deviation1'] * 10**3 , '.', m
arkersize = 1, label = "Section {}".format(i))

        ax[0].plot(flange2['distance'], flange2['deviation2'] * 10**3 , '.', m
arkersize = 1, label = "Section {}".format(i))

    ax[0].axhline(y=0, xmin=0, xmax=1, linestyle='dashed', color='k')
    ax[1].axhline(y=0, xmin=0, xmax=1, linestyle='dashed', color='k')

    ax[0].set_title(name)

    ax[0].set_xlabel("Distance Along Flange (mm)")
    ax[0].set_ylabel("Deviation ($\mu$m)")

    ax[1].set_xlabel("Distance Along Flange (mm)")
    ax[1].set_ylabel("Deviation ($\mu$m)")

plt.show()


In [11]:
# spring in plots, each section separated

for name, df in meanAngles.items():
    sectionList = sections[name]
    fig, ax = plt.subplots(figsize=FIGSIZE)
    for i, section in enumerate(sectionList):
        ax.errorbar(section.positions, section.angles, section.uncertainties,
marker='.', linestyle='solid', capsize=5, label = "Section {}".format(i))

    ax.set_title(name)
    ax.set_xlabel("Distance Along Flange (mm)")
    ax.set_ylabel("Spring-in Angle (°)")
    ax.set_ylim(bottom = 0, top = 2.5)
    ax.set_xlim(left = 0, right = 180)
    ax.legend()
plt.show()



In [12]:
# spring in plots, each section averaged
```

183

```python
for name, df in meanAngles.items():
    fig, ax = plt.subplots(figsize=FIGSIZE)
    ax.errorbar(df['positions'], df['angles'], df['std devs'], marker='.', lin
estyle='solid', capsize=5, label = name)
    ax.set_title(name)
    ax.set_xlabel("Distance Along Flange (mm)")
    ax.set_ylabel("Spring-in Angle (°)")
    ax.set_ylim(bottom = 0, top = 2.5)
    ax.legend()
plt.show()
```

In [15]:
```python
# spring in plots combined

fig, ax = plt.subplots(figsize=FIGSIZE)
for name, df in meanAngles.items():
    ax.errorbar(df['positions'], df['angles'], df['std devs'], marker='.', lin
estyle='solid', capsize=5, label = name)
    #ax.plot(df['positions'], df['angles'], marker='.', linestyle='solid', lab
el = name)


ax.set_xlabel("Distance Along Flange (mm)", fontsize=18)
ax.set_ylabel("Nominal Spring-in Angle (°)", fontsize=18)
ax.set_ylim(bottom = 0, top = 2.5)
ax.set_xlim(left = 0, right = 180)
plt.xticks(fontsize=16)
plt.yticks(fontsize=16)
ax.legend(fontsize=16)
plt.show()
```

In [14]:
```python
for name, df in meanAngles.items():
    with open("{}.csv".format(name), "w") as f:
        f.write("Positions (mm), Angles (Deg), Std Devs\n")
        for i in range(len(df)):
            f.write("{}, {}, {}\n".format(df["positions"].iloc[i], df["angles
"].iloc[i], df["std devs"].iloc[i]))

        f.close()
```

The following script utilizes an OLS fit function [149] which determines the spring-in slope of the previous Python outputs. This script intakes the spring-in results and errors from the previous script

and output a linear best fit line with slope and intersection errors. The slope were representations of specimen flange warpage as explained in section 0. The slopes and errors were plotted in Chapter 4:. This code is written by author.

```python
import numpy as np
import matplotlib.pyplot as plt
import glob
from pathlib import Path
%matplotlib inline
```

In [1]:
```python
def OLSfit(x, y, dy=None):
    """Find the best fitting parameters of a linear fit to the data through the
    method of ordinary least squares estimation. (i.e. find m and b for
    y = m*x + b)

    Args:
        x: Numpy array of independent variable data
        y: Numpy array of dependent variable data. Must have same size as x.
        dy: Numpy array of dependent variable standard deviations. Must be same
            size as y.

    Returns: A list with four floating point values. [m, dm, b, db]
    """
    if dy is None:
        #if no error bars, weight every point the same
        dy = np.ones(x.size)
    denom = np.sum(1 / dy**2) * np.sum((x / dy)**2) - (np.sum(x / dy**2))**2
    m = (np.sum(1 / dy**2) * np.sum(x * y / dy**2) -
        np.sum(x / dy**2) * np.sum(y / dy**2)) / denom
    b = (np.sum(x**2 / dy**2) * np.sum(y / dy**2) -
        np.sum(x / dy**2) * np.sum(x * y / dy**2)) / denom
    dm = np.sqrt(np.sum(1 / dy**2) / denom)
    db = np.sqrt(np.sum(x / dy**2) / denom)
    return([m, dm, b, db])
```

```python
with open("WarpageValues.csv", "w") as f:
    for file_name in glob.glob(r"C:\Users\gavintao\notebooks\Convergent coll
aboration\sam\*.csv"):

        data = np.genfromtxt(file_name,delimiter=',',skip_header=1)

        Position = data[:,0]
        SpringInAngle = data[:,1]
        StDev_SpringInAngle = data[:,2]

        plt.errorbar(Position,SpringInAngle,yerr=StDev_SpringInAngle,fmt='o',
ms=5,color='black',alpha=0.75)
        plt.gcf().set_size_inches(15,10) # This sets the size of the plot
        plt.ylim(0,2.5) # This sets the range of the x-axis
        plt.xlim(0,180) # This sets the range of the y-axis
        plt.grid(True) # This toggles whether gridlines are displayed
        plt.xlabel('Distance along flange (mm)',fontsize=16)
        plt.ylabel('Nominal Spring-in Angle (degree)',fontsize=16)

        bestfit = OLSfit(Position,SpringInAngle,StDev_SpringInAngle)
        print (SpecimenName)
        print(bestfit)
        slope = bestfit[0]
        intercept = bestfit[2]
        SpecimenName=(Path(file_name).stem)

        f.write("{}, {}, {}, {}, {}\n". format(SpecimenName, bestfit[0], bestf
it[1], bestfit[2],bestfit[3]))
```

# Appendix C  L-shaped Specimen Thickness Measurements

The complete thickness measurement for all specimens fabricated in this study is presented in this section. All measurements are in mm. The location for thickness measurements are shown in Figure 4.18. Note the specimens are arranged by flange length. Average values across the width of L-shape is reported.

| | Bottom Flange | | | | | | | | Top Flange | | | | | | |
|---|---|---|---|---|---|---|---|---|---|---|---|---|---|---|---|
| **L34** | 2.92 | 2.949 | 2.98 | 2.989 | 2.967 | 2.985 | 2.957 | Middle | 2.955 | 2.969 | 2.989 | 2.977 | 2.979 | 2.981 | 2.918 |
| | 2.881 | 2.944 | 2.982 | 2.979 | 2.942 | 2.977 | 2.992 | | 2.997 | 2.999 | 2.976 | 2.966 | 2.949 | 2.959 | 2.903 |
| | 2.909 | 2.989 | 2.974 | 2.98 | 2.974 | 2.986 | 3.009 | | 3.043 | 2.991 | 3.017 | 2.978 | 2.941 | 2.979 | 2.922 |
| | 2.915 | 2.977 | 2.965 | 2.981 | 2.968 | 3.03 | 2.982 | | 3.01 | 2.999 | 2.986 | 2.998 | 2.955 | 2.957 | 2.929 |
| Average | 2.9063 | 2.9648 | 2.9753 | 2.9823 | 2.9628 | 2.9945 | 2.985 | | 3.0013 | 2.9865 | 2.9905 | 2.9798 | 2.9545 | 2.9675 | 2.918 |
| | Bottom Flange | | | | | | | | Top Flange | | | | | | |
| **L46** | 2.928 | 2.919 | 3.001 | 2.965 | 2.951 | 2.969 | 2.997 | Middle | 3.007 | 3.002 | 2.982 | 2.959 | 2.949 | 2.969 | 2.902 |
| | 2.917 | 2.957 | 2.989 | 2.97 | 2.971 | 2.984 | 3.005 | | 2.999 | 2.989 | 2.975 | 2.997 | 3.005 | 2.984 | 2.907 |
| | 2.909 | 2.971 | 2.995 | 3.009 | 2.96 | 2.976 | 3.005 | | 3.01 | 3.006 | 2.969 | 3.015 | 2.976 | 2.977 | 2.919 |
| | 2.924 | 2.978 | 3.032 | 2.989 | 3.003 | 3.014 | 3.014 | | 3.004 | 3.012 | 2.997 | 2.971 | 2.992 | 2.994 | 2.959 |
| Average | 2.918 | 2.9563 | 3.0028 | 2.9818 | 2.9713 | 2.9843 | 3.0053 | | 3.005 | 3.0023 | 2.9793 | 2.9855 | 2.9805 | 2.981 | 2.9203 |
| | Bottom Flange | | | | | | | | Top Flange | | | | | | |
| **L30** | 2.838 | 2.978 | 2.959 | 2.979 | 2.949 | 2.932 | 2.976 | Middle | 2.905 | 2.952 | 2.948 | 2.972 | 2.958 | 2.937 | 2.834 |
| | 2.826 | 3.001 | 2.977 | 2.998 | 2.99 | 3.012 | 3.017 | | 3.025 | 2.99 | 2.976 | 2.996 | 2.991 | 3.004 | 2.894 |
| | 2.761 | 2.995 | 2.981 | 2.982 | 2.976 | 3.018 | 3.029 | | 3.023 | 3.001 | 3.019 | 2.986 | 2.989 | 2.991 | 2.891 |
| | 2.794 | 2.967 | 2.942 | 2.982 | 2.986 | 2.981 | 3.028 | | 2.99 | 2.985 | 3.009 | 3 | 2.99 | 2.982 | 2.895 |
| Average | 2.8048 | 2.9853 | 2.9648 | 2.9853 | 2.9738 | 2.9858 | 3.0125 | | 2.9858 | 2.982 | 2.988 | 2.9885 | 2.982 | 2.9785 | 2.8785 |
| | Bottom Flange | | | | | | | | Top Flange | | | | | | |
| **L38** | 2.923 | 2.949 | 2.964 | 2.929 | 3.011 | 2.964 | 2.921 | Middle | 2.999 | 2.966 | 2.946 | 2.978 | 2.979 | 2.941 | 2.913 |
| | 2.885 | 2.976 | 2.96 | 2.947 | 2.99 | 2.993 | 2.968 | | 2.997 | 2.993 | 2.976 | 2.966 | 2.949 | 2.959 | 2.903 |
| | 2.9 | 2.945 | 2.945 | 2.934 | 2.963 | 2.954 | 2.958 | | 2.997 | 2.952 | 2.982 | 2.958 | 2.972 | 2.971 | 2.91 |
| | 2.955 | 2.997 | 2.992 | 2.99 | 3.025 | 3 | 3.003 | | 3.016 | 2.966 | 2.987 | 2.961 | 2.979 | 2.98 | 2.928 |
| Average | 2.9158 | 2.9668 | 2.9653 | 2.95 | 2.9973 | 2.9778 | 2.9625 | | 3.0023 | 2.9693 | 2.9728 | 2.9658 | 2.9683 | 2.9628 | 2.9135 |
| | Bottom Flange | | | | | | | | Top Flange | | | | | | |
| **L62** | 2.879 | 2.949 | 2.976 | 2.978 | 2.981 | 2.997 | 3.008 | Middle | 2.979 | 3.006 | 3.027 | 2.99 | 2.987 | 2.986 | 2.94 |
| | 2.881 | 2.944 | 2.982 | 2.979 | 2.942 | 2.977 | 2.992 | | 2.997 | 2.999 | 2.976 | 2.966 | 2.949 | 2.959 | 2.903 |
| | 2.909 | 2.98 | 2.992 | 2.963 | 3.007 | 3.004 | 3.038 | | 3.021 | 2.976 | 2.988 | 2.978 | 2.98 | 2.977 | 2.901 |
| | 2.91 | 2.969 | 2.958 | 2.968 | 2.988 | 3.003 | 2.987 | | 3.012 | 2.992 | 3.019 | 2.968 | 2.971 | 2.979 | 2.955 |
| Average | 2.8933 | 2.959 | 2.977 | 2.972 | 2.9795 | 2.9953 | 3.0063 | | 3.0023 | 2.9918 | 3.0025 | 2.9755 | 2.9718 | 2.9753 | 2.9248 |
| | Bottom Flange | | | | | | | | Top Flange | | | | | | |
| **L58** | 2.925 | 2.991 | 2.948 | 2.932 | 2.968 | 2.965 | 2.948 | Middle | 2.972 | 2.93 | 2.951 | 2.974 | 2.968 | 2.931 | 2.905 |
| | 2.893 | 2.961 | 2.973 | 3.024 | 2.955 | 2.964 | 3.019 | | 3.01 | 2.956 | 2.965 | 2.99 | 2.98 | 2.955 | 2.89 |
| | 2.886 | 2.984 | 2.975 | 2.932 | 2.961 | 2.962 | 2.979 | | 2.988 | 2.949 | 2.969 | 2.934 | 2.984 | 2.932 | 2.925 |
| | 2.898 | 2.996 | 2.983 | 2.958 | 2.981 | 3.012 | 2.997 | | 2.996 | 2.94 | 2.931 | 2.985 | 2.99 | 2.967 | 2.94 |
| Average | 2.9005 | 2.983 | 2.9698 | 2.9615 | 2.9663 | 2.9758 | 2.9858 | | 2.9915 | 2.9438 | 2.954 | 2.9708 | 2.9805 | 2.9463 | 2.915 |
| | Bottom Flange | | | | | | | | Top Flange | | | | | | |
| **L15** | | | | | | | | Middle | 2.9464 | 2.921 | 2.921 | 2.921 | 2.9464 | 2.9464 | 2.921 |
| | | | | | | | | | 2.9718 | 2.9464 | 2.9464 | 2.9718 | 2.9531 | 2.9464 | 2.921 |
| | | | | | | | | | 2.9718 | 2.9464 | 2.9464 | 2.9464 | 2.921 | 2.921 | 2.8956 |
| | | | | cut away for microscopy | | | | | 2.921 | 2.921 | 2.8956 | 2.921 | 2.8702 | 2.8702 | 2.8702 |
| Average | #DIV/0! | #DIV/0! | #DIV/0! | #DIV/0! | #DIV/0! | #DIV/0! | #DIV/0! | | 2.9528 | 2.9337 | 2.9274 | 2.9401 | 2.9242 | 2.921 | 2.902 |
| | Bottom Flange | | | | | | | | Top Flange | | | | | | |
| **L6** | 1.4478 | 1.4478 | 1.4732 | 1.4732 | 1.4859 | 1.4732 | 1.4986 | Middle | 1.4986 | 1.4732 | 1.4732 | 1.4605 | 1.4478 | 1.4478 | 1.4224 |
| | 1.4732 | 1.4986 | 1.4986 | 1.4986 | 1.4986 | 1.4986 | 1.5494 | | 1.524 | 1.4986 | 1.4986 | 1.4986 | 1.4986 | 1.4732 | 1.4478 |
| | 1.4859 | 1.4986 | 1.4986 | 1.5113 | 1.5113 | 1.524 | 1.6002 | | 1.5494 | 1.524 | 1.4986 | 1.4986 | 1.4732 | 1.4732 | 1.4478 |
| | 1.4478 | 1.4986 | 1.4986 | 1.4986 | 1.5113 | 1.524 | 1.5748 | | 1.524 | 1.4986 | 1.4986 | 1.4986 | 1.4732 | 1.4478 | 1.4224 |
| Average | 1.4637 | 1.4859 | 1.4923 | 1.4954 | 1.5018 | 1.505 | 1.5558 | | 1.524 | 1.4986 | 1.4923 | 1.4891 | 1.4732 | 1.4605 | 1.4351 |
| | Bottom Flange | | | | | | | | Top Flange | | | | | | |
| **L13** | 1.4986 | 1.4986 | 1.4986 | 1.4986 | 1.4986 | 1.4986 | 1.524 | Middle | 1.524 | 1.4986 | 1.4732 | 1.4732 | 1.4732 | 1.4478 | 1.4478 |
| | 1.524 | 1.4986 | 1.524 | 1.524 | 1.524 | 1.524 | 1.5494 | | 1.5494 | 1.4986 | 1.524 | 1.4986 | 1.524 | 1.4986 | 1.4732 |
| | 1.4478 | 1.4986 | 1.4986 | 1.4986 | 1.4986 | 1.524 | 1.5748 | | 1.5494 | 1.524 | 1.524 | 1.4986 | 1.4986 | 1.4986 | 1.4732 |
| | 1.4478 | 1.4732 | 1.4986 | 1.4986 | 1.4986 | 1.4986 | 1.524 | | 1.4986 | 1.4986 | 1.4986 | 1.4732 | 1.4986 | 1.4986 | 1.4986 |
| Average | 1.4796 | 1.4923 | 1.505 | 1.505 | 1.505 | 1.5113 | 1.5431 | | 1.5304 | 1.505 | 1.505 | 1.4859 | 1.4986 | 1.4859 | 1.4732 |

| | Bottom Flange | | | | | | | Middle | Top Flange | | | | | | |
|---|---|---|---|---|---|---|---|---|---|---|---|---|---|---|---|
| L21 | 2.8956 | 2.321 | 2.3718 | 2.321 | 2.321 | 2.3464 | 2.3464 | Middle | 2.3718 | 2.3718 | 2.3718 | 2.321 | 2.3718 | 2.321 | 2.8702 |
| | 2.321 | 2.3464 | 2.3718 | 2.3718 | 2.3464 | 2.3718 | 2.3718 | | 3.0226 | 2.3718 | 2.3718 | 2.3718 | 2.3464 | 2.321 | 2.8702 |
| | 2.321 | 2.3464 | 2.3372 | 2.3718 | 2.3464 | 2.3718 | 3.0226 | | 3.0226 | 2.3372 | 2.3718 | 2.3464 | 2.3464 | 2.3464 | 2.8702 |
| | 2.8956 | 2.321 | 2.3464 | 2.3718 | 2.3464 | 2.3718 | 2.3718 | | 2.3372 | 2.3464 | 2.3464 | 2.3464 | 2.3464 | 2.9083 | 2.8194 |
| Average | 2.9083 | 2.3337 | 2.3718 | 2.3531 | 2.3401 | 2.3655 | 2.3782 | | 3.0036 | 2.3718 | 2.3655 | 2.3464 | 2.3528 | 2.3242 | 2.8575 |
| L22 | 1.4224 | 1.4732 | 1.4986 | 1.4986 | 1.4986 | 1.4986 | 1.4986 | Middle | 1.4986 | 1.4986 | 1.4986 | 1.4986 | 1.4732 | 1.4986 | 1.397 |
| | 1.4224 | 1.4732 | 1.4986 | 1.524 | 1.4986 | 1.4986 | 1.524 | | 1.524 | 1.4986 | 1.4986 | 1.4986 | 1.4859 | 1.4478 | 1.3716 |
| | 1.4732 | 1.4986 | 1.4986 | 1.524 | 1.5113 | 1.524 | 1.524 | | 1.524 | 1.4986 | 1.524 | 1.4986 | 1.4986 | 1.4859 | 1.3716 |
| | 1.4224 | 1.4732 | 1.4732 | 1.4732 | 1.4986 | 1.4986 | 1.4986 | | 1.524 | 1.524 | 1.4986 | 1.4859 | 14.859 | 1.4732 | 1.3716 |
| Average | 1.4351 | 1.4796 | 1.4923 | 1.505 | 1.5018 | 1.505 | 1.5113 | | 1.5177 | 1.505 | 1.505 | 1.4954 | 4.8292 | 1.4764 | 1.378 |
| L1 | 2.321 | 2.3464 | 2.321 | 2.3464 | 2.3718 | 2.321 | 2.3718 | Middle | 2.3372 | 2.3845 | 2.3845 | 2.3718 | 2.3464 | 2.3718 | 2.8956 |
| | 2.321 | 2.3718 | 2.3464 | 2.3531 | 2.3464 | 2.3464 | 2.3372 | | 3.0099 | 2.3372 | 2.3372 | 2.3845 | 2.3718 | 2.3718 | 2.321 |
| | 2.321 | 2.3718 | 2.3718 | 2.3464 | 2.3718 | 2.3718 | 2.3372 | | 2.3372 | 2.3372 | 2.3718 | 2.3718 | 2.3718 | 2.3372 | 2.321 |
| | 2.8956 | 2.3464 | 2.3464 | 2.3464 | 2.321 | 2.3464 | 2.3464 | | 2.3718 | 2.3718 | 2.3718 | 2.3718 | 2.321 | 2.3718 | 2.8956 |
| Average | 2.3147 | 2.3591 | 2.3464 | 2.3496 | 2.3528 | 2.3464 | 2.3782 | | 2.394 | 2.3877 | 2.3813 | 2.375 | 2.3528 | 2.3782 | 2.3083 |
| L24 | | | 1.3208 | 1.4986 | 1.4732 | 1.4986 | 1.524 | Middle | 1.4986 | 1.4986 | 1.4986 | 1.4986 | 1.3208 | | |
| | | | 1.3462 | 1.4732 | 1.4986 | 1.524 | 1.5434 | | 1.524 | 1.4986 | 1.4986 | 1.4986 | 1.4732 | | |
| | | | 1.2954 | 1.4986 | 1.4986 | 1.524 | 1.5434 | | 1.5434 | 1.524 | 1.4986 | 1.4986 | 1.3462 | | |
| | | | 1.3716 | 1.4478 | 1.4478 | 1.4986 | 1.524 | | 1.4986 | 1.4732 | 1.4732 | 1.3462 | 1.2954 | | |
| Average | | | 1.3335 | 1.4796 | 1.4796 | 1.5113 | 1.5367 | | 1.5177 | 1.4986 | 1.4923 | 1.4605 | 1.3589 | | |
| L14 | | | 2.8956 | 2.321 | 2.3718 | 2.3464 | 2.3464 | Middle | 2.3464 | 2.3718 | 2.321 | 2.3464 | 2.8956 | | |
| | | | 2.321 | 2.3464 | 2.3464 | 2.3718 | 2.3372 | | 2.3372 | 2.3464 | 2.3464 | 2.321 | 2.8702 | | |
| | | | 2.321 | 2.3718 | 2.3718 | 2.3718 | 2.3372 | | 2.3372 | 2.3718 | 2.3464 | 2.3464 | 2.8956 | | |
| | | | 2.8702 | 2.8956 | 2.321 | 2.321 | 2.3464 | | 0.4064 | 2.3464 | 2.321 | 2.8702 | 2.794 | | |
| Average | | | 2.902 | 2.3337 | 2.3528 | 2.3528 | 2.3718 | | 2.3368 | 2.3591 | 2.3337 | 2.321 | 2.8639 | | |
| L16 | | | 1.3716 | 1.4732 | 1.4986 | 1.4478 | 1.4986 | Middle | 1.4732 | 1.4732 | 1.4986 | 1.3208 | 1.2954 | | |
| | | | 1.3462 | 1.3462 | 1.524 | 1.4986 | 1.524 | | 1.524 | 1.4986 | 1.4986 | 1.4732 | 1.397 | | |
| | | | 1.3716 | 1.4605 | 1.4986 | 1.524 | 1.524 | | 1.4986 | 1.4986 | 1.4986 | 1.4732 | 1.397 | | |
| | | | 1.3716 | 1.3208 | 1.4986 | 1.4478 | 1.4986 | | 1.4986 | 1.4732 | 1.4986 | 1.4478 | 1.2954 | | |
| Average | | | 1.3653 | 1.4002 | 1.505 | 1.4796 | 1.5113 | | 1.4986 | 1.4859 | 1.4986 | 1.4288 | 1.3462 | | |
| L7 | | | 1.4732 | 1.4732 | 1.4478 | 1.4732 | 1.4986 | Middle | 1.4732 | 1.4986 | 1.4986 | 1.4986 | 1.4732 | | |
| | | | 1.4986 | 1.4986 | 1.4986 | 1.4986 | 1.4986 | | 1.5113 | 1.4986 | 1.4986 | 1.4986 | 1.4732 | | |
| | | | 1.4732 | 1.4986 | 1.4986 | 1.524 | 1.4986 | | 1.524 | 1.4986 | 1.4986 | 1.4986 | 1.4986 | | |
| | | | 1.4732 | 1.4986 | 1.4986 | 1.4986 | 1.524 | | 1.4986 | 1.4986 | 1.4859 | 1.4732 | 1.4478 | | |
| Average | | | 1.4796 | 1.4923 | 1.4859 | 1.4986 | 1.505 | | 1.5018 | 1.4986 | 1.4954 | 1.4923 | 1.4732 | | |
| L23 | | | 2.321 | 2.321 | 2.321 | 2.3718 | 2.321 | Middle | 2.3464 | 2.321 | 2.321 | 2.8956 | 2.8956 | | |
| | | | 2.3464 | 2.3464 | 2.3372 | 2.3464 | 2.3718 | | 2.3372 | 2.3464 | 2.3464 | 2.8956 | 2.321 | | |
| | | | 2.321 | 2.321 | 2.3464 | 2.3718 | 2.3718 | | 2.3372 | 2.3718 | 2.321 | 2.8956 | 2.8702 | | |
| | | | 2.321 | 2.8956 | 2.321 | 2.321 | 2.321 | | 2.3464 | 2.3464 | 2.321 | 2.8956 | 2.8702 | | |
| Average | | | 2.3274 | 2.321 | 2.3464 | 2.3528 | 2.3464 | | 2.3718 | 2.3464 | 2.3274 | 2.8956 | 2.8893 | | |
| L8 | | | 2.8702 | 2.8956 | 2.321 | 2.8956 | 2.321 | Middle | 2.321 | 2.321 | 2.3464 | 2.3464 | 2.8956 | | |
| | | | 2.8956 | 2.321 | 2.321 | 2.3464 | 2.3718 | | 2.3464 | 2.3464 | 2.3464 | 2.3464 | 2.321 | | |
| | | | 2.8956 | 2.9083 | 2.8956 | 2.321 | 2.3718 | | 2.321 | 2.3464 | 2.321 | 2.321 | 2.321 | | |
| | | | 2.321 | 2.8956 | 2.321 | 2.321 | 2.3718 | | 2.321 | 2.3464 | 2.321 | 2.321 | 2.8702 | | |
| Average | | | 2.8956 | 2.9051 | 2.3147 | 2.321 | 2.3591 | | 2.3274 | 2.3401 | 2.3337 | 2.3337 | 2.902 | | |
| L32 | | | 2.308 | 2.328 | 2.334 | 2.363 | 2.355 | Middle | 2.371 | 2.353 | 2.36 | 2.324 | 2.886 | | |
| | | | 2.895 | 2.983 | 2.965 | 3.028 | 3.035 | | 3.027 | 2.96 | 2.996 | 2.99 | 2.928 | | |
| | | | 2.929 | 2.996 | 2.99 | 2.99 | 3.037 | | 3.019 | 3.009 | 2.985 | 2.966 | 2.921 | | |
| | | | 2.897 | 2.94 | 2.918 | 2.909 | 2.892 | | 2.904 | 2.911 | 2.912 | 2.932 | 2.866 | | |
| Average | | | 2.9073 | 2.9618 | 2.9518 | 2.974 | 2.9798 | | 2.9803 | 2.9583 | 2.9633 | 2.953 | 2.9003 | | |
| L18 | | | | | 1.27 | 1.4478 | 1.4732 | Middle | 1.4732 | 1.4478 | 1.4224 | | | | |
| | | | | | 1.4478 | 1.4986 | 1.524 | | 1.4986 | 1.524 | 1.4478 | | | | |
| | | | | | 1.4478 | 1.524 | 1.5367 | | 1.524 | 1.5113 | 1.4478 | | | | |
| | | | | | 1.4478 | 1.4478 | 1.4732 | | 1.524 | 1.4732 | 1.4224 | | | | |
| Average | | | | | 1.4034 | 1.4796 | 1.5018 | | 1.505 | 1.4891 | 1.4351 | | | | |

188

| | Bottom Flange | | | | Top Flange | | |
|---|---|---|---|---|---|---|---|
| | | | | | | | |
| L19 | 2.8956 | 2.9972 | 2.9972 | Middle | 2.9718 | 2.9972 | 2.921 |
| | 2.8956 | 2.9718 | 3.0099 | | 3.0226 | 2.9718 | 2.8956 |
| | 2.921 | 2.9718 | 2.9718 | | 2.9972 | 2.9718 | 2.8956 |
| | 2.8448 | 2.921 | 2.9464 | | 2.9718 | 2.9464 | 2.8956 |
| Average | 2.8893 | 2.9655 | 2.9813 | | 2.9909 | 2.9718 | 2.902 |
| | Bottom Flange | | | | Top Flange | | |
| L4 | 2.9464 | 2.9718 | 3.0226 | Middle | 2.9972 | 2.9972 | 2.921 |
| | 2.921 | 2.9972 | 3.0226 | | 3.0226 | 2.9718 | 2.8956 |
| | 2.9464 | 2.9718 | 3.0226 | | 2.9972 | 2.9464 | 2.921 |
| | 2.9718 | 2.9718 | 2.9972 | | 2.9972 | 3.0226 | 2.9464 |
| Average | 2.9464 | 2.9782 | 3.0163 | | 3.0036 | 2.9845 | 2.921 |
| | Bottom Flange | | | | Top Flange | | |
| L9 | 2.8956 | 2.9718 | 3.0226 | Middle | 2.9972 | 2.9972 | 2.9464 |
| | 2.8956 | 2.9718 | 3.048 | | 2.9972 | 2.9972 | 2.8956 |
| | 2.8956 | 2.9718 | 3.0226 | | 3.0226 | 2.9718 | 2.8956 |
| | 2.8956 | 2.9718 | 2.9718 | | 2.9718 | 2.9464 | 2.8956 |
| Average | 2.8956 | 2.9718 | 3.0163 | | 2.9972 | 2.9782 | 2.9083 |
| | Bottom Flange | | | | Top Flange | | |
| L3 | 1.4732 | 1.4986 | 1.4732 | Middle | 1.4986 | 1.4732 | 1.4478 |
| | 1.4986 | 1.524 | 1.524 | | 1.524 | 1.4986 | 1.4478 |
| | 1.4732 | 1.4986 | 1.524 | | 1.524 | 1.4986 | 1.4732 |
| | 1.4732 | 1.4986 | 1.4986 | | 1.5113 | 1.4986 | 1.4732 |
| Average | 1.4796 | 1.505 | 1.505 | | 1.5145 | 1.4923 | 1.4605 |
| | Bottom Flange | | | | Top Flange | | |
| L5 | 2.8702 | 2.9464 | 2.9464 | Middle | 2.9972 | 2.9972 | 2.9464 |
| | 2.8956 | 2.9464 | 2.9972 | | 2.9972 | 2.9718 | 2.921 |
| | 2.8956 | 2.9718 | 2.9972 | | 3.0226 | 2.9972 | 2.921 |
| | 2.8956 | 2.9718 | 2.9972 | | 2.9718 | 2.9718 | 2.9464 |
| Average | 2.8893 | 2.9591 | 2.9845 | | 2.9972 | 2.9845 | 2.9337 |
| | Bottom Flange | | | | Top Flange | | |
| L10 | 2.9718 | 2.9972 | 2.9972 | Middle | 2.9718 | 2.9464 | 2.8956 |
| | 2.921 | 2.9718 | 2.9718 | | 2.9718 | 2.9972 | 2.8956 |
| | 2.921 | 2.9718 | 2.9718 | | 2.9718 | 2.9718 | 2.8702 |
| | 2.9464 | 2.9464 | 2.921 | | 2.9464 | 2.9718 | 2.8956 |
| Average | 2.9401 | 2.9718 | 2.9655 | | 2.9655 | 2.9718 | 2.8893 |
| | Bottom Flange | | | | Top Flange | | |
| L20 | 2.8956 | 2.9464 | 2.9464 | Middle | 2.9464 | 2.9464 | 2.8956 |
| | 2.8956 | 2.9464 | 2.9972 | | 2.9972 | 2.9718 | 2.9464 |
| | 2.8702 | 2.9718 | 2.9972 | | 2.9718 | 2.9464 | 2.921 |
| | 2.8702 | 2.9464 | 2.921 | | 2.8956 | 2.921 | 2.921 |
| Average | 2.8829 | 2.9528 | 2.9655 | | 2.9528 | 2.9464 | 2.921 |
| | Bottom Flange | | | | Top Flange | | |
| L11 | 1.4224 | 1.4986 | 1.524 | Middle | 1.4986 | 1.4986 | 1.4605 |
| | 1.4478 | 1.4732 | 1.4986 | | 1.4986 | 1.4986 | 1.4732 |
| | 1.4478 | 1.524 | 1.524 | | 1.4986 | 1.4986 | 1.4478 |
| | 1.4478 | 1.4986 | 1.4986 | | 1.4986 | 1.4478 | 1.4478 |
| Average | 1.4415 | 1.4986 | 1.5113 | | 1.4986 | 1.4859 | 1.4573 |
| | Bottom Flange | | | | Top Flange | | |
| L29 | 2.767 | 2.851 | 2.867 | Middle | 2.861 | 2.864 | 2.842 |
| | 2.828 | 2.972 | 2.988 | | 2.992 | 2.991 | 2.899 |
| | 2.854 | 2.977 | 2.993 | | 2.991 | 2.989 | 2.864 |
| | 2.861 | 2.916 | 2.903 | | 2.946 | 2.927 | 2.985 |
| Average | 2.8275 | 2.929 | 2.9378 | | 2.9475 | 2.9428 | 2.8975 |
| | Bottom Flange | | | | Top Flange | | |
| L64 | 2.944 | 2.995 | 3.004 | Middle | 2.975 | 2.952 | 2.903 |
| | 2.904 | 2.977 | 3.013 | | 3.011 | 2.949 | 2.891 |
| | 2.94 | 2.987 | 3.018 | | 3.001 | 2.96 | 2.905 |
| | 2.913 | 2.97 | 3.021 | | 3.005 | 2.983 | 2.93 |
| Average | 2.9253 | 2.9823 | 3.014 | | 2.998 | 2.961 | 2.9073 |
| | Bottom Flange | | | | Top Flange | | |
| L48 | 2.372 | 3.021 | 3.004 | Middle | 3.013 | 3.006 | 2.971 |
| | 2.924 | 2.997 | 3.003 | | 3.003 | 2.976 | 2.917 |
| | 2.94 | 2.988 | 3.019 | | 3.01 | 2.956 | 2.903 |
| | 2.986 | 2.981 | 3.004 | | 2.971 | 2.968 | 2.938 |
| Average | 2.9555 | 2.9968 | 3.0075 | | 2.9993 | 2.9765 | 2.9323 |

| | | | | | Bottom Flange | | | | | Top Flange | | | | | |
|---|---|---|---|---|---|---|---|---|---|---|---|---|---|---|---|---|
| L40 | | | | | 2.92 | 2.979 | 2.955 | Middle | 3.006 | 2.977 | 2.931 | | | | |
| | | | | | 2.883 | 2.977 | 2.972 | | 2.934 | 2.968 | 2.882 | | | | |
| | | | | | 2.893 | 2.984 | 2.996 | | 3.015 | 2.965 | 2.897 | | | | |
| | | | | | 2.92 | 2.971 | 2.965 | | 2.969 | 2.963 | 2.943 | | | | |
| Average | | | | | 2.904 | 2.9778 | 2.972 | | 2.996 | 2.9683 | 2.9133 | | | | |
| L60 | | | | | Bottom Flange | | | | | Top Flange | | | | | |
| | | | | | 2.921 | 2.978 | 2.984 | Middle | 2.956 | 2.952 | 2.916 | | | | |
| | | | | | 2.895 | 2.977 | 3 | | 2.935 | 2.941 | 2.89 | | | | |
| | | | | | 2.883 | 2.958 | 2.975 | | 2.967 | 2.94 | 2.859 | | | | |
| | | | | | 2.935 | 2.942 | 2.924 | | 2.924 | 2.895 | 2.874 | | | | |
| Average | | | | | 2.91 | 2.9638 | 2.9708 | | 2.9605 | 2.932 | 2.8848 | | | | |
| L36 | | | | | Bottom Flange | | | | | Top Flange | | | | | |
| | | | | | 2.921 | 2.956 | 2.958 | Middle | 2.976 | 2.994 | 2.942 | | | | |
| | | | | | 2.937 | 3.021 | 3.034 | | 3.052 | 3.006 | 2.961 | | | | |
| | | | | | 2.939 | 3.004 | 3.073 | | 3.04 | 3 | 2.917 | | | | |
| | | | | | 2.929 | 2.946 | 2.96 | | 2.96 | 2.945 | 2.905 | | | | |
| Average | | | | | 2.9315 | 2.9818 | 3.0063 | | 3.007 | 2.9863 | 2.9313 | | | | |
| L33 | | | | | Bottom Flange | | | | | Top Flange | | | | | |
| | | | | | 2.92 | 2.938 | | Middle | 2.936 | 2.955 | | | | | |
| | | | | | 2.895 | 2.987 | | | 3.011 | 2.926 | | | | | |
| | | | | | 2.93 | 2.992 | | | 3.002 | 2.906 | | | | | |
| | | | | | 2.921 | 2.947 | | | 2.966 | 2.924 | | | | | |
| Average | | | | | 2.9165 | 2.966 | | | 2.9788 | 2.9278 | | | | | |
| L37 | | | | | Bottom Flange | | | | | Top Flange | | | | | |
| | | | | | 2.907 | 2.929 | | Middle | 2.909 | 2.865 | | | | | |
| | | | | | 2.893 | 2.989 | | | 2.998 | 2.88 | | | | | |
| | | | | | 2.929 | 3.032 | | | 3.005 | 2.894 | | | | | |
| | | | | | 2.882 | 2.919 | | | 2.953 | 2.867 | | | | | |
| Average | | | | | 2.9028 | 2.9673 | | | 2.9663 | 2.8765 | | | | | |
| L45 | | | | | Bottom Flange | | | | | Top Flange | | | | | |
| | | | | | 2.917 | 2.971 | | Middle | 2.9 | 2.894 | | | | | |
| | | | | | 2.878 | 2.988 | | | 2.934 | 2.868 | | | | | |
| | | | | | 2.884 | 2.981 | | | 2.952 | 2.878 | | | | | |
| | | | | | 2.911 | 2.948 | | | 2.918 | 2.916 | | | | | |
| Average | | | | | 2.8975 | 2.972 | | | 2.926 | 2.889 | | | | | |
| L57 | | | | | Bottom Flange | | | | | Top Flange | | | | | |
| | | | | | 2.877 | 2.908 | | Middle | 2.942 | 2.885 | | | | | |
| | | | | | 2.911 | 3.002 | | | 3.004 | 2.922 | | | | | |
| | | | | | 2.904 | 3.006 | | | 3.001 | 2.934 | | | | | |
| | | | | | 2.887 | 2.952 | | | 2.937 | 2.895 | | | | | |
| Average | | | | | 2.8948 | 2.967 | | | 2.971 | 2.909 | | | | | |
| L61 | | | | | Bottom Flange | | | | | Top Flange | | | | | |
| | | | | | 2.921 | 2.954 | | Middle | 2.924 | 2.897 | | | | | |
| | | | | | 2.922 | 3.028 | | | 3.028 | 2.936 | | | | | |
| | | | | | 2.905 | 3.01 | | | 2.937 | 2.923 | | | | | |
| | | | | | 2.925 | 2.958 | | | 2.952 | 2.954 | | | | | |
| Average | | | | | 2.9183 | 2.9875 | | | 2.9753 | 2.9275 | | | | | |